Multi-Scale Effects of Stretch on Peripheral Nerves



Fabio Bianchi

Balliol College

University of Oxford

A thesis submitted for the degree of

Doctor of Philosophy

Trinity Term, 2018

Abstract

Multi-Scale Effects of Stretch on Peripheral Nerves

Fabio Bianchi, Balliol College

Submitted Trinity Term, 2018

Peripheral nerve injury, leading to loss of motor and sensory function, is a burdensome consequence of trauma, surgery or chronic conditions. Mechanical forces play a substantial role in the onset of injury, and affect peripheral nerves at varying length scales, from tissues to individual cells. A multi-scale approach is therefore required to understand how supraphysiological levels of deformation at the nerve level can affect function at the single-cell level.

The aim of this project was to investigate the multi-scale effects of stretch at the tissue and cell length scales, through the development of experimental *in vitro* models of peripheral nerve injury. At the macroscopic (tissue) level, the aim was to quantify the partitioning of strain between nerve and neurons, by measuring microscopic strains during *in situ* extension of peripheral nerves. At the microscopic level, the aim was to quantify the effects of cell strain and mechanical properties on the electrophysiolgical activity of neurons.

At the whole tissue level, the transfer of tissue-scale strain to the micro-scale was investigated by X-ray diffraction and MPM imaging during tensile loading. Axially, the strain in peripheral nerves was shown to partly transfer to the axially aligned collagen

fibres ensheathing the nerve core. The transfer of axial strain to axons was evaluated by using Nodes of Ranvier as markers for digital image correlation, providing a direct relationship between tissue and cell scale mechanics. Radially, a small fraction of the induced compression was transferred to the myelin sheath, suggesting a high stiffness and a potential protective role. Plastic damage in collagenous tissue was examined by evaluating changes in micro-scale mechanical properties, showing distinct behaviours at the collagen fibril and molecule levels. These results establish a mechanical link between nerve extension and microscopic deformations that affect individual cells within the tissue.

In order to investigate the effect at the microscopic cell scale, novel *in vitro* models were developed. A cell-stretching device was designed to apply uniaxial strain to cultured neurons, and simultaneously allow electrophysiological measurements. Human induced pluripotent cells were differentiated to functional motor neurons, and the effect of uniaxial strain was evaluated by measuring the alterations in network and single-cell electrophysiology. Calcium flux imaging showed an immediate decrease in spontaneous network activity with applied strain, and whole-cell patch clamping was used to show changes in ion channel dynamics. C-Laurdan imaging showed a linear fluidisation effect of stretch on the lipid packing of neural membranes, suggesting that the mechanical state of the membrane is changed during straining. Altering the cell membrane's mechanical properties by increasing cholesterol was shown to reduce membrane fluidisation and significantly mitigate the loss of spontaneous activity due to strain.

The development of multi-scale mechanical models can help tissue engineers and clinicians understand how trauma directly affects the functionality of cells. In peripheral nerves that are continuously exposed to mechanical forces, a better understanding of how strain is transferred from the macro-scale to the micro-scale and how this affects neuron activity will help advance preventive and treatment strategies, as well as inform and validate computational models and the design of artificial nerve tissue replacements.

Acknowledgements

First and foremost, I would like to thank my supervisors, Dr. Cathy (Hua) Ye and Dr. Mark Thompson, who supported me throughout this long journey. This thesis and all the work it contains would never have been completed without their guidance, advice, and help. I would also like to thank the EPSRC for the funding granted, as well as China Regenerative Medicine International for funding. A special thanks goes to Balliol College, middle common room friends, staff and fellows, for providing a unique environment to live and work in.

I would also like to thank all collaborators who were involved in parts of the work presented in this thesis. Without them all, this work would have been much less complete, if at all. Dr. Julian George, an endless source of ideas and constant help throughout my work, from designing experiments to writing manuscripts. Dr. Majid Malboubi, for his patience during electrophysiology experiments, and refreshing views on the academic world. Dr. Felix Hofmann and Mr. Rowan Nicholls for their help with X-ray diffraction experiments. Dr. Andrew Smith of Diamond Light Source, for invaluable constant support during experiments. Dr. Antoine Jerusalem and Prof. Zhangfeng Cui for their feedback during the process of transfer and confirmation of status. Dr. Francis Szele, Dr. Zameel Cader, Dr. Satyan Chintawar and Yichen Li, for their help with iPS work. Dr. Mark Richards and Prof. Shankar Srinivas for helping me source tissues for experiments.

Ruby Sedgwick and Linda Li for help during various stages of experiments. Thomas Chui for feeding my cell cultures countless times during my absences.

My gratitude also goes to James Fisk and David Salisbury, for helping me translate ideas, at times far-fetched, into workable designs, and to Graham Brown for technical help with microscopy.

A personal thanks goes to my family, who always supported me during this process, as well as to friends within and without the lab, especially Valerio Pereno, Kya Shoar and Helen Taylor for endless evening of distraction. Finally, a very special thanks goes to Emily Carrington Freeman, who was always by my side during the hardest times of this process, supporting me when the end goal seemed but a far away vision.

Declaration

I hereby declare that this submission is my own work and to the best of my knowledge it contains no materials previously published or written by another person, or substantial proportions of material which have been accepted for the award of any other degree or diploma at the University of Oxford or any other educational institution, except where due acknowledgement is made in the thesis. Any contribution made to this research by others, with whom I have worked at the University of Oxford or elsewhere, is explicitly acknowledged. Any third party content is reproduced either under CC BY or with permission obtained through Copyright Clearance Center.

Dissemination

Parts of this thesis, and work related to the topics covered in this thesis have been published, presented, or are in the process of being published as follows (chapter indicated where publication is directly included or referred to in this thesis).

Journal Publications (In Chronological Order)

1. Fabio Bianchi, Felix Hofmann, Andrew J. Smith and Mark S. Thompson (2016). Probing multi-scale mechanical damage in connective tissues using X-ray diffraction. Published, Acta Biomaterialia, 45, pp.321-327 (**Chapter 2**).

2. Erfan Soliman, Fabio Bianchi, James N. Sleigh, Julian H. George, Zameel M. Cader, Zhangfeng Cui, and HUa Ye (2017). Engineered method for directional growth of muscle sheets on electrospun fibers. Published, Journal of Biomedical Materials Research Part A, 106(5), p. 1165-1176 (**Chapter 5**).

3. Fabio Bianchi, Felix Hofmann, Andrew J. Smith, Hua Ye, Mark S. Thompson. (2018) 'Probing multi-scale mechanics of peripheral nerve collagen and myelin by x-ray diffraction'. Published, Journal of the Mechanical Behaviour of Biomedical Materials, 87,

(2018), p. 205-212 (**Chapter 2**) .

4. Fabio Bianchi, Majid Malboubi, Yichen Li, Julian H. George, Antoine Jerusalem, Francis Szele, Mark S. Thompson, Hua Ye. 'Rapid and efficient differentiation of functional motor neurons from human iPSC for neural injury modelling'. Published, Stem Cell Research, 32, (2018), p126-134 (**Chapter 3**)

5. Sandra Sanchez-Gonzlez, Nazely Diban, Fabio Bianchi, Hua Ye, Ane Urtiaga. 'Composite poly(-caprolactone) and graphene-base nanomaterial membranes: Comparison of GO and rGO on the differentiation and maturation of human neural progenitor cells'. Published, Macromolecular Bioscience 18.11 (2018): 1800195.

6. Fabio Bianchi, Ruby Sedgwick, Hua Ye and Mark S. Thompson. 'Strain partitioning between nerves and axons: estimating axonal strain using sodium channel staining in intact peripheral nerves'. Published, Journal of Neuroscience Methods 309 (2018), p1-5 (**Chapter 2**).

7. Man Ting Kwong, Fabio Bianchi, Majid Malboubi, Julian A Garcia-Grajales, Lina Homsi, Mark Thompson, Hua Ye, Ludovic Noels, Antoine Jerusalem. '3D finite element formulation for mechanical-electrophysiological coupling in axonopathy'. Published, Computer Methods in Applied Mechanics and Engineering 346 (2019): 1025-1050.

8. Fabio Bianchi, Julian H. George, Majid Malboubi, Antoine Jerusalem, Mark S. Thompson and Hua Ye. 'Engineering a uniaxial substrate-stretching device for simultaneous electrophysiological measurements and imaging of strained peripheral neurons'.

Published, Medical Engineering and Physics (March 2019) (**Chapter 3**).

9. Wei-Chun Wei, Fabio Bianchi, Yang-Kao Wang, Ming-Jer Tang, Hua Ye, Maike D. Glitsch. 'Coincidence detection of extracellular pH and membrane stretch by the Gq coupled receptor OGR1'. Published, Current Biology 28.23 (2018): 3815-382

10. Majid Malboubi and Fabio Bianchi, Julian George, Mark Thompson, Hua Ye, Antoine Jerusalem. 'Mechanical and electrophysiological response of SH-SY5Y human neuroblastoma cell line to different culture substrates'. Submitted to The International Journal of Polymeric Materials and Polymeric Biomaterials on 18/07/2018.

11. Fabio Bianchi, Majid Malboubi, Valerio Pereno, Julian H. George, Antoine Jerusalem, Mark S. Thompson and Hua Ye. 'Ionic current and Action Potential alterations in peripheral neurons subject to uniaxial strain'. Published, Journal of Neuroscience Research (March 2019) (**Chapter 4**).

12. Fabio Bianchi, Majid Malboubi, Valerio Pereno, Julian H. George, Antoine Jerusalem, Mark S. Thompson and Hua Ye. 'Membrane mechanical properties regulate the effect of strain on network electrophysiology in iPSC-derived neurons'. Published, Neuroscience 404 (2019): 165-174 (**Chapter 4**).

Conference Presentations (In Chronological Order)

1. Probing multi-scale damage effects and mechanical properties of connective tissues by x-ray diffraction (Poster Presentation) Size-Strain VIII, Oxford, UK, Sept 2015

2. Probing multi-scale damage effects and mechanical properties of connective tissues by x-ray diffraction (talk) European Society of Biomechanics, Lyon, July 2016

3. Collagen to Axons Mechanical effects on peripheral nerves (talk) MEIBioeng 2016, Oxford, UK, Sept 2016

4. 'Mechanically induced functional alterations in peripheral nerves' - International Brain Mechanics and Trauma Lab Workshop, Oxford, 2018

5. 'Membrane cholesterol addition reduces functionality loss in stretch-injured neurons' World Congress of Biomechanics (poster presentation), Dublin, 2018

6. 'Tensile loading with in situ x-ray diffraction suggests high myelin sheath stiffness in peripheral nerve' World Congress of Biomechanics (talk), Dublin, 2018

Contents

1 Introduction **1**

1.1 Anatomy of The Peripheral Nervous System 3

1.2 Mechanisms of Nerve Function 5

1.3 Tensile Forces in the PNS 8

1.4 *In Vitro* Nerve Damage Modelling 14

1.5 Project Aims 15

1.6 Thesis Structure 16

2 Macroscopic Effects Of Nerve Stretch **18**

2.1 Introduction and Background 18

2.2 Probing Multi-Scale Mechanics of Peripheral Nerve Collagen and Myelin by X-Ray Diffraction 25

2.3 Probing Multi-Scale Mechanical Damage in Connective Tissues Using X-Ray Diffraction 41

2.4 Strain Partitioning Between Nerves and Axons: Estimating Axonal Strain Using Sodium Channel Staining in Intact Peripheral Nerves 56

2.5 Chapter Summary 66

3 Development Of *In Vitro* Neuron Stretch Models 70

3.1 Introduction and Background - Neural Cells 70

3.2 Rapid and Efficient Differentiation of Functional Motor Neurons From Human iPSC for Neural Injury Modelling 74

3.3 Supplementary Unpublished Information 93

3.4 Introduction and Background - Cell Stretching Devices 96

3.5 Engineering a substrate-stretching device for simultaneous electrophysiology and uniaxial stretching of cultured peripheral neurons 99

3.6 Supplementary Unpublished Information 121

3.7 Chapter Summary 123

4 Microscopic Effects Of Nerve Stretch 126

4.1 Introduction and Background 126

4.2 Membrane mechanical properties regulate the effect of strain on network electrophysiology in iPSC-derived neurons 138

4.3 Ion current and action potential alterations in peripheral neurons subject to uniaxial strain 156

4.4 Chapter Summary 168

5 Future Work: Towards A Full *In Vitro* PNS Stretch Model 171

5.1 Introduction 171

5.2 *In Vitro* Myelination 173

5.3 Chapter Summary and Future Work 182

6 Conclusions 185

6.1 Overview 185

6.2 Ethical Considerations 188

6.3 Unanswered Research Questions 191

6.4 Summary of Findings and Conclusions 193
6.5 Concluding Remarks 196

Bibliography **198**

List of Figures

1.1 Anatomy of the neuron 4

1.2 Anatomy of the peripheral nerve 5

1.3 The Action Potential 6

1.4 Sunderland nerve injury classification 9

1.5 Tensile forces in axon development 12

2.1 Collagen structure 21

2.2 Bragg's law and X-ray scattering 22

2.3 Quasi-crystalline elements of the peripheral nerve 27

2.4 Experimental setup for nerve X-Ray diffraction experiments 29

2.5 Representative X-Ray diffraction patterns from nerve collagen and myelin . 32

2.6 Tissue strains as a function of load 34

2.7 Molecular strains as a function of load 34

2.8 Collagen and myelin strain partitioning 35

2.9 Molecular strains against tissue strains for axial and radial directions . . . 36

2.10 Putative mechanism of nerve mechanics 37

2.11 Experimental setup for tendon collagen x-ray diffraction experiments . . . 43
2.12 Fibril D-period and amino-acid spacing variation with damage 47
2.13 Stress-strain curves from in situ tensile loading of tendon fascicles, and elastic modulus relation to damage 49
2.14 Molecular elongation and rearrangement contributions to fibril deformation 50
2.15 Effects of X-ray exposure on collagen 55
2.16 Experimental setup overview for MPM nerve imaging 59
2.17 Node of Ranvier staining in whole sciatic nerves 60
2.18 Measured axonal strain with appied tissue strain 62

3.1 Cell sources used in currently published research on *in vitro* neuron deformation 71
3.2 Differentiation pathways from pluripotent stem cell to different neural fates 72
3.3 iPSC to motor neuron differentiation timeline 79
3.4 Neural progenitor marker expression 83
3.5 Expression of motor neuron progenitor markers 84
3.6 Expression of neuron markers 85
3.7 Calcium activity and patch-clamping of iPSC-derived motor neurons . . . 86
3.8 Validation of differentiation protocol in a second iPSC line 87
3.9 Network spontaneous activity decreases with unixial strain 89
3.10 iPSC puripotency staining (alkali phosphatase) 94
3.11 Comparison of neural progenitor cell expansion in different basal mediums 94
3.12 Cell stretching device components and cells 103
3.13 Methods for experimental and simulated substrate strain quantification . . 105
3.14 Patch clamping of stretched neurons 109
3.15 Calcium imaging on microgrooved surfaces 110
3.16 Nucleus height measurement in stretched neurons 111

3.17 Experimental and simulated strain characterisation 112
3.18 Effect of microgrooves on substrate strain 113
3.19 Nucleus and membrane deformation 114
3.20 Slopes of membrane and nucleus strains as a function of applied strain . . 121
3.21 Effect of cell orientation on nucleus and membrane strain 122

4.1 Most common configurations of the patch-clamp technique 135
4.2 Experimental setup for cell straining and calcium imaging 140
4.3 Calcium imaging protocol 142
4.4 C-Laurdan spectral imaging of lipid packing 143
4.5 Strain measurements in cell nuclei and membranes 146
4.6 Changes in lipid packing with applied strain 147
4.7 Changes in network electrophysiology with applied deformation for cholesterol-enriched and control cells 148
4.8 Experimental setup for cell straining and patch-clamping 159
4.9 Whole-cell patch clamp of stretched and unstretched F11 neurons (sodium currents) 161
4.10 Whole-cell patch clamp of stretched and unstretched F11 neurons (potassium currents) 162
4.11 Action potential and membrane resting potential during stretch 163

5.1 Characterisation of primary cells for myelination assays 176
5.2 Flow cytometry characterisation of ADSC multipotency markers 178
5.3 Differentiation of rat ADSC and human MSC to Schwann-like cells 180
5.4 Neurite extension for primary neurons co-cultured with ADSCs 181
5.5 MSC culture on aligned microgrooves 182
5.6 Towards a full PNS model of mechanical damage 183

List of Abbreviations and Acronyms

ADSC ..... Adipose Derived Stem Cells

AFM ..... Atomic Force Microscopy

ALS ..... Amyotrophic Lateral Sclerosis

ANOVA ..... ANalysis Of VAriance

AP ..... Action Potential

ATP ..... Adenosine TriPhosphate

BDNF ..... Brain Derived Neurotrophic Factor

bFGF ..... Fibroblast Growth Factor

BMP ..... Bone Morphogenic Protein

BSA ..... Bovine Serum Albumen

CASPR ..... Contact ASsociated PRotein

CNC ..... Computer Numerical Control

CNS ..... Central Nervous System

DAI ..... Diffuse Axonal Injury

DAPI 4,6-diamidino-2-phenylindole

DIC ..... Digital Image Correlation

DMSO ..... DiMethyl SulfOxide

DRG ..... Dorsal Root Ganglion

EB ..... Embryoid Body

EDTA ..... EthyleneDiamineteTraacetic Acid

EGF ..... Epidermal Growth Factor

ESC ..... Embryonic Stem Cell

FACS ..... Fluorescence-Activated Cell Sorting

FBS ..... Foetal Bovine Serum

FEM ..... Finite Element Method

FITC ..... Fluorescein Isothiocyanate

FWHM ..... Full Width Half Maximum

GDNF ..... Glial Derived Neurotrophic Factor

GP ..... Generalised Polarisation

GTP ..... Guanosine Triphosphate

HD ..... High Definition

HEPES ..... 4-(2-hydroxyethyl)-1-piperazineethanesulfonic acid

HH ..... HedgeHog

HRG ..... Heregulin

iPSC ..... Induced Pluripotent Stem Cell

KV ..... Voltage Gated Potassium Channels

L-AA ..... L-Ascorbic Acid

MBCD ..... Methyl-Beta-Cyclodextrin

MG ..... MatriGel

MN ..... Motor Neuron

MNP ..... Motor Neuron Progenitor

MPM ..... Multi-Photon Microscope

MRP ..... Membrane Resting Potential

MSC ..... Mesenchymal Stem Cell

NaV ..... Voltage Gated Sodium Channels

NBM ..... NeuroBasal Medium

NEAA ..... Non-Essential Amino Acids

NGF ..... Nerve Growth Factor

NMJ ..... NeuroMuscular Junction

NoR ..... Node of Ranvier

NPC ..... Neural Progenitor Cell

NT-3 ..... NeuroTrophin-3

PBS ..... Phosphate Buffered Saline

PDGF ..... Platelet-Derived Growth Factor

PDMS ..... Polydimethylsiloxane

PLO ..... Poly-L-Ornithine

PNI ..... Peripheral Nerve Injury

PNS ..... Peripheral Nerve System

qPCR ..... Quantitative Polymerase Chain Reaction

RA ..... Retinoic Acid

ROCK ..... Rho-associated Protein Kinase

ROS ..... Reactive Oxygen Species

SAG ..... Smoothened Agonist

SAXS ..... Small Angle X-ray Diffraction

SC ..... Schwann Cell

SEM ..... Scanning Electron Microscope

SHH ..... Sonig HedgeHog

SNP ..... Single-Nucleotide Polymorphism

SPR ..... Strain Partitioning Ratio

TBI ..... Traumatic Brain Injury

TGF ..... Transforming Growth Factor

TTX ..... Tetrodotoxin

WAXS ..... Wide Angle X-ray Diffraction

XRD ..... X-Ray Diffraction

CHAPTER 1

Introduction

The disciplines of tissue engineering and mechanobiology have been closely linked since the inception of regenerative medicine. In the human and animal bodies alike, tissues and cells are continuously exposed to mechanical stresses and stimuli, and have adapted to withstand the mechanical environment in which they operate. Mechanotransduction is a key stimulus at both the tissue and cellular level, with effects on cell proliferation, differentiation, phenotype regulation, gene and protein expression and on the interaction between microscopic cells and macroscopic tissues [1]. Tissue engineering therefore requires an in-depth understanding of the mechanical properties of cells and tissues; by applying mechanical stimuli similar to those occurring *in vivo*, highly functional tissue repair solutions can be engineered *in vitro*. Furthermore, experimental *in vitro* models can provide a platform to gain a better understanding of damage mechanisms, leading to novel strategies for damage prevention and repair.

Nerve injury is a common problem that has been documented for thousands of years. Researchers have postulated that the earliest known record of nerve injury is to be found in biblical texts where, in the Book of Genesis, Jacob is described to have suffered what is believed to be a sciatic neuropathy from hip damage following battle with the angel [2].

Research interests have historically been more focussed towards central nervous system (CNS) injuries. A simple PubMed search reveals an approximately five-fold increase in results pertaining to CNS versus peripheral nervous system (PNS) injury. However, PNS trauma can also lead to seriously impaired quality of life and to a heavy financial burden on the healthcare system. In the US, peripheral nerve injuries (PNI) account for 150 billion USD in annual medical costs, and 200,000 related surgeries [3]. Nerve damage associated with trauma has severe outcomes including paralysis, sensory impairment, loss of motor function and lack of autonomic control, and is a widespread burdensome condition for both patients and healthcare services. In Europe alone, upwards of 300,000 working-age people suffer from PNI each year, of which less than half regain full function following treatment [4]. Around 3-5% of all trauma cases in the USA alone (arising from motor vehicle accidents, industrial accidents, falls and wartime injuries) include varying degrees of peripheral nerve involvement [5]. Traumatic dislocation and fracture of joints are also common causes of PNI, especially in the sciatic nerve, with an average incidence of 10% in adults [6]. PNI is not limited to adults. Erb's palsy, an infant condition caused by brachial plexus overstretching at birth, can cause temporary or chronic loss of sensory and motor function and affects 0.1% of US births annually [7]. Nerve damage may also be caused by chronic conditions such as carpal tunnel syndrome (CTS), where the median nerve is compressed within the carpal tunnel at the wrist resulting in nerve pinning and abnormal stress and strain distribution during movement. CTS has a prevalence in the United Kingdom of 5-16% annually and requires decompression surgery in 0.05% of the UK population [8, 9]. Trauma is not the only cause of nerve injury: around 12% of peripheral

neuropathies are iatrogenic; perioperative injuries caused by limb misplacement during operational anaesthesia leading to injury in nerve trunks and roots [10].

The high incidence and prevalence of PNI contrasts with the slow development of novel approaches to prevention and treatment. Treatment options vary with injury severity. Severe PNI usually requires surgery, either by end-to-end suturing of severed nerve ends or by using a nerve graft or conduit (autologous or tissue engineered). Biological, chemical and electrical stimuli have been used to help restore function in less severe injuries, as well as to promote regrowth within grafts and conduits [11]. Due to the mechanosensitivity of PNS cells, tissue engineering approaches to nerve repair such as artificial conduits require an extensive understanding of the biomechanical environment, and therefore mechanical properties have been considered as key design constraints for the development of novel tissue engineering solutions [12, 13, 14].

The lack of development of *in vitro* PNS models has been recognised as a factor hindering the development of clinical PNI treatment and of preventive strategies [15]. There is an urgent need for *in vitro* models aimed at understanding the effect of mechanical stretch on peripheral nerves and how this leads to injury, allowing researchers access to lower cost, controllable, and customisable experimental environments to further the understanding of process of nerve damage and to test novel repair and prevention strategies. Due to the complexity and heterogeneity of peripheral nerve tissue, a multi-scale approach is required, to understand how stretch applied at the macroscopic tissue level is translated to the cellular scale, and how this affects nerve function.

1.1 Anatomy of The Peripheral Nervous System

The mammalian peripheral nervous system (PNS) is made up of the somatic nervous system (including somatic (voluntary) motor nerves and somatic sensory nerves), and the autonomic nervous system controlling unconscious automatic mechanisms [16].

The smallest component of peripheral nerves are nerve fibres: outgrowths of neurons housed in the spinal cord and ganglia, which can be myelinated or unmyelinated. Myelin is an electrically insulating protein and phospholipid layer formed by Schwann cells (SCs) wrapped multiple times around the axon, which allows the conduction of high-speed saltatory action potential signals down the nerve. Most neurons share common morphological features: a cell body (soma) housing the nucleus and other organelles, an axon transmitting signals away from the neuron, and dendrites relaying signals to the neuron (figure 1.1). Primary sensory neurons have no dendrites, instead two axonal processes carrying signals away from (central axon) and towards (peripheral axon) the cell bodies housed in dorsal root ganglia. [16].

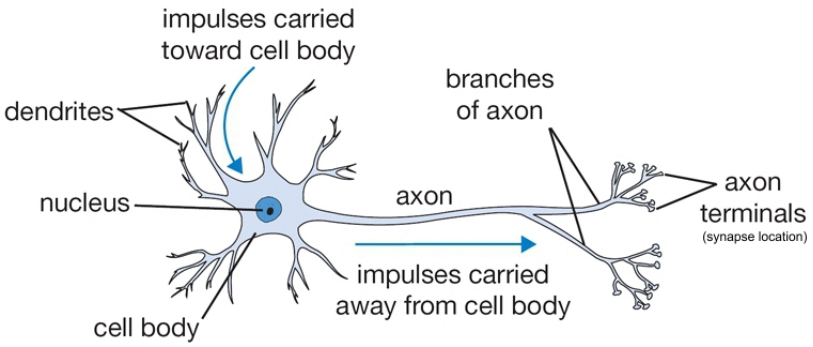
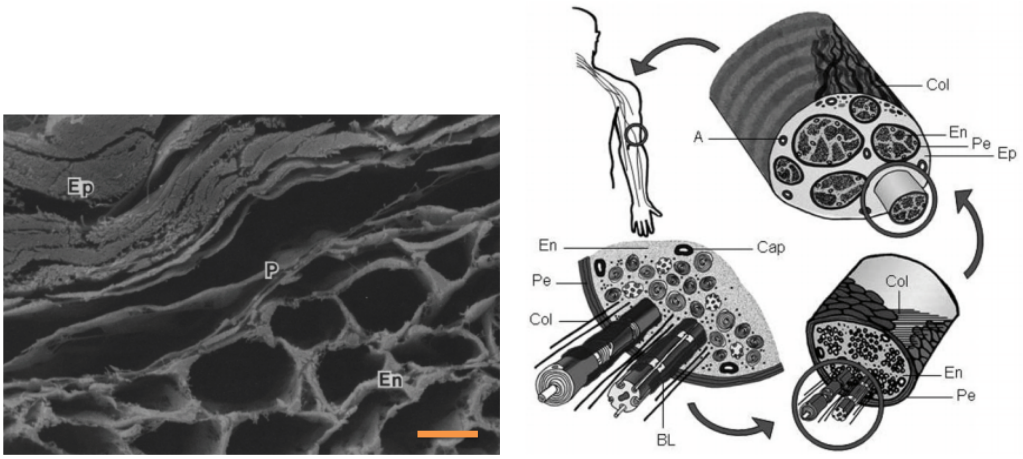


Figure 1.1: The basic components of neurons showing multiple afferent branches (dendrites), one efferent branch (axon), terminal synapses, and the cell body containing nucleus and other organelles

Nerve fibres are surrounded by multiple layers of collagenous connective tissue. The smallest in scale is the endoneurium, which surrounds the individual nerve fibres and consists of loosely packed axially aligned collagen fibre 'tubes' and sparse fibroblasts (figure 1.2). Surrounding the bundles of nerve fibres is the perineurium, a cell-rich environment made up of radially-aligned collagen fibres with a minor presence of elastin. At the largest hierarchical scale is the epineurium, made up of dense collagen fibres mostly parallel to the direction of the nerve trunk axis, with a minor presence of elastin fibres and sparse fibroblasts of elongated morphology [17, 18]. This is the thickest and most dense layer,

which together with the perineurium has been implicated as the main load-bearing element in peripheral nerve [19].



(a) (b)

Figure 1.2: (a) Scanning electron microscopy of the structure of collagen in the three layers of acellularised peripheral nerve connective tissues [17]. (b) Anatomy of the peripheral nerve, showing the hierarchical structure of connective tissue and myelinated nerve fibres [20]. Col = collagen fibres. En = endoneurium. Pe = perineurium. Ep = epineurium. BL = basal lamina. Cap = capillaries. A = arterioles. Scale bar = 5μm.

1.2 Mechanisms of Nerve Function

The PNS is made up of spinal and cranial nerves, and its function is to relay afferent and efferent signals between the CNS and the periphery of the body. Signals are transmitted by rapid reversals in the membrane potential of excitable neural cells, termed action potentials (APs). At rest, neural membrane potential is kept at around -60mV by active and passive processes. Ionic diffusion is balanced by electrostatic forces, and ion exchange pumps (for example the sodium/potassium pump) regulate intracellular ionic concentrations maintaining the resting potential. Chemical, mechanical, or electrical stimuli cause a rapid increase (depolarisation) in neural membrane potential, and if a threshold is reached then an AP is initiated. During AP firing membrane potential reverses, and reaches a peak around +30 mV before re-polarising. If the resting potential is overshot, the neu-

ron is hyperpolarised and a latency period follows, during which the membrane potential slowly returns to the resting value and no further AP can be initiated (figure 1.3).

In prevalent neural membrane theory, neuron depolarisation and repolarisation are mediated by ion channels; gated transmembrane proteins that, when open, are permeable to specific ions [21, 22]. The largest population of ion channels are voltage-gated, relying on changes in membrane potential to determine the transition between open and closed states. During AP initiation voltage-gated sodium channels (NaVs) rapidly open, allowing an influx of Na^+ ions and depolarising the membrane. At positive membrane potentials the channels inactivate, stopping the Na^+ influx. At this point voltage-gated potassium channels (KVs) have also opened (as KV channel opening time constant is much larger than that of NaVs), causing efflux of K^+ ions that sets up a rectifying outwards current, repolarising (and then hyperpolarising) the membrane. Voltage-gated Na^+ and K^+ channels can inactivate following continuous levels of membrane potential above activation thresholds, thus avoiding uncontrolled auto-excitation and introducing a latency between successive channel openings. This causes the membrane to undergo a refractory period, which stops antidromic signal propagation (figure 1.3) [23, 22].

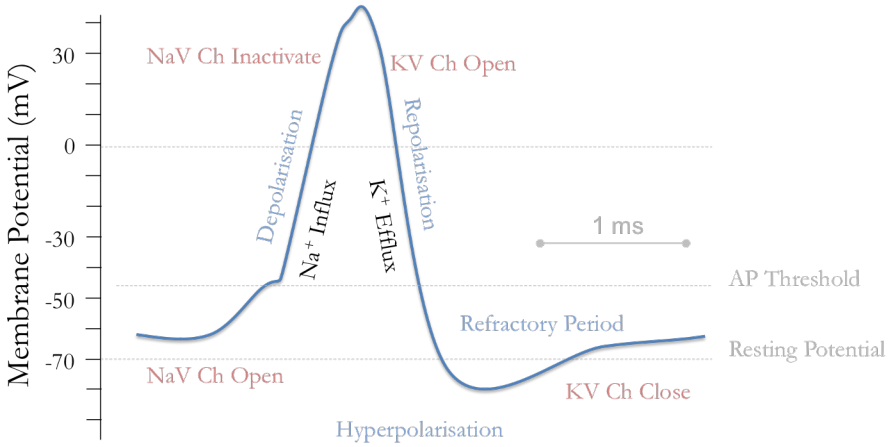


Figure 1.3: Action potential mechanism, showing changes in membrane potential, and ion channel state during initiation and firing.

The neural growth process coincides with axonal myelination. Myelin is laid in a continuous pattern with periodic gaps between successive SCs called nodes of Ranvier (NoR). During myelination, SC envelopment causes rearrangement of axonal ion channels, leading to increased sodium channel clustering at nodes and potassium channel dispersion along the internodal region [24]. Myelin is an electrical insulator, and therefore forces micro-currents to establish between NoRs, where the axonal membrane and ion channels are exposed to the surrounding fluid. This depolarises the axon in discrete sections, increasing the speed of signal transmission. High NaV density at NoRs allows for AP propagation at lower thresholds, and thus the AP signal 'saltates' between nodes resulting in an overall ten-fold increase in conduction speed compared to unmyelinated nerves. In non myelinated axons, local membrane depolarisation causes micro-currents that in turn depolarise the axon region ahead of the advancing AP [16].

The arrival of an action potential at the neuron's synaptic terminal triggers an influx of calcium ions through voltage-gated calcium channels that in turn initiates the release of neurotransmitters. G-coupled protein receptors and ligand-gated ion channels at the postsynaptic neuron are activated by the neurotransmitter, and can cause excitation or inhibition of the postsynaptic cell. In cases of electrical synapsing, inter-cell communication does not involve chemical signalling but instead relies on ion flow between pre- and post-synaptic cells through gap junctions. If the overall stimulus is predominantly excitatory, the postsynaptic neuron will fire, and an AP will propagate down the axon [22, 16].

1.3 Tensile Forces in the PNS

1.3.1 Nerve Damage and Regeneration

The absence of an ossified protective structure exposes the PNS to mechanical trauma, as well as to straining during everyday movement. When stresses and strains in nerves exceed physiological levels, injury of cells and connective tissues can result. Supraphysiological extension of nerves can cause deficits in conduction, leading to temporary or chronic loss of sensory or motor function, and in severe cases compromise the nerve continuity [25, 26].

Nerve damage is classified according to a scale originally developed by Sunderland in the mid 20th century (figure 1.4), and can be caused by tension, compression, shear, or transection [27]. Whilst the latter involves compromised neuronal continuity, less extreme compression and tension injuries cause altered functionality without loss of structural integrity. Axonotmesis involves the disruption of axonal continuity with minor involvement of connective tissues, whilst neurotmesis implies a full truncation of the nerve implicating connective tissues and cell-cell interactions (figure 1.4) [5, 27].

Prognosis after trauma implicates anatomical features beyond the localised injury site, with changes at the soma of the damaged cell, wider neural network, and innervation target organ [28, 29]. Minor nerve damage caused by mild compressions or stretch induces conduction blocks (neuropraxia), where axons fail to propagate action potentials. This can lead to impaired sensory and motor function, although the long-term consequences are often not severe [5]. With increasing injury complexity, the factors affecting the probability of successful regeneration multiply, and a multi-scale understanding of the effects of trauma is increasingly important to identify early targets for treatment.

At the cellular scale, nerve damage initiates multiple cascades of biochemical signals. In the first days following injury axons in the distal portion of the nerve undergo Wallerian degeneration, where axonal cytoskeletal elements are broken down by calcium-mediated

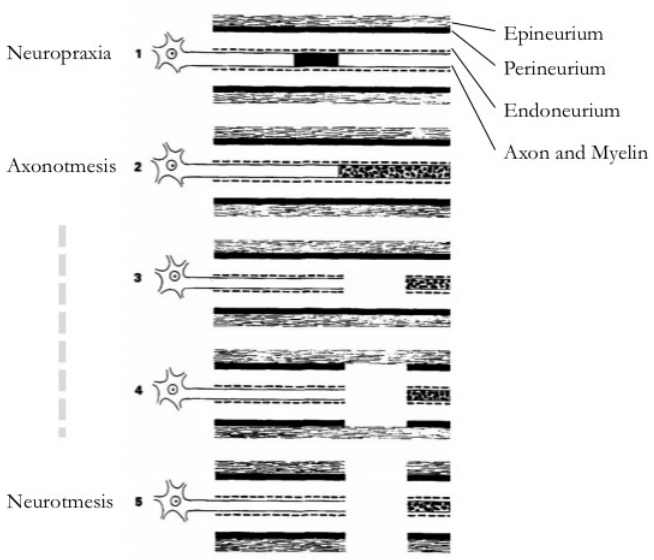


Figure 1.4: Classification of nerve injury, with implication of different structural components of the peripheral nerve. Adapted from [30]

proteases, and neurons increase in volume and upregulate the production of regenerative proteins. Schwann cells (SCs) undergo phenotypic change and revert to a regenerative, non myelinating state. Macrophages are recruited to the damaged site, and clear myelin and axonal debris. SCs downregulate structural proteins of the myelin sheath and basal lamina, and upregulate cell adhesion molecules and neurotrophic factors. Following debris removal, SCs migrate to form aligned structures called Bands of Büngner that provide topographical and neurotrophic cues to facilitate reinnervation. Bodies of damaged neurons undergo chromatolysis and revert to a growth state similar to that observed in embryonic neurons. Neurons that successfully revert to a regenerative state then extend growth cones down the bands of Büngner and pull axons towards re-innervation target points at approximately three mm per day. [29, 31, 32]

Innervation target organs at the distal end of the injured nerve are also affected by injury. Muscle atrophy can occur if deinnervation is sustained for weeks. Sensory organs such as Merkel cell complexes (for pressure sensing) and Ruffini corpuscles (for kinesthetic finger control) don't atrophy and can be reinnervated long after injury [29, 31].

Partial compound action potential recovery can be observed within 12 weeks of axonotmesis [33], whilst reversible conduction blocks caused by neuropraxia tend to recover faster [34], but the mechanisms linking peripheral nerve injury and changes in function are not completely understood, resulting in few treatment options. The success of nerve regeneration following trauma is largely dependent on injury severity, and incomplete regeneration can leave patients with severely debilitating losses of sensory and motor function. Age, time from injury, fibrosis, and injury location can further decrease regenerative outcome.

Strategies for treatment of nerve damage also vary depending on injury severity. For small defects surgical intervention is limited to suturing distal and proximal ends of the nerve, and allowing natural re-growth. The successful outcome of re-suturing is however limited by axon misdirection, potentially resulting in incorrect function, leaking of neurotrophic factors outside the nerve, and scar tissue formation. Furthermore, suturing can create high stress concentrations in tissues, further hindering regeneration. For larger defects, nerve conduits promoting re-growth and re-innervation are required. Autologous grafting is the gold standard, providing fresh growth-permissive tissue, but requires an invasive operation sacrificing an expendable nerve elsewhere in the body, resulting in high donor site morbidity [15, 35, 11]. Allographs from non-human tissues pose the risk of immune rejection and are not guaranteed to be freshly excised, making them less growth-permissive. Tissue engineering solutions such as nerve conduits and acellularised allographs, which include supporting cells (autologous Schwann cells, mesenchymal stem cells), neurotrophic factors, and electrical stimulation have been used as alternative strategies for peripheral nerve repair [15, 35, 11]. Mechanical compatibility of artificial conduits is also an important factor. In order to provide a growth-permissive long-term platform for regeneration, the replacement material must match the mechanical properties of the injured nerve [12, 13, 14]. Despite research efforts and commercial product development,

there still exists a large discrepancy between technologies developed in laboratories and products used in the clinic, in part attributed to the insufficient understanding of the mechanical, biological and physical cues that govern regeneration [15].

Mechanical tension itself has also been investigated as a regenerative strategy. Nerves and axons are known to grow in response to low-rate stretching [36], and this has been used to develop prototypes of fixation devices that grip the two ends of a severed nerve, and grow it by applying constant tensile force [37, 38]. Tension-growth has been evaluated in animal models, but has not yet been applied in a clinical setting [37, 38, 39]. A better understanding of the transfer of macroscopic strain to the nerve microstructure and the effect this has on nerve functionality can help to further develop these techniques as well as improve prevention and intervention for PNI, and improve the design of artificial nerve replacement materials.

1.3.2 Forces in PNS Development

Mechanical forces are not only implicated in nerve damage, but vitally contribute to the development of the nervous system. During early development axonal growth is regulated by the growth cone, made up of structural microtubles terminating with an actin network driving growth by tension applied through the retrograde flow of actin filaments [40]. The growth cone leads the neuron to its target innervation point where a synaptic connection is formed. With organism growth the neuron, fixed at both ends, elongates by stretching (figure 1.5) [41]. In 1984, Bray showed that this process is stretch-rate limited with a clear boundary between growth and rupture, using an *in vitro* model of micropipetter-tethered axonal elongation [42]. In 1991, Zheng et Al. showed how this process is very sensitive to the rate of imposed elongation, and postulated that the axon grows by interstitial membrane addition during stretch [43]. More recently, this process has been used to produce stretch-grown dorsal root ganglion cells up to 10 cm in length without disconnection [36],

which were shown to retain their electrical conduction properties and ion channel dynamics [44]. Previous work has also shown that during stretch-growth axons first thin and then thicken back to normal values, suggesting a time-delayed transport process activated during stretch [36]. Interestingly, stretch-growth and traumatic elongation have very different effects on neuron eletrophysiology. Loverde and Pfister have shown that sub-injury stretch stimulates growth whilst maintaining unaltered electrophysiological and morphological properties in dorsal root ganglion neurons, whereas traumatic stretching causes alterations in electrophysiology and cell morphology [45]. Schwann cells have also been shown to respond to sustained sub-lethal tension by elongating and growing [46]. All these results point to a specific threshold of mechanical stimulus above which conduction blocks and cellular damage occur, and below which axonal growth is stimulated. This points to two distinct regimes of loading: a regenerative regime that can be exploited to produce stretch-grown axons and to regenerate severed nerves, and a traumatic regime, where the nerve is damaged to the point that it fails to propagate action potentials.

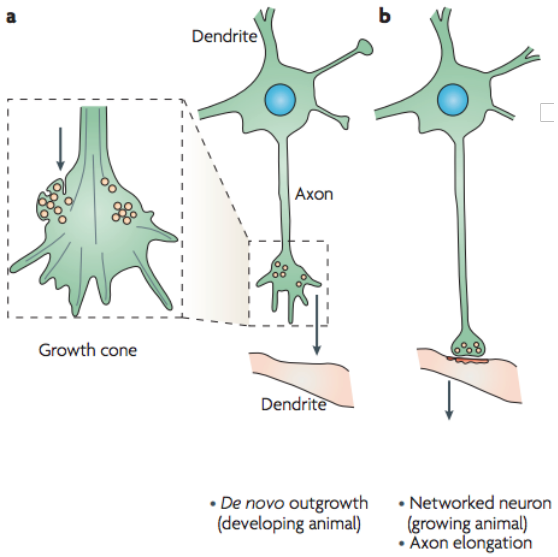


Figure 1.5: Mechanisms of axon elongation during development, showing the effect of tensile forces on neurons. (a) The growth cone drives axonal outgrowth. (b) The neuron synapses with its innervation target, and is stretched during organism growth. Adapted from [47]

1.3.3 Everyday Forces in the PNS

Peripheral nerves are subject to daily stresses and strains, and must be able to stretch and deform to accommodate limb and joint movement. Nerve excursion and strain induced by limb movement have been studies in both cadavers and patients, as well as in animal models. For example, flexion of the hip during knee extension has been shown to induce an increase in strain of 2-4% [48], and hip flexion during straight leg raise test induced strains between 2.3 and 5.5% in the tibial nerve and between 1.06 and 1.22% in the plantar nerve [49]. The reported variability can be attributed to non-homogeneous nerve mechanical properties, which have been linked to the proximity to joints in a rat model, where higher strain and lower stiffness has been measured at joint nerve sections, compared to non-joint sections [50, 18].

Multiple mechanisms allow nerves to withstand daily straining. The whole nerve trunk is allowed to 'glide' within the limbs, by a layer of tissue which tethers it to the surrounding tissue [51]. This allows for excursion of the nerve during limb movement, without build-up of strain. Within the nerve trunk, the core (containing nerve fibres) and sheath (mainly consisting of connective tissues) are connected by an interface layer that allows sliding of the core within the sheath [52]. This allows for further movement of the nerve without loading the fragile neural fibres within. The nerve is further protected from excessive straining by crimping, which can be observed both in connective tissues and in the nerve fibres [20, 53], and which disappears only beyond physiological strain limits where the collagenous tissue is disrupted [54]. Crimping allows slackening of the crimp undulations at low strains, before the tissue starts bearing load. It has been shown that nerves in Rorqual whales, which elongate by up to 160% during feeding, have extremely thick epineuriums (up to 96% of cross sectional area), and exhibit multiple levels of waviness to endure extreme elongation without resulting in functional failures [55].

1.4 *In Vitro* Nerve Damage Modelling

In vivo animal models are the gold standard for the study of peripheral nerve damage, but low specificity and growing ethical concerns have seen a recent push for the development of *in vitro* models [56, 57]. Due to its size and surgical accessibility, the sciatic nerve is widely used as an animal model of nerve injury and regeneration [58]. Computational *in silico* models to simulate the effects of injury at a structural and functional level in PNS and CNS have been developed, but require experimental data for calibration and validation, and often are unable to capture the extensive complex interactions between mechanical, biochemical, and electrical alterations in damaged nerves [59, 60, 61]. The advantage of *in vitro* models is that they allow the study of single cell behaviour as well as cell-cell and cell-extracellular matrix interactions in an environment where the number of variables can be controlled. In both *in silico* and *in vitro* models, a better understanding of how bulk tissue strains and stresses are transferred to the cellular scale would help advance understanding of thresholds for mechanical injury in neurons [61, 62, 63].

Although not fully representative of PNS structure or physiology, a number of *in vitro* and *in vivo* CNS tissue injury models have been developed, and can provide some insight on PNS functional alterations as a result of trauma. Models for PNS injury are not as common, and are mostly limited to 2D cell culture models [64, 65]. Some efforts have been made to produce *in vitro* 3D models of the structure of peripheral nerves [66, 67], but there is an unmet need for specialised *in vitro* models targeted at mechanical injury investigation. In recent years, with increased understanding of stem cell differentiation, various groups have started developing PNS models based on neurons and SCs derived from human stem cells [56]. This encourages reduction of animal testing, whilst providing physiologically accurate results from models which more closely resemble

human physiology. Despite this, *in vitro* neuron dysfunction and damage studies using stem cells remain limited.

1.5 Project Aims

In order to develop novel strategies for the prevention and treatment of PNI, a multi-scale approach involving mechanical, biochemical, and electrophysiological understanding of the processes involved in mechanical damage is required.

The aim of the work presented in this thesis was to experimentally investigate the multi-scale effects that mechanical tension produces in peripheral nerves.

Starting at the macroscopic scale, the aim was to quantify the relationship between whole-tissue deformation and strain at the cellular level, in order to understand the microscopic implications of whole nerve loading. By using X-ray diffraction and high-resolution microscopy methods, the mechanical behaviour and damage mechanisms in peripheral nerve collagen, axons, and myelin were investigated to relate macroscopic tissue-scale deformation to microscopic cell-scale changes.

At the microscopic level, the aim was to quantify the effect of tensile cellular deformation on neural functionality by developing *in vitro* cell-stretching models and observing how cell electrophysiological activity was altered by deformation, both at a network and single-cell level.

In the long-term, the future of this project is to use a co-culture of human stem-cell derived peripheral neurons and Schwann cells to produce a physiologically accurate PNS model, combining this with the strain damage model developed here. This would produce a flexible platform to investigate PNS injury, and for testing of preventive and regenerative strategies.

The results presented in this thesis, alongside the methods developed, provide a comprehensive insight of the multi-scale mechanical behaviour of peripheral nerve subject to

stretch. The outcomes from this project have two main applications. Tissue engineered solutions for nerve repair can be improved in the future by designing materials and structures to replicate the mechanical functioning of the native tissue. The results relating to the macroscopic mechanical behaviour, as well as to the transfer of strains from macroscopic to microscopic scales, can be used to design mechanically biomimetic constructs for nerve repair. The second application would bring together the results from all length-scales investigated to calibrate and help develop a comprehensive computational model of the effect of stretch on peripheral nerve, which combines the material effect of strain with a prediction of the effects on cellular function. By increasing the complexity of the *in vitro* model (for example by including myelination), a computational model model can be refined based on experimental data, and can help model traumatic events, prevention strategies, and post-injury intervention methods.

1.6 Thesis Structure

This thesis follows the integrated thesis structure, where articles published (or submitted for publication) in peer-reviewed journals are presented without content changes. Bibliographies and figure numbers from all articles have been merged to provide continuous referencing throughout the thesis. Article abstracts have been removed for reader clarity. The contribution of all authors named in the articles is clearly acknowledged at the end of each chapter, and published versions of the articles are referenced.

This thesis is arranged around three main themes, reflected by the three central chapters. The first chapter details macroscopic (tissue-scale) effects of stretch, reporting three sets of experimental results aimed at relating nerve strains at the macro-scale to strain and mechanical properties at the micro- and nano-scale. The second chapter reports the development of in vitro PNI models to study the effects of stretch on peripheral nerve. A protocol for the differentiation of induced pluripotent stem cells to motor neurons for

neural injury studies is presented, and the design of a novel substrate-stretching device to study electrophysiological alterations in stretched neurons is presented and characterised. The third chapter focuses on microscopic (cell-scale) effects of nerve stretch, reporting experimental investigations of network and single-cell electrophysiological alterations caused by stretch. A final chapter, presenting exploratory work, will introduce the future direction of this research towards building a full PNS models for mechanical deformation studies.

CHAPTER 2

Macroscopic Effects Of Nerve Stretch

2.1 Introduction and Background

Three studies are presented in this chapter. The first aimed to evaluate the mechanical behaviour of myelin and collagen in rat sciatic nerves subject to axial tensile loading using X-ray diffraction. Strain magnitudes used were physiologically representative of values at which conduction blocks are observed in peripheral nerves.

The second XRD study focused on collagen structural damage, using rat-tail tendons as a model to investigate changes in mechanical and structural properties of collagen at the fibril and molecular level following a pre-applied plastic deformation corresponding to the lower bound of conduction block inducing strain ($\sim$ 5%). Tendons have been investigated as a possible source of material for nerve grafts, suggesting a mechanical similarity between the two [68].

The final section of this chapter presented a study reporting experimental work aimed at relating macroscopic nerve strains with microscopic cellular strains, using MPM imaging of nodes of Ranvier as fiducial markers during whole-nerve elongation to establish a direct mechanical link between tissue and neuron deformation.

All tissues used for experimental work described in this chapter were obtained from animals sacrificed for unrelated experiments.

2.1.1 Mechanical Models of Peripheral Nerve

The mechanical behaviour of peripheral nerves has been extensively characterised both *in vivo* [69, 34] and *ex vivo* [70, 71]. Peripheral nerves have been described as composite viscoelastic materials made up of a soft core and a stiffer outer sheath. Anatomically, the water-rich core represents the endoneurium, the inner part of the perineurium, and myelinated and unmyelinated axons, whilst the outer sheath represents the epineurium and outer perineurium, connected by a sliding interface layer [52, 51, 19]. Nerves loaded in axial tension have been shown to axially extend non-linearly and to contract circumferentially, with a toe region at lower loads and stiffer behaviour at higher loads [72], and exhibit a characteristic load-deformation (or stress-strain) curve consisting of a prolonged toe region (where connective tissue and axonal crimps straighten), followed by a linear region until failure [54, 73, 74].

The epineurium and perineurium have both been implicated as the main load-bearing structures, whilst the inner core has been shown to be significantly less stiff than the surrounding sheath [74, 70, 75]. This suggests that the outer collagenous layers of connective tissues have a significant mechanical role, and reduce the deformation of the sensitive core elements. Accordingly, hereditary genetic collagen disorders such as Ehlers-Danlos are thought to impact nerve mechanical properties, reducing their ability to withstand stress [76]. Second harmonic imaging of strained nerves has been used to show that the

peripheral nerve collagen structure is affected from strains as low as 4%, and becomes compromised between 15 and 20% strain [54]. It is therefore important to understand how peripheral nerve collagen behaves during loading, and how damage processes affect the microscopic structure of collagenous connective tissues.

The myelin sheath is also thought to contribute to the mechanical properties of the nerve, but the extent of this is not well understood. Mechanical testing of acellularised (and therefore demyelinated) peripheral nerves has been used to shown a significant change in some mechanical properties (ultimate stress, work to failure), but no difference in others (Young's modulus, ultimate strain). In the same paper, these changes have been speculatively attributed to the decellularisation process itself, rather than to the contribution of myelin to the nerve mechanical properties [77]. In chick embryo spinal cords, demyelinated tissues have been shown to be significantly less stiff, although again the demyelination process itself may have affected tissue properties [78]. AFM indentation studies have shown significant stiffness and resilience differences between myelinated and unmyelinated nerve fibres, suggesting a more significant mechanical role for myelin in compression [79, 80], but no direct relationship between myelin deformation and nerve axial elongation has yet been established.

2.1.2 Collagen and Myelin Structure

During early development, nerve fibres are ensheathed by immature Schwann cells (SCs) that deposit basal lamina material (primarily non-fibril forming collagen-IV). The same SCs start producing fibrillar collagen at late development stages, after which fibroblasts migrate to the developing nerve and produce the bulk of structural fibrillar collagen (types I, III and V) [81]. Collagen is the most abundant protein in mammalian organisms, making up $30-40\%$ of all protein content. Type I is the most abundant collagen subtype, and is organised in a hierarchical structure (figure 2.1): at the smallest scale three amino-acid

alpha chains form a 1.5 nm diameter triple helix, with a 0.29 nm axial intra-amino-acid spacing. This molecule, termed procollagen, is assembled within the cytoplasm of fibroblasts. Once the procollagen molecule is secreted from the cell, the non helical ends are cleaved by specific peptidases, leaving mature collagen molecules that self-assemble into fibrils $10 - 300$ nm in diameter [82, 83]. Within fibrils, collagen molecules arrange in a five-staggered semi-crystalline structure, with a characteristic 67 nm D-period given by the sum of the gap and overlap regions of neighbouring molecules (figure 2.1). Fibrils are then closely packed into fibres where the packing density and strength of cross-linking are determinant factors for tissue mechanical properties. [82, 83, 84]

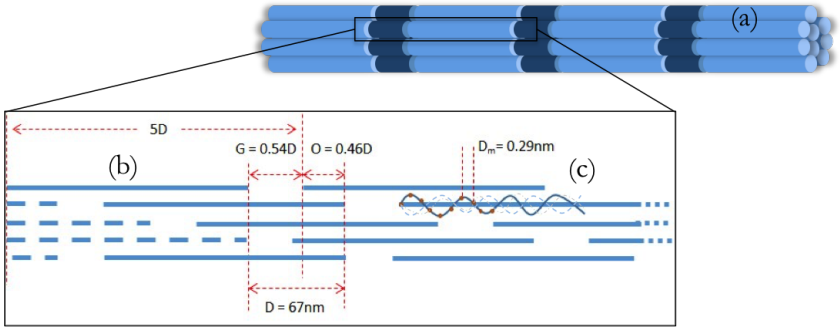


Figure 2.1: Hierarchical composition of collagen, showing fibres (a), fibrils (b) and triple-helix alpha chains (c), indicating characteristic lengths and D-periods.

Once mature, the majority of SCs cease collagen production and become myelinating. During myelination, SCs migrate along axons to periodically spaced locations, and alter their morphology by wrapping their membrane multiple times around the axon. This results in the myelin sheath: overlapping layers of lipid membrane with a repeating periodicity of 18 nm forming an electrically insulating layer around the axon.

Both collagen and myelin form quasi-crystalline, regularly spaced structures within peripheral nerve, and therefore their structure can be probed by X-ray diffraction.

2.1.3 X-Ray Diffraction (XRD)

X-ray diffraction (XRD) is a technique used to determine nano-scale structures of crystalline materials, which can also be used to probe nanoscopic quasi-crystalline structures in biological tissues, as the wavelength of the radiation used is of smaller scale compared to the periodic spacings in the material. Measurements of spacing between lattice planes in a crystalline structure follows Bragg's diffraction law (figure 2.2).

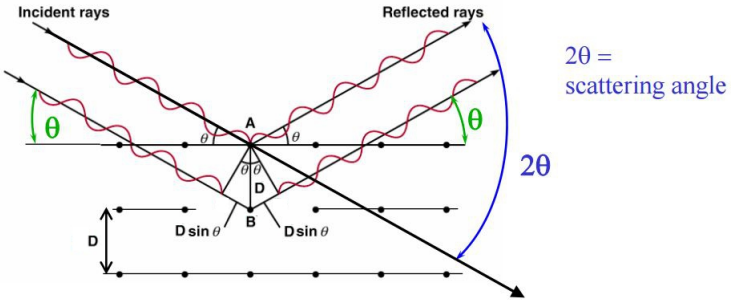


Figure 2.2: X-ray scattering from crystal lattice. 'D' indicates D-period between crystal lattice planes A and B. θ represents the incident x-ray angle

Incident X-rays are reflected and diffracted by lattice planes, resulting in scattering patterns with peaks at locations where the diffracted rays are in phase and combine in constructive interference (figure 2.2). Two X-rays of wavelength λ diffract from lattice planes (A and B) separated by a distance D. In order for the diffracted rays to be in phase, the difference in path-length between planes must equal an integer multiple of the ray's wavelength [85]. Hence, equating the path difference to nλ gives:

$$2Dsin(\theta) = n\lambda \tag{2.1}$$

Where n is an integer, λ is the wavelength of the X-ray beam, D is the measured spacing (D-period), and θ is the scattering angle. λ (in Å) can be calculated from the measured beam energy as:

$$\lambda = \frac{hc}{E} \tag{2.2}$$

Where h is Planck's constant (6.63×10^{-34} m^2 kgs^{-1}), c is the speed of light (2.99×10^{8} ms^{-1}) and E is the energy of the beam (in Joules).

Synchrotron X-rays can be used to probe two quasi-crystalline collagen length scales: molecular and fibril. At a fibril level, the 67 nm D-period creates a typical meridional diffraction pattern observable using a small angle (SAXS) detector [86]. At a molecular level, a single signal peak can be observed corresponding to the 0.29 nm spacing between successive amino-acids along the helix axis [86, 87]. Due to the inverse proportion between D and scattering angle, molecular signals will be observable on a wide angle (WAXS) detector.

The myelin sheath produces a diffraction pattern at 90° to the axial collagen signal, as the quasi-crystalline organisation of the overlapping membrane layers is circumferential [88, 89, 90].

Regardless of the structure observed, strain can be measured by observing the change in D-period as a result of applied load, as:

$$\epsilon_D = \frac{(D - D_0)}{D_0} \tag{2.3}$$

Where D_0 is the reference spacing (with no load applied), and D is the measured spacing in the loaded state.

In the widely accepted Hodge-Petruska model of collagen packing, the 67 nm fibrillar D-period is made up of a gap (G = 0.54*D) and overlap (O = 0.46*D) region, as a result of individual molecules being 4.46D in length and arranged in a five-staggered pattern (figure 2.1) [91]. This is confirmed by patterning observed in electron micrographs showing a two-phase electron density distribution [92]. The Hodge-Petruska model accounts for two methods contributing to collagen D-period variation with axial strain: uniform affine molecular elongation, and molecular rearrangement (gap increase and/or overlap decrease) [93, 91]. Changes in the Overlap to D-period (O/D) ratio can be calculated

from experimental results as the change in relative intensity (I) of consecutive peaks [94] :

$$\frac{I_{n+1}}{I_n} = (\frac{n}{n+1})^2[\frac{sin((n+1)\pi[O/D])}{sin(n\pi[O/D])}]^2 \tag{2.4}$$

Where n is the peak order. Due to the better intensity data from low-order peaks, O/D is conventionally calculated using the 3rd and 2nd order peak intensities [95, 96, 91].

2.2 Probing Multi-Scale Mechanics of Peripheral Nerve Collagen and Myelin by X-Ray Diffraction

Fabio Bianchi, Felix Hofmann, Andrew J Smith, Hua Ye and Mark S. Thompson

Published, Journal of the Mechanical Behaviour of Biomedical Materials (JMBBM), 25th July 2018. Original available at [97].

2.2.1 Introduction

Peripheral nerves are continuously subjected to mechanical forces, elongation, and compression during everyday movement, without suffering functional losses and damage. Traumatic events and inappropriate continuous mechanical loading, however, are associated with common disabling and painful entrapment, overstretch, or compression neuropathies. Carpal tunnel syndrome, for example, has a prevalence in the United Kingdom of 5-16% annually, varying by age and gender group, with decompression surgery provided for 43-74 people per 100,000, annually [8, 9]. Erbs palsy, caused by excessive stretching of infant heads and arms during birth, induces loss of sensation and abnormal motor function in 0.1% of births in the US [7]. In sciatic nerves and brachial plexus, stretch due to trauma and abnormal limb positioning during operations are widespread causes of debilitating iatrogenic injury, both temporary and chronic [10]. Mechanical tension has also been proposed as a regenerative method, with mild stretch inducing axonal and whole-nerve elongation and growth, although the multi-scale effects of this elongation have not been studied [36, 37, 98]. A better understanding of the multi-scale link between macroscopic loading and loss of function in peripheral nerve is required for effective prevention and treatment of neuropathies, and to explore tension as a strategy for injury prevention and regeneration [12].

Multiple concurrent factors cause functional alterations in peripheral nerves. Occlusion of nerve blood supply, leading to hypoxia, occurs at macroscopic strains above 15% [99]. A reduction in electrical conduction has also been observed as a result of stretch, with Compound Action Potential magnitude decreasing with increasing strain [26, 69], and completely subsiding at strains of 5-20% [26, 34]. At a cellular level, strains above 10% have been shown to affect axonal transport, responsible for motility of cytoskeletal elements, energy production, and growth factor trafficking [71, 100], and AFM studies on single axons showed that the compression required to block axonal transport was variable, between 65 and 540 Pa [101]. Furthermore, voltage-gated sodium channels clustered at Nodes of Ranvier, fundamental for saltatory impulse conduction, have been shown to disperse with applied nerve elongation[102]. Axonal tensile strains of 5% can cause growth cone collapse [103], membrane permeabilisation [104], and morphological changes in neurons [105], also potentially leading to loss of function.

The mechanical properties of peripheral nerve tissue derive from its complex structural organisation. Substructures in peripheral nerves include the endoneurium, a loose structure of collagenous channels in which myelinated and unmyelinated axons are embedded, surrounded by the perineurium, made up of multiple layers of transversely aligned lamellar collagen. The epineurium, a thick layer of densely packed collagen fibres, envelopes the whole nerve in an axially aligned pattern, showing fibril waviness and crimp (figure 2.3) [17]. The properties of these collagenous substructures have been shown to be similar to those of tendon [18] and either or both the epineurium and perineurium have been described as the main load bearing structures [74, 73, 70, 52]. Here, we analyse the partitioning of strain between whole tissue and collagen molecules, to compare the mechanical properties of axially aligned eipneurial collagen to those of other load-bearing collagenous tissues such as tendon.

Mechanically, peripheral nerves have been modelled as concentric, two-layer composites: a more compliant, water-rich core representing endoneurium, the inner part of the perineurium, and myelinated and unmyelinated axons, and a stiffer outer sheath representing the epineurium and the outer perineurium, connected by a sliding interface layer [52, 75, 19]. Independent mechanical testing characterises the core as significantly softer and more compliant than the sheath, and indicates that, during tensile loading of the nerve, the outer sheath applies a compressive force on the core, which is resisted by a positive endoneurial pressure [19, 75]. The loose organisation of endoneurial tissue suggests that, at low loads, components within the core rearrange, rather than compress, during whole tissue compression [72]. The transverse compression induced by tensile loading has been observed in vitro, but its effect on the microstructural elements within the core has not been studied [20, 72].

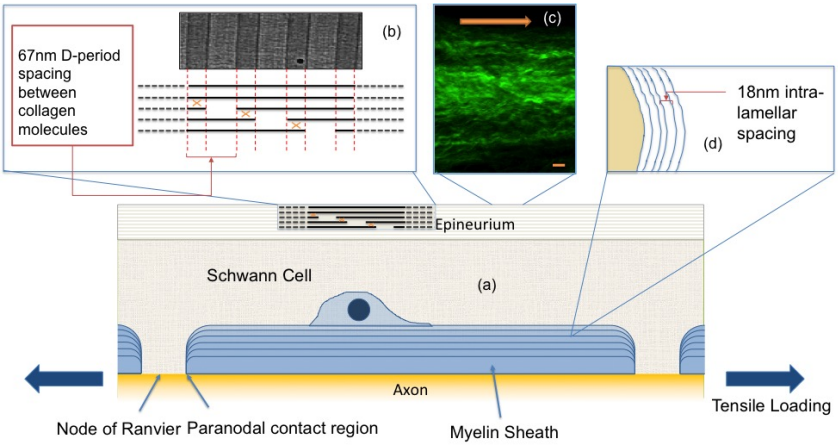


Figure 2.3: (a) Peripheral nerves consist of axons projecting from neuron bodies, which can be myelinated by Schwann cells or unmyelinated. The structure of quasi-crystalline elements (collagen and myelin) can be observed by x-ray diffraction. (b) Eipneurial, axially aligned collagen fibril structure, with characteristic 67 nm D-period between molecules. (c) Multi-photon second harmonic microscopy of rat sciatic nerve collagen, showing crimped wavy pattern of axially aligned fibres. Scale bar = 100 μm. Arrow indicates direction of nerve axis. (d) Cross-sectional view of myelin sheath, showing 18 nm spacing between lamellae.

Within the nerve core, chemical demyelination has been shown to reduce nerve axial stiffness, implying that myelin contributes to tissue mechanical properties [78]. Additionally, AFM studies have shown that digestion of Schwann cell basal lamina reduces nerve

fibre circumferential stiffness and resilience significantly [79], suggesting a protective role for myelin during nerve deformation. However, the mechanical role of myelin is not yet clear, as it has mostly been studied in isolation, rather than within the multi-scale mechanical environment of the whole nerve. Here, we aim to characterise the mechanical properties of the myelin sheath during circumferential compression induced by whole-nerve elongation.

Linking macroscopic loading of peripheral nerves with changes in cell function and damage requires knowledge of the multi-scale mechanical behaviour of nerves. Current knowledge of the micro-scale effects of macroscopic loading is limited, and a better multi-scale understanding is required to successfully prevent and treat mechanically-induced peripheral neuropathy and functionality loss [12]. X-ray diffraction is an ideal modality for *in situ* strain measurements of micro-scale quasi crystalline structures. In nerve, it has been shown to effectively probe collagen fibres [106] as well as the intra-lamellar spacing in the myelin sheath [88, 89, 90], but it has not been applied to studying the mechanical properties of these structures during *in situ* loading. Here we investigate the multi-scale mechanical properties of peripheral nerve during tensile loading, by probing the microstructure of peripheral nerve collagen and myelin by x-ray diffraction during macroscopic tensile loading.

2.2.2 Materials and Methods

Sciatic Nerve Harvesting and Imaging

Sciatic nerves were harvested from 300-350 g (10-12 week old), male Sprague-Dawley rats, sacrificed by cervical dislocation for an unrelated study. Briefly, following skin removal, the sciatic nerves were exposed by dorsal incision of the gluteus muscle. Nerves were excised proximally close to the spinal cord, and distally at the tibial-peroneal branching. Nerve samples were stored in Phosphate Buffered Saline (PBS, Gibco, UK), immediately

frozen at -20 ° until use. This has been previously shown not to not alter the mechanical properties of collagenous tissues [107, 91], as well as retraction properties of sciatic nerves [19]. Furthermore, Wallarian degeneration of axons and the myelin sheath has been shown to be delayed by low temperatures [108]. Together, these suggest that freezing nerves upon excision and thawing prior to experiments should retain the tissue mechanical properties. After thawing and mounting, ink marks were made on samples, for optical measurement of whole tissue strain as previously used for spinal cord and tendon strain measurements [78, 109].To highlight the crimped epineurial collagen structure, nerves were imaged using multi-photon second harmonic generation (SHG) imaging using a Zeiss LSM780 microscope (20x lens), with excitation set at 880nm.

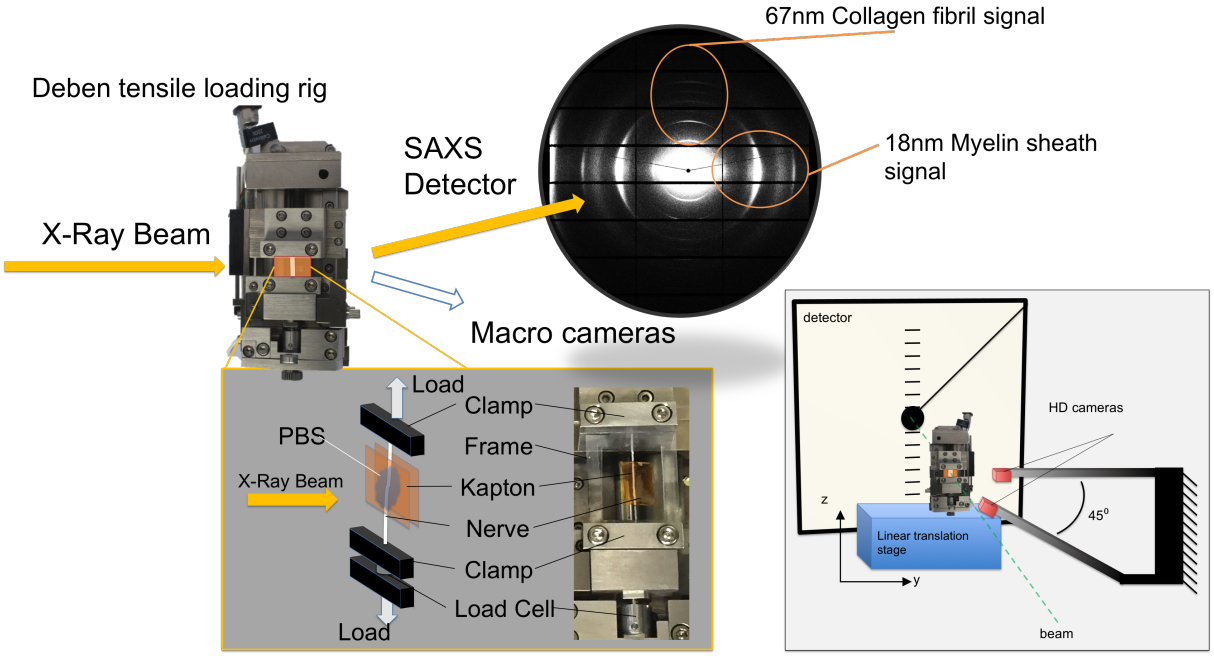


Figure 2.4: Experimental setup and data acquisition. X-ray beam is diffracted by nerve sample loaded in tension by Deben rig. Kapton film and PBS keep the samples under physiological hydration conditions. Small angle scattering of X-rays is detected, showing peaks corresponding to intra-molecular spacing in epineurial collagen fibrils, and peaks corresponding to the intra-lamellar spacing in the myelin sheath. Inset shows diagrammatic view of camera setup, as seen from the X-ray source.

In situ Loading

Sciatic nerves were loaded *in situ* to failure (defined as complete tissue disconnection) using a Deben Microtest (Deben, UK) tensile loading stage, equipped with a 2N load cell. Samples were glued to a rectangular plastic frame using cyanoacrylate glue (Loctite, UK). Frames were mounted in the Deben stage by clamps (figure 2.4). Before experiments, the sides of the frames were cut, leaving the nerve as the only load bearing element between the clamps. Two rectangular sheets of Kapton film (Goodfellows, UK) film were placed either side of the nerves, and PBS was added to the samples to maintain physiological hydration, and to hold the Kapton film together by capillary action. The loading rig was mounted vertically, and rotated by 45° to avoid blocking detectors. Two cameras were placed, facing the sample, at 45° relative to each other (figure 2.4, inset).

For 6 sciatic nerve samples, increasing tensile loads were applied, and diffraction patterns recorded at approximately 0.1 N intervals. In order to avoid creep-like effects, X-ray diffraction images were taken during continuous loading, at the instant when the load cell indicated the required load. Loading was assumed to be constant during acquisition, as a quasi-static loading at 0.1 s^{-1} strain rate was used, much slower than acquisition time.

X-Ray Diffractometry

Diffraction experiments were carried out at beamline I22, Diamond Light Source, UK. The X-ray beam dimensions were approximately 300×100 μm^2 FWHM Horizontal x Vertical, with the largest dimension parallel to the sample axis (z-direction in figure 2.4, inset). A photon energy of 12.4012 ± 0.0014 KeV was selected ($\frac{dE}{E} = 1.12 \times 10^{-4}$), corresponding to an X-ray wavelength of $0.0997 \pm -1.0066 \times 10^{-5}$ nm. SAXS data was collected over a q range of $0.0026 - 0.13$ $Å^{-1}$, and over an azimuthal range of 360° using a 2D Pilatus P3-2M detector (DECTRIS, Switzerland) placed 6.539 meters downstream of the sample and with a typical exposure time of 0.15 s. Beam centre on the detector was determined

using the Debye-Scherrer rings from Silver Behenate, and the sample-detector distance was determined using the diffraction from chicken tendon collagen standard reference samples.

Pilot experiments showed small angle X-ray scattering (SAXS) of peripheral nerve with a highly textured, axially aligned collagen diffraction pattern, with peaks corresponding to multiple diffraction orders of the 67 nm axial spacing (D-spacing) between molecules within fibrils (figure 2.3b), whilst myelin diffraction produced equatorial peaks at 90° orientation to the collagen, measuring the 18 nm average spacing between lamellae (figure 2.3C).

X-Ray Diffraction Pattern Analysis

SAXS diffraction patterns were converted from polar detector coordinates to Cartesian coordinates, showing diffraction data as a function of azimuthal angle, χ, and scattering vector magnitude, q (figure 2.5). The geometrical parameters of the experimental setup, essential for this remapping, were determined by calibration SAXS measurement of chicken tendon collagen standard reference samples. Gaussian profiles were fitted to the 1st, 3rd, 5th and 9th order meridional collagen peaks, and their maxima used to determine peak position. Similarly, myelin diffraction patterns were extracted by fitting Gaussians to two equatorial peaks from the same images.

Q-scale peak positions were then divided by the diffraction peak order number, converted to D-spacing measurements, and averaged over the number of fitted peaks. Nominal strain was measured by the displacement of average peak position relative to an unloaded state, using equation 2.5, where X can refer to any spacing parameter observed, and X_0 being the value of the parameter in the unloaded state.

$$\epsilon_X = \frac{X - X_0}{X_0} \tag{2.5}$$

Stress-strain data was calculated only for axial tissue and collagen deformation. Stress values for collagen were calculated assuming that the epineurium constituted 50% of nerve cross-sectional area [110]. For all other measurements where area could not be approximated, data was presented as load against strain plots, showing material stiffness. Load, being the controlled variable, is plotted on the horizontal axis, unlike in stress-strain curves, as previously used to characterise the mechanical properties of other collagenous tissues [111]. Linear and non-linear regression and curve fitting is carried out using GraphPad PRISM. Non-linear fitting is used for macroscopic tissue strains, where non-linear relationships between applied force and elongation have been previously reported [72, 19].

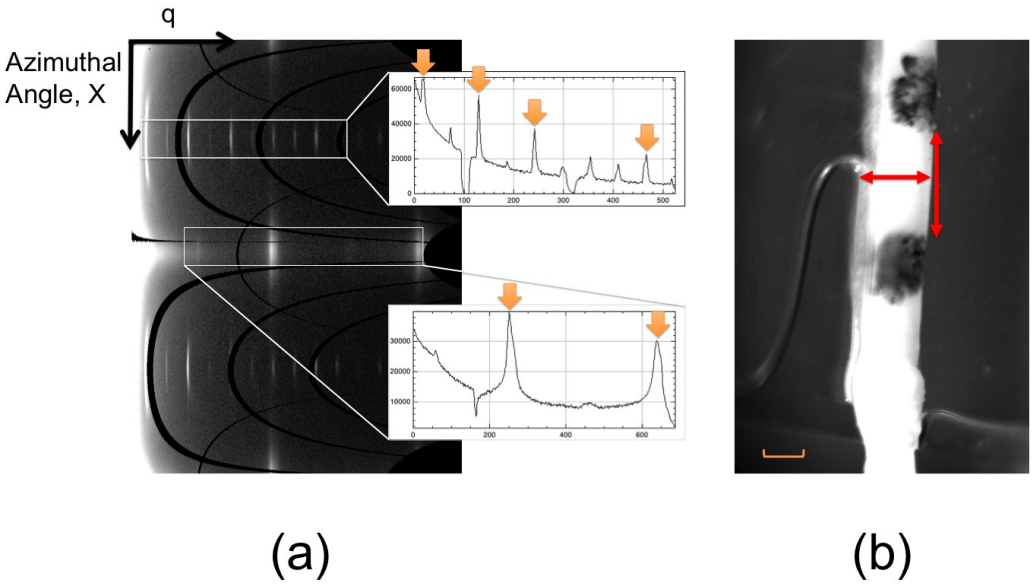


Figure 2.5: (a) Small angle diffraction pattern from rat sciatic nerve, following conversion from Polar to Cartesian coordinates, showing characteristic peak patterns from collagen (top) and myelin (bottom). Yellow arrows show fitted peaks after line profile plotting. (b) Camera image for video extensiometry measurement, showing black marks used for tissue strain computation. Arrows show transverse and axial lengths measured. Scale bar = 1mm

Whole Tissue Strain Calculations

Strain in the whole tissue was measured axially and transversely from images taken by a HD camera (AlliedVision, Germany). Axial tissue strain was estimated using marker

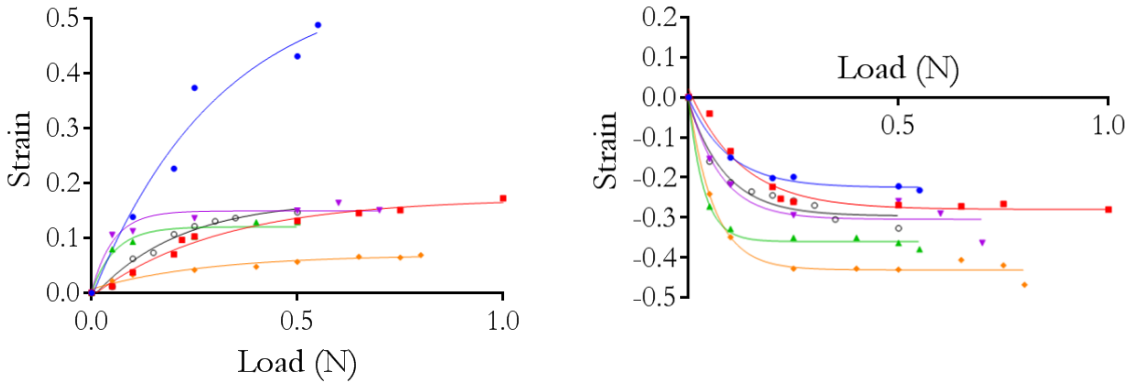
tracking of the black surface ink marks. A custom MATLAB code was used, which estimates strain by extracting centroid coordinates of the ink marks and calculating the change in distance between marks. This was validated by manual measurement of the distance between marks. In the transverse direction, contraction with applied load was measured by extracting nerve diameter from images, by measuring full width at half maximum of line profiles across the nerve. The nerve was split into 50 axial segments, and the diameter calculated as the average of the diameter value measured in each section. Tissue strain measurements and relation to molecular strains assume circular geometry and symmetry.

2.2.3 Results

Tissue and Molecular Strains

With increased tensile load, nerve tissue elongates axially, with simultaneous circumferential compression (figures 2.6a and 2.6b). In the axial direction, the tissue extends at a faster rate at lower loads, a non-linear behaviour (average $R^2 > 0.87$) consistent with previously published results [72, 20]. Circumferential compression is also non-linear, with a higher rate of compression at lower loads, and with strain reaching a limiting value at higher loads (average $R^2 > 0.9$), consistent with the hypothesis that internal core components rearrange before being loaded during induced compression [20, 72].

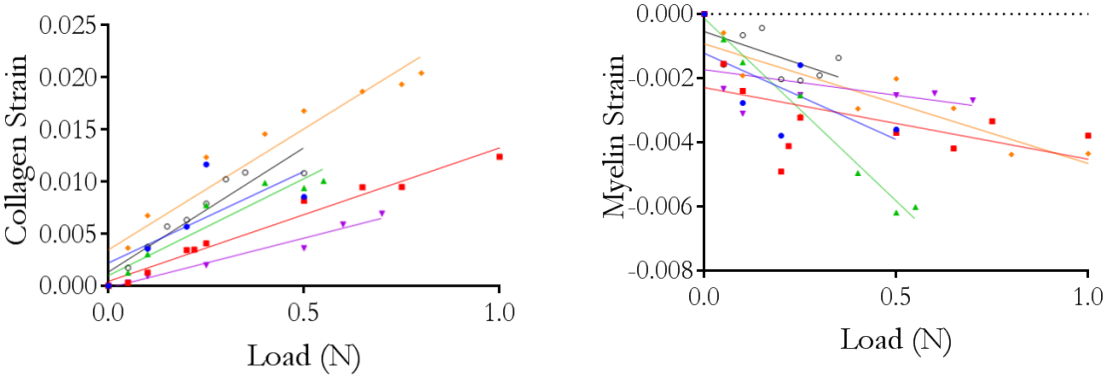
Loading modulus (calculated from the linear section of the loading curves) for whole nerves was 5.31 $\pm$ 2.55 MPa, in accordance with previously reported values for sciatic nerve stiffness [20]. Assuming epineurial thickness to be 50% of nerve volume [110], loading modulus of epineurial collagen fibrils was 92.34 $\pm$ 35.01 MPa, lower than that of rat tail tendon collagen fibrils measured by x-ray diffraction [109], but in line with other reported moduli for collagen fibres [96].



(a) (b)

Figure 2.6: Tissue-level strains as a function of load. Axial tissue strain (a) is positive and increasing with load, circumferential strain (b) is negative (compression) and increasing in magnitude with load. Both deformations are nonlinear with applied load.

With increasing applied load, the average molecular D-spacing measured in collagen increased linearly in all samples (average $R^2 > 0.9$) up to strains of 2% (figure 2.7a). Concurrently, average spacing between lamellae in the myelin sheath decreased, reaching strains of up to -0.6% (figure 2.7b).



(a) (b)

Figure 2.7: Molecular-level strains in collagen axial (a) and myelin circumferential (b) as a function of load in rat sciatic nerves (N=6). In the collagen matrix, a positive strain (elongation) is observed. In the myelin sheath, a negative strain (compression) is observed.

Strain Partitioning Between Length Scales

Partitioning of strain can be measured in both collagen and myelin (figure 2.8). Tissue level axial strain exceeds collagen fibril strain, indicating the existence of multiple mechanisms for tissue extension in addition to collagen fibril elongation, as reported for other collagenous connective tissues [95, 109]. Tissue circumferential compressive strain is also larger than the myelin layer compression suggesting that the myelin sheath significantly stiffer than its surroundings. Average myelin stiffness is higher than circumferential tissue stiffness, with a ratio of the slopes of linear portions of load-strain curves of 100 (figure 2.8b). For collagen, the same slope ratio is 10 (figure 2.8a), indicating that collagen bears a higher proportion of axial load than the proportion of circumferential compression borne by myelin.

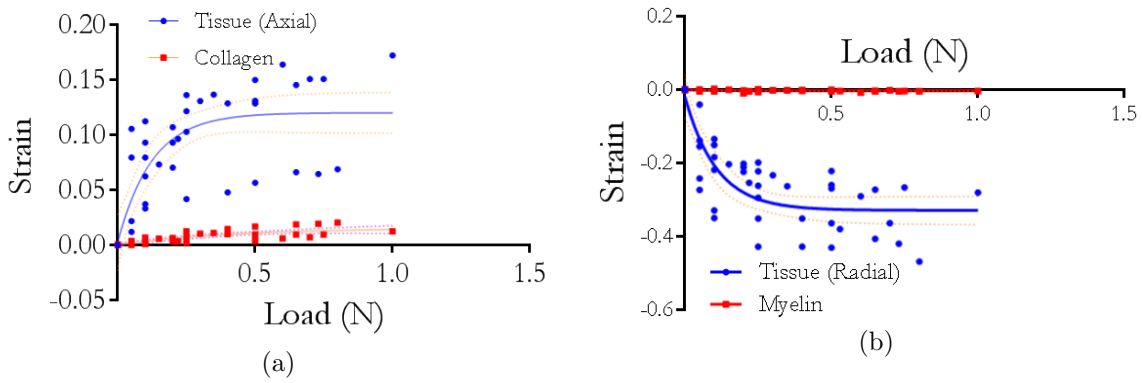
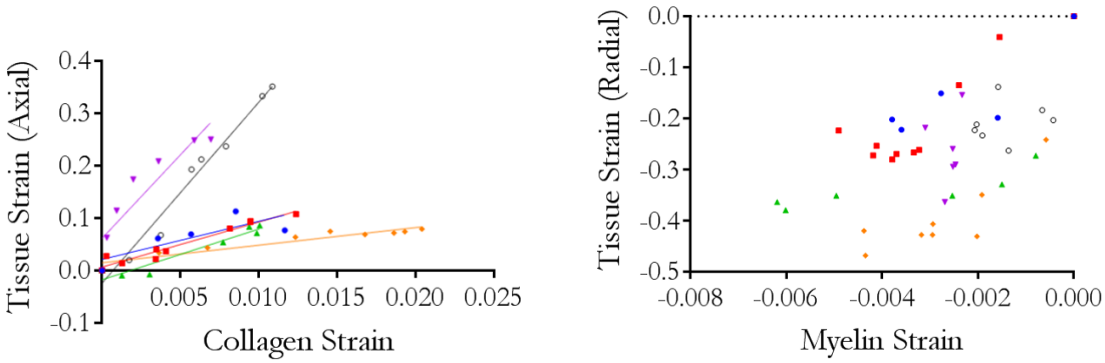


Figure 2.8: Strain partitioning between molecular (red) and tissue (blue) levels, for collagen (a) and myelin (b). In both cases, straining of the observed molecular structure only accounts for a fraction of the total tissue strain in the same direction. Lines correspond to non-linear fit as shown in figure 2.6. Dotted lines = 95% confidence interval.

The difference between tissue and molecular strain at each loading point represents straining due to mechanisms other than molecular deformation, such as molecular sliding and structural rearrangements. Axially, rearrangements in collagen structure account for more than 90% strain at lower loads, and molecular elongation increases at higher loads.

Circumferentially, myelin compression accounts for less than 2%, on average, of tissue compression.

Macroscopically, axial tissue strain correlates linearly (average $R^2 = 0.87$) with collagen strain (figure 2.9a), indicating a direct mechanical relation between the two length scales. Variations in slope of tissue strain to collagen strain relations are due to the higher variability of tissue strain measurement, as previously shown for whole tendon tissue strains measured using a similar technique [109]. Circumferentially, no linear correlation is observed between molecular and tissue strain (figure 2.9b), suggesting that induced macroscopic compression is not the only mechanism contributing to myelin deformation.



(a) (b)

Figure 2.9: Molecular strain increases linearly with tissue strain in axially aligned collagen (a), but shows no relationship axially during myelin compression (b)

2.2.4 Discussion

Using x-ray diffraction and HD video extensiometry during *in situ* tensile loading, we have investigated the multi-scale mechanical properties of peripheral nerves. By using x-ray diffraction, molecular-level mechanical behaviour was observed in both axially-aligned epineurial collagen, and in the myelin sheath enveloping axons. Results presented show a pronounced circumferential compression in rat sciatic nerves during axial elongation. At a molecular level, the spacing between myelin lamellae decreases, with indication of

high compressive stiffness of myelin, and epineurial collagen elongates, showing similar properties to those of load-bearing connective tissues.

A pronounced macroscopic circumferential compression is observed during tensile loading of sciatic nerves. This supports previously proposed models, where a compression of the nerve trunk occurs during tensile loading [75, 20, 72]. Evidence of epineurial thickness remaining constant during elongation [112] indicates that compressive strain is localised in the core. The loose organisation of perineurial and endoneurial tissue suggests that components within the core can rearrange, rather than compress, with decreasing nerve diameter [72]. The non-linear behaviour observed here at tissue level (figure 2.6b) confirms the presence of softer structures that allow rearrangement under small loads, and stiffer structural elements contributing to the behaviour at higher loads.

Our results show that, when a peripheral nerve is elongated axially, the average spacing between lamellae in the myelin sheath decreases linearly (figure 2.7b). This suggests that myelin is being deformed throughout the loading curve, both at lower loads, during rearrangement of softer structures, and at higher loads, where the nerve exhibits higher circumferential stiffness. No direct correlation between axial tissue compression and myelin compression is observed (figure 2.9b), indicating that the circumferential compression is not the only mechanism causing myelin compression.

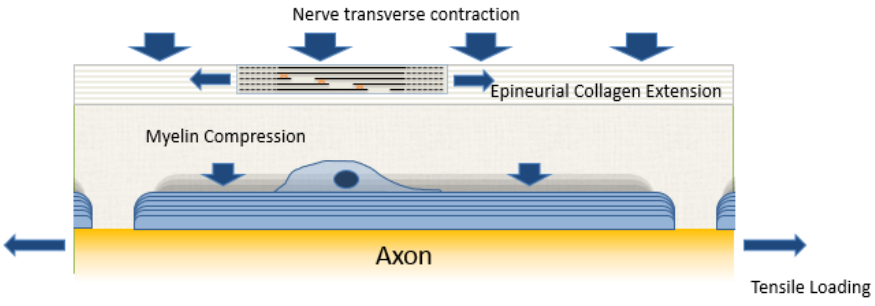


Figure 2.10: Proposed mechanism of myelin compression as a result of nerve tensile loading. Epineurial collagen elongates axially, taking most of the load, with some load being taken by the axons and myelin sheath. The myelin sheath, which is tether at paranodes, elongates with the axons, and is compressed circumferentially. The combined effect of induced tissue compression and axonal elongation induces a compression of myelin layers

Myelin has been shown to have significant compressive stiffness [79, 78]. The observed behaviour can be explained if myelin compression is not solely caused by tissue compression. Previously, it has been shown that axial elongation of myelinated nerve fibres is both due to a lengthening of the internodal region [113, 114], as well as a more prominent widening of the Nodes of Ranvier [115, 71, 102]. This suggests that axons are being loaded in tension, and that the myelin sheath, despite contributing to tensile stiffness, is being elongated with the axons. The myelin sheath is tethered to the axons it surrounds through contact proteins located at the paranodal region. If axons are also loaded in tension, the spacing between myelin lamellae would decrease, as it cannot slide along the axons (figure 2.10), explaining behaviour at low loads [89]. At higher loads, the stiff myelin sheath is further compressed with induced circumferential strain, but acts as a stiff protective layer to reduce potentially damaging axonal compression.

When peripheral nerves are loaded in tension, axially aligned collagen fibrils present in the epineurial outer sheath also extend, showing a linear relation between axial tissue strain and collagen molecular strain (figure 2.9a). In tendon collagen, a load-bearing energy storing structure of similar fibrillar morphology and density [17] subjected to continous physiological tensile loading, accepted deformation mechanisms accounting for differences in molecular and tissue axial strain include both geometric rearrangement of collagen fibrils (uncrimping) and relative sliding of discontinuous fibrils [109, 95]. Similarly, when a peripheral nerve is stretched, part of this elongation is due to extension of the axially aligned epineurial collagen fibres, and part is due to molecular rearrangements and deformation of other components. We have shown that strain due to factors other than collagen molecular straining are more dominant at lower loads, and vary non-linearly with applied load. This is in accordance to models of collagenous materials which include fibril recruitment, where wavy fibrils are first recruited, and start bearing a higher proportion of load once they have been fully straightened [116]. This also agrees with mechanical

testing performed on separated nerve cores and sheaths, where the outer layer has been shown to bear load only after an initial toe region [52]. Loading modulus of epineurial collagen measured here is smaller than that reported from x-ray diffraction studies on rat tail tendon collagen [109], suggesting that other elements of the peripheral nerve, such an perineurial collagen and axons, bear a fraction of the applied tensile load, but confirming that the epineurium has a vital mechanical role during tensile loading. The large inter-species variability, as well as the differences in mechanical properties between functionally specialised tendons may also contribute to the difference measured [117].

Limitations of This Study

The study presented here is limited by the small sample number, and by the elements that are observable using x-ray diffraction. Direct information about the deformation of axons, blood vessels and other structures within the nerve would provide further explanation for the mechanisms of deformation, and could lead to a better quantification of induced compressive strain partitioning. Previous work on tracking axonal strain using surface protein markers suggests a technique which could be employed [118]. This study is further limited by the lack of information about volume fraction of materials present in peripheral nerves. This information would allow stiffness of nerve collagen and myelin to be better estimated. Another limitation is the absence of information about myelin properties in tension, which would further refine the whole-nerve model. The loading methods should be considered as a factor further limiting these results. *In situ* tensile loading does not precisely reproduce *in vivo* nerve loading conditions, where the nerve is not clamped at both ends. This could affect the way in which nerve core elements are strained. Furthermore, a thorough characterisation of the differences between freshly excised tissues and frozen tissues would provide stronger evidence that sample preservation did not affect its mechanical properties.

This study could be the base for further studies to observe how larger deformations translate to the micro-scale, and damage peripheral nerves, as well as to study the effect of demyelinating disease models on the mechanical behaviours described here.

2.2.5 Conclusions

In this study, we probe the micro-mechanical behaviour of peripheral nerve collagen and myelin during *in situ* tensile loading, by x-ray diffraction. Results show a non-linear compression of the nerve induced by tensile loading, confirming previous hypotheses that soft nerve core elements rearrange before being loaded. We show that at the microscopic level, the spacing between lemellae of the myelin sheath decreases with applied whole-nerve tensile load, but myelin exhibits a much higher stiffness than the whole nerve. This suggests that myelin is mechanically significant in compression as well as in tension, protecting underlying axons from compressive damage.

Axially, we confirm strain partitioning in epineurial nerve collagen, similar to that observed in tendons, suggesting similar load-bearing properties.

These results have implications in understanding mechanical behaviour of peripheral nerve tissues, as well as mechanisms of cellular damage caused by macroscopic loading. Furthermore, understanding the microscopic nerve mechanical environment during mechanical loading is fundamental to devise appropriate strategies for injury prevention and regeneration strategies [12].

Further investigation, including analysis of axon deformation during whole nerve loading, is required to fully understand how the functional properties of nerve tissues are altered during mechanical loading.

2.2.6 Conflicts of Interest

The authors declare that they have no conflict of interest.

2.3 Probing Multi-Scale Mechanical Damage in Connective Tissues Using X-Ray Diffraction

Fabio Bianchi, Felix Hofmann, Andrew J Smith and Mark S. Thompson

Published, Acta Biomaterialia, August 2016. Original available at [109].

2.3.1 Introduction

The mechanical properties of tendons are determined by collagen structure, and microdamage accumulation in the collagen fibrils has been associated with tendon injury [119]. Tendon injury and pathology are painful and disabling, and understanding the mechanisms underlying collagen damage can lead to novel strategies to diagnose and prevent injury, and facilitate regeneration. This requires comprehensive knowledge of collagen mechanics, cell-matrix interactions, and of the structural and biochemical response to loading and damage accumulation. [120] Tendons are composite materials, where collagen accounts for 86% of dry mass [82]. Three alpha chains, consisting of 1056, 0.29-nm spaced amino-acid residues arranged in a Gly-X-Y repeat pattern, combine to form 300 nm long triple-helical collagen molecules. These assemble into five-staggered microfibrils with a characteristic 67nm D-period, forming the base crystallographic unit of collagen; as described by the consensus axial packing model, formulated by Hodge and Petruska in 1964 [84, 121]. The fibrillar D-period is made up of a gap region of lower electron density, and an overlap region, where laterally adjoining, non-helical molecule terminals are cross-linked, stabilising the structure [122, 123]. Interlaced microfibrils form fibrils, which combine with a proteoglycan-rich matrix, that maintains physiological hydration, to form fibres [95]. Tenocytes, specialised fibroblastic cells of elongated cytoplasm morphology, sparsely populate the tendon, and maintain homeostasis of the tissue. [120] Due to this complex hierarchical organisation, strain partitioning between structural levels

and damage mechanisms in tendons are not well understood. Whole tendon deformation results from fibrillar straining and intra-fibrillar matrix deformation. Fibrillar straining, in turn, is a compound effect of molecular deformation and molecular rearrangement [95, 96]. Micro-damage accumulation at small length scales may lead to pain and loss of functionality and ultimately macroscopic failure. [116]

Deformation mechanisms and mechanical properties at the nanoscale can be probed using in situ loading experiments with x-ray diffraction, due to the quasi-crystalline organisation of collagen at fibril and molecular level. Small angle diffraction (SAXS) has been used to measure the 67nm D-period between repeat units in fibrils [122] [124], while wide-angle diffraction (WAXS) can measure the 0.29nm intra-amino acid spacing along the molecular axis [86]. Fibrillar and molecular strain can be estimated from the shifting of diffraction peaks during in situ loading [96]. Further analysis of the diffraction patterns can provide structural information: The ratio of integrated intensities of the second and third order SAXS peaks is directly correlated to the ratio of the overlap region length to that of the whole D-period [96, 91], capturing structural changes due to load. Furthermore, lateral packing and fibril distribution affect damage mechanisms, and have been probed in recent years using x-ray ptychography [125]. Previous x-ray diffraction (XRD) investigations of non-physiological damage to fibrillar collagen through dehydration and heating have shown changes to lateral packing tightening and fibrillar D-period shrinking to 64nm, resulting in a loss of gap-overlap periodicity and a shearing of molecular packing [122, 126]. However physiological mechanical damage mechanisms have not been investigated using these techniques. The aim of this investigation is to describe collagen material property changes at three length scales following mechanical damage applied under phyisiological conditions, and to suggest potential underlying deformation and damage mechanisms. This was achieved using in situ mechanical loading and x-ray

scattering to compute the multi-scale mechanical properties at each hierarchical level, to investigate the relationship between these properties and pre-applied mechanical damage.

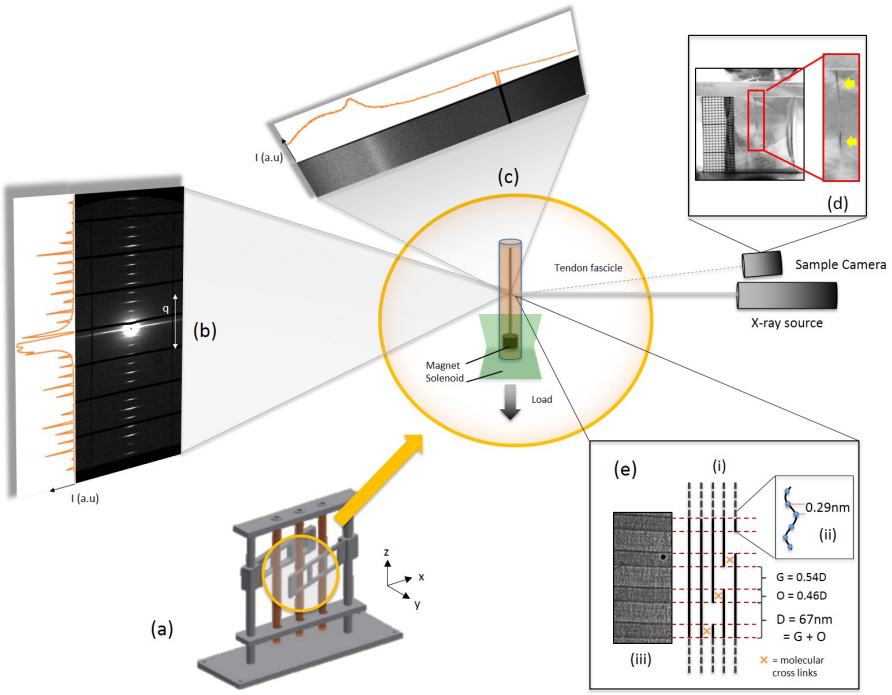


Figure 2.11: Experimental setup and data acquisition. (a) Sample rig, placed on precision linear table and allowing remote load application to the fully hydrated tendon. (b) SAXS signal detector output, showing collagen diffraction peaks (up to 12th order), where distance between peaks corresponds to 67nm D-period arising from the five-staggered arrangement within fibrils. (c) WAXS detector output, showing single peak corresponding to the 0.29nm intra amino-acid spacing along alpha chain. (d) High definition camera collecting images to measure macroscopic tissue strain. Yellow Arrows indicate permanent marks (e) Collagen nanostructure (i) Arrangement of molecules within fibrils, showing the characteristic 67nm D-period, which is the sum of gap and overlap regions. (ii) Single alpha-chain with amino-acid residues (iii) electron micrograph of fibril, showing gap and overlap contrast due to the square-wave variation of electron density along the fibril.

2.3.2 Materials and Methods

Tendon harvesting

Tendons were harvested from $300 - 350$ g ($10 - 12$ week old), male Sprague-Dawley rats, sacrificed by cervical dislocation for an unrelated study, by adapting the method described in [107]. Briefly, individual fascicles were separated, and selected based on diameter (0.22

mm ± 0.05 mm, measured using an optical micrometer (Keyence, Milton Keynes, UK; precision 1×10^{-5} mm).) A tendon sub-population was pre-damaged, and all samples were fixed to neodymium magnets (8 mm diameter by 10 mm) using epoxy putty, and frozen at -20 in Phosphate Buffered Saline (PBS, Gibco, UK) until use, to not alter the mechanical properties of the tendons [91]. Black ink marks (see arrows in figure 2.11 (d)) were made on all samples, for optical measurement of whole tissue strain.

Pre-damage application

Tendons (n = 6) were pre-damaged using a bench top uniaxial strain machine (Bose Electroforce, Eden Prairie, MN), by applying a continuous 10 MPa load for 500 s. Samples were then placed in PBS for 2 minutes, and damage quantified by manual measurement of permanent change in length between two ink marks. A length change greater than 5% was selected as the damage threshold. Multiphoton microscopy of other samples damaged to this level confirmed microstructural changes as described previously [127]. This level of damage is physiologically relevant for induction of tendinopathy in animal models of disease.[127]

In situ loading

Tendons were loaded in situ using an electromagnetic loading setup, consisting of a remotely operated, current-controlled solenoid, applying forces up to 0.5 N. Samples were placed in PBS-filled Kapton tubing, sealed using Polydimethylsiloxane (PDMS, Corning, UK) to maintain hydration, and held by a custom-built experimental rig, designed to fit within the sample space of the I22 beamline at the Diamond Light Source, UK, and mounted on a linear translation table for positioning (Figure 2.11, (a)). Each magnet, weighing 6.1 g, produced a 0.06N tare load when the solenoid was inactive.

X-Ray Diffractometry

Diffraction experiments were carried out at beamline I22, Diamond Light Source, UK. The x-ray beam was coarsely focused to 90 $\times$ 110 μm^2 (full width at half maximum), with the largest dimension parallel to the sample axis (z-direction in fig. 1 (a) The optical design of I22 typically generates beamsizes at the sample of 300 $\times$ 100 μm^2, horizontal $\times$ vertical (Full width at half maximum) by directly reimaging the X-ray source in a 1:1 focussing arrangement. For these experiments the beamsize was reduced to 110 x 90 μm^2, horizontal x vertical, using collimating slits with an attendant loss of flux. This represents a compromise between minimising beamsize and maximising flux whilst maintaining the naturally low divergence of I22 (80 $\times$ 50 μ rad, horizontal x vertical) essential for high quality SAXS data collection. Smaller beamsizes without loss of flux could be achieved through the use of additional focussing optics, however the increased demagnification here would be offset by increased beam divergence that would negatively impact data quality. A photon energy of 12.4012$\pm$0.0014 KeV was selected ($\frac{\Delta E}{E} = 1.12 \times 10^{-4}$), corresponding to an X-ray wavelength of $0.0997 \pm 1.066 \times 10^{-5}$ nm. SAXS data was collected over a q range of $0.0025 - 0.15A^{-1}$, and over an azimuthal range of 360° using a 2D Pilatus P3-2M detector (DECTRIS, Switzerland) placed 9 meters from the sample and with an exposure time of 5 s. WAXS data was collected for a 2θ range of 16 to 50° on a 1D Pilatus P300k-W detector (DECTRIS, Switzerland), for 5s at every loading point (figure 1, (b), (c)). A high definition camera placed above the beamline exit, triggered by the beamline software, and focused on the sample was used to record sample images for macro strain computation by image correlation (Figure 2.11, (e)).

X-ray diffraction pattern analysis

SAXS diffraction patterns, showing distinct meridional peaks up to the 12th order were converted from polar to Cartesian coordinates, using dried chicken collagen as a calibration

reference (figure 2.11, (b)). Hence, a radial line profile for the 12 peaks was extracted, using both upper and lower reflections. Gaussian curves fitted to the peaks were used to compute peak position, full width at half maximum (FWHM) and integrated intensity. WAXS diffraction patterns were collected in 1D due to detector geometry. Calibration of the detector geometry was performed using a CeO_2 standard. A single peak was extracted by fitting a Gaussian curve to the line profile obtained by averaging the detector output in the y direction. Peak position, FWHM and integrated intensities were calculated.

Sample camera tissue strain

High definition, 1292 $\times$ 962 pixel images of samples taken at each load point were used to compute tissue strain with a custom-written Matlab digital image correlation routine.

Statistical Analysis

Statistical analysis (paired, two-tailed t-tests) was carried out using Graphpad PRISM. $p<0.05$ indicated statistical significance of results (95% confidence interval).

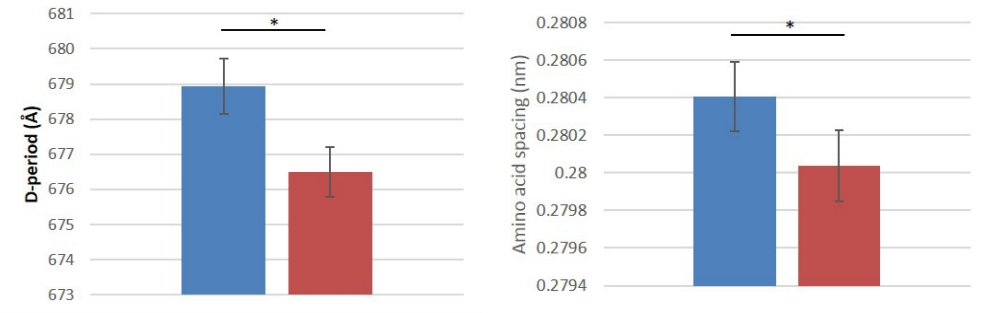
Ethics approval

All tissues were harvested from rats sacrificed for unrelated experiments, and thus no ethical approval was required.

2.3.3 Results and Discussion

D-period variation with damage

Comparison between damaged (N=6) and undamaged (N=6) populations tare load D-period (i.e. before solenoid activation) indicates a significant decrease in both fibrillar D-period and intra-amino-acid spacing with damage application (Figure 2.12).



(a) Tare-load fibrillar D-period variation with damage. n = 6. Bars = mean ± SD. * = p < 0.05 by t-test

(b) Tare-load intra amino-acid spacing along molecular axis, variation with damage. n = 6. Bars = mean ± SD. * = p < 0.05 by t-test

Figure 2.12: Fibril D-period and amino-acid spacing variation with damage. Blue = undamaged, Red = pre-damaged

Significant shortening of intra amino-acid spacing and shortening of fibrillar D-period (Figure 2.12a and 2.12b) have been shown to be related to x-ray radiation damage [91] and dehydration [128]. Due to minimal exposure to x-rays, and continuous sample hydration by immersion in PBS, neither mechanism could explain the change in D-periods observed here. This was verified by comparison of measured D-period before and after a full scan, showing no significant change, on average, in D-period (data not shown).

Strain Partitioning and Stiffness Changes with Damage

During fascicle elongation, the strain induced by applied stress is distributed between the collagen fibrils and the interfibrillar ground substance [95]. The fibril strain is in itself a compound effect of an affine elongation of the collagen molecules, and a rearrangement of the molecular structure within the five-staggered unit [96]. Here, we can evaluate how this partitioning of strain is affected by deformation damage, by simultaneous collection of WAXS, SAXS and Macroscopic high definition sample camera data.

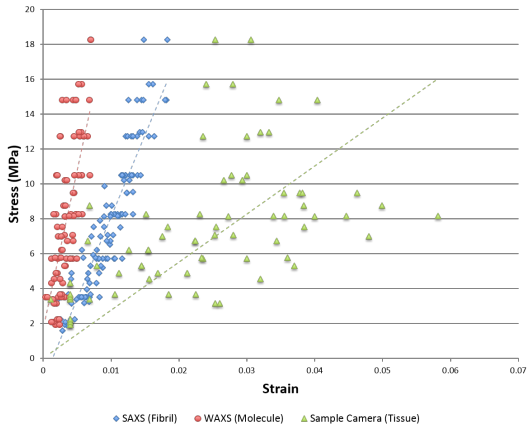
From peak positions of SAXS and WAXS patterns and from macro images, straining of the characteristic measured length was calculated as:

$$\epsilon_X = \frac{X - X_0}{X_0} \tag{2.6}$$

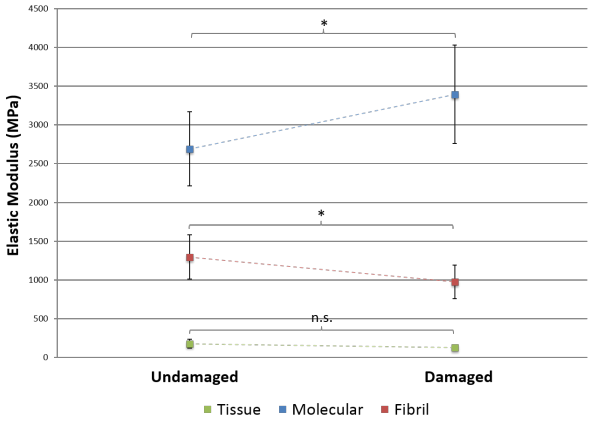
Where X_0 denotes the average characteristic length (D-period for SAXS, amino-acid spacing for WAXS, macro length for sample camera) of the unloaded sample and X denotes the characteristic length calculated from the loaded diffraction pattern. X_0 for SAXS and WAXS was calculated as an average of measurements taken twice at 5 positions along the tendons axis, for n=3 unloaded tendons. Unloaded D-period for SAXS was computed as $674.5\mathring{A} \pm 0.07\%$. Unloaded intra amino-acid spacing from WAXS was calculated as $2.798\mathring{A} \pm 0.09\%$.

Elastic Moduli of Fibril, Molecule and Tissue

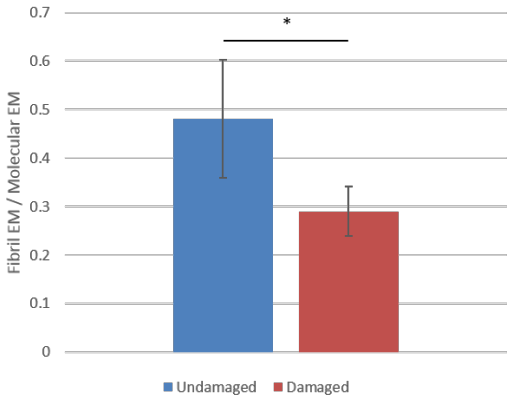
Strains measured at the three length scales probed were plotted against stress. Stress calculations assumed tight lateral packing of molecules and fibrils. Stress-strain curves for molecules and fibrils show linear increasing trends for all samples (Figure 2.13a), confirming the elastic nature of the material, allowing elastic moduli to be calculated from the curve slopes. Figure 2.13a confirms strain partitioning at the three structural levels: molecular elongation is lower than that of fibrils, which in turn is lower than whole tissue elongation. This confirms additional mechanisms involved during loading of tendon samples, with a rearrangement of collagen molecules accounting for the additional strain measured in fibrils, and ground substance deformation and fibril superstructure rearrangement contributing to higher strains measured in the whole tissue sample.[95] Studies of cross-link deficient tendons have shown an increase in this effect, indicating the cross-link locations as the areas which are deformed during straining [129].



(a) Stress-Strain curves for all measurement levels and damage levels, showing partitioning of strain between tissue, fibril and molecule



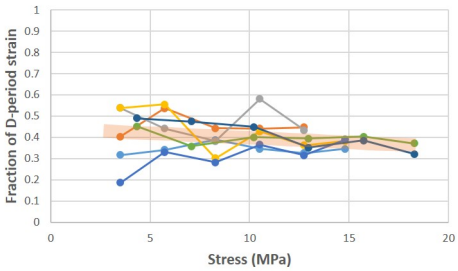
(b) Fibril modulus (SAXS) and Molecule modulus (WAXS) as a function of damage level. Mean ± SD. * = $p < 0.05$ by t-test



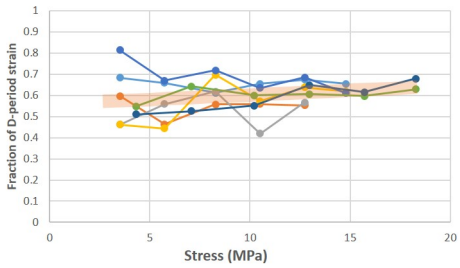
(c) Ratio of fibril elastic modulus to molecule elastic modulus, in relation to damage level. * = $p < 0.05$ by t-test. n = 6. Mean ± SD

Figure 2.13: Stress-strain curves from in situ tensile loading of tendon fascicles probed by x-ray diffraction, and elastic modulus relation to damage.

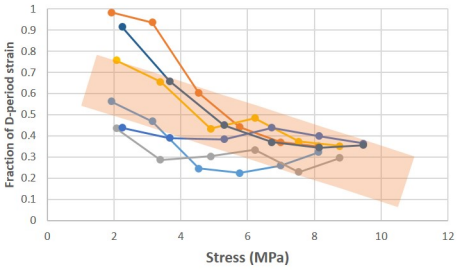
Tissue-level stiffness was not significantly affected by pre-applied damage (figure 2.13b). Mean fibril elastic modulus, decreased significantly ($p<0.05$) from 1300 to 900 MPa with pre-applied damage (figure 2.13b). Conversely, average molecular Elastic modulus significantly ($p<0.05$) increases from 2690 to 3395 MPa with damage. This divergent behavior indicates permanent changes to the structural organisation of the tissue following damage application. Qualitatively, molecular stiffening observed might be explained by a change in triple helix geometry, as reported for mechanically overloaded tendon collagen, which



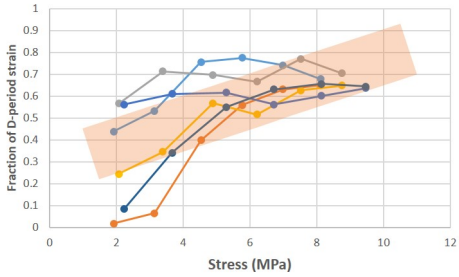
(a) Fraction of fibril (D-period) strain due to molecular elongation. Undamaged samples



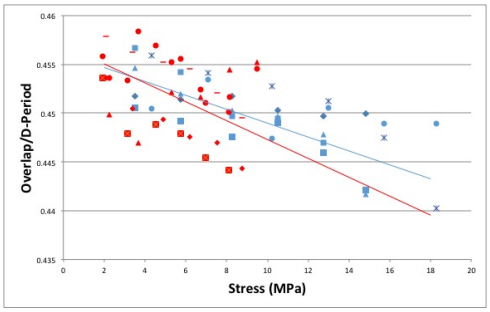
(b) Fraction of fibril (D-period) strain due to molecular rearrangements. Undamaged samples



(c) Fraction of fibril (D-period) strain due to molecular elongation. Damaged samples



(d) Fraction of fibril (D-period) strain due to molecular rearrangements. Damaged samples



(e) Ratio of Overlap to D-Period as a function of stress. Blue = undamaged, Red = Damaged

Figure 2.14: Molecular elongation and rearrangement contributions to fibril deformation. Red bars = average slope of data sets from corresponding condition. Red bar thickness represents deviation of slopes (thicker bar = higher deviation, a.u.)

denatures with load application. Previous studies on overloaded collagen fibrils showed a reduction in enthalpy of denaturation, and proposed that the collagen molecules were uncoiled into a stable denatured state, consistent with our observations. [130] This may

reduce axial mobility of neighboring amino-acids and thus reducing the increase in intra-amino-acid spacing as load is applied. [131] The loss of stiffness at the fibril level implies ulterior deformation mechanisms in fibril straining, not limited to affine deformation from triple helix straining.[129, 94]

Damage alters tendon deformation modalities

Combining simultaneous WAXS and SAXS data, the contributions of deformation modes to the overall deformation of the tissue were calculated. Assuming fibril elongation to be an additive effect of an affine molecular stretch and molecular rearrangements, then:

$$E_D = E_M + M \tag{2.7}$$

Where E_D is the elongation (nm) at the fibrillar D-period level, E_M is the elongation of intra-amino-acid spacing along a molecule (nm), and M includes all molecular rearrangement effects. Hence, overall stretch of the fibril D-period can be described by:

$$(1 + \epsilon_D) * D_0 = D_0(1 + \epsilon_M) + M \tag{2.8}$$

Where D_0 is the fibril D-period in unloaded state and ϵ_m is the strain at the molecular level.

From equation 2.8, using WAXS and SAXS data, undamaged samples qualitatively show a more uniform partitioning of D-period deformation between molecular elongation and rearrangement, with an average decrease in elongation and increase in rearrangements with stress (figures 2.14a, 2.14b). Molecular elongation decreases rapidly in damaged samples (fig 2.14c), with rearrangements conversely increasing (fig 2.14d), apparent at low stresses (<6MPa). In both groups, molecular elongation converges to approximately 0.38% of D-period strain at high stresses.

Damage causes changes in structure

Changes in the molecular arrangement, caused by sliding of laterally and axially adjacent molecules, cause a variation in the ratio of the overlap region to the total D-period. These changes account for the higher straining of fibrillar D-period compared to only an affine molecular deformation.

Assuming the electron density along a fibril is described by a square function with a period of 67 nm, having a low period (gap) of 0.54D and a high period (overlap) of 0.46D, a variation in gap and overlap would result in a change in the relative integrated intensities of successive SAXS peaks [132, 96]. This can be described as:

$$\frac{I_{n+1}}{I_n} = (\frac{n}{n+1})^2[\frac{sin((n+1)\pi[O/D])}{sin(n\pi[O/D])}]^2 \tag{2.9}$$

Where n is the peak order, O is the overlap length, and D is the D-period length. Qualitative analysis of O/D values plotted against stress indicates a steeper average decrease for damaged samples compared to undamaged samples (figure 2.14e). Since the D-period has been shown to decrease with damage (figure 2.12a), this effect must be due to the overlap region shrinking faster in damaged samples. This region corresponds to the location of cross-links between terminals of laterally adjacent collagen molecules within fibrils, and an increased deformation as a result of applied stress may implicate cross-link damage as the location of tensile damage. In artificially-induced hyper-cross linking, the opposite effect is observed [91], suggesting that damage accumulation decreases cumulative cross-linking strength.

Limitations of experimental method and analysis

To further understand the mechanisms of damage in collagenous connective tissues, the ability to probe lateral packing of fibrils and helical arrangement of molecules simultane-

ously would allow for a more complete appraisal of structural changes with damage, by measuring triple helix pitch and fibril helical characteristics [133, 121, 134].

2.3.4 Conclusions

Understanding collagen damage at the nanoscale is key to preventing injury from accumulated micro-damage, as well as to develop strategies for encouraging healing. X-ray diffraction allows us to probe biological collagenous tissues at the nanoscale. By performing in situ mechanical loading it is possible to probe the mechanical properties at various scales within the collagenous superstructure. Simultaneous data collection is key to studying the molecular, fibrillar and tissue behaviour under load, and exploring the relationship between these three structural levels.

Here, we focus on the effects of mechanical damage induced by tensile elongation on the mechanical properties of rat tail tendons at two scales: the fibril and the molecular scales. We show a significant decrease in both fibril D-period and molecular intra-amino acid spacing as a result of applied damage, which is indicative of damage mechanisms at both scales. We have shown significant loss of fibril level stiffness and significant increase of stiffness at the molecule level following damage, indicating distinct mechanisms at the two levels. The overlap region of the fibrillar D-period exhibits a faster reduction in length in damaged samples than the gap region, indicative of potential damage being localised here, where laterally adjacent collagen molecules are cross-linked. This is consistent with the observed inhomogeneous partitioning of D-period strain between molecular elongation and rearrangements observed in damaged samples, once again indicating damage localised where the mechanisms allowing molecules to move relative to one another are found.

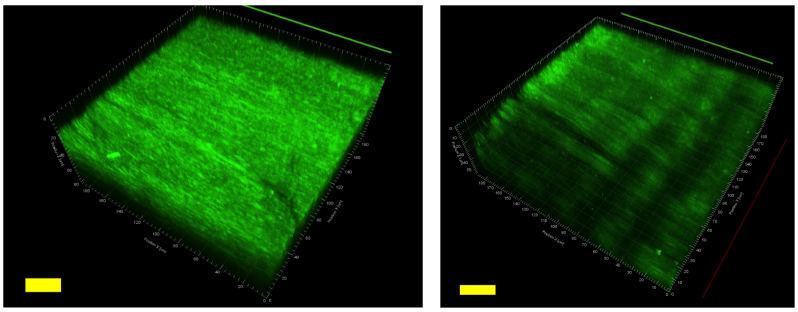
2.3.5 Acknowledgements

This work was supported by the Rosetrees Trust (award M186-F1) for materials and EPSRC (DTP Programme studentship funding). We acknowledge Diamond Light Source for time on beamline I22 under proposal SM10601-1.

2.3.6 Supplementary Information: X-ray Damage (Unpublished)

Multi-Photon Microscopy of XRD-Induced Damage

X-ray radiation is known to produce heating an ionising effects in tissues, which could alter the tissue mechanical properties [135]. As previously shown by Fessel et al., short esposures (< 20 min) to X-ray radiation do not affect measured tendon collagen D-period [91].



(a) (b)

Figure 2.15: Effects of short-term (a) and long-term (b) X-ray exposure on tendon collagen. Green line shows direction of tendon axis. Scale bars = 30μm

In order to verify this result, tendon samples were exposed to the X-ray beam for long time periods (> 20 min) and examined for damage using a Zeiss LSM 780 Multi-Photon Microscope (MPM). In MPM, two incident excitatory photons of a set wavelength combine to give one emission photon of half the wavelength (and thus double the frequency) allowing greater imaging depth within tissue samples. Collagen, a highly non-centrosymmetric molecule, will emit light at $350 - 375$ nm when excited with two photons at $700 - 750$ nm. This phenomenon is called second harmonic generation (SHG) [136].

MPM SHG images showed distinct damage patterns in long-exposure tendons, indicating collagen denaturation. No similar loss of signal was observed in short-exposures consistent with exposure times for loading experiments (figure 2.15). This confirms that the effects observed and reported here are not due to X-ray damage.

2.4 Strain Partitioning Between Nerves and Axons: Estimating Axonal Strain Using Sodium Channel Staining in Intact Peripheral Nerves

Fabio Bianchi, Ruby Sedgwick, Hua Ye and Mark S. Thompson.

Published, Journal of Neuroscience Methods, 08 August 2018. Original available at [137].

2.4.1 Introduction

The peripheral nervous system lacks ossified protective structures, exposing it to continuous mechanical deformation. Supraphysiological elongation of peripheral nerves causes injury, which can range from blocks in signal conduction (neuropraxia) to complete transection (neurotmesis) [20]. At strains of 5-20% functional deficits occur, which result in impaired sensory and motor function [34, 69, 25].

The mechanism that leads to conduction deficits is not entirely understood. Peripheral nerves are mechanically modelled as concentric composites, made up of an outer sheath (consisting of the thick collagenous epineurium and outer perineurium), and a soft inner core, containing myelinated and unmyelinated axons, connected by a layer which allows relative sliding (mesoneurium) [52, 75, 72]. It has been hypothesised that excessive axonal elongation causes excessive separation of nodes of Ranvier, resulting in impaired signal conduction [12, 102]. Clinically, nerve elongation occurs as a result of traumatic injury such as joint dislocation [138], or chronically due to compression syndromes such as carpal tunnel syndrome, where localised compression results in nerve stretch during wrist movement [139]. Understanding the mechanical properties of peripheral nerve is also of considerable importance in designing artificial nerve grafts and conduits. Tissue engineering approaches to nerve repair must consider the biomechanical properties of the

tissue, to design compatible replacements [13]. The partitioning of axial strain between tissue and axons is not understood, and could help explain altered functionality as a result of stretch. This has previously been investigated in fibrous tissues, with implications in tissue engineering designs [140]. A better understanding of strain transfer in peripheral nerve could impact the design on nerve grafts and artificial conduits, where biomechanical properties are increasingly recognised as fundamental design parameters [13].

Axonal damage thresholds have been estimated in central nervous system white matter by comparing morphological deformation and electrophysiological impairment [63], but do not provide information about the local axon strain. Multi-scale computational models of brain mechanics account for partitioning of strain between tissue and axon, but lack non-invasive experimental confirmation [60, 141]. Fourier analysis of periodic Bands of Fontana that result from axon tortuosity has been used to estimate microstructural strains, but do not provide a reliable direct measurement of axonal strain [53].

Nodes of Ranvier, the periodically spaced gaps between myelinating Schwann cells, present an ideal intrinsic feature to measure axon strain. In previous work, contactin-associated proteins (CASPR) have been stained, and used as fiducial markers during spinal cord elongation [118]. However, CASPR staining requires paraformaldehyde fixation and surfactant permeabilisation, which significantly alter tissue mechanical properties [142, 143]. Sodium channels, which cluster at nodes of Ranvier, are formed of four transmembrane alpha subunits - and one transmembrane beta subunit - which contains an extracellular domain accessible without permeabilisation (figure 2.16) [144].

Digital image correlation (DIC) is a non-invasive technique which uses surface feature matching to calculate strains between images, and has been previously used to evaluate strain partitioning between meniscus tissue and chondrocytes [145] and within annulus fibrous cells [146].

The aim of this study is to measure localised axonal strains during whole-nerve elongation to quantify axial strain partitioning in peripheral nerves, using multi-photon imaging of nerves without fixation or permeabilisation. This was achieved by staining of extracellular domains of sodium channel beta subunits in nodes of Ranvier by immunocytochemistry without fixing or permeabilising the nerve, and using DIC to estimate axonal strain during tissue elongation. The onset of Wallerian degeneration, which causes axonal breakdown in injured nerves, is delayed by freezing of excised nerves [108], which has been shown not to alter the mechanical properties of the tissue [19]. This technique can be further applied to studying alterations in axon mechanical properties in diseased nerves, as well as helping understand multi-scale strain partitioning for nerve tissue engineering.

2.4.2 Materials and Methods

Sciatic Nerve Harvesting

Sciatic nerves were harvested from 300-350 g (10-12 week old), male Sprague-Dawley rats, sacrificed by cervical dislocation for an unrelated study. Briefly, following skin removal, the sciatic nerves were exposed by dorsal incision of the gluteus muscle. Nerves were excised proximally close to the spinal cord, and distally at the tibial-peroneal branching. Nerve samples were stored in Phosphate Buffered Saline (PBS, Gibco, UK), immediately frozen at -20°C until use. Freezing and thawing has been extensively used in nerve biomechanical experiments [59, 80, 147], and shown not to alter specific mechanical properties of peripheral nerves [19] as well as those of other collagenous tissues [148], and lowering tissue temperature has been shown to delay the onset of Wallarian degeneration [108].

Sodium Channel Staining

Sciatic nerves were incubated at 4°C in 1:50 dilution of primary antibodies against extracellular sodium channel subunits I and IV (Alomone Labs, Israel) in PBS with 1%

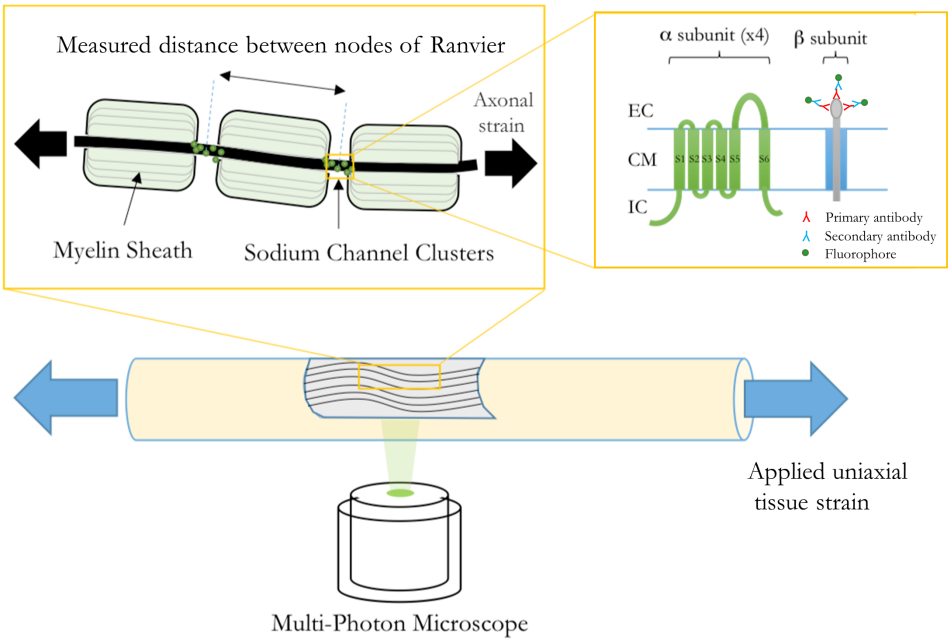
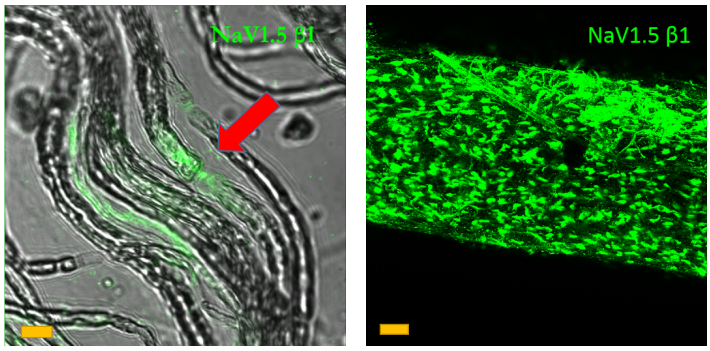


Figure 2.16: Experimental setup overview. Rat sciatic nerves were subject to displacement controlled tensile loading, and induced axonal strains were measured by digital image correlation of multi-photon images of stained sodium channels clustered at nodes of Ranvier. Inset shown sodium channel structure, with primary antibody targeted to extracellular β-subunit and secondary antibody (fluorophore) binding to primary antibody. EC = extracellular, CM = cell membrane, IC = intracellular

bovine serum albumin (BSA, Sigma Aldrich, UK), for 48 hours on an orbital shaker. Samples were then washed in PBS with 1% BSA five times, for five minutes each time, and incubated with AlexaFluor488 secondary antibody (ThermoFisher) for a further 48 hours at 4°C on an orbital shaker. Samples were then washed twice more in cold PBS, and mounted on glass coverslips or stretching machine for imaging. A control for non-specific staining was carried out by incubating nerve tissue with secondary fluorophore only, resulting in no fluorescent signal after washing.

Nerve Stretching and Imaging

To test the antibody protocol, stained nerves were stripped of the epineurium, and individual fibres teased using fine forceps. Fibres were imaged using a Zeiss LSM 708 inverted confocal microscope (100x oil immersion lens), simultaneously acquiring green



(a) (b)

Figure 2.17: (a) Co-localisation of node of Ranvier morphology (red arrow, transmitted light image) and sodium channels (NaV1.5β subunit, green), imaged by confocal microscopy in excised rat sciatic nerves, stained without fixation or permeabilisation. Scale bar = 10 μm. (b) Maximum intensity projection of multi-photon imaging z-stack through nerve. Scale bar = 50 μm.

fluorescence and transmitted light signals. Whole nerves were imaged during stretch using multi-photon microscopy (MPM), which allows imaging through thicker tissue sections. MPM images (20x lens) were taken using a Zeiss LSM 780 inverted microscope during graded nerve elongation, applied using a custom-built uniaxial stretching device with modified clamps directly gripping the nerves [149]. Nerves were stretched in 5% grip-to-grip strain increments, from 0% to 20%, at 0.1 s^{-1} strain rate. This strain range starts below *in vivo* level of pre-strain, in order to construct a full plot for strain partitioning up to strains recognised as the threshold for conduction blocks [34, 69]. Z-stack images with slice thickness of 4 μm were taken at each value of applied strain, with laser power correction to account for nerve thickness. Nerves were kept hydrated by manual addition of PBS. Five nerves were prepared for testing, of which four are reported here. One sample (nerve 4) failed due to slipping at the clamp grip at 20% applied strain. Another sample was damaged during mounting.

Digital Image Correlation

Average axonal strain was estimated by DIC. Maximum intensity projections of z-stacks of stained nerves were used as patterns to calculate average strains. GOM Correlate (GOM

GmbH, Germany) was used to calculate strain parallel to elongation direction between images from successive applied deformation levels. Only points which were successfully tracked at all levels of applied strain were used for analysis. DIC measurements correspond to an average axonal strain in the same direction as tissue loading. Compared to tracking individual axons [118], this method does not require manual tracking of individual axons (which would not be possible without further staining requiring fixation and permeabilisation) and returns a higher number of points used for correlation.

Statistical Analysis

Statistical analysis was carried out using PRISM (GraphPad, USA). Data was fitted by linear regression. Changes in measured axonal strain with applied nerve strain were tested for significance by one way paired ANOVA testing, with Tukeys multiple comparison between successive applied strain values. Results reported as significant if $p < 0.05$.

2.4.3 Results and Discussion

Sodium Channels can be Stained Without Fixation and Permeabilisation

Confocal images of stained teased fibres show co-localisation of sodium channel staining and nodes of Ranvier (figure 2.17a), confirming that the protocol used is suitable for whole-nerve preparations without fixation or permeabilisation. Multi-photon z-stacks show staining of nodes of Ranvier within the thickness of the nerve, from which a maximum intensity projection can be used to obtain a pattern for DIC (figure 2.17b). Previously Singh et al. estimated white matter axonal strains during tissue deformation by following paranodal regions of nodes of Ranvier. In their experiments, spinal cords were stretched, and fixed overnight in the deformed position. Tissues were then sliced, permeabilised using Triton X-100 and stained for CASPR, found at paranodal regions of nodes of Ranvier, which were used as fiducial markers to estimate axonal strains [118]. Fixation of

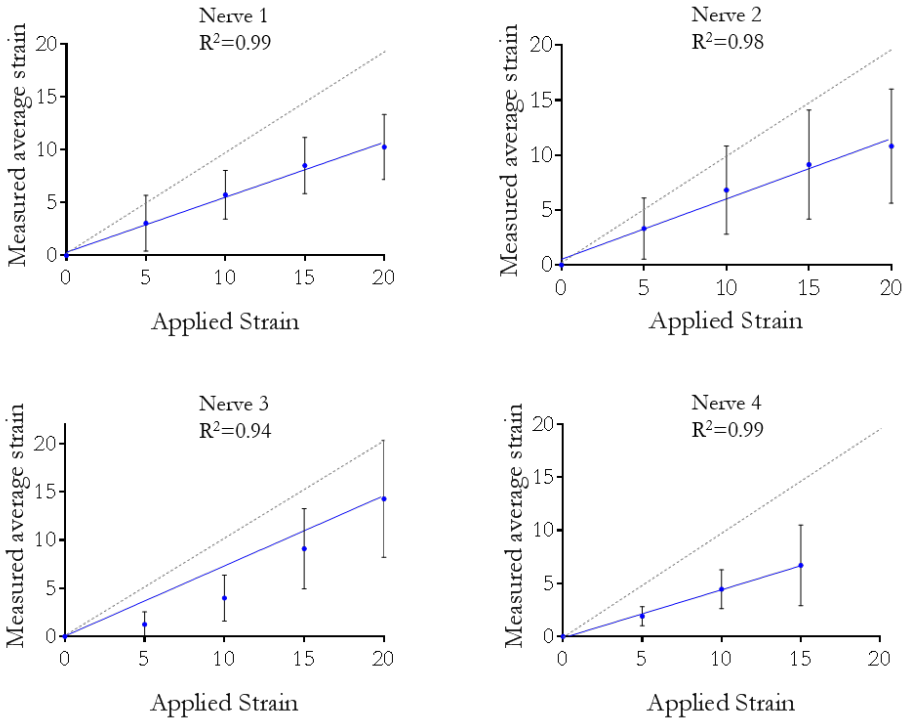


Figure 2.18: Measured axonal strain (%) increases linearly with applied tissue strain (%) for all four nerves tested. Points show average, errors bars show S.D. Blue lines are linear regression fits. Dotted lines show unity slope.

tissues cross-links cellular structure, irreversibly altering the mechanical properties of the tissue [142]. Furthermore, slicing alters tissue ultrastructure, possibly resulting in altered mechanical properties. In the method presented here, staining extracellular elements does not require permeabilisation of the cell membrane using surfactants, and freezing allows tissue preservation without fixation. Stretched nerves therefore closely resemble in vivo conditions.

Measured Axonal Strain Increases Linearly with Tissue Strain

DIC was used to estimate the average strain at the axon level, by averaging over 50 points for each applied strain level. For all four nerves tested, measured average axonal strain increased linearly with applied tissue strain (figure 2.18, R^2 = 0.99, 0.98. 0.94 and 0.99). In all four nerves, axonal strain increased significantly between each incremental level of

applied strain ($p < 0.001$ between successive strains for all nerves), with a small deviation from linear behaviour observed at higher strains for nerves one and two. Singh et al. report a similar nonlinearity in spinal cords [118], attributing this to axon disconnection during stretch. Bain and Meaney [63] have estimated by comparing morphological and electrophysiological changes in white matter, a threshold of approximately 20% tissue strain which causes axonal damage, in line with strain values where we see the greatest departure from linearity. The average slope from linear regression was 0.56 ± 0.10, representing the ratio between applied strain and measured strain. Strain transfer properties have been shown to vary between tissue types, depending on tissue architecture and isotropy [140]. In peripheral nerves, where axons are constrained within endoneurial collagen tubes surrounded by stiff perineurial and epineurial collagen strain may partition axially to avoid excessive axonal elongation. Peripheral nerve axons are known to be crimped, less stiff than surrounding perineurial and epineurial collagen, and connected to the outer sheath only by the thin mesoneurial layer that allows sliding [72, 75]. When the nerve is strained, the stiffer collagenous tissue will limit the overall extension. The axial collagen layer also exhibits crimp visible under MPM second harmonic generation, which decreases with applied strain but does not completely disappear at 20% strain (data not shown). Axons within the nerve core will uncrimp, and slide within the stiffer outer sheath, resulting in lower axonal strain. Love et al. showed, using Fourier analysis of periodic bands of Fontana, that nerves retain some periodic axonal waviness at strains up to 20% [53]. This indicates that in our experiments axons will not be fully uncrimped at maximum applied strains (20%). Due to the well-established differences in mechanical properties between nerve core and outer sheath [19, 75], these results provide further evidence of a protective mechanical role for outer sheath collagen. By allowing sliding of nerve core and outer sheath, the full load applied to the tissue is not transferred to the core, thereby protecting the softer axons from mechanical damage. In the outer sheath,

collagen fibres are also crimped when unloaded. It has been shown, however, that collagen uncrimps significantly faster than axons [53, 150], again suggesting that the outer sheath will protect the underlying core during stretch by bearing load before axons are strained beyond repair. Schwann cells are known to have a significant role in providing resilience and compressive strength to axons [79]. Axially, spinal cord demyelination has been shown to lower tissue stiffness and ultimate tensile strength, suggesting a mechanical role for myelin, although demyelination methods may directly alter tissue mechanical properties [78]. Furthermore, nodes of Ranvier have been shown to elongate significantly during nerve stretch [71]. Because we use inter-nodal distance to estimate axonal strain, our results may underestimate axonal elongation.

2.4.4 Conclusions

Conduction deficits and loss of sensory and motor function are known to occur when peripheral nerves are stretched supraphysiologically. A multi-scale understanding of nerve mechanics is required to understand the damage processes. Currently, the mechanical relationship between tissue deformation and axonal strain is not well characterised. Current techniques are limited because sample preparation alters the mechanical properties of the tissue. Here, we show that average axonal strain can be estimated by multi-photon microscopy of whole nerves, stained for sodium channel extracellular subunit β-1, without tissue fixation or permeabilisation. We show that axons strain increases linearly with applied tissue strain, with a slope of approximately 0.55, indicating that axons only take up half the tissue deformation. Both axons and collagen exhibit crimp patterns that allow the nerve to withstand high strains without significantly loading the axonal fibres. This experimental approach can be used in the future to study strain partitioning between tissue and axons in models of degenerative diseases. The results presented here can be used to calibrate single-cell deformation models, aimed at eliciting the relationship be-

tween nerve stretch and neural function loss. Although these conclusions are limited by the small number of nerves tested, the method presented should be of interest for understanding the biomechanical properties of peripheral nerve, and how they translate to impaired neural function.

2.5 Chapter Summary

The work presented in this chapter aimed to relate peripheral nerve deformations at the macroscopic level with structural alterations at the micro- and nano-scopic scale. When peripheral nerves are deformed, neurons, Schwann cells, and other cells are in turn deformed by alterations in extracellular structure. The relation between applied macroscopic and effective microscopic strains was quantified by using high-definition multi-photon microscopy and X-ray diffraction methods.

Overall, the results presented in this chapter present a link between the macro-mechanical properties of peripheral nerves and the deformations at smaller length scales. Understanding the mechanisms involved in nerve deformation and the localisation of damage within the tissue micro-structure helps establish the aetiology of peripheral nerve dysfunction following trauma or injury.

Statement of Authorship for joint/multi-authored papers for PGR thesis

To appear at the end of each thesis chapter submitted as an article/paper

The statement shall describe the candidate's and co-authors' independent research contributions in the thesis publications. For each publication there should exist a complete statement that is to be filled out and signed by the candidate and supervisor

Title of Paper	Probing multi-scale mechanical damage in connective tissues using X-ray diffraction
Publication Status	☑ Published ☐ Accepted for Publication ☐ Submitted for Publication ☐ Unpublished and unsubmitted work written in a manuscript style
Publication Details	Bianchi, F., Hofmann, F., Smith, A.J. and Thompson, M.S., 2016. Probing multi-scale mechanical damage in connective tissues using X-ray diffraction. Acta biomaterialia, 45, pp.321-327.

Main Author

Name of Principal Author (Candidate)	Fabio Bianchi		
Contribution to the Paper	Planned and designed experiments, carried out experiments, carried out analysis (unless specified), wrote manuscript		
Signature		Date	06/08/2018

Co-Author Contributions

Name of Co-Author	Dr. Felix Hofmann
Contribution to the Paper	Helped plan experiments, helped carry out experiments, first analysis of SAXS data, reviewed manuscript

Name of Co-Author	Dr. Andrew J. Smith
Contribution to the Paper	Technical help during experiments, reviewed manuscript

Name of Co-Author	Dr. Mark S. Thompson
Contribution to the Paper	Supervision throughout the process, helped write manuscript

Name of Co-Author	
Contribution to the Paper	

Please cut and paste additional co-author panels here as required.

Supervisor Confirmation

By signing the Statement of Authorship, you are certifying that the candidate made a substantial contribution to the publication, and that the description described above is accurate.

Supervisor name and title:	Dr Mark S Thompson		
Signature		Date	09/08/2018

This completed form should be included in the thesis, at the end of the relevant chapter.

Statement of Authorship for joint/multi-authored papers for PGR thesis

To appear at the end of each thesis chapter submitted as an article/paper

The statement shall describe the candidate's and co-authors' independent research contributions in the thesis publications. For each publication there should exist a complete statement that is to be filled out and signed by the candidate and supervisor

Title of Paper	Probing multi-scale mechanics of peripheral nerve collagen and myelin by X-ray diffraction
Publication Status	☑ Published ☐ Accepted for Publication ☐ Submitted for Publication ☐ Unpublished and unsubmitted work written in a manuscript style
Publication Details	Bianchi, Fabio, et al. "Probing multi-scale mechanics of peripheral nerve collagen and myelin by x-ray diffraction." Journal of the Mechanical Behavior of Biomedical Materials (2018).

Main Author

Name of Principal Author (Candidate)	Fabio Bianchi		
Contribution to the Paper	Planned and designed experiments, carried out experiments, carried out analysis (unless specified), wrote manuscript		
Signature		Date	06/08/2018

Co-Author Contributions

Name of Co-Author	Dr. Felix Hofmann
Contribution to the Paper	Helped plan experiments, helped carry out experiments, first analysis of SAXS data, reviewed manuscript

Name of Co-Author	Dr. Andrew J. Smith
Contribution to the Paper	Technical help during experiments, reviewed manuscript

Name of Co-Author	Dr. Hua Ye
Contribution to the Paper	Supervision throughout the process, reviewed manuscript

Name of Co-Author	Dr. Mark S. Thompson
Contribution to the Paper	Supervision throughout the process, helped write manuscript

Please cut and paste additional co-author panels here as required.

Supervisor Confirmation

By signing the Statement of Authorship, you are certifying that the candidate made a substantial contribution to the publication, and that the description described above is accurate.

Supervisor name and title:	Dr Mark S Thompson		
Signature		Date	09/08/2018

This completed form should be included in the thesis, at the end of the relevant chapter.

Statement of Authorship for joint/multi-authored papers for PGR thesis

To appear at the end of each thesis chapter submitted as an article/paper

The statement shall describe the candidate's and co-authors' independent research contributions in the thesis publications. For each publication there should exist a complete statement that is to be filled out and signed by the candidate and supervisor

Title of Paper	Strain partitioning between nerves and axons: estimating axonal strain using sodium channel staining in intact peripheral nerves
Publication Status	☑ Published ☐ Accepted for Publication ☐ Submitted for Publication ☐ Unpublished and unsubmitted work written in a manuscript style
Publication Details	Accepted for Publication, Journal of Neuroscience Methods

Main Author

Name of Principal Author (Candidate)	Fabio Bianchi		
Contribution to the Paper	Planned and designed experiments, carried out experiments, carried out analysis (unless specified), wrote manuscript		
Signature		Date	06/08/2018

Co-Author Contributions

Name of Co-Author	Ruby Segdwick
Contribution to the Paper	Helped plan and carry experiments

Name of Co-Author	Dr. Hua Ye
Contribution to the Paper	Supervision throughout the process, reviewed manuscript

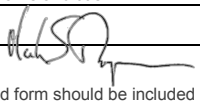
Name of Co-Author	Dr. Mark S. Thompson
Contribution to the Paper	Supervision throughout the process, reviewed manuscript

Name of Co-Author	
Contribution to the Paper	

Please cut and paste additional co-author panels here as required.

Supervisor Confirmation

By signing the Statement of Authorship, you are certifying that the candidate made a substantial contribution to the publication, and that the description described above is accurate.

Supervisor name and title:	Dr Mark S Thompson		
Signature		Date	09/08/2018

This completed form should be included in the thesis, at the end of the relevant chapter.

CHAPTER 3

Development Of *In Vitro* Neuron Stretch Models

This chapter is divided into two sections. The first details the development of a protocol to differentiate human iPSCs into functional motor neurons for use in PNI modelling. The second half presents the characterisation of a novel cell-stretching device, deigned to investigate changes in neural network and single-cell electrophysiology with applied uniaxial strain.

3.1 Introduction and Background - Neural Cells

Understanding the processes involved in neural dysfunction following mechanical trauma has been partially limited by the models used to study them. Fresh human nerve tissue is complex to obtain for testing due to severe associated donor site morbidity, and therefore research must heavily rely on surrogates. Aside from few experiments on human cadavers [151, 49] and post-mortem isolated human nerves [147, 74], animal models are the most common.

At the cellular level, culturing primary neurons represents a technical challenge as they are terminally differentiated cells and therefore do not proliferate. Primary human neurons are extremely expensive, and geographically limited to countries where research on human foetal tissue is allowed [152]. Animal cells are therefore widely used as models. The first experiments of the effect of mechanical loading on single-cells were carried out on giant squid axons, the largest known single-nerve fibre [153]. Murine primary neurons are today the most commonly used cell source for mechanical neuropathy studies (figure 3.1), however there are significant inter-species differences, potentially leading to poor translational value [154].

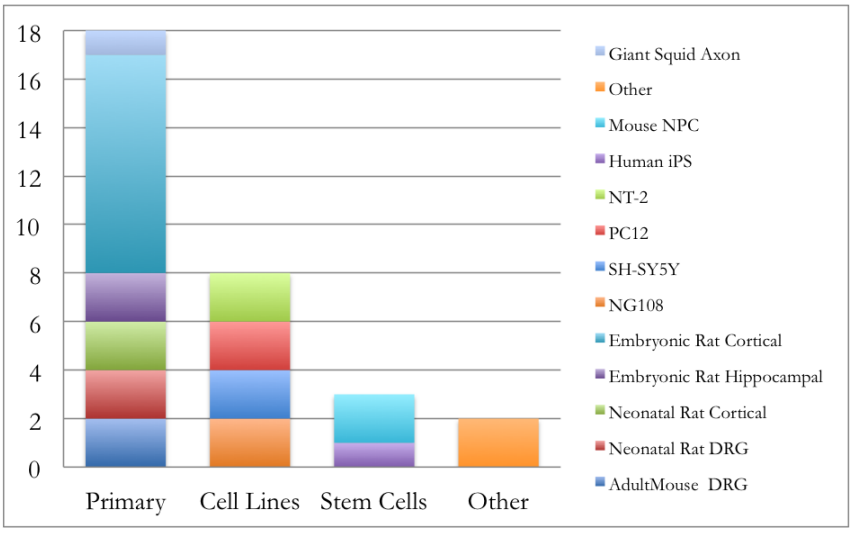


Figure 3.1: Analysis of published work cited in this thesis on *in vitro* neural cell deformation organised by cell source, showing how primary rodent cells represent the vast majority of studies, followed by immortalised neural cell lines. A very limited number of studies exists which use stem-cell derived neurons. NPC = neural progenitor cells, DRG = dorsal root ganglion cells.

Immortalised neural cell lines of human or animal origin represent alternatives to primary cells. These are derived from cancerous biopsies and 'neuralised' either by differentiating factors (such as SH-SY5Y [155], PC-12 [156], NG108-15 [157] or NT-2 [158] cells) or by hybridisation with primary neurons (such as F11 cells [159]). Immortalised cell lines are inexpensive, rapidly available, and easily manipulated sources of neural-like cells, but they are variably inadequate to model the physiological responses of human

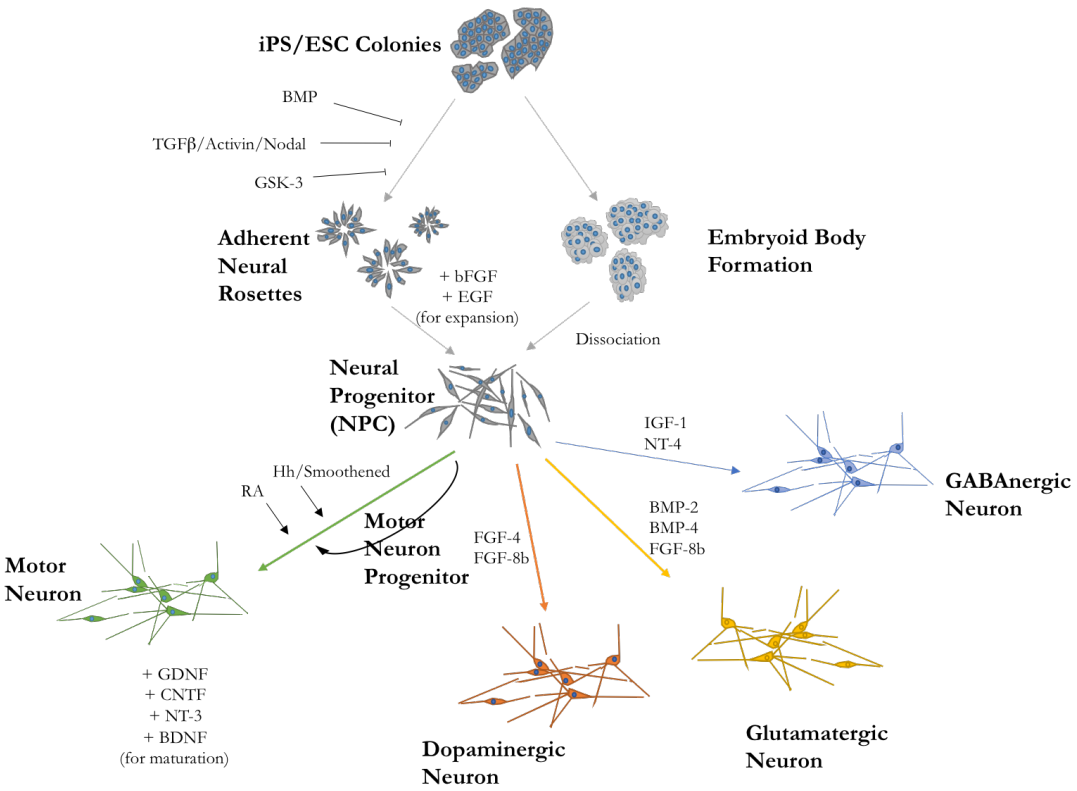


Figure 3.2: Differentiation pathways from pluripotent stem cell to different neural fates.

neurons, except for specific applications for which the cell line has been developed and extensively characterised [160].

Neuronal cultures can also be established by differentiating stem cells. Neural tissue develops from the ectoderm, the outermost early embryonic germ layer when during the third week of gestation the ectoderm thickens and the neural plate develops. Subsequently the neural plate folds to create the neural tube, which gives rise to the majority of neurons, and a small portion of tissue is left out forming the neural crest from which a subset of sensory neurons and Schwann cells are derived [16]. Functional human neurons can be differentiated from embryonic stem cells (ESCs) by following the same developmental cues *in vitro* [161]. The use of embryonic cells for research is however tightly regulated worldwide, and their application in research limited [162].

In 2006, Takahashi and Yamanaka produced the first induced pluripotent stem cells from reprogrammed mouse fibroblasts by ectopic expression of four reprogramming factors, Oct3/4, Sox2, c-Myc and Klf4 [163]. A year later, the same group successfully reprogrammed adult human dermal fibroblasts using the same method, to create the first human induced pluripotent stem cell (iPSC) line [164]. iPSCs posses embryonic-like self-renewal properties and are pluripotent: they are capable of differentiating into cells from all three human germ layers without senescence. Neural differentiation of both iPSCs and ESCs can be achieved by inhibition or activation of specific pathways by small molecule and cytokine addition, resulting in cells of multiple neural fates (figure 3.2) [165].

3.2 Rapid and Efficient Differentiation of Functional Motor Neurons From Human iPSC for Neural Injury Modelling

Fabio Bianchi, Majid Malboubi, Yichen Li, Julian H. George, Antoine Jerusalem, Francis Szele, Mark S. Thompson and Hua Ye.

Published, Stem Cell Research, 26/09/2018.

3.2.1 Introduction

Supraphysiological elongation of peripheral nerves causes conduction blocks, resulting in chronic or temporary debilitating loss of motor function [5, 166]. For example, brachial plexus birth palsy, initiated by excessive brachial plexus stretching during birth, causes motor and sensory impairment in 0.4% of US births [167]. Conduction blocks implicate multiple nerve components including myelin [168], axonal paranodes [25] and blood vessels [99], but impairment of electrical transmission with strain has also been shown in isolated unmyelinated neuronal axons [153]. Current studies on stretch-related conduction blocks are limited to animal tissue models [25, 168], and the majority of *in vitro* studies on the effect of mechanical injury on neurons are limited to using rodent primary neurons [169, 170], rodent neural stem cells [171], or immortalised cell lines [172]. Animal models provide simple, inexpensive models for neural damage studies, but concerns exist about the translational value of results from animal models to human conditions [154]. For example, candidate drugs for neuroprotection have failed human clinical trials after positive results in animal models [173]. The use of human induced pluripotent stem cells (iPSCs) provides physiologically relevant insights into the mechanics of human neural injury and motor function loss, overcoming potential issues of interspecies variability.

The induction of pluripotency in adult human cells provides an alternative cell source, both for *in vitro* studies and for clinical applications [164], avoiding ethical and regulatory

complications of embryonic stem cell (ESC) use. Concerns about reproducibility and efficiency of iPSC differentiation, coupled with high costs and lengthy timeframes, have however limited their use [174, 175]. Pluripotency induction by forced expression of defined factors generates iPSCs from adult cells, which can then be differentiated into adult cell lineages, including multiple neural fates such as dopaminergic [176], GABAergic [177] and motor neurons (MNs) [178], by following developmental cues found *in vivo* [179]. iPSC-derived neurons have multiple uses, including disease modelling [180], *in vitro* neural injury modelling [181] and transplantation trials [174], for which differentiation protcol requirements vary. In modelling diseases such as amyotrophic lateral sclerosis (ALS), cells must acquire the diseased phenotype, and generally need to be kept in culture for extended periods of time [180, 182]. In injury modelling, the emphasis is on large scale, rapid production of functional cells, which are only kept in culture until experiments are performed [181].

Current human iPSC MN induction protocols vary in timescale and efficiency, with few protocols achieving both high efficiency and rapid MN generation. Faravelli et al. reviewed MN induction protocols from both human ESCs and iPSCs, showing high variability in efficiency and timescale of protocols, ranging from 30 days to more than six weeks [178]. Measures of efficiency include specific marker expression, morphological analysis, electrophysiological analysis and animal transplantation, and depend on the intended use for iPSC-derived MNs [178]. Sances et al reviewed protocols used to derive MNs specifically for ALS modelling, reporting differentiation efficiencies from 20% to 95% and with timeframes ranging from 12 to 130 days, but without taking into account the quality of characterisation, the protocol difficulty, or the intended MN use [180].

In directed differentiation, iPSCs are induced to become neural progenitor cells (NPCs) through neuralisation, either by embryoid body (EB) formation, or by dual SMAD inhibition in monolayer cultures. EB formation, where suspension cells spontaneously arrange

and grow in three-dimensional aggregates upon withdrawal of factors promoting pluripotency, is the most widely used neuralisation method [183, 184, 185, 186]. However, EB formation requires lengthy protocols, the use of undefined culture conditions often including animal serum [185], and is tedious to perform [187, 188]. More recently, techniques for neural neuralisation in adherent monolayer cultures have been developed, using defined small molecules for dual-SMAD signalling inhibition: bone morphogenic protein (BMP) and TGF-β/nodal/activin inhibition has been shown to effectively convert human iPSCs to NPCs in adherent cultures [187, 189].

Noggin, an endogenous polypeptide, was the first factor to be used for BMP inhibition [187], but selective small molecule BMP inhibitors dorsomorphin and DMH1 have been shown to increase inhibition efficiency [190, 191]. Additionally, TGF-β/activin/nodal inhibition by small molecule SB431542 has widely been used in both EB and monolayer cultures to induce neuralisation [187, 192, 183]. Following the establishment of adherent monolayer neuralisation protocols, additional factors have been tested to enhance neuralisation. CHIR-99021, a Wnt activator by GSK-3 inhibition, has been shown to further increase neuralisation efficiency, and notch signalling inhibition by γ-secretase inhibitor compound-E has been found to accelerate neuralisation [193, 189].

NPCs, expressing transcription factors Sox1 and Pax6, and intermediate filament nestin, are then induced to MNs. Following *in vivo* gradients of retinoic acid (RA), responsible for MN specification along the rostrocaudal axis [194], and hedgehog (HH), controlling ventral specification [195], NPCs are directed to motor neuron progenitors (MNPs) [178]. Addition of soluble RA, and HH signalling activation by addition of direct smoothened agonist small molecules purmorphamine and SAG [186, 193, 184], or of soluble sonic HH (SHH) [196], result in OLIG2-positive MNPs. MNPs are then matured by culturing with growth factors, resulting in electrophysiologically functional spinal MNs,

expressing MN-specific markers HB9, ISL1 and ChAT as well as neuron-specific markers such as β-III tubulin and MAP2 [197, 198, 186, 178].

Here, we report the development of a fast induction protocol, aimed at rapid production of electrophysiologically active MNs for use in peripheral nerve mechanical injury studies. The aim was to rapidly produce adherent MN populations with high proportions of electrophysiologically active cells showing a mechanosensitive response to injury. Our protocol relies only on serum-free, adherent cultures, providing a facile method for the production of functional neurons. iPSCs monolayers are induced to NPCs in serum free conditions, by dual SMAD inhibition using dorsomorphin and SB431542, coupled with GSK-3 inhibition by CHIR-99021 and γ-secretase inhibition by compound-E. Following neuralisation, soluble RA, SHH, SAG, and purmorphamine are used to specify spinal MN fate. We assess MN maturity by whole cell patch clamping and calcium imaging, evaluating electrophysiological activity of differentiated neurons, and we characterise the mechanosensitivity of MNs generated by this protocol by measuring network activity modulation when subjected to uniaxial deformation. The differentiation protocol was validated in two iPSC lines independently reprogrammed from human dermal fibroblasts from unrelated control patients.

3.2.2 Materials and Methods

iPSC Culture

All reagents were purchased from ThermoFisher and growth factors from Peprotech unless otherwise specified.

Two iPSC lines were used in this study. Cell culture at all stages was carried out on tissue culture plastic well plates and imaging dishes (IBIDI μ-dish), unless otherwise specified. Line SB-AD3-1 was generated by StemBANCC, Oxford. In brief, dermal fibroblasts were obtained from skin biopsy of healthy individuals following appropriate

ethical consent. iPSC generation was performed using the CytoTune-iPS 2.0 Sendai Reprogramming Kit (Invitrogen). The cultures undergoing reprogramming were maintained at 37°C and 5% CO_2 in human ESC medium on feeder layers for two to three weeks or until colonies with typical human ESC morphology appeared. Individual colonies were mechanically dissected and plated onto fresh feeder plates for up to eight passages before being adapted to feeder free conditions which involved plating on Matrigel-coated plates (MG, Corning) with mTeSR1 media (Stem Cell Technologies), which was also the medium used in further experiments.

The second iPSC line (010S-1) was induced from a skin biopsy of a 18 year old female healthy subject, at the Highfield Unit, Warneford Hospital, Oxford. Skin fibroblasts were cultured from skin biopsy taken from the inner upper arm of the subject, and subsequently reprogrammed to iPSCs with CytoTune-iPS 2.0 Sendai Reprogramming Kit. The transfected cells were plated on mouse embryonic fibroblasts feeders to allow initial appearance of iPSC clones (about first 18 days). Picked clones were expanded, in a feeder-free manner, on Matrigel with mTeSR1 medium supplemented with 1% P/S. Colony 010S-1 was expanded to passage 13 and cryopreserved as the master stock. One vial from the master stocks was thawed in mTeSR medium on matrigel coated plates to perform quality control steps (data not shown) including normal speed of growth after thawing, CytoTune clearance assay by qPCR, flow-cytometry analysis of pluripotency markers NANOG and TRA-1-60, and SNP analysis of genomic integrity using an Illumina Human CytoSNP-12v2.1 beadchip array.

MG was diluted on ice in cold KnockOut-DMEM according to the batch-specific dilution factor, and added to well plates for 4-12 hours before cell seeding. Thawed cells were plated in mTeSR supplemented with 1% Penicillin/Streptomycin and 1% Revita-Cell (ROCK inhibitor and antioxidant compound) was added during the initial 24 hours. Medium was replaced daily. Colonies were passaged by incubating for 3.5 minutes in

versene (0.48 nM EDTA), lifted by washing with mTeSR medium using a large-bore pipette, and plated in mTeSR.

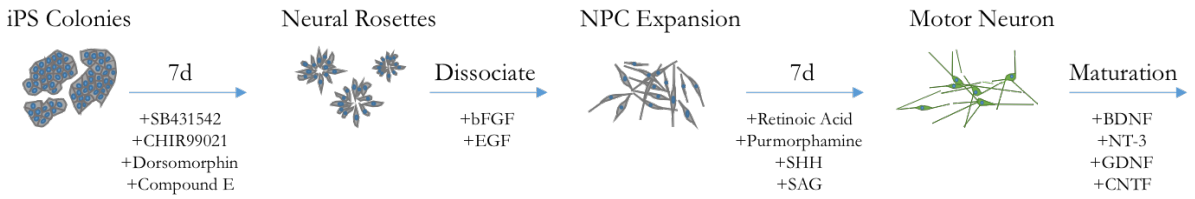


Figure 3.3: Differentiation timeline. iPS colonies were neuralised by dual-SMAD , GSK-3 and γ-secratase inhibition for 7 days. Dissociated neural rosettes were expanded before differentiation to motor neurons by caudalisation and ventralisation for 7 days.

iPSC Differentiation to NPC

The differentiation protocol (figure 3.3) was performed using iPS line SB-AD3-1, and validated in line 010S-1 by evaluating differentiation end-points (neuron staining and electrophysiology).

Confluent iPSCs were dissociated using accutase and plated at 0.5×10^6 cells/well on MG-coated 6-well plates in neural induction medium (NIM), consisting of a 1:1 mix of KO-DMEM/F:12 and neurobasal medium (NBM) supplemented with 10% KnockOut Serum Replacement, 1% Non-Essential Amino Acids (NEAA), 1% GlutaMAX, 0.1 mM L-ascorbic acid (L-AA, Sigma-Aldrich), 2 μM SB431542 (Cell Guidance Systems), 3 μM CHIR99021 (Sigma Aldrich), 1 μM dorsomorphin (StemCell) and 1 μM Compound E (StemCell). 1% RevitaCell was added for the first 24 hours only.

NIM was replaced daily for six days, after which cells were dissociated with Accutase, and plated in NPC expansion medium, consisting of a 1:1 mix of KO-DMEM:F12 and NBM, supplemented with 1% P/S, 1% B27, 1% N2, 1% NEAA, 1% GlutaMAX, 0.1 mM L-AA, 10 ng/ml bFGF and 10 ng/ml EGF. Cells were either expanded for banking, or

kept for MN differentiation. One fifth of cells were retained at each passage for marker analysis. Cells were expanded for up to four passages.

NPC Differentiation and MN Maturation

NPCs were cultured for six days in MN induction medium, consisting of a 1:1 mix of KO-DMEM:F12 and Neurobasal Medium supplemented with 1% P/S, 1% B27, 1% N2, 1% Non-Essential Amino Acids, 1% GlutaMAX , 0.1 mM L-ascorbic acid, 10 μM all-trans retinoic acid (Sigma Aldrich), 100 ng/ml recombinant SHH, 1 μM Purmorphamine (Abcam) and 1 mM SAG Dihydrochloride (Sigma Aldrich). After seven days, cells were dissociated using Accutase, and re-plated in maturation medium, consisting of 1:1 KO-DMEM:F12 and NBM, supplemented with 1% P/S, 1% B27, 1% N2, 1% NEAA, 1% GlutaMAX , 0.1 mM L-AA, 10 ng/ml CNTF, 10 ng/ml BDNF, 10 ng/ml NT-3 and 10 ng/ml GDNF.

Immunocytochemistry, Imaging and Analysis

Cells were fixed in 3.75% paraformaldehyde (Sigma Aldrich) solution in phosphate buffered saline (PBS) for 15 minutes at 4°C, blocked and permeabilised using 0.1% Triton-X, 0.1% Tween-20 and 2.5% BSA in PBS for 30 minutes at 37°C. Primary antibodies (all from AbCam, at 1:1000 unless specified) to Sox1, Pax6, Nestin, HB9, MAP2, NeuroFilament, Tuj1 and Olig2 (1:300, Millipore) were added and kept overnight at room temperature, and counter-stained with AlexaFluor secondary antibodies for four hours at room temperature. Nuclei were labelled with NucBlue. Cells were imaged using a Nikon TI-E inverted fluorescence microscope. Image analysis was carried out using ImageJ. Statistical analysis was carried out using GraphPad PRISM.

Calcium Activity

Calcium activity was imaged using Oregon Green 488 BAPTA-2 calcium indicator [199]. Cells were incubated in a 4 μM dye solution in FluoroBrite-DMEM Imaging Medium for 30 minutes, washed twice in PBS, and further incubated in fresh FB-DMEM for 30 minutes. Cells were imaged using standard FITC filters at 10 fps for four minutes, and fluorescence intensities from individual segmented cells recorded in time. Intensity values were adjusted for fluctuations by subtracting average background, and expressed as $I = \frac{I(t)}{I(t=0)}$.

Electrophysiology

A Digidata 1440A digitizer and a MultiClamp 700B amplifier piloted through pCLAMP 10 Software (all from Molecular Devices, CA) were used. Intracellular solution contained 140 mM KCl, 5 mM NaCl, 0.5 mM $CaCl_2$, 2 mM $MgCl_2$, 10 mM HEPES, 1 mM GTP, and 2 mM ATP, and was adjusted to 7.4 pH by KOH and 300 OsmL^{-1} by glucose addition. Bath solution contained 130 mM NaCl, 5 mM KCl, 2 mM $CaCl_2$, 1 mM $MgCl_2$, 10 mM glucose, and 10 mM HEPES (all from Sigma-Aldrich), and was adjusted to 7.4 pH by NaOH and 290 OsmL^{-1} by glucose addition. Following gigaseal formation, whole-cell patch clamp was established. Ion currents were recorded by stimulation from -70 to +20 mV under voltage-clamp recording, and action potentials (APs) were evoked in current clamp mode by stimulating current pulses from -50 pA to +30 pA.

Cell Injury Methods

Cell mechanosensitivity was tested by applying uniaxial strain to maturing cell networks. Previuosly, similar methods have been used to replicate *in vitro* traumatic brain injury, using rodent primary neurons [200, 201]. A custom-built substrate deformation device (Bianchi et al, 2018, submitted for publication, under review), allowing simultaneous

uniaxial cell deformation and high-frequency imaging was used to apply graded strains of up to 70% and 0.1 s^{-1} strain rate, with simultaneous network activity monitoring by calcium imaging. Cells were strained, and calcium flux was imaged from cells kept in the strained state. MNs were seeded onto MG-coated custom-made rectangular deformable silicone wells with ultra-thin (50 μm) silicone culture surfaces measuring 10.0 $\times$ 6.5 mm at a density of 500 cells/mm^2 in maturation medium, and kept in culture two days before experiments.

Data Analysis and Statistics

Images were analysed using FIJI (Fiji Is Just ImageJ), and calcium imaging data was processed using a custom-written MATLAB code to filter data, extract and measure peaks. Statistical analysis was carried out using GraphPad PRISM v6.

3.2.3 Results

iPSCs Differentiate to Motor Neurons

During neuralisation, cell morphology changed from expanding colonies to neural rosettes, with radially arranged cell groups. Neuralisation was quantified after six days by expression of Sox1, Pax6 and Nestin. Increase of Pax6, Sox1 and Nestin positive cells were observed in neuralised samples, compared to undifferentiated iPSC colonies (Fig. 3.4). 76% $\pm$ 10% of neuralised cells expressed Sox1, 83% $\pm$ 11% expressed Pax6 and 89% $\pm$ 2% expressed nestin, all significant increases from iPSC.

MN specification induced a significant decrease in Pax6 and Sox1, whilst Nestin levels did not decrease significantly (Fig. 3.4). Olig2 expression after five days MN induction was significantly increased, with 88% $\pm$ 2% of cells positive for Olig2, indicating specification of MN fate. No significant Olig2 expression was detected in NPCs. Expression of Tuj1

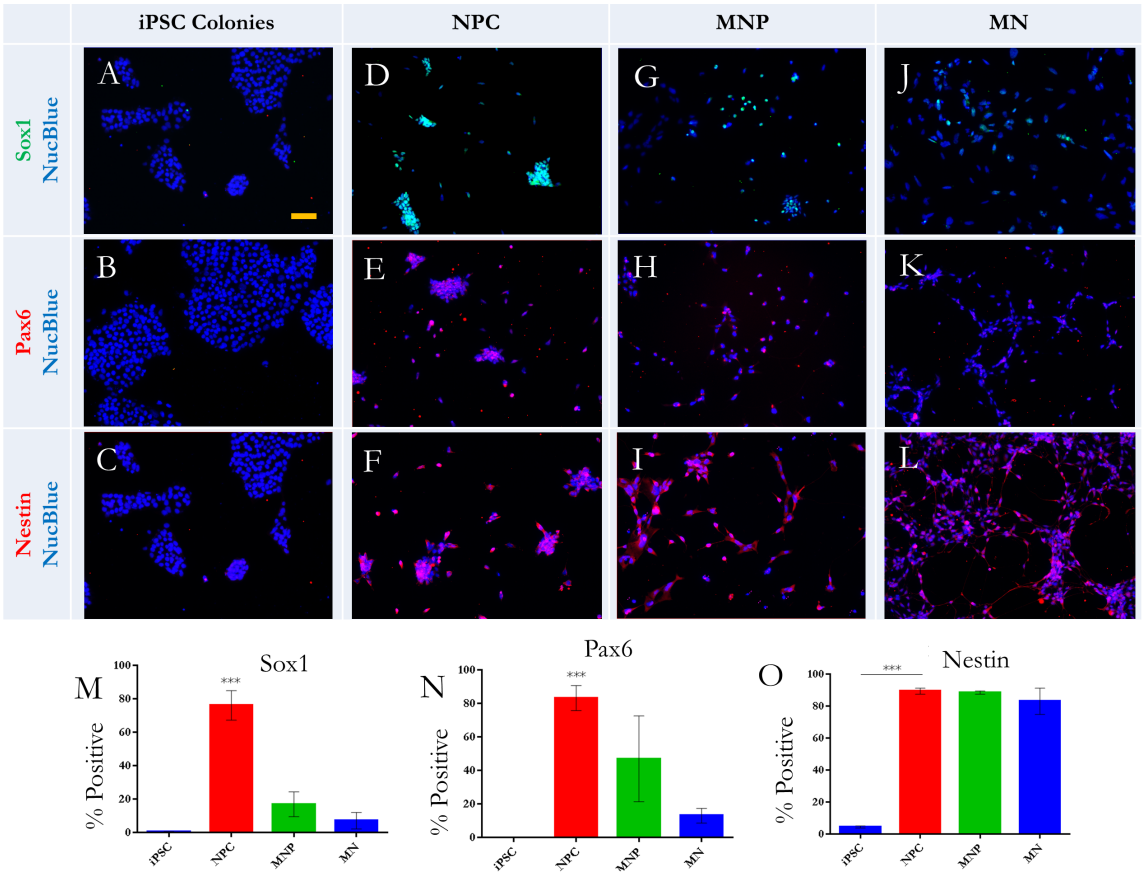


Figure 3.4: Undifferentiated iPSC colonies did not express neural progenitor markers (A-C). iPSCs neuralised by dual SMAD, γ-secretase and GSK-3 inhibition formed neural rosettes and express neural Progenitor Markers Sox1, Pax6 and Nestin (D-F). Expression was reduced after MN specification (G-I) and maturation (J-L). Quantification of marker expression (M-O), bars show mean $\pm$ SD, n $>$ 3, **** = $p < 0.0001$, *** = $p < 0.005$ by Anova testing with Tukey's multiple comparisons. Scale bar = 100 μm

also increased significantly, with 89% $\pm$ 4% of cells expressing β-III tubulin, showing induction to neural lineage (Fig. 3.5).

MN Maturation

Cell morphology was altered during maturation, with reduced cell soma area and membrane spreading, and thin, extended projections connecting adjacent cells (Fig. 3.6 G). After 21 days in maturation medium, NPC marker expression was reduced significantly (Fig. 3.4), and neuron-specific structural proteins, Tuj1 (β-III Tubulin), NeuroFilament and MAP2, were expressed (Fig. 3.6). Synaptophysin was detected at cell junctions,

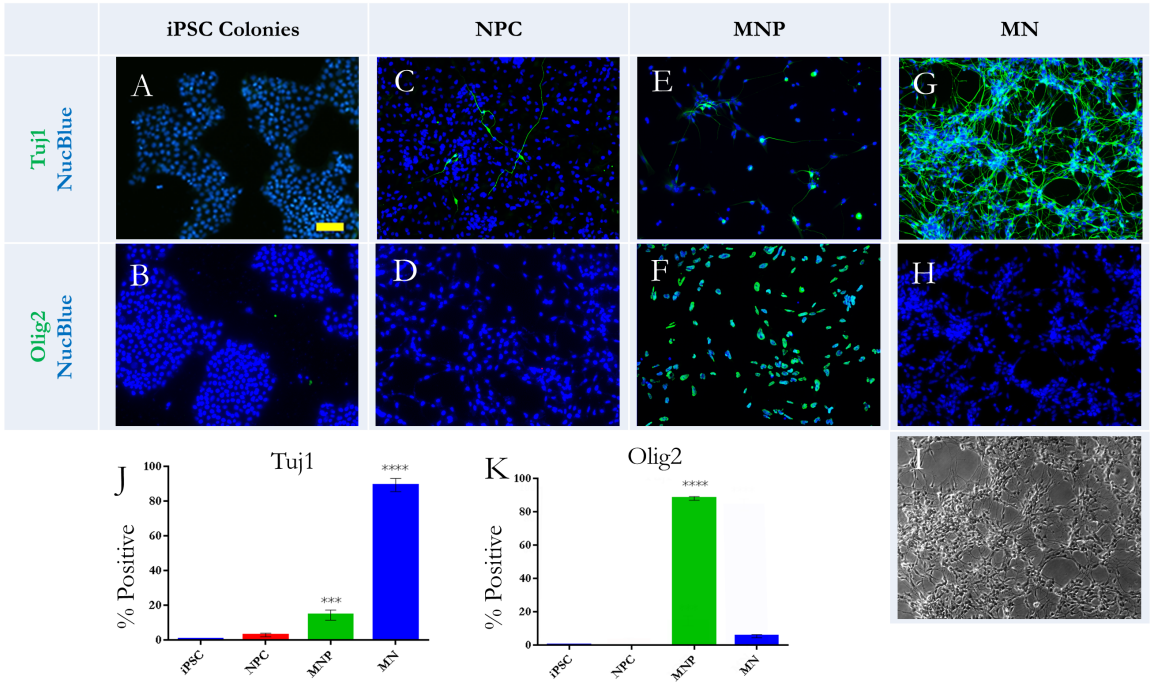


Figure 3.5: Undifferentiated iPSC colonies did not express Tuj1 and Olig2 (A,B). NPCs showed low Tuj1 expression, and absence of Olig2 (C,D). MN specification increased Tuj1 expression (E), and induced significant Olig2 expression (F). MNs expressed Tuj1 (G) but no Olig2 (H). MNs show neuronal morphology with small somatas and extensive neurite networks (I). Quantification of marker expression (J,K), bars show mean ± SD, n > 3, *** = p < 0.005 by one way unpaired Anova testing with Tukey's multiple comparisons. Scale bar = 100 μm

suggesting synaptic connectivity. Positive staining for ChAT in somatas and HB9 in nuclei confirmed MN lineage for maturing cells (Fig. 3.6), with 73±5% of cells positive for MN-specific HB9.

Efficiency of Maturation to Functional Motor Neuron

Neurons cultured in maturation medium for five days showed some calcium activity, with low spike magnitude and rate, and no bursting activity. Ion currents and induced APs were weak, indicative of successful differentiation but insufficient maturation (Fig. 3.15, A, B, D and E). Neurons cultured in maturation medium for 21 days showed faster rising spikes, higher spiking frequency, some bursting behaviour, defined ion currents, and induced APs, all indicative of neurons successfully maturing towards active cells (Fig. 3.15). After 21

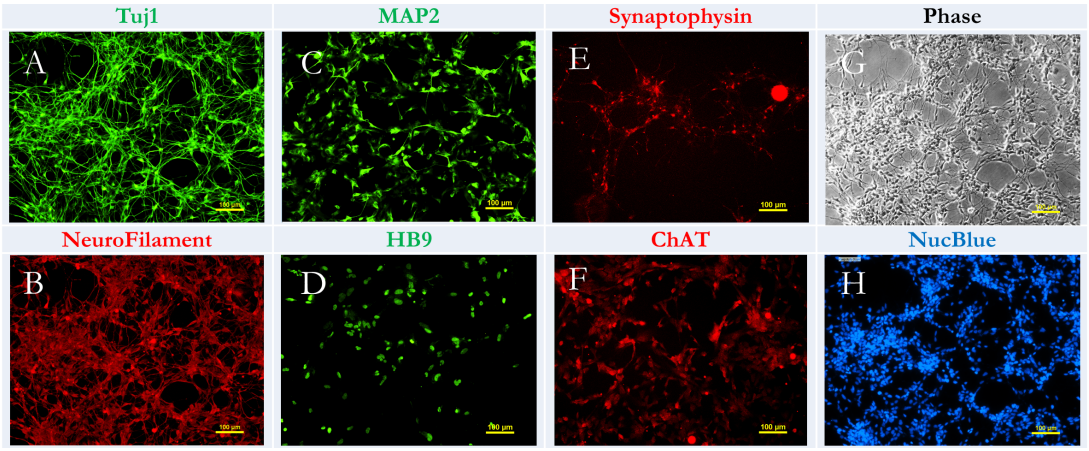


Figure 3.6: Differentiated MNs expressed neural structural proteins Tuj1 (A), NF (B), MAP2 (C), MN specific markers HB9 and ChAT (D,F) and Synaptophysin (E). Phase contrast imaging showed elongated morphology (G). Cells were counterstained by NucBlue (H).

days maturation, 75% ± 3% of cells (N = 8 independent culture dishes) were active, significantly more than after day 5 of maturation (Fig. 3.15, C). The average magnitude of calcium spikes, measured as a percentage of the baseline value, was 4.8% at day 5, and 15.2% at day 21 of maturation. The ratio of rise to fall time of peaks was 0.42 and 0.29 and the average rise slope was 0.035 and 0.095, at day 5 and day 21 respectively.

iPSC-derived MNs Form Functional Connections

Network connectivity at maturation day 21 was assessed from calcium imaging recordings. Spontaneous oscillations in intracellular calcium have been widely used as an indirect reporter of neural activity, as well as of functional synaptic connectivity [202, 199]. Detection of concurrent calcium spikes in distinct neuron somatas was used as a marker of connectivity, as previously used in whole-brain network reconstruction [203]. Maturing neurons successfully formed synaptic connections. Connected cells showed synchronised action potential firing, traceable along the connecting axon (Fig. 3.15). Cell connectivity was observed in all samples of maturing MNs tested (N = 8), indicating that neurons formed functional networks. No connectivity was observed after five days of maturation, indicating network maturation in time. To further confirm this, positive synaptophysin

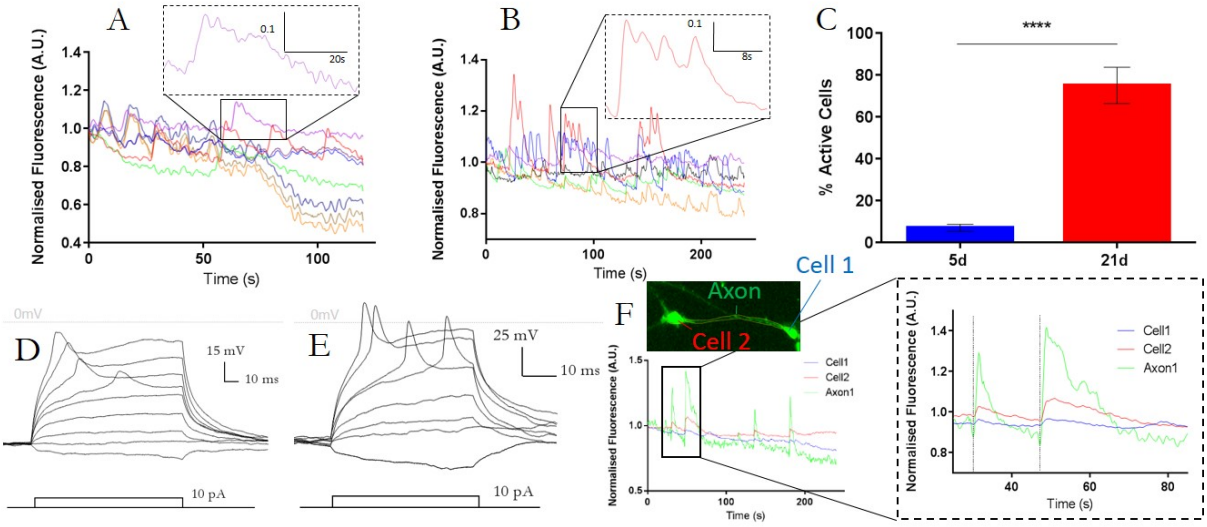


Figure 3.7: Immature MNs showed low magnitude, low frequency calcium activity. Insert shows characteristic peak shape (A). Cells cultured in maturation media for 21 days showed higher frequency firing, with some bursting behaviour. Inset shows characteristic peak shape (B). Maturation for 21 days induced 75% of cells to active neurons, compared to 7% at day 5 (C, n = 8, **** = $p < 0.0001$ by unpaired t-test). Patch clamping current-clamp recordings showed immature neurons at day 5 (D) and maturing neurons at day 21 (E). Neurons formed connected networks, with signals propagating down axons between cells (F).

puncta staining was observed in neural cultures after 21 days in maturation medium (Fig. 3.6).

Validation of Differentiation to Maturing MN

Successful differentiation was validated by repeating the protocol using iPSC line 010S-1, and evaluating end-point functionality and neural marker expression as 010S-1 cells differentiate to motor neurons. After 21 days in maturation medium, cells show extensive neurite networks, and electrophysiological activity indicative of maturation. Voltage-clamp experiments show induced action potentials (figure 3.8 (A)), including AP train firing (Fig. 3.8 (B)). Calcium imaging analysis shows functional network connectivity, as previously shown in cell line SB-AD3-1 (Fig. 3.8 (C)). Marker staining shows positive expression of NPC markers after seven days neuralisation (figure 3.8 (D-G)), and positive expression of MN markers after 21 days maturation (figure 3.8 (H-K)). Qualitatively, cells

tend to become more confluent during the same culture time, and a higher percentage of cells starts expressing Tuj1 early, compared to the same timepoint staining of NPC derived from SB-AD3-1 (Fig. 3.8 (E) vs Fig. 3.5 (C)).

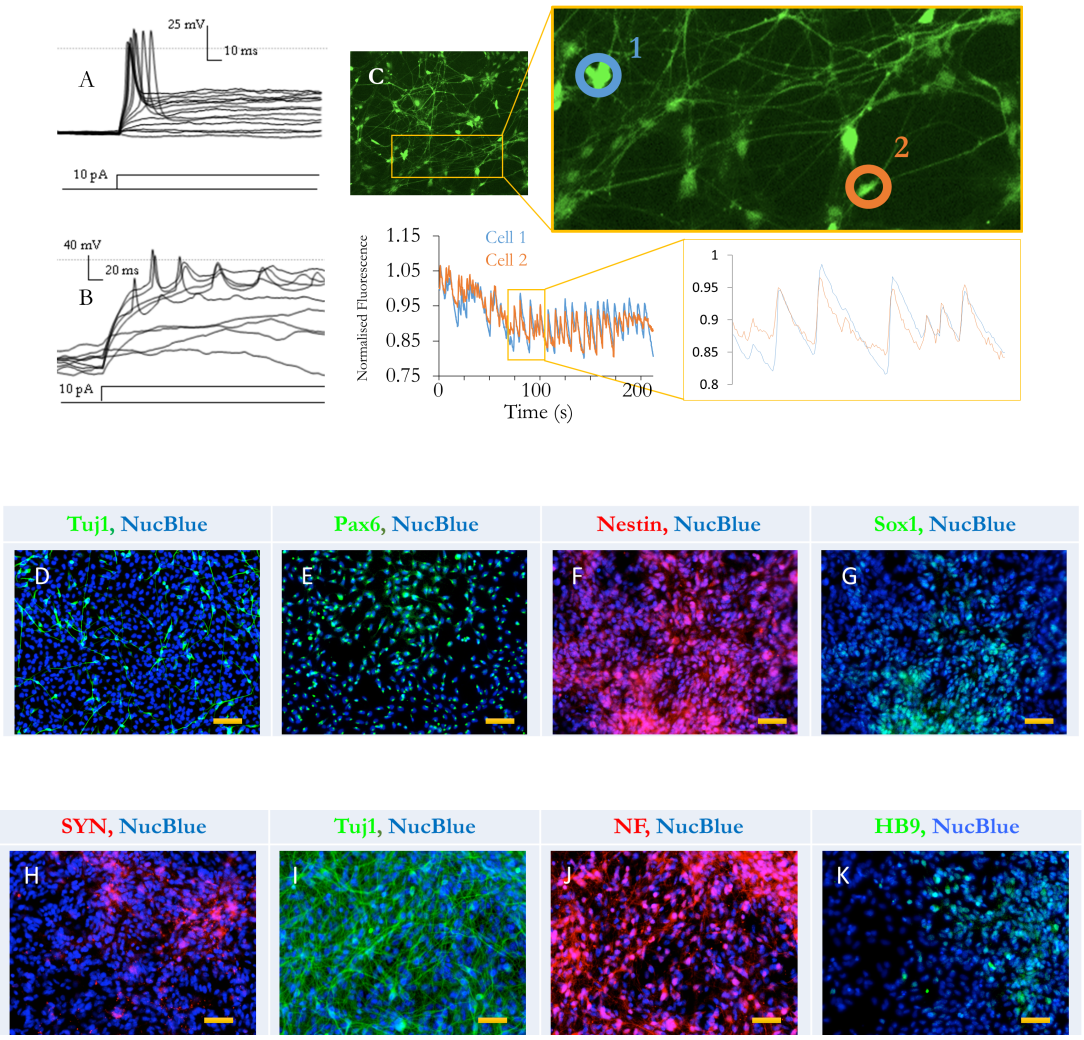


Figure 3.8: Neural differentiation and maturity is validated by differentiation of independently induced iPS line 010S-1. After 21 days maturation, cells show strong induced AP signals (A), including AP train bursts (B), networked spontaneous activity (C). Staining of NPCs shows positive expression of NPC markers (D-G) and staining of maturing neurons shows positive expression of MN markers (H-K). Scale bar = 100 μm.

Deformation Injury Affects Network Activity

Uniaxial stretch of cultured neurons has been previously used as a model for traumatic brain inury (TBI), where primary embryonic rat hippocampal neurons have been shown to respond to stretch by a marked decrease in spontaneous activity [200]. However, inter-species differences in response to stretch injury possibly decrease the translational value of these results, and provide motivation to develop human iPSC-based *in vitro* models [181]. In order to test the response of iPSC-derived MN spontaneous calcium oscillations to uniaxial stretch, MNs matured for 21 days were subjected to increasing levels of stretch (25%, 45% and 75% strain at 0.1 S^{-1} strain rate), during which calcium imaging recordings were performed. Network activity was measured by calcium imaging for four minutes before deformation, and at each sequential deformation level. The number of active cells, measured as the percentage of cells within the field of view exhibiting spontaneous calcium spikes, decreases linearly with applied deformation, and does not recover immediately after stretch release (Fig. 3.9). A significant decrease in active cells was observed at each level, both compared to the un-stretched (control) condition, and compared to the previous stretch level (incremental effect).

3.2.4 Discussion

The establishment of simple, reproducible protocols for successful differentiation of human iPSC is paramount for facilitating more widespread use of iPS-derived cells for human *in vitro* MN injury modelling. Here, we aimed to develop a simple, rapid protocol for the efficient directed differentiation of electrophysiologically active, MNs from human iPSCs, aimed at producing active cultures for short-term neural injury studies. Efficiency of differentiation was measured by specific marker expression, and number of electrophysiologically active cells, measured in synaptically active networks, indicating cell populations suitable for neural injury experiments. The mechanosensitivity of cells was evaluated by

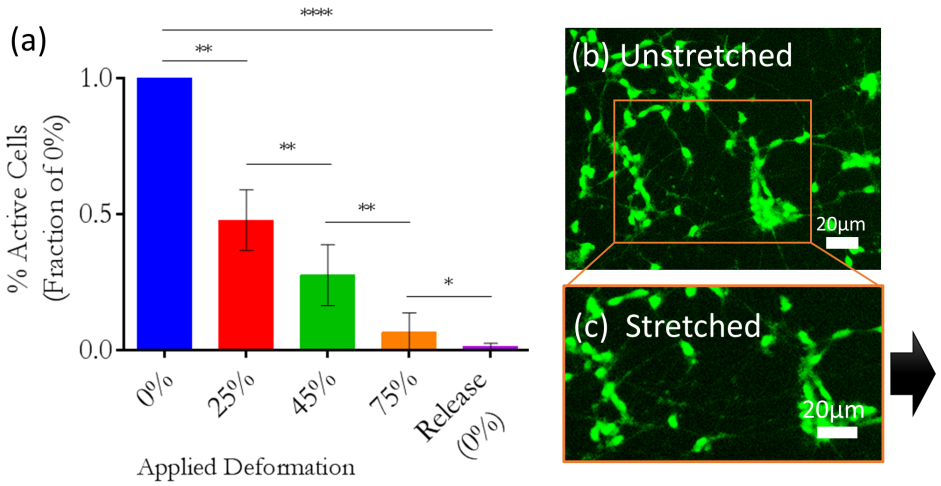


Figure 3.9: Deformation of active networks (a) modulates spontaneous activity. With increased applied substrate deformation, the percentage of active cells decreases. n = 7 independent samples. **** = $p < 0.0001$, ** = $p < 0.01$, * = $p < 0.05$, by one way paired ANOVA with Tukey's multiple comparisons. Cell bodies and neurites (b) are subjected to deformation (c). Arrow indicates direction of stretch. Scale bars = 20 μm.

exposing spontaneously active networks to uniaxial strain, and recording changes in network activity.

Adherent culture differentiation by dual-SMAD inhibition eliminates the need for EB formation, a complex and inefficient culture technique widely used in iPSC neural differentiation protocols [183, 184, 185, 191], and increases efficiency of neuralisation [180, 187, 178]. Here, we combine dual-SMAD inhibition with wnt activation and γ-secretase inhibition, to further increase efficiency, resulting in 83% PAX-6 and 76% Sox1 positive NPCs after six days. Previous use of four neuralisation factors involved either EB formation or suspension culture step following neuralisation, and did not demonstrate efficiency in terms of electrophysiological maturation of cells and networks [193, 183]. NPCs are induced to MNPs by dual HH activation, through addition of soluble SHH and direct smoothened activators purmorphamine and SAG. This results in highly pure MNP populations, with 88% of cells positively expressing OLIG2, in line with the highest values reported in literature [204, 205].

After 21 days in maturation medium, 89% of cells positively expressed Tuj1, 73% of cells positively expressed MN-specific HB9, and 75% of cells differentiated to electrophysiologically functional MNs within five weeks from iPSC thawing. Other protocols validated by electrophysiology range between 20 and 70% efficiency, and between 5 and 18 weeks duration [180, 178]. After 21 days of maturation, we show functional network formation by calcium imaging, positive expression of punctuated synaptophysin suggesting synapse formation, and positive expression of motor-neuron specific factors HB9 and ChAT, combined with neural-specific markers Tuj1, MAP2 and NeuroFilament. Moreover single-cell electrophysiology shows how, after 21 days, induced APs can be recorded, and waveform analysis of calcium spikes indicates maturation, with an increase in spike magnitude, decrease in rise and fall time, and increase in rise rate [206]. The same protocol was validated in 010S-1 cell line, a human dermal fibroblast derived iPSC line, unrelated to the SB-AD3-1 line, showing electrophysiological characteristics after 21 days maturation, and expression of neural progenitor and neural markers, confirming successful differentiation. For both cell lines, videos of calcium activity can be seen in supplementary material V1 and V2.

Maturing MNs forming spontaneously active networks were stretched to evaluate cell mechanosensitivity. Uniaxial strain can be used to model the mechanical environment of the peripheral nerve under physiological and traumatic conditions, where movement induces elongation along the nerve axis deforming tissues and neural fibres [12]. A significant decrease in cells exhibiting spontaneous calcium spiking was observed during deformation, and no recovery of activity was measured following stretch release. This is consistent with results reported for primary embryonic and neonatal cortical and hippocampal rat neurons subjected to stretch [207, 200, 208], and confirms that human iPSC-derived MNs are suitable for use in neural injury experiments. Videos of calcium activity in networks before and after stretch can be seen in supplementary materials V3 and V4. We present

the first human MN-specific *in vitro* injury model, focussing on electrophysiological alterations caused by mechanical deformations, to provide a human relevant cell model for the study of mechanical deformation and injury.

Using MN-only cultures allows the functional response of neurons to stretch to be isolated. To further develop this as an *in vitro* model of human PNI, co-culture with Schwann cells could provide myelination, a key component of the nervous system which is disrupted by mechanical trauma [168], and that enhances neuron maturation and long-term survival. To maintain the premise of physiological relevance to human PNI, human stem cell-derived Schwann cells should be used. Although human iPSC-derived neurons have been myelinated by rodent primary Schwann cells [209], and human fibroblasts have been successfully reprogrammed to myelinating Schwann cells [210], to the best of our knowledge no co-culture model exists that would allow the development of a stem-cell derived human myelinated PNI injury model.

3.2.5 Conclusions

In summary, we present a protocol to facilitate the production of electrophysiologically active MNs from human iPSCs, for short-term cultures, aimed at *in vitro* human neural injury modelling. In five weeks from iPSC culture establishment, we show efficient differentiation of electrophysiologically active neurons, with 75% of cells showing spontaneous calcium activity, and expressing neural and MN markers. Compared to other protocols showing electrophysiological maturity, this represents an improvement in terms of time as well as in efficiency. We show that human iPSC-derived MNs are suitable for *in vitro* neural injury modelling by measuring functionality alterations in networks exposed to uniaxial strain. This protocol improves efficiency of rapid MN directed differentiation, producing populations of highly active neurons expressing MN specific markers within five weeks, providing an accessible, easily implementable alternative to animal cells. Despite

maintanining advantages in terms of cost, complexity and range of applications, concerns raised over the translational value of rodent models in neurotrauma, including differences in nociception [211] and response to traumatic injury [212], indicate the importance of developing *in vitro* alternatives using human cells.

3.2.6 Acknowledgements

The authors would like to acknowledge Dr. Zameel Cader and Dr. Satyan Chintawar for kindly providing SB-AD3-1 cells through StemBANCC. Authors acknowledge China Regenerative Medicine Limited (CRMI) for funding and the EPSRC DTP award number 1514540 for F.B. funding. M.B. and A.J. acknowledge funding from the European Union's Seventh Framework Programme (FP7 20072013) ERC Grant Agreement No. 306587.

3.3 Supplementary Unpublished Information

3.3.1 Cyropreservation of iPSCs, NPCs and MNs

Cyopreservation allows storage of cells for extended periods of time, as well as facilitating transport. In differentiation protocols, cells can be cryopreserved at different stages thereby reducing the time required for differentiation to the final stage. Cryopreservation agents, such as dimethylsulfoxide (DMSO) are commonly used to protect cells from rapid freezing and thawing, by avoiding the formation of harmful ice crystals. Reactive oxygen species (ROS) scavengers and inhibitors of Rho-associated Kinase (ROCK) are often used to supplement medium to ensure good cell viability and recovery post-thawing [213].

Here, iPSC were cryopreserved in custom-mixed medium, composed of 50% mTeSR, 30% ES-qualified foetal bovine serum (Thermo Fisher), 10% KO-DMEM (Thermo Fisher) and 10% DMSO (Sigma-Aldrich), as reccommended by StemBANCC Oxford.

3.3.2 iPSC Morphology and Pluripotency After Cryopreservation

After thawing, iPSC morphology consisted of flat, tightly packed polygonal colonies with sharp boundaries and no signs of spontaneous differentiation. Alkaline Phosphatase (AP) staining was performed at each cell thaw to confirm pluripotency. mTeSR medium was removed from iPSC colonies which were then washed in PBS, and incubated in fresh mTeSR with 1:500 dilution of AP-AF488 (ThermoFisher) live stain for 20 minutes. Cells were then washed twice in fresh mTeSR and imaged immediately using standard FITC filters (490/530 nm excitation/emission) [214].

Positive AP staining indicated that cells retained pluripotency after thawing (figure 3.10). Nuclei counterstaining revealed tightly packed colonies, as well as high nucleus to cytoplasm ratio, as expected for healthy human iPSCs [164].

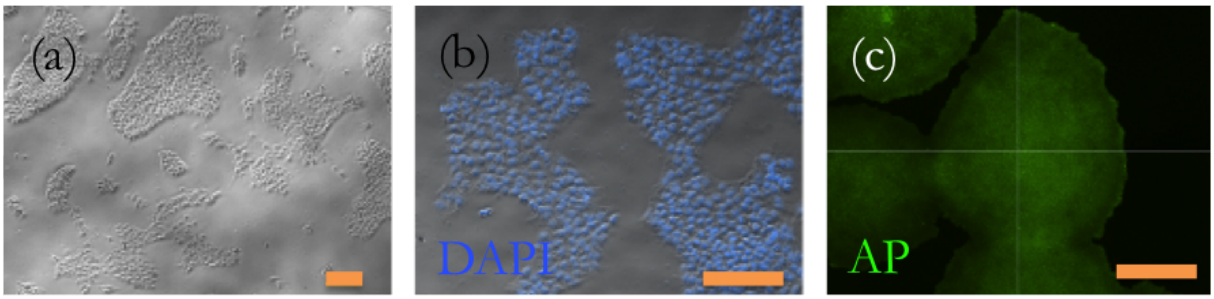


Figure 3.10: iPSC morphology and pluripotency indicated by alkaline phosphatase staining. Scale bars = 100 μm.

3.3.3 NPC Expansion

Neural progenitor cell populations were expanded following neuralisation of iPSCs, to increase the supply of cells available for differentiation. Different medium formulations were tested to optimise the expansion of NPCs.

A cell proliferation assay was carried out by analysing cell coverage of culture surface using a SpectraMax i3x Multi-Mode detection device (Molecular Probes). Plates were imaged at 37°C without lid removal to ensure sterility and maintain cell viability. 15 images were taken for each well, and the percentage cell coverage calculated, measured at days 1, 3 and 7 after seeding. Three basal mediums were tested: DMEM:F12 only, NBM only and 50% DMEM:F12 50% NBM, all supplemented with 10 ng/ml EGF and 10 ng/ml FGF.

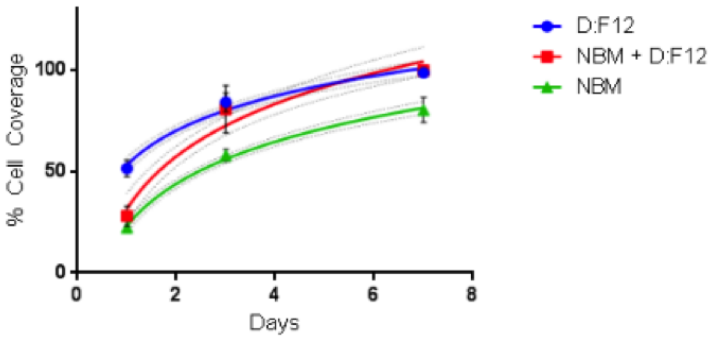


Figure 3.11: Comparison of neural progenitor cell expansion in different basal mediums. D:F12 = KnockOut-DMEM:F12, NB = Neurobasal Medium.

An equal part mixture of NBM and KO-DMEM:F12 was used for all following NPC expansion, as it yielded the fastest growth rate (figure 3.11). Variation in basal medium did not affect the expression of key NPC markers Nestin, Sox1 and Pax6 (data not quantified), although cells expanded using NBM (green curve in figure 3.11) tended to elongate, suggesting a premature partial differentiation possibly accounting for the lower expansion rate.

3.4 Introduction and Background - Cell Stretching Devices

Mechanotransduction is a vital process in tissues, regulating cellular proliferation, differentiation, and protein production [1]. Due to tissue complexity, *in vitro* models must be used in order to observe the response of individual cells to mechanical stimuli in isolation. Models of mechanotransduction have been developed extensively for multiple applications, from studying contracting cardiomyocytes to endothelial cell deformation in blood vessels [215]. In neuroscience, mechanotransduction is often related to the field of traumatic injury, where *in vitro* models have been extensively used to investigate the effects of TBI, as previously thoroughly reviewed [216, 217].

Mechanical neural injury models can be classified according to the kind of injury they aim to reproduce.

In *transection* models, injury by axonotomy is applied to cultured cells either at the macroscopic scale by syringe needle [218], plastic puncher tools [219] or rotating scribe tools [220], or at the microscopic scale by selective laser ablation [221]. These somewhat crude methods are limited in the range of injury they can be used to model. Transection represents only the most extreme form of neural injury, therefore limiting the clinical significance as models for neural damage.

In *compression* models, direct compressive deformation is applied to tissue slices [222] or cultured tissue models [223] by weight drop or percussion. Since a direct blunt trauma to neural tissue is very rare due to protection by the skull and spinal vertebrae, compression models are limited in physiological relevance. Furthermore, they rely on three-dimensional tissues or cultures, limiting the possible methods to evaluate cell behaviour following injury. Direct compression has also been used, applied by micropipette contact with cells but is limited by low experimental throughput and physiological relevance [224].

Inertial and Shear traumas are used to model impact-induced inertial injury relevant to TBI, and range from simple models of accelerating/decelerating cell culture flasks [225] to cultured 3D cell constructs subject to controlled shear loading [226].

Fluid shear stress models use flow to induce cellular deformation either through a rotating disk in contact with the fluid above cultured cells [158], or by sterile air discharge from a micropipette [227]. In neural tissue, and especially in peripheral nerve, fluid shear force is unlikely to be the primary cause of injury, making fluid shear force models less relevant.

Direct *stretch-injury* is the most commonly used model, due to its physiological relevance and ease of use. Adherent cultured cells are subject to deformation when the underlying substrate is stretched. This can be achieved by direct substrate clamping [156, 228, 201, 171], air pressure pulses [172, 229, 230], vacuum pulses [231] or by substrate deformation by hollow intenders [157, 231, 181] resulting in uniaxial or biaxial deformation. Deformation of soft substrates in proximity to the cells has also been used to investigate mechanotransduction of sensory neurons, but does not allow precise control over deformation [232].

3.4.1 Design Parameters

The development of the cell-stretching device presented in this chapter was constrained by the required functionality. The two major requirements included compatibility with high-resolution confocal imaging and with direct electrophysiological measurements during cell stretch. No previously described cell-stretching device allows both kinds of measurements while keeping cells in a stretched state. Furthermore, compatibility of the device with multiple models of microscope stages, as well as ease of transport and set-up, were required deign parameters.

High resolution imaging required substrate thickness to be smaller than the working distance of high-magnification lenses, usually below 200 μm. Since high-magnification lenses overwhelmingly work by oil immersion, the device design had to be compatible with inverted microscopes.

Electrophysiology by patch clamping required direct access to cell bodies by a micropipette controlled by a micromanipulator, and a ground electrode placed in the cell medium. Cell culture compartments within the stretching device therefore had to be open to allow top-side access to cells. This compromises sterility, limiting the use of the device for short-term studies. However, sterility limitations apply to most other stretching devices which are not fully enclosed, therefore not representing a major design disadvantage compared to existing devices.

Based on these design parameters, a novel cell-stretching device was designed, manufactured, and tested.

3.5 Engineering a substrate-stretching device for simultaneous electrophysiology and uniaxial stretching of cultured peripheral neurons

Fabio Bianchi, Julian H. George, Majid Malboubi, Antoine Jerusalem, Hua Ye and Mark Thompson.

Under Review, Medical Engineering and Physics, 06/10/2018.

3.5.1 Introduction

The peripheral nervous system (PNS) is subject to continuous mechanical stresses during ordinary movements, but supraphysiological extension can lead to injury. Nerve damage can be a result of traumatic events, a by-product of surgery, or due to chronic conditions. Erbs palsy, for example, is caused by excessive stretching of infant heads and arms during labour inducing loss of sensation and abnormal motor function in 0.1% of births in the US [7].

At the cellular level, axons projecting from nerve roots through collagenous endoneurial channels experience deformation during limb movement [20]. Cell bodies within roots and ganglions are also exposed to strain during traumatic motions such as hip over-flexion [233]. Neuron deformation has been shown to alter ion channel functionality [234], depress neural network activity [208], and cause cytoskeletal damage and collapse [103], reaffirming the importance of considering the role of mechanotransduction in neural damage.

To better understand the mechanisms involved in deformation and injury, cell-scale *in vitro* models reproducing the mechanical environment of the peripheral nerve are required. The current gold standard is *ex vivo* animal tissue, which does not allow for the investigation of cell response in isolation. *In vitro* single-cell experimental devices have

been designed to investigate a wide variety of biological responses to mechanical stimuli, but no device has been specifically designed for PNS modelling (see review by Kamble et al. [215]).

Existing devices can be classified by actuation mechanism. Electromagmetic actuation, where substrate deformation is directly induced by a motor, includes unaxial [201, 235] and biaxial [104] systems. Air-pressure pulse actuated systems provide equibiaxial strain, and deliver highly uniform strain fields to deformed substrates [230]. Fluid flow actuated devices are used to investigate shear force as a mechanical stimulus [158]. Other actuation mechanisms such as piezoelectric [236] and thermal [237] have been used in cell-stretching devices, but can deliver only limited magnitudes of strain. The peripheral nerve is a highly anisotropic structure with axially aligned connective tissues and nerve fibres exposed predominantly to strain along the axis of the nerve [20]. Biaxial systems, developed to model brain impacts and TBI, are therefore less suited for PNS injury studies, pointing to direct uniaxial electromagnetic actuation as the most suited method.

PNS conduction disruptions due to nerve straining are poorly understood, partly due to the lack of *in vitro* models to study the direct effect of strain on nerve electrophysiological function. Previous studies on the effect of mechanical deformation on neural electrophysiological activity mostly separate mechanical stimulus from the electrical recording, introducing a time delay in the effects observed [208, 234]. Flexible multi-electrode array (MEA) systems have been developed and used to quantify the effect of strain and shear on *in vitro* and *in vivo* neural electrophysiology [207, 238, 170], but do not allow for confocal imaging of cells and do not provide information about changes in single-cell ion channel dynamics. A substrate-towing device used to produce stretch-grown dorsal root ganglion neurons has previously been combined with patch clamping, calcium imaging, and confocal imaging [45]. This device was however aimed at studying stretch-growth and cannot be used at high strains or strain rates that would cause axonal disconnec-

tion. Furthermore, the device works by having cell bodies and growth cones adhere to a solid substrate, and therefore it is not clear how the strain is distributed between cells and axons. Indirect electrophysiology measurements by calcium flux imaging have been carried out simultaneously with applied strain [239], but do not probe the response of individual cells. Most non-electromagnetically actuated systems require bulky equipments, complex disassembling for transport, and do not give users the flexibility to perform multi-physics experimental recordings. Commercially available systems such as FlexCell FX-5000 (USA) [155], Strex STB-10 (Japan) [240] and ALA scientific MEASSuRE (USA) offer limited flexibility of system design and experimental parameters, and are therefore unsuited for integration with multi-physics measurement setups.

Cell alignment is a key parameter to replicate the *in vivo* mechanical environment of peripheral nerves, where neurons are aligned and physically supported by Schwann cells and endoneurial collagen channels [20]. Neurons have been shown to align to substrate features at the micro- and nano-scale [241]. In existing straining device designs, cell alignment has been achieved by using growth templates applied before seeding, which are then removed before strain application [235, 242]. This approach successfully aligns cells prior to deformation, but does not provide structural support to during and after deformation as endoneurial structures do *in vivo*. Furthermore, cells can be damaged when the growth templates are removed. Alternatively, neurons have been aligned in enclosed microfluidic channels and exposed to mechanical stimuli [243]. In enclosed designs, cells are not accessible for electrophysiology, and the limited methods of mechanical stimulation poorly replicate the *in vivo* physical PNS environment.

Here, we introduce the first substrate-stretching device, operated under displacement control, with the aim of recording high-resolution wide-field and confocal microscopy, single-cell patch clamping, and indirect network electrophysiology measurements during the application of uniaixal strain to cultured neurons. The use of manufactured

deformable cell culture wells with aligned grooved substrates replicates the *in vivo* morphological environment of peripheral nerves. We present a compact system, allowing easy transport and setup, simultaneous direct (patch clamp) and indirect (calcium imaging) electrophysiological measurements during uniaxial strain. We characterise the substrate deformation by experimental measurements and finite element method simulations, to precisely calibrate the use of this device for neuron deformation experiments.

3.5.2 Materials and Methods

Device Design and Manufacturing

The cell stretching device was designed in four parts: the motor (Zaber Technologies NA08B30-T4 linear actuator driven by an X-MCB1 controller and Zaber Console software), the sample holder, the deformable well and the microscope stage adaptor (Figure 3.12). Microscope stage adaptors were designed to fit Nikon and Zeiss microscope stages, and CNC-machined from black anodised aluminium to minimise imaging glare. The sample holder was manufactured by stereolithographic 3D printing (Form 2 printer, FormLabs) using clear photocurable resin, with a layer height of 25 μm. Following printing, components were cured in 90% ethanol for 30 minutes then left to air-dry for two hours.

Design and Manufacturing of Deformable Wells

The deformable wells were manufactured from polydimethylsolixane (PDMS, Dow Corning) cast in a 3D printed mould (manufactured by stereolithographic 3D printing (Form 2 printer, FormLabs) using clear photocurable resin) measuring 45 $\times$ 20 $\times$ 3 mm, with a 10 $\times$ 6.5 mm rectangular feature at the centre. PDMS was mixed at 1:10 ratio between curing and base agents, vacuum degassed, injected into the mould using a syringe at 2.5 ml per mould, and cured at 60°C for four hours. Ultra-thin 50 and 100 μm ($\pm$ 5%) PDMS films (Elastosil, Silex ltd) were bonded to the bottom of the well pieces using a thin layer

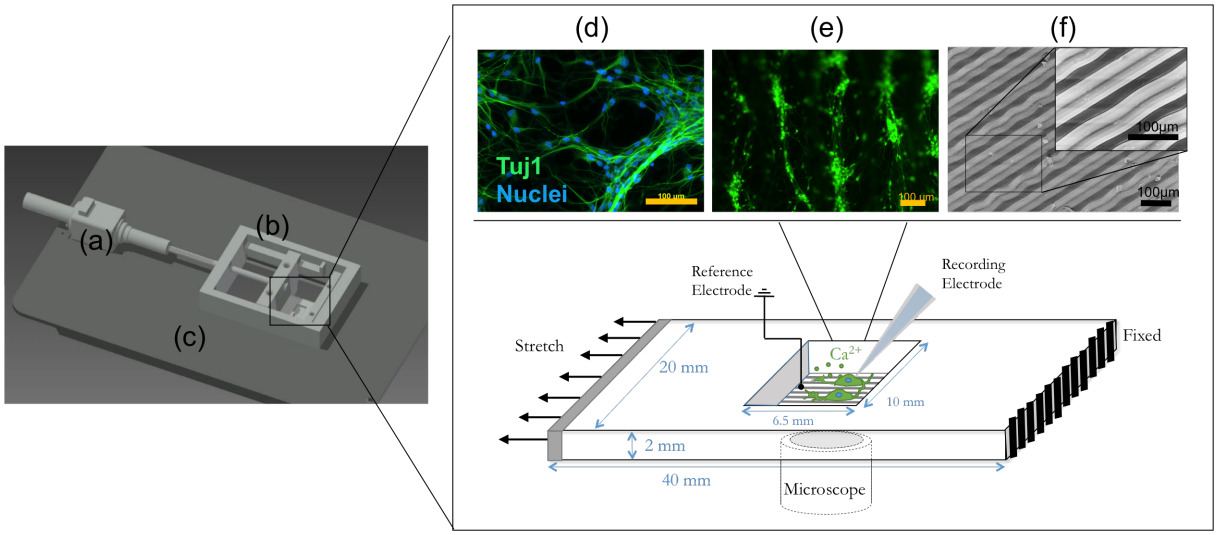


Figure 3.12: Cell-stretching device setup on Nikon microscope stage adaptor. (a) Linear actuator controller is separated from actuator, and connected via USB to the controlling PC. (b) Sample holder and clamps. Mounting and unmounting of deformable sample wells can be carried out without removing the device from the microscope stage. (c) Microscope stage adaptor. Magnification: Detail of deformable substrate, showing grooved surface, and simultaneous stretch, imaging and electrophysiology. (d - e) iPSC-derived neurons cultured on deformable well substrates extend neurites and form networks. Fluorescent labelling of Tuj1 (β-III tubulin, green) and nuclei (blue) on unpatterned surfaces (d), and on aligned substrates (Tuj1 only) (e). (f) SEM images of aligned grooves. Scale bars = 100 μm

of PDMS and cured for one hour at 60°C, to create watertight wells with thin transparent bases. To simulate neural alignment present in peripheral nerves, PDMS films with aligned microgrooves were manufactured by casting a thin layer of PDMS on a template (microgroove vinyl record 'Bird Sounds in Up Close' by Victor C. Lewis, which ensures consistent groove width and depth), and curing it for one hour at 60°C. Grooved film thickness was measured using a manual micrometer at 130 $\pm$ 30 μm (n = 5 independently cast films).

Scanning Electron Microscope (SEM) Imaging

Grooved PDMS surfaces were placed on adhesive carbon discs and imaged using a Hitachi TM3030plus tabletop SEM, in high vacuum and 15 kV acceleration voltage.

Table 3.1: Mechanical properties of PDMS at 1:10 mixing ratio cured at 60°C for four hours [244, 245].

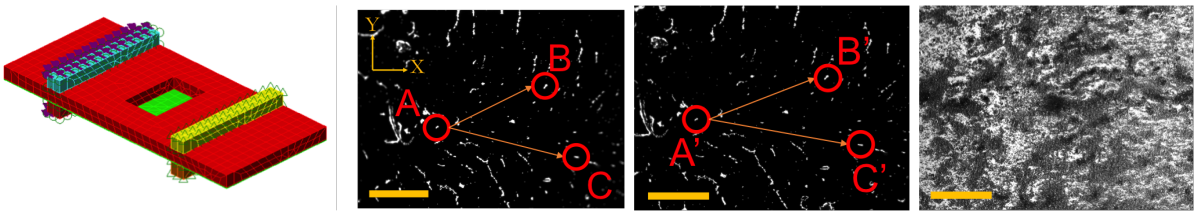
Linear elastic		**Hyperelastic (Ogden)**	
Material Constant		*Material Constant*	
Young's Modulus (MPa)	1.7	μ_1	63.49
Poissons Ratio	0.5	μ_2	0.41
Density (g/cm^2)	0.97	α_1	6.37×10^{-10}
		α_2	3.81
		Bulk mod. K (MPa)	962

Finite Element Method Simulations

Finite element (FEM) simulations were carried out using Simulation Mechanical (Autodesk Inc.). The model was simplified to include only the clamps, deformable well, and grooved or smooth substrate. Non-slip conditions were assumed between clamps and well and between the well and substrate. The stationary clamp was constrained in all directions, whilst the towing clamp was constrained in every direction other than that parallel to the direction of towing. A prescribed displacement was applied to the towing clamp, to simulate displacement-controlled deformation. Gravity and thermal effects were neglected. Material properties of the clamps were simulated as linear elastic acrylonitrile butadiene styrene (ABS) plastic, whilst elastic and hyperelastic properties for PDMS were taken from literature (Table 1). The model was meshed using an absolute mesh size of 1.5 mm, matched at contact points (Figure 3.13a). Surface strains inside the well were measured by averaging across 160 points around the centre of the well after convergence.

Strain Quantification by Point Tracking

To manually compute surface strains, a 1% solution of 5 μm diameter green fluorescent beads (ThermoFisher, 490/520 nm excitation/emission wavelength) in 70% Ethanol was applied to the surface of the deformable well and dried under laminar flow. Incremental deformation was applied to deformable wells, and bead patterns were imaged (10× lens).



(a) (b) (c) (d)

Figure 3.13: Strain field quantification methods. (a) FE Model showing mesh and constraints. (b - c) Example of bead pattern for strain quantification, before deformation (b) and after 15% prescribed displacement (c). Red arrows show vectors constructed between point triplets. (d) Speckle pattern for digital image correlation quantification. Scale bars = 500 μm

Multiple (n = 10 from three independent substrates) triplets of distinct points in the bead pattern were used for analysis (Figures 3.13b and 3.13c) using a Cauchy-Green tensor method automated using a custom-written MATLAB script [201].

Digital Image Correlation Strain Quantification

Digital image correlation (DIC) is a non-invasive method to quantify strains based on surface patterns, and has previously been used to characterise biaxial strain fields applied to substrates and cells [246]. For DIC, surfaces were coated with a 10% solution (v/v) of 1 μm diameter polystyrene beads in 70% ethanol (Figure 3.13d) to create random patterns, and imaged during deformation (4× lens). DIC was performed using GOM Correlate (GOM GmbH), and strains in the X and Y directions were averaged over the entire imaging area (300 points covering 2.5 × 1.6 mm) at the centre of the deformable well.

Cell Culture, Immunocytochemistry and Imaging

Deformable wells were sterilised by immersion in 70% ethanol for two hours and air dried under sterile laminar flow, followed by exposure to UV light for 15 minutes. Wells were then treated for 90 seconds in an Oxygen Plasma Generator (Diener Technologies) to

promote cell attachment. Culture surfaces were then coated with 1% matrigel solution (Corning) and incubated for one hour at 37 °C.

Human iPSC-derived motor neurons (iPSCs from StemBANCC, Oxford, UK) differentiated following an established protocol [247] were dissociated using Accutase (ThermoFisher), and seeded at 30,000 cells/well two days prior to stretch experiments. IPSC-derived neurons were cultured in maturation medium, consisting of 50% KO-DMEM:F12 and 50% neurobasal medium (ThermoFisher), supplemented with 1% penicillin/streptomycin (ThermoFisher), 1% B27 supplement (ThermoFisher), 1% N2 supplement (ThermoFisher), 1% non-essential amino-acids (ThermoFisher), 1% GlutaMAX (ThermoFisher) , 0.1 mM L-ascorbic acid (Sigma-Aldrich), 10 ng/ml ciliary neurotrophic factor (Peprotech), 10 ng/ml brain derived neurotrophic factor (Peprotech), 10 ng/ml NT-3 (Peprotech) and 10 ng/ml glial cell derived neurotrophic factor (Peprotech). Culture medium was replaced every 24 hours. Good cell attachment and extension was observed both on unpatterned and grooved surfaces (Figures 3.12 (d) and 3.12 (e)).

F11 cells (from ECACC, UK), a rat neuroblastoma and primary dorsal root ganglion neuron hybrid, were chosen as model cells for electrophysiology due to their well characterised action potential firing [159, 248]. F11s were seeded at 5000 cells/well and differentiated for five days in high glucose DMEM medium (ThermoFisher) supplemented with 1% foetal bovine serum (ThermoFisher), 1% P/S (Sigma-Aldrich), 0.5% insulin transferrin selenium (ITS, ThermoFisher), 10 μM 3-Isobutyl-1-methylxanthine (IBMX, Sigma-Aldrich), 50 ng/ml nerve growth factor (Peprotech), 2 μM all-trans retinoic acid (Sigma-Aldrich) and 0.5 mM bromoadenosine 3',5'-cyclic monophosphate (Sigma-Aldrich).

For immunocytochemistry, cells grown on flat and grooved surfaces were fixed in 3.7% paraformaldehyde (Sigma-Aldrich), permeabilised and blocked using 0.1% triton-X, 0.1% tween-20 and 1% bovine serum albumen (all from Sigma-Aldrich) solution in phosphate buffered saline (PBS, ThermoFisher). Cells were labelled with chicken anti β-III tubulin

primary antibody (AbCam), followed by anti-chicken AlexaFluor488 secondary antibody (ThermoFisher), and nuclei were counterstained with NucBlue (ThermoFisher). Widefield images were taken using an inverted Nikon Ti-E microscope with multi-LED excitation (CoolLED). Confocal images were taken using a Zeiss 710 confocal microscope (63× lens, oil immersion).

Stretching Procedure

Deformable wells were clamped in place (Figure 3.12), and the driving rod retracted until in contact with the towing clamp. The initial distance between towing and stationary clamp was measured using digital callipers, and used to calculate displacement and velocity for desired strain and strain rates. Cells were exposed to strains of 25, 45 and 70%. This is within the range used in previous experiments to reproduce mild to severe injuries to *in vitro* neurons [201]. In peripheral nerves, a wide range of strains is reported to cause conduction blocks [69], but the amount of strain transferred from the tissue scale to the cell scale is unclear and therefore the ability to apply a large range of strains is desirable.

Quantification of Cell Morphology Changes

To evaluate the effect of substrate strain on cell morphology, membranes and nuclei of live cells were stained by incubating cells for 20 min with 1% CellMask Green and NucBlue (both from ThermoFisher). Nuclei shapes were measured using Ovuscule, an ImageJ plugin (ImageJ, NIH) which fits an ellipse to areas of high contrast and returns major and minor axes measurements [249]. Membrane stretch was measured manually by selecting distinct membrane features and measuring lengths in the same direction as the nucleus major and minor axes. Cell orientation angle was measured as angle of major axis from horizontal. Six independent cell populations on smooth and grooved surfaces were stretched in 10%

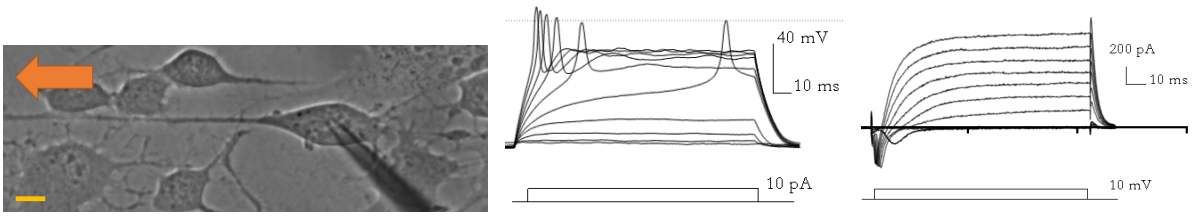
prescribed displacement increments up to 30%. Cell morphology during deformation was measured for neurons cultured on both aligned groove, and unpatterned surfaces.

Whole-Cell Patch Clamping

The experimental setup for electrophysiological recording consisted of a Digidata 1440A Digitizer and a MultiClamp 700B Amplifier piloted through pCLAMP 10 Software (all from Molecular Devices). Glass micropipettes were pulled to a resistance of 8-10 MΩ from thin wall borosilicate tubing (BF100-78-10, Sutter Instruments) using a Flaming/Brown micropipette puller (Model P-1000, Sutter Instruments). Pulling parameters were optimised according to previous work to obtain desired micropipette shape and surface properties [250]. The intracellular solution contained: 140 mM KCl, 5 mM NaCl, 0.5 mM $CaCl_2$, 2 mM $MgCl_2$, 10 mM HEPES, 1 mM GTP and 2 mM ATP, with pH adjusted to 7.4 by addition of KOH and osmolarity adjusted to 300 $mOsmL^{-1}$ by glucose addition. The bath solution contained: 130 mM NaCl, 5 mM KCl, 2 mM $CaCl_2$, 1 mM $MgCl_2$, 10 mM glucose and 10 mM HEPES, with pH adjusted to 7.4 by addition of NaOH and osmolarity adjusted to 300 $mOsm/L^{-1}$ by glucose addition. To evoke voltage dependent currents, stretched cells were stimulated with a series of depolarising pulses from -90 mV to +70 mV with a step size of 10 mV and currents were recorded in voltage clamp mode. Action potentials were evoked in current clamp mode by a series of current pulses from -50 pA to +80 pA with a step size of 10 pA.

Functional Calcium Imaging

Calcium activity was imaged using Oregon Green 488 BAPTA-2 calcium indicator [199]. Cells grown on aligned substrates were incubated in a 4 μM dye solution in FluoroBrite-DMEM imaging medium (ThermoFisher) for 30 minutes, washed twice in calcium free PBS, and further incubated in fresh FluoroBrite-DMEM for 30 minutes. Cells were imaged



(a) (b) (c)

Figure 3.14: Whole-cell patch clamp recordings from a cell subject to 45% strain ((a), arrow = direction of alignment and stretch). In current clamp mode (b), invoked action potentials were recorded. In voltage clamp mode (c), inwards sodium currents and outwards rectifying potassium currents were recorded. Dotted line = 0 mV. Scale bar = 10 μm.

using standard FITC filters (144/530 nm ex/em) at 10 frames per second for four minutes, and fluorescence intensities from individual cells were recorded over time.

Statistical Analysis

Statistical analysis was carried out in PRISM v6 (Graphpad, USA). Data was tested for significance using unpaired T-testing corrected for multiple comparisons by Tukey's test. All graphed data is reported as mean ± standard deviation, unless otherwise specified.

3.5.3 Results

Single Cell Electrophysiology Measurements During Strain Application

Differentiated F11 cell populations were strained by 45% and whole-cell current and voltage clamp recordings were acquired while the stretch was maintained, to demonstrate the compatibility of our device with simultaneous direct electrophysiology measurements. Inwards (sodium) and outwards (potassium) currents and induced action potentials were recorded from deformed cells (Figure 3.14), demonstrating how this system can be used to record neural electrophysiology during acute cell deformation to examine the mechanisms involved in immediate mechanotransduction and primary ion channel and membrane damage.

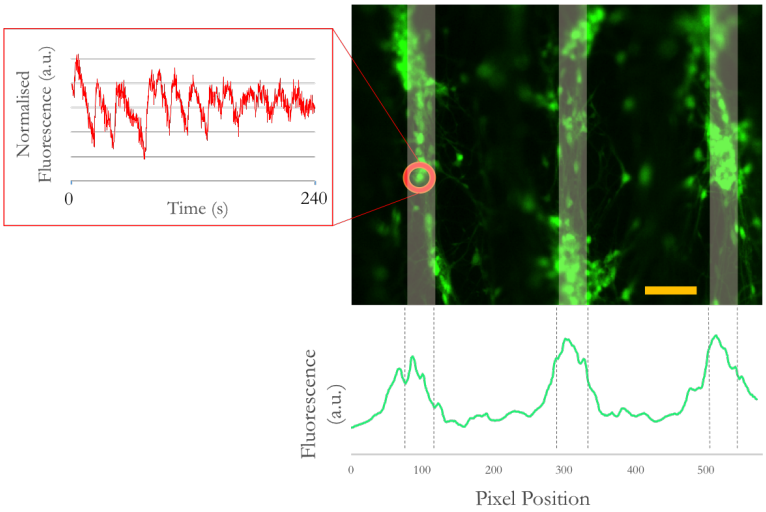


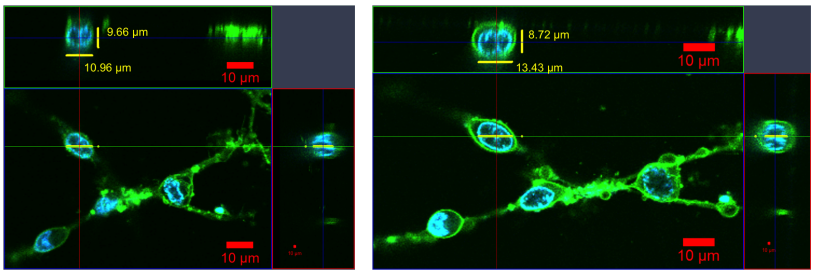
Figure 3.15: Oregon green BAPTA-1 functional calcium imaging of human iPS neurons on aligned microgrooved substrates. Surface grooved have been highlighted, and fluorescence intensity profile averaged across the vertical axis plotted (lower graph). Representative calcium signal profile shows spiking activity (left). Scale bar = 100 μm

Functional Calcium Imaging

Calcium flux imaging of human iPS-derived neurons on aligned grooved surfaces was acquired for four minutes. Cell activity (Figure 3.15) shows that iPSC-derived neurons on grooved deformable substrates undergo maturation to form spontaneously active networks which can be imaged using our device. This allows the study of alterations in neural network activity and connectivity under strain. The vertical fluorescence profile from Oregon Green BAPTA-1 stained cells was plotted to show cell clustering within grooves, with distinct peaks corresponding to groove positions (Figure 3.15, lower plot). This confirmed cell localisation within substrate features and the formation of aligned bundles of highly polar cells, representative of nerve fibre bundles in peripheral neurons.

Confocal Imaging During Strain Application

Human iPSC-derived neurons were imaged using high-magnification (63× lens, oil immersion) confocal microscopy in both unstrained and strained conditions (45% strain) to reconstruct Z-profiles of cell membranes and nuclei. Cells were imaged in 2 μm thick



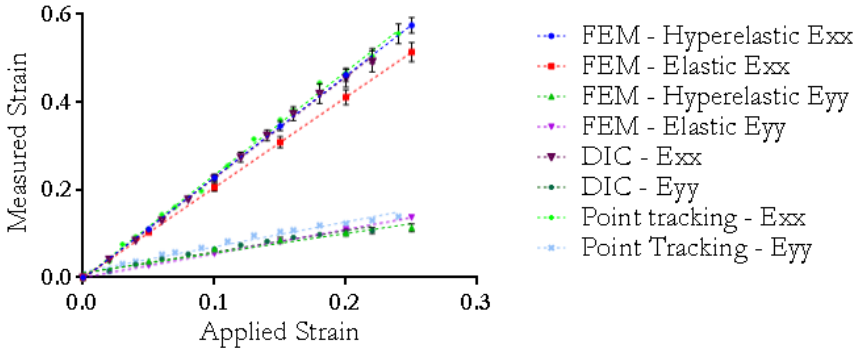
(a) (b)

Figure 3.16: High-resolution z-slice imaging of iPSC-derived neuron nuclei and membranes during strain application. Volume reconstructions shows how cell nuclei are compressed as a result of substrate deformation. Confocal z-slice imaging of cells stained for membrane and nuclei is used to measure nucleus height before (a) and after (b) a 45% substrate deformation. Yellow line shows measurement of nucleus height. Scale bar = 10 μm.

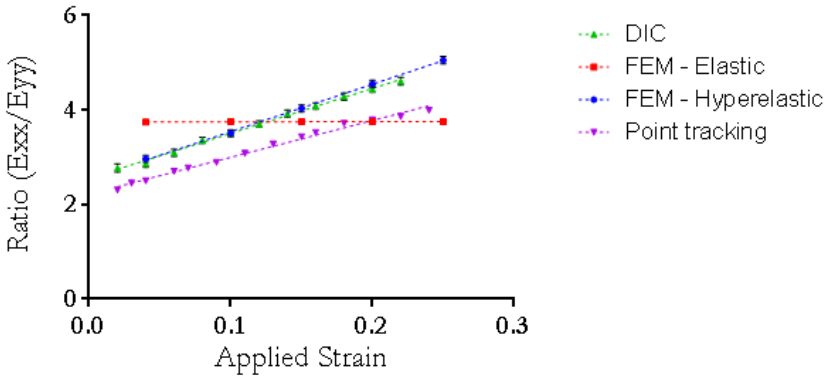
Z-slices, and nucleus heights were reconstructed and measured. Cell nuclei were subjected to induced vertical compression and nucleus height decreased by 10% when stretch was applied (Figure 3.16).

Experimental and Simulated Substrate Strain Characterisation

The mechanical properties of the deformable wells were characterised by simulated surface strain as a result of applied grip-to-grip strain, validated by experimental measurements. Experimental and simulated strains all showed strong linear correlations with applied grip-to-grip strain (Figure 3.17a, average $R^2 > 0.97$). Simulated and experimental values of strains parallel (E_{xx}) and perpendicular (E_{yy}) to the applied deformation were strongly correlated, indicating that the simulations robustly predicted system mechanical properties. The best fit was achieved by using Ogden hyperelastic PDMS properties (Table 3.1), as reported in literature [244, 251]. Average slope values for hyperelastic simulated and experimental data were 2.325 ($\pm$ 0.02) and 0.501 ($\pm$ 0.05) for E_{xx} and E_{yy} respectively. E_{xx} to E_{yy} ratio increased linearly with applied strain ($R^2 > 0.99$), except in elastic material model simulations, for which the ratio was constant (Figure 3.17b).



(a)



(b)

Figure 3.17: (a) Absolute measured experimental strains parallel (E_{xx}) and perpendicular (E_{yy}) to applied deformation, for experimental and simulated data. (b) Ratio of parallel (E_{xx}) to perpendicular (E_{yy}) strain for increasing applied (grip-to-grip) strain, for experimental and simulated data

Surface Strain of Microgrooved Substrates

Microgroove topography was characterised by SEM imaging (Figure 3.12 (f)). The average groove width was 50 ± 1.7 μm (n = 30, from three independently cast samples), the groove depth was estimated to be 20 μm, and the alignment was measured at 0.53°, characterised by the standard deviation of groove angle with respect to the horizontal. With the selected well geometry, the strain field at the centre of the substrate was found to be uniform for both smooth and patterned surfaces (Figure 3.18 a and b). Strain simulations showed that the presence of microgrooves did not affect the average mechanical behaviour of the deformable wells (Figure 3.18 c and d). The experimental calibration curve derived from

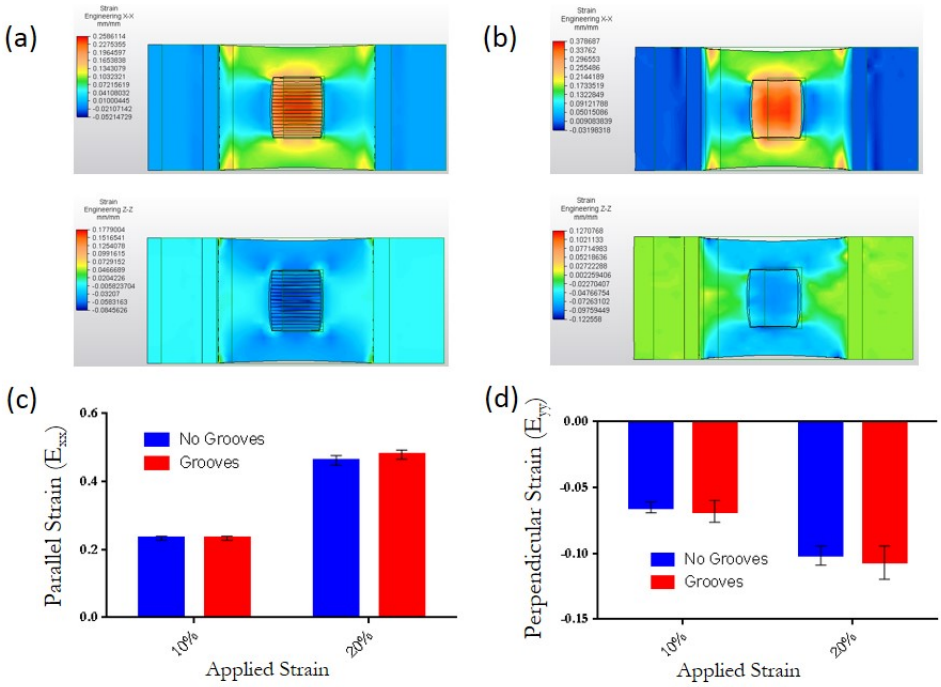
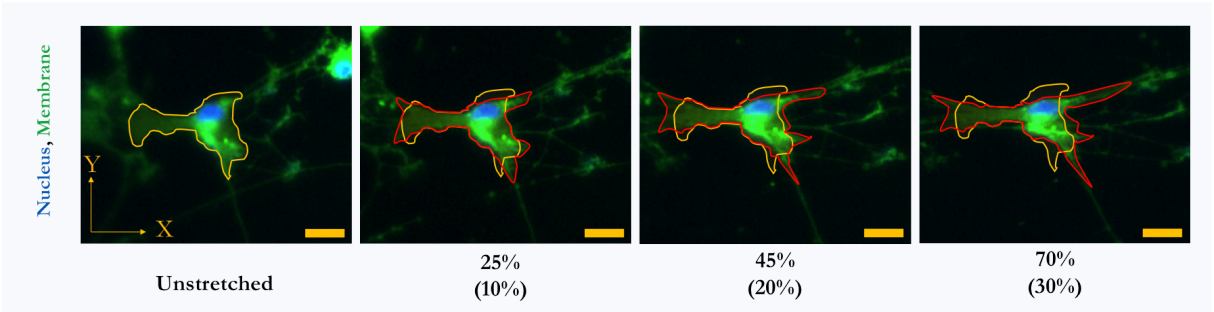


Figure 3.18: Simulation results show that grooves do not significantly affect substrate strains. (a) Axial strain is not significantly altered by grooves, neither is longitudinal strain (b). Strain heat maps for grooved (c) and smooth (d) surfaces show uniform strain distribution around centre of well.

DIC and point tracking (Figure 3.17a) can therefore also be used for grooved surfaces. These results show how a grooved substrate, which promotes cell growth along the axis of deformation, can be combined with uniaxial stretch to more realistically model peripheral neuron deformation.

Cell Deformation in Aligned Microgrooves

Nuclei and membranes were measured during strain to evaluate the effect of grooved substrates on the change in cell shape (Figure 3.19a). On unpatterned substrates, cell response was heterogeneous with a large range of positive and negative strains recorded along the cell major axes. Patterned, grooved substrates induced cell and neurite alignment along the surface topography (Figure 3.12) and resulted in higher average nucleus and membrane strains and lower standard deviation (Figure 3.19c, 3.19b).



(a)

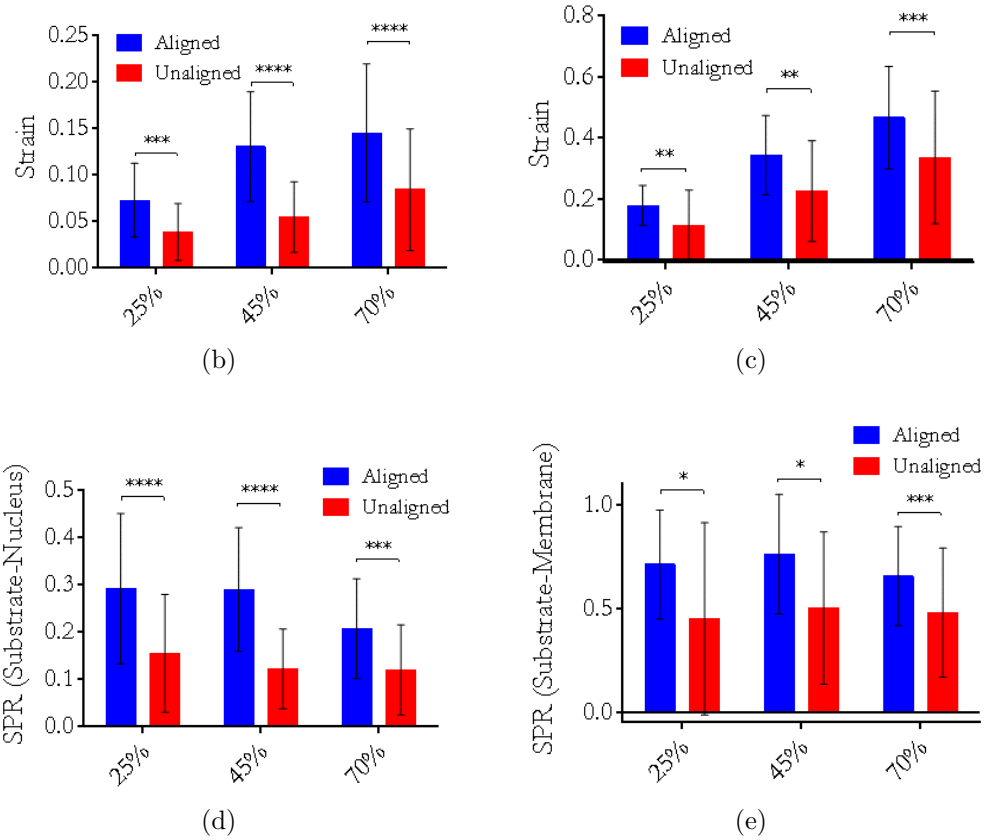


Figure 3.19: (a) Incremental cell deformation (nuelcues stained with nucblue and membrane stained with cellmask green). Strain values in brackets represent applied grip-to-grip strain (along x-axis). Scale bar = 10 μm. Yellow outline shows initial cell shape (at 0% strain). Red outline shows deformed cell at each strain. Nucleus (b) and membrane (c) average strain is significantly higher for cells cultured on parallel groove surfaces, compared to unpatterned surfaces. Nucleus (d) and membrane (e) SPR is significantly higher, on average, for cells cultured on parallel groove surfaces, compared to unpatterned surfaces. X-axis values show applied grip-to-grip strain. Bars show mean ± S.D. **** = $p < 0.0001$, *** = $p < 0.001$, *= $p < 0.05$. $n > 25$ for all measurements.

Another measure of cellular deformation is strain transferred from the substrate to the cell membrane and from the cell membrane to the nucleus, termed strain partitioning

ratio (SPR) [146]. The cell membrane, adhering through focal adhesions to the substrate, deforms as a result of applied displacement and the cytoskeleton transfers a proportion of strain to the nucleus [252]. Comparing cells stretched on aligned grooves and unpatterned substrates, the SPR increased significantly with alignment for both membranes and nuclei and did not vary significantly with increased deformation (Figure 3.19d and 3.19e). Average substrate-nucleus SPR was 30% in aligned, and 15% in unaligned cells. Average substrate-membrane SPR was 65% in aligned, and 50% in unaligned cells.

3.5.4 Discussion

Electrophysiological measurements and imaging during cell straining

Understanding the multi-scale mechanics of peripheral nerve can help to identify mechanisms of conduction blocks and sensory and motor function alteration due to trauma. Existing cell-stretching devices do not allow simultaneous cell deformation and electrophysiological recording [208, 234, 200, 253], introducing a time-delay between damage application and measurements and not capturing ion currents and action potential dynamics of cells in the stretched state. Flexible MEA-based devices allow for measurement of spontaneous electrophysiological activity of neurons subject to shear in cultured cells [207], and strain in hippocampal tissue slices and sciatic nerves [238, 170], but are limited in compatibility with imaging setups and do not provide data about ion channel functionality, which is known to play a key role in the electrophysiological response to strain [234, 208]. Our results show how, using our device, we can acquire both single-cell and network electrophysiology measurements from cells in a stretched state. In previous studies, simultaneous single-cell electrophysiology and direct mechanical perturbation has only been achieved by indentation with a micropipette, or by directing a high-speed stream of fluid onto the cell [254, 224], which apply localised strain to a small area of the cell membrane, do not represent physiological deformation conditions, and do not allow pre-

cise control over the magnitude of deformation applied to the cell. In peripheral nerves, macroscopic tissue deformation will produce a more uniform deformation of cells, and is unlikely to result in localised strain. The design of our device allows uniform deformation transferred from substrate to cells during electrophysiological measurements.

Another key system feature is the compatibility with multiple imaging setups, as most existing designs do not allow high resolution imaging during stretch [228]. Due to the lightweight modular construction, our device can be mounted on inverted or upright microscope stages, and the ultra-thin deformable substrates used are compatible with imaging using high magnification lenses, allowing reconstructions of Z-stacks for 3D imaging. The ability to measure nucleus height before and during straining (Figure 3.16) shows the adaptability of this stretching device to high-resolution imaging during *in situ* cell deformation, and can be applied to studies of the effect of cytoskeletal manipulation on cell mechanics.

Strain Characterisation

Simulation results for resulting local strain at the deformable well surface were validated by experimental measurements (Figure 3.17a). Finite element method simulations were used to design the well such that the strain field generated at the surface of the culture substrate was uniform around the centre. This was achieved by optimising the well shape and size (data not shown). The size of the well was optimised to reduce reagent waste, while containing enough medium to avoid rapid evaporation, previously highlighted as key design parameters [215].

Strain results were used to construct a calibration curve, relating the applied grip-to-grip strain to the local surface strain. A linear ratio of 2.325 ($\pm$ 0.02) and 0.501 ($\pm$ 0.05) for E_{xx} and E_{yy} was found, representing the factors by which grip-to-grip strain is transferred to the cell culture surface.

A key property of the system is the ratio of E_{xx} to E_{yy}. Biomechanical studies on peripheral nerve have shown an unique Poisson behaviour with nerves compressing radially during axial elongation [20], which needs to be captured in an *in vitro* model. The ratio of E_{xx} to E_{yy} increased with grip-to-grip strain, and experimental measurements validated hyperelastic simulation results (Figure 3.17b), confirming that hyperelastic properties better describe PDMS, and indicating that the non constant ratio can be explained by material properties instead of grip slipping.

Microgrooved Surface Characterisation

Deformable substrate surfaces were patterned with aligned microgrooves, which induce cells to grow parallel to the direction of applied strain. Bipolar cells such as neurons have cytoskeletons aligned with cell polarity [255], which allows more deformation in cells parallel to applied substrate deformation. This results in anisotropic cell deformation, which has been shown to translate from the cytoskeleton to the nucleus [256, 252]. Deformation is therefore more reproducible and uniform, which is more representative of the physiological conditions in peripheral nerves, where neural fibres are aligned axially and therefore exposed to strains aligned with their polarity.

Our results show that aligning cells by embedded substrate topography reduces the variability of deformation, more closely resembling *in vivo* peripheral nerve conditions, whilst maintaining accessibility for electrophysiology and access for inverted microscopy. The presence of substrate grooves also provides physical support to cells, more closely replicating the mechanical environment of peripheral nerve.

Compartmentalised microfluidic devices have been previously used to induce alignment and study injury applied by a localised pressure pulse [243]. This requires cells to be fully enclosed, precluding access for electrophysiology. Furthermore, localised injury is less representative of peripheral nerve trauma, compared to whole-cell stretch. Pressure-pulse

systems, developed to investigate the effect of stretch on axons [230] and subsequently used in numerous studies [257, 242, 258] have also been used with growth templates to align axons [259]. However, the pressure-pulse design requires an enclosed pressure chamber, again precluding access to cells for direct electrophysiology. Growth template masks have also been used to align neurons during before applying uniaxial stretch [235]. Because masks are removed before straining, they do not provide physical support, and can damage cultures during removal. By patterning the cell culture substrate, we can induce cell alignment without risking cell damage, while allowing access for electrophysiological measurements.

3.5.5 Conclusions and Limitations

Research into the effects of mechanical strain on the PNS has implications in trauma prevention, recovery and regeneration. To better understand the effects of macro-scale deformation on individual neurons, *in vitro* models replicating the mechanical environment of peripheral nerve tissue are required.

Cell-substrate stretching devices have been used extensively to model TBI and to study the effect of uniaxial [201, 235, 230] and biaxial [157] strain, and have been coupled with flexible multi-electrode arrays [260, 238], but no system allows direct single-cell electrophysiological measurements of cells deformed within an environment which emulates peripheral nerve tissue morphology, coupled with high resolution microscopy.

In peripheral nerves, neuronal projections are aligned in endoneurial conduits [20]. The use of alignment cues in neural cultures to replicate this morphology provides a physical environment similar to that found *in vivo*. In previous work, growth templates have been used to align neurons before stretch [235, 242], however these methods do no provide physical support to neurons, and can damage cultures when the template mask is removed.

We present and characterise a novel substrate-stretching device which can be used to apply axial strains to populations of neurons grown on ultra-thin deformable substrates, both smooth and patterned with aligned grooves. We show compatibility with high-magnification imaging, single-cell and network electrophysiology recordings of cells during the application of strain.

Compatibility with patch clamping was shown by current and voltage clamp recordings of ionic membrane currents and induced action potentials from cells subjected to strain. Device compatibility with network electrophysiology measurements was shown by functional calcium imaging. 3D reconstruction of stretched cells using confocal microscopy demonstrated system compatibility with high-magnification imaging. The ability to simultaneously perform single cell and network electrophysiology, as well as imaging cellular components during stretch, shows how the device can be used as a platform for an experimental multi-physics investigation of the effect of stretch on peripheral neurons.

The mechanical behaviour of unpatterned and grooved deformable culture surfaces was characterised experimentally and numerically, to precisely calibrate cell strains. Surface patterning with aligned microgrooves was shown to induce cell alignment, reduces variability in cell response to stretch, and provide alignment cues to stimulate parallel anisotropic neurite extension without significantly altering the mechanical properties of the substrate.

Overall, the device presented provides a compact, flexible, and adaptable tool for peripheral nerve mechanobiology and electro-mechanical studies. The thorough characterisation provides a repeatable *in vitro* model for the study of the effect of stretch on peripheral neurons, which can help understand the causes of traumatic neuropathy as well as optimise strategies for damage prevention and repair.

The device still presents some limitations that will be tackled in the near future. For instance, myelination of PNS axons is known to play a role in the response to mechani-

cal damage [78]. Integrating aligned Schwann cell-neuron co-cultures would increase the physiological relevance of the model, and allow studies of regeneration following mechanical trauma. The separation of neural cell bodies and axons would also increase the similarity between PNS tissue and model. The current design of the device relies solely on displacement control. Force control can be implemented, and parameters matched to experimentally obtained properties of nerve tissue during tensile testing. Another limitation is the fact that cells are not kept in a temperature controlled, sterile, or humidified environment during stretching. This, together with medium evaporation from the stretch chamber makes the device unsuitable for long-term experiments.

3.5.6 Acknowledgements and Conflict of Interests

Authors acknowledge China Regenerative Medicine Limited (CRMI) for funding and the EPSRC DTP award number 1514540 for F.B. funding. M.B. and A.J. acknowledge funding from the European Union's Seventh Framework Programme (FP7 20072013) ERC Grant Agreement No. 306587. The authors would like to thank Mr. James (Jim) Fisk and Mr. David Salisbury for their assistance with manufacturing, Mr. Graham Brown for help with confocal microscopy, Dr. Kalin Dragnevski for help with SEM operation and Ms. Linda Li for early work on the device. The authors declare no conflict of interests.

3.6 Supplementary Unpublished Information

3.6.1 Nucleus and Membrane Deformation Correlation with Cell Orientation

Materials and Methods

To quantify the relationship between cell deformation and orientation relative to strain axis, iPSC-derived neurons were stretched incrementally up to 70% strain, and membrane and nucleus major and minor axis were measured at each point, as previously detailed in 3.5.2. The angle of each cell major axis was measured with respect to the horizontal, in order to investigate correlations between orientation and deformation.

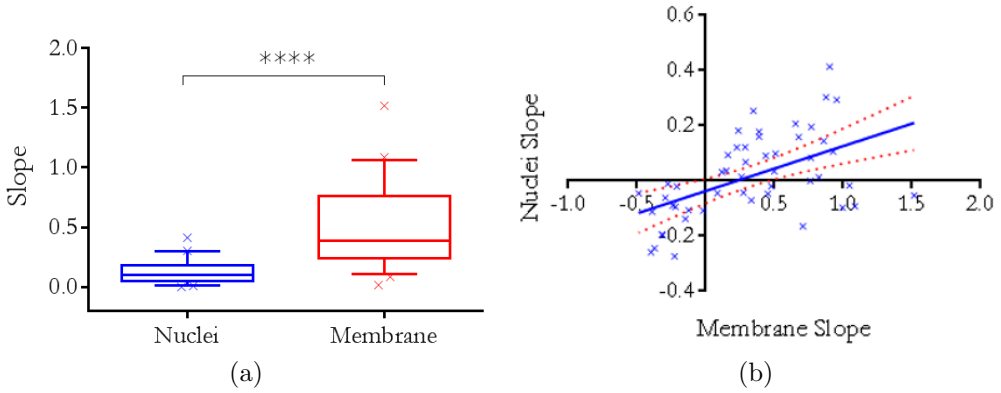


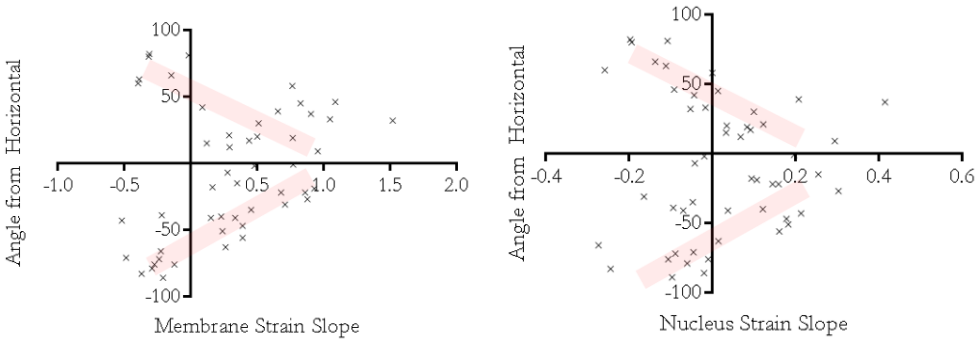
Figure 3.20: (a) Slope of membrane strain (absolute magnitudes) are larger than nuclei. Box = median with 25th to 75th percentile. Whiskers = 5th to 95th percentile, x = outliers (included in analysis), **** = $p < 0.0001$ by unpaired t-test. (b) Membrane strain slopes correlate with nucleus strain slopes. Blue line = linear fit. Red dotted lines = 95% C.I

Results

Linear regression fitting was performed for nucleus and membrane deformation as a function of applied substrate strain. Slope magnitudes were significantly higher in membranes compared to nuclei (figure 3.20a), indicating that membranes deform at a higher rate. Plotting nucleus strain slope against membrane slope showed a linear correlation indi-

cating direct coupling between the two, probably represented by the actin cytoskeleton [261].

The slope of membrane and nucleus strains further correlated with the angle of the cell major axis (figure 3.21). At large angles (positive or negative) membrane slopes were negative, indicating a contraction along the major axis. Slope values increased as cell orientation approached the horizontal, indicating extension along the major axis. These results confirm the importance of alignment in the study of mechanotransduction, as heterogeneous repose to strain due to anisotropic cell alignment could introduce uncertainties in the response measured within a large cell population.



(a)

Figure 3.21: (a) Membrane strain slope increases when cells angle approaches 0° (horizontal). (b) Nucleus strain slope increases as cell orientation approaches 0° (horizontal). Red bars indicate trends (arbitrary orientation and magnitude).

3.7 Chapter Summary

This chapter detailed the development and characterisation of an *in vitro* model the effect of uniaxial strain on peripheral nerve function. Two aspect of the model were presented: the establishment of a protocol for human motor neuron differentiation from iPSCs, and the development of the cell-stretching device for simultaneous cell straining and electrophysiological measurement. *In vitro* modelling allows precise control over the number of variables measured and over the conditions of testing compared to whole-tissue models, and permits new investigations into the effect of strain at the cellular scale.

Statement of Authorship for joint/multi-authored papers for PGR thesis

To appear at the end of each thesis chapter submitted as an article/paper

The statement shall describe the candidate's and co-authors' independent research contributions in the thesis publications. For each publication there should exist a complete statement that is to be filled out and signed by the candidate and supervisor

Title of Paper	Rapid and efficient differentiation of functional motor neurons from human iPSC for neural injury modelling
Publication Status	☐ Published ☐ Accepted for Publication ☑ Submitted for Publication ☐ Unpublished and unsubmitted work written in a manuscript style
Publication Details	Submitted to Stem Cell Research, May 2018. First Reviewed July 2018.

Main Author

Name of Principal Author (Candidate)	Fabio Bianchi		
Contribution to the Paper	Planned and designed experiments, carried out experiments, carried out analysis (unless specified), wrote manuscript		
Signature		Date	06/08/2018

Co-Author Contributions

Name of Co-Author	Dr. Majid Malboubi
Contribution to the Paper	Carried out patch-clamping experiments, reviewed manuscript

Name of Co-Author	Yichen Li
Contribution to the Paper	Carried out validation experiments, reviewed manuscript

Name of Co-Author	Dr. Julian H. George, Dr. Antoine Jerusalem, Dr. Fancis Szele, Dr. Mark Thompson
Contribution to the Paper	Reviewed manuscript

Name of Co-Author	Dr. Hua (Cathy) Ye
Contribution to the Paper	Supervised work, reviewed manuscript

Please cut and paste additional co-author panels here as required.

Supervisor Confirmation

By signing the Statement of Authorship, you are certifying that the candidate made a substantial contribution to the publication, and that the description described above is accurate.

Supervisor name and title:	Dr. Hua (Cathy) Ye		
Signature		Date	10/08/2018

This completed form should be included in the thesis, at the end of the relevant chapter.

GSC 18.23 **Annex A**

Statement of Authorship for joint/multi-authored papers for PGR thesis

To appear at the end of each thesis chapter submitted as an article/paper

The statement shall describe the candidate's and co-authors' independent research contributions in the thesis publications. For each publication there should exist a complete statement that is to be filled out and signed by the candidate and supervisor

Title of Paper	Engineering a uniaxial substrate-stretching device for simultaneous electrophysiological measurements and imaging of strained peripheral neurons
Publication Status	☐ Published ☐ Accepted for Publication ☑ Submitted for Publication ☐ Unpublished and unsubmitted work written in a manuscript style
Publication Details	Submitted to Annals of Biomedical Engineering, June 2018. First Reviewed July 2018.

Main Author

Name of Principal Author (Candidate)	Fabio Bianchi		
Contribution to the Paper	Planned and designed experiments, carried out experiments, carried out analysis (unless specified), wrote manuscript		
Signature		Date	06/08/2018

Co-Author Contributions

Name of Co-Author	Dr. Majid Malboubi
Contribution to the Paper	Carried out patch-clamping experiments, reviewed manuscript

Name of Co-Author	Dr. Julian H. George
Contribution to the Paper	Contributed to design, reviewed manuscript

Name of Co-Author	Dr. Antoine Jerusalem
Contribution to the Paper	Reviewed manuscript

Name of Co-Author	Dr. Mark S. Thompson / Dr. Hua (Cathy) Ye
Contribution to the Paper	Supervised work, reviewed manuscript

Please cut and paste additional co-author panels here as required.

Supervisor Confirmation

By signing the Statement of Authorship, you are certifying that the candidate made a substantial contribution to the publication, and that the description described above is accurate.

Supervisor name and title:	Dr Mark S Thompson		
Signature		Date	09/08/18

This completed form should be included in the thesis, at the end of the relevant chapter.

CHAPTER 4

Microscopic Effects Of Nerve Stretch

4.1 Introduction and Background

The following chapter will focus on the effects of strain on the electrophysiological functionality of neurons. By using the iPSC and stretch models presented in chapter three, the effect of strain on the functionality of individual neurons and neural networks will be investigated, with the aim of linking deformation to changes in activity. Two studies of the effects of stretch on neurons are presented in this chapter. In the first, the effect of strain and of the cell membrane mechanical properties on neural network activity were assessed by calcium imaging of iPSC-derived neurons subject to uniaxial strain. In the second, whole-cell patch clamping was used to evaluate the changes caused by uniaxial strain at the single-cell level, by measuring ion channel dynamics from deformed cells.

4.1.1 Ion Channels, Action Potentials and The Hodgkin-Huxley Model

Ion channels are the transmembrane proteins that regulate the flow of ions between cells and their surroundings. Ions involved in cellular processes include potassium (K^+), sodium (Na^+), calcium (Ca^{2+}), magnesium ($Mg2^+$), chlorine (Cl^-) and bicarbonate (HCO_3^+) as well as proteins, which are negatively charged at physiological pH. Whilst concentrations of HCO_3^+ (necessary for pH regulation) and $Mg2^+$ (involved in ATP generation and use) are regulated by transporter proteins, K^+, Na^+, Ca^{2+} and Cl^- concentrations are controlled by ion channels [22]. These transmembrane pore-forming proteins are responsible for the regulation of ion-specific membrane permeability. Ion channels can be broadly classified by two criteria: their ion specificity and their activation mechanism. Within these categories, many sub-families have been discovered and described, and are exhaustively collated and reviewed yearly by the British Journal of Pharmacology [262].

The function of ion channels as regulators of ionic concentration within cells is intimately linked with thermodynamic principles. In the late 19th century, the Boltzmann equation was developed to describe entropy in gasses, and can be visualised by taking the case of two compartments separated by a membrane containing a small aperture. If a gas in injected into one compartment, provided that the temperature exceeds absolute zero, the gas molecules will passively diffuse into the second compartment until equilibrium is reached. This can be described by the Boltzmann equation:

$$\frac{p_1}{p_2} = e^{\frac{u_1 - u_2}{kT}} \tag{4.1}$$

Where p_x is the probability of finding a particle in a given compartment x, u_x is the particle energy, T is the temperature in Kelvin and k is the Boltzmann constant (a measure of energy per temperature increment) [263, 264].

Equation 4.1 can also be used to describe the diffusion of ions across the cell membrane, which can be thought of as a partition between intra and extracellular environments, permeable to specific ions. By substituting p_x with a given ion concentration c_x, and u_x by the molar energy U_x:

$$\frac{c_1}{c_2} = e^{\frac{U_1 - U_2}{kT}} \tag{4.2}$$

Taking the case of potassium ions (K^+), which exist in much higher concentrations within the cell cytoplasm compared to the extracellular environment, chemical diffusion should induce ionic outflow from the cell. However, because of the membrane potential, positively charged potassium ion diffusion is also regulated by an electrical diffusion gradient. Therefore the overall flux of K^+ ions through the membrane will be regulated by the combination of a simple diffusion term (by Fick's law) and an ion mobility term due to the interaction between the charged ion particles and the membrane's electric field. Equilibrium will occur when total flux is zero. From equation 4.2, taking natural logarithms of both sides, rearranging, and expressing molar energies as $U_1 - U_2 = Z_k F(E_1 - E_2)$, where $E_1 - E_2$ is the potential difference across the membrane, Z_k is the valency of the ion (+1 for K^+) and F is Faraday's constant (electric charge per mole), then:

$$E_1 - E_2 = E_k = \frac{kT}{Z_k F} ln \frac{[K^+]_o}{[K^+]_i} \tag{4.3}$$

Where E_k is the potassium equilibrium potential and $[K^+]_o$ and $[K^+]_i$ are the potassium concentrations outside and inside the cell. This is the Nernst equation, describing equilibrium conditions for potassium ions. The overall membrane equilibrium potential will be given by the combination of multiple iterations of equation 4.3 for all ions present. This equilibrium is maintained by ion movement across the membrane, mostly regulated by the opening and closing on ion channels. [263, 264]

The family of ion channels most closely involved in neural action potential (AP) generation and propagation are gated by the membrane potential. These voltage-gated ion channels are most commonly formed of a central pore and gate surrounded by voltage-sensing subunits. In neurons, voltage-gated Ca^{2+} channels allow influx of calcium ions at synapses that triggers the release of neurotransmitters, voltage-gated Na^{+} channels initiate membrane depolarisation by rapid influx of positively charged Na^{+} ions, and voltage-gated K^{+} channels act as negative-feedback elements that open slowly in response to membrane depolarisation and induce an outwards flux of potassium ions re-polarising the membrane to resting potentials (figure 1.3). [22]

Structurally, Na^{+}, Ca^{2+} and K^{+} channels share similar features. Na^{+} and Ca^{2+} α subunits, which regulate the gating and form the central pore structure, are made up of four domains, whereas K^{+} channel subunits are made up of a single domain similar in structure to one of the four in Na^{+} and Ca^{2+} channels. Putative structures for all channel type domains consists of six transmembrane alpha-helix segments, with the central channel pore located between segments 5 and 6 [23]. Pore domains are therefore intrinsically linked to the membrane lipid bilayer, suggesting a close relationship between membrane mechanics and ion channel function, as shown by the fact that that all channels are sensitive to some degree to the mechanical state of the membrane [265].

Many models exist to describe the electrical behaviour of excitable cells, but the best known and most widely cited remains that developed in 1952 by Alan L. Hodgkin and Andrew F. Huxley [21]. This model treats the cell membrane as a capacitor, ion channel populations as variable conductance elements (each affecting a specific ion current) and ion-specific electrochemical gradients as voltage sources. Therefore, currents through ion channels can be expressed by Ohm's law. For the example of potassium currents (I_k):

$$I_k = g_k(E - E_k) \tag{4.4}$$

Where g_k is the specific conductance of potassium channels (related to the number of open potassium channels) and E_k is the potassium equilibrium potential (or Nearnst potential from equation 4.3). In an equivalent circuit representation this corresponds to a variable conductance element and a voltage source. The cell can therefore be represented by a circuit containing multiple conductances and voltage sources corresponding to different ions involved in neural function.

In the original Hodgkin-Huxley theory, voltage-dependant channel gating is explained by the presence of charged gating particles whose position within the membrane determines the opening and closing of channels. In order to affect channel state, gating charges are moved from the inner to the outer membrane across the membrane potential, activating the gating mechanism. The Boltzmann equation (equation 4.1) can be used to relate the probability of channels being open (O) or closed (C) to the energy difference between the two states:

$$\frac{O}{C} = e^{-}(\frac{w - zeE}{kT}) \tag{4.5}$$

$$\text{or:} \qquad \frac{O}{O+C} = \frac{1}{1+e^{\frac{w-zeE}{kT}}} \tag{4.6}$$

Where w is the energy increase from conformational changes upon opening the channel (in absence of membrane potential), and $-zeE$ is the voltage-dependent term due to movement of gating charge of valence z against the membrane potential E (e is the elementary charge) [22, 263].

Assuming that ion channels can either be open, closed or inactivated, then total conductance for a given ion will be proportional to the number of ion channels in the open state. Therefore the Boltzmann equation can be used to fit the normalised conductance of a population of ion channels at steady-state, where the difference in free energy is a

function of the membrane potential, as:

$$\frac{g}{g_{max}} = \frac{1}{1 + e^{ze(\frac{E_{1/2}-E}{kT})}} \tag{4.7}$$

Where $E_{1/2}$ is the potential where $g = g^{max}/2$, corresponds to the inflexion point in the conductance curve and is known as the half-maximum activation potential. This is commonly used to evaluate changes in ion channel activation dynamics, for example in studies of pharmacological modulation of ion channel activity [22, 23].

Further families of ion channels involved in neural activity include ligand-gated and mechanosensitive ion channels. Although not directly involved in action potential generation, these ion channels play key roles in neural network connectivity and in generating the stimuli that initiate APs. Ligand gated channels are specialised in neuron-to-neuron signalling, and respond to binding of specific neurotransmitters. They are located primarily at synapses, where presynaptic neurons release neurotransmitters into the synaptic cleft activating postsynaptic ligand-gated ion channels. Structurally, ligand-gated ion channels are formed of a transmembrane pore unit, and an extracellular domain containing the ligand binding site that regulates channel gating. Ligand-gated ion channels can further be classified as intracellular and extracellular, depending on the origin of the gating ligand. [22, 266]

Mechanosensitive ion channels, also known as stretch-activated ion channels, are modulated by the mechanical state of the membrane. Their main function is to respond to stimuli such as touch, inducing AP firing to relay sensory information to the central nervous system. Other ion channels, including members of both voltage and ligand gated families, have been shown to be varyingly sensitive to mechanical stimuli and therefore are potential targets of mechanical injury [267].

4.1.2 Mechanotransduction and Mechanosensitivity in Neurons

Force and force sensing is an integral and vital function of life. External mechanical stimuli such as touch and hearing are felt at the periphery of the body, and are relayed to the central nervous system by afferent nerve fibres. Internal subconscious force sensing, such as blood pressure or bladder extension, regulates vital processes.

At the microscopic level individual neurons sense and generate forces, are susceptible to mechanical stimuli, and their function can be impaired or altered when mechanical stimuli exceed physiological measures. The cytoskeleton provides the structure of the cell, and is involved in force production and regulation. Actin, microtubles, neurofilaments and other filament proteins regulate the transduction of external forces within the cell as well as tensile integrity of the membrane, an can generate force through polymerisation and depolymerisation [268]. However, reductionist experimentation on single ion channels reconstituted in lipid membranes without the underlying structure show that channel mechanosensitivity is conserved, implicating the lipid membrane as the principle ion channel mechanoregulator, a phenomenon termed 'force-from-lipid' [269, 270, 271].

Neural electrical activity is also closely related to mechanical forces. Axons have been shown to circumferentially expand during action potential propagation [272], and externally applied electric fields can generate dipole moments that lead to elastic deformation of neural membranes [273]. Mechanical displacements have also been recorded at synapses, where neurotransmitter vesicle release causes actin-mediated twitching [274].

At the molecular level, transmembrane proteins such as ion channels are sensitive to mechanical forces that deform the membrane. Stretch-activated ion channels have been shown to produce mechanically-activated currents in dissociated dorsal root ganglion sensory neurons, with differential responses to nociceptive and non-nociceptive stimuli, indicating a finely mechanosensitive mechanism [275]. Voltage-gated ion channel gating charges, whose displacement regulates channel opening and closing, are embedded within

the hydrophobic interior of the lipid bilayer and thus are sensitive to changes in bilayer mechanical properties [276]. During opening and closing, ion channels substantially alter their shape, and therefore a proportion of free energy involved in channel state transition is transferred to remodel the connections with surrounding lipids [277]. It has been shown that multiple ion channel families, even if not directly mechanically gated, exhibit varying degrees of mechanosensitivity and are therefore potentially affected by mechanical deformation and trauma [267]. Widely used anaesthetics such as Ketamine are thought to act on ion channels by modifying the lipid membrane biophysical environment that in turn affects channel open/closed probabilities shifting the neurons to a less excitable state [278]. Mechanosensitivity has also been identified as a potential therapeutic target, but requires a better understanding of the link between cell membrane mechanics and neural function for clinical development [279].

Mechanical stimuli can also cause structural damage to neurons. Axonal blebbing, identified as a key marker of diffuse axonal injury (DAI) following TBI is caused by microtuble breakage causing dysfunctional axonal transport and cytoskeletal damage, leading to accumulation of proteins within blebs on the axon [259, 105]. Axon bundles mechanically compressed by contact with a micropipette tip show neurofilament disruption, leading to axonal disconnection [227]. The cell membrane has been shown to porate and permeabilise as a result of shear and tensile strain [105, 104]. Due to the link between cytoskeleton, nucleus, cell membrane, and ion channels, structural alterations are likely to affect functionality together with direct membrane disruption.

Currently, the mechanisms whereby a mechanical impact or stretch at the tissue level translates to the cellular level, and how this in turn affects the cell at the molecular level altering functionality are poorly understood. By using *in vitro* models, the response of neural networks and single neurons can be studies in isolation.

4.1.3 Techniques for Electrophysiology

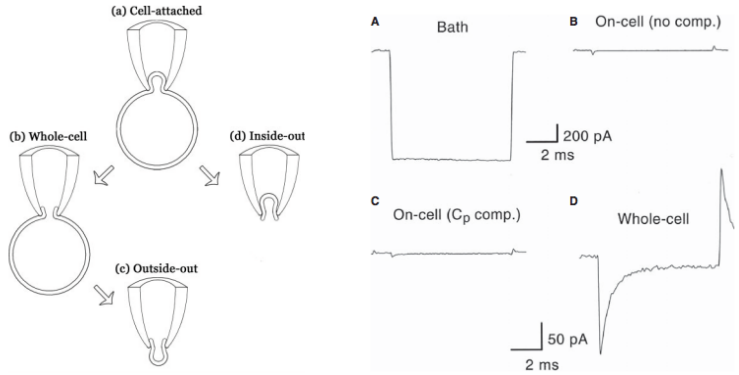
Electrophysiology is the study of the electrical properties of biological tissues and cells, and its origins can be traced back to the 17th century when isolated neuromuscular preparations were shown to respond to external stimulation by muscle twitch. Despite refinement of theories and techniques to explain bio-electrical phenomena, intracellular recordings did not occur until the mid 20th century when Cole and Curtis, closely followed by Hodgkin and Huxley, developed intracellular recording electrodes. In 1978, Neher and Sakmann developed the patch-clamping technique utilising sharp tip micropipettes to form a gigaohm resistance seal at the cell membrane, thereby isolating microscopic membrane patches from which they recorded ion currents [280, 281].

Today, techniques for electrophysiological recording vary in scale from molecular to macroscopic, and can be broadly classified between direct electrical recording methods, and indirect imaging-based techniques.

Direct Electrophysiology - Patch Clamping

From the pioneering work performed in the 1980s by Hamill, Marty, Neher, Scakmann and Sigworth to contemporary protocols, all patch-clamping methods rely on gigaseal formation, a gigaohm-resistance seal which spontaneously forms between polished micropipettes and cell membranes with application of mild suction [282]. This creates an isolated patch of membrane and ion channels, which can be studied in isolation from the rest of the cell. The pipette, filled with electrolyte solution, contains a recording electrode, and a ground electrode is placed in the extracellular bath forming a closed circuit. Once a gigaseal is formed, ion current recordings through a small number of ion channels can be made in cell-attached mode, the least disruptive for the cell (figure 4.1a (a)). If following gigaseal formation the patched membrane portion is excised from the cell (figure 4.1a (d)), the configuration is called inside-out patching, and allows access to the cytoplasmic mem-

brane side. This technique is favoured for studying internally ligand-gated ion channels. The whole-cell configuration (figure 4.1a (b)) is the most commonly used patch-clamping protocol. By applying a second pressure pulse, the membrane inside the pipette is ruptured, and the cell cytoplasm forms a liquid continuum with the pipette solution. This allows full control over the cell potential and observation of the compound ion currents from all ion channels. If following establishment of whole-cell configuration the pipette is raised away from the cell, the membrane is excised and spontaneously reseals, forming an outside-out patch (figure 4.1a (c)) useful for studying externally ligand-gated channels [283, 284].



(a) (b)

Figure 4.1: (a) Four most common configurations of the patch-clamp technique. From [284] and (b) Real-time montiroing of electrode resistance through small voltage pulses allows the user to track microelectrode position and gigaseal formation. From [283].

Pipettes used for whole-cell patch clamping are heat-pulled from borosilicate glass capillary tubes to approximately 10 μm diameter with blunt endings, and have low resistances (5-15 $M\Omega$). To establish whole-cell configuration the electrode pipette is lowered gently towards the cell membrane, while monitoring the waveform of a small voltage pulse. When contact between pipette and cell is made, the resistance rapidly increases, and by applying mild suction and a small negative holding voltage, a gigaseal is formed, with electrode resistances rising to $> 1G\Omega$. Here, pipette capacitance is compensated through

software control (figure 4.1b, (B) and (C)). To break into whole-cell configuration, further suction is applied until the membrane is ruptured, resulting in the waveform shown in figure 4.1b, (D). The resting membrane potential can be measured immediately after breaking into whole-cell configuration, holding current at zero. Series resistance and capacitance compensation are then set and spontaneous action potentials can be recorded by keeping current injection at zero and recording membrane potential. Thereafter, ion currents can be measured by holding cell membrane potential at increasing voltage clamp levels. Alternatively, membrane potential variations including induced AP firing can be measured in response to setting and holding clamp currents [283].

Overall, the advantage of patch clamping is the specificity of measurement, allowing precise recordings of ion currents and membrane potential. The disadvantages compared to other direct electrophysiological measurements such as multi-electrode arrays (MEAs) lies in the low throughput, and in the inherent invasiveness of patch clamping where individual cells are sacrificed at each recording.

Indirect Electrophysiology - Calcium Imaging

The development of increasingly complex *in vitro* cultured neural networks requires electrophysiological techniques which allow high throughput, non-invasive measurements. Image-based techniques such as calcium imaging and voltage-sensitive dyes provide a valid option.

Calcium imaging relies on the tracking of free intracellular calcium ions, and has been widely used as a surrogate indicator of electrical activity. Due to the presence of voltage and ligand-gated calcium channels in neurons, rapid increases in intracellular free calcium concentration can be used as a proxy indicator for action potential firing, although generally limited to firing at frequencies below 100 Hz [285].

Free calcium in neurons is regulated by multiple mechanisms. Calcium efflux is governed by membrane calcium ATPase and by sodium-calcium exchangers, whilst influx of calcium occurs through voltage gated calcium channels, glutamate-activated NMDA and CP-AMPA receptors, and G-protein coupled receptors. Endoplasmic reticulum and mitochondrial calcium stores buffer excess calcium influx and can contribute to cytosolic calcium release [199].

Calcium indicators have evolved in parallel with cellular dye and imaging technologies. The first calcium indicators were based on photo-proteins such as aequorin, which spontaneously emit photons upon calcium binding, but have a limited fluorescence lifespan. Calcium chelator-fluorophore complexes, such as Fura-2, Fluo-4 or Oregon Green BAPTA, contain a fluorophore that exhibits a shift in emission wavelength after calcium binding, and provide a more versatile and stable alternative to photo-proteins. They can be delivered as cell-permeable complexes with acetoxymethyl (AM) esters, which are cleaved by intracellular esterases, exposing the fluorophore and resulting in fluorescent emission proportional to the intracellular free calcium concentration [199].

4.2 Membrane mechanical properties regulate the effect of strain on network electrophysiology in iPSC-derived neurons

Fabio Bianchi, Valerio Pereno, Julian H. George, Mark S. Thompson and Hua Ye.

Under review, Neuroscience, 13/08/2018.

4.2.1 Introduction

During mechanical injury to the nervous system, multi-scale partitioning of strains and stresses results in cell deformation, which in turn affects cellular function [61]. In peripheral nerves, conduction blocks are observed following supraphysiological extension of 5-20% [25], suggesting induced electrophysiological dysfunction. In white matter, tissue strain has been shown to affect axons and cell bodies at the microscopic level [63, 118], but the mechanisms that lead to impaired electrical activity are not fully understood. The wide range of putative injury mechanisms point to multi-scale alterations, from aberrant synaptic connectivity to dysfunctional electrophysiological mechanisms in individual cells.

Network electrophysiological activity is initiated from synaptic connection between functional neurons, and is known to be vulnerable to mechanical insult [286]. Using a shear-flow injury model coupled with multi-electrode array recordings, Prado et al. have shown that mechanical injury causes partial or complete cessation of spontaneous electrical activity in cultured cortical rat neurons, linking it with increased membrane permeability [207]. Magou et al. indirectly assessed changes in spontaneous network activity from rat neocortical neurons by imaging calcium flux, showing dramatically decreased firing rates 30 minutes after injury (60% strain at $30s^{-1}$ strain rate) and concurrent hyperexcitability of non-injured neurons within injured cultures, indicating aberrant synaptic connectivity [200].

Ion channels, the transmembrane proteins responsible for the regulation of membrane potential and for the initiation and propagation of action potentials (APs), are embedded in the cell membrane, and are known to be mechanosensitive [267]. The forces regulating ion channel gating originate from the surrounding lipid membrane, suggesting a close relationship between membrane mechanics and electrophysiological activity [265, 287]. For example, membrane stiffening by stomatin-like protein-3 (STOML3) has been shown to finely control mechanically gated ion channel activity in sensory neurons [288]. This is not limited to mechanosensitive channels, as voltage- and ligand-gated channels have also been shown to be variably mechanosensitive, and their activity altered by localised membrane suction [234, 276, 289, 290]. The cell membrane has further been implicated in neural mechanical damage, which leads to membrane poration and increased permeability [62, 104, 207].

Cholesterol, physiologically accounting for approximately half of the cell membrane by molar fraction, can be used to modify membrane mechanical properties [291]. Cholesterol level can be manipulated by addition of methyl-β-cyclodextrin (MβCD); addition of unloaded MβCD causes depletion of cholesterol from cell membranes, whereas cholesterol-loaded MβCD enriches cholesterol content [292]. In turn, this alters the mechanical properties of the membrane [293, 291, 294], and affects synaptic activity [295, 296] and the function of transmembrane proteins including ion channels [297, 298, 299, 300]. The effects of membrane stretch and cholesterol depletion are strikingly similar. Both cause accelerations in ion channel current time-course, alterations in APs [301], and blocking of synaptic transmission in networks [295]. This remarkable resemblance suggests that both processes affect ion channel and synaptic function by altering the mechanical environment of the cell membrane. Currently, no study has investigated the role of membrane mechanical properties on the consequences of strain applied to neurons.

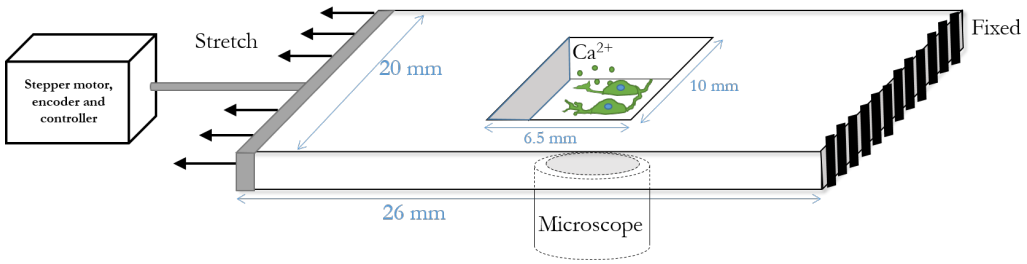


Figure 4.2: Experimental setup for cell straining. Neurons cultured on deformable PDMS substrates were subjected to uniaxial strains, and network activity measured by calcium imaging using an inverted fluorescence microscope.

The aim of this study was to quantify the changes in spontaneous network activity in human iPSC-derived neurons subject to uniaxial strain, and how changing the membrane mechanical properties affect cells subject to strain. Using a custom-built substrate-straining device [Bianchi et Al., 2018, submitted for publication] we applied uniaxial strain to human iPSC-derived neurons with and without cholesterol addition, and recorded activity using calcium flux imaging. To quantify the effect of stretch and cholesterol addition on the mechanical properties of the membrane, we use c-Laurdan spectral imaging to quantify membrane lipid packing.

Understanding the mechanisms of electrophysiological dysfunction in neurons and the importance of membrane mechanical properties during cell deformation can provide useful insights on the mechanisms underlying conduction blocks in peripheral sensory and motor tracts, aiding the development of protective and restorative strategies and the understanding of heightened neural vulnerability following sub-lethal injury.

4.2.2 Materials and Methods

Cell Culture

Human motor neurons were differentiated from induced pluripotent stem cells (iPSC) obtained through StemBANCC, Oxford, following a previously established protocol [247]. Following differentiation by dual-SMAD inhibition and differentiation to motor neuron

lineage, neurons were matured for a minimum of 21 days in media consisting of 50% knockout-dulbecco's modified eagle medium:F12 (KO-DMEM:F12 ThermoFisher, UK) and 50% neurobasal medium (ThermoFisher, UK), supplemented with 1% penicillin streptomycin (P/S, Sigma-Aldrich, UK), 1% B27 (ThermoFisher, UK), 1% N2 (ThermoFisher, UK), 1% non essential amino acids (ThermoFisher, UK), 1% glutaMAX (ThermoFisher, UK), 0.1 mM L-ascorbic acid (Sigma-Aldrich, UK), 10 ng/ml ciliary neurotrophic factor (Peprotech, UK), 10 ng/ml brain derived neurotrophic factor (BDNF, Peprotech, UK), 10 ng/ml NT-3 (Peprotech, UK), and 10 ng/ml glia derived neurotrophic factor (GDNF, Peprotech, UK).

Cell Stretching

Cells were deformed using a custom-built substrate stretching device (figure 4.2), delivering uniaxial strain to cells cultured on ultrathin (50-100 μm) polydimethylsiloxane (PDMS) substrates (Silex, UK) and allowing for simultaneous high-resolution microscopy and electrophysiological recording (Bianchi et al., 2018, under review for publication). iPSC-derived neurons were seeded on deformable substrates at 30,000 cells/substrate.

For network activity experiments, iPSC-derived neurons were subjected to graded strain applications, from 0% (unstretched) to 25%, 45% and 75% strain and released back to 0%, all carried out at 0.1 s^{-1} strain rate (figure 4.3). At each strain point time-lapse imaging of intracellular calcium concentration was recorded for 4 minutes. The same stretch protocol was repeated for cell samples loaded with cholesterol and for c-Laurdan lipid packing imaging.

Live Cell Staining and Strain Measurement

Cell membranes were stained using cellmask green (ThermoFisher, UK) live cell dye, at 1:1000 concentration, for 5 minutes at 37°C. Nuclei were stained using nucblue (Ther-

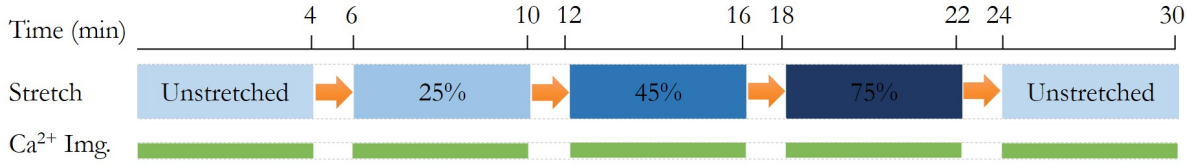


Figure 4.3: Typical strain and calcium imaging protocol, with graded increase in applied stretch, and four minutes calcium imaging at each condition.

moFisher, UK) at 2 drops/ml, for 15 minutes at 37°C. Images were taken using a Nikon Ti-E inverted fluorescence microscope (20x lens) using standard DAPI and FITC filters (360/460 and 490/520 nm excitation/emission). Nucleus morphology was measured using ImageJ plugin Ovuscule, a FIJI (Fiji Is Just ImageJ, NIH, USA) which fits an ellipse to areas of high contrast and returns major and minor axis measurements [249]. Membrane strain was measured manually by selecting distinct membrane features and measuring lengths along cell major and minor axis.

Membrane Cholesterol Addition

Membrane cholesterol levels were increased by addition of water-soluble cholesterol in methyl-β-cyclodextrin saturated complexes (CH-MCD, 4% Cholesterol content (w/w), Sigma-Aldrich, UK) in culture medium at a final concentration of 200 μM. Cells were incubated 30 minutes prior to experiments. Saturated CH-MβCD complexes have been shown to act as efficient cholesterol donors towards cell membranes, when added to culture medium at this concentration [292, 302, 301].

Cholesterol addition was assessed by filipin III staining. Cells, both cholesterol loaded and control, were fixed in 4% paraformaldehyde (Sigma-Aldrich, UK) in phosphate buffered saline (PBS, ThermoFisher, UK), for 20 minutes at room temperature. Filipin III (Santa Cruz Biotechnologies, USA) was dissolved in dimethylsulfoxide (DMSO, Sigma-Aldrich, UK) and added to cell medium at a final concentration of 50 μg/ml. Cells were incubated for two hours at room temperature and imaged using standard DAPI filters (360/460 nm

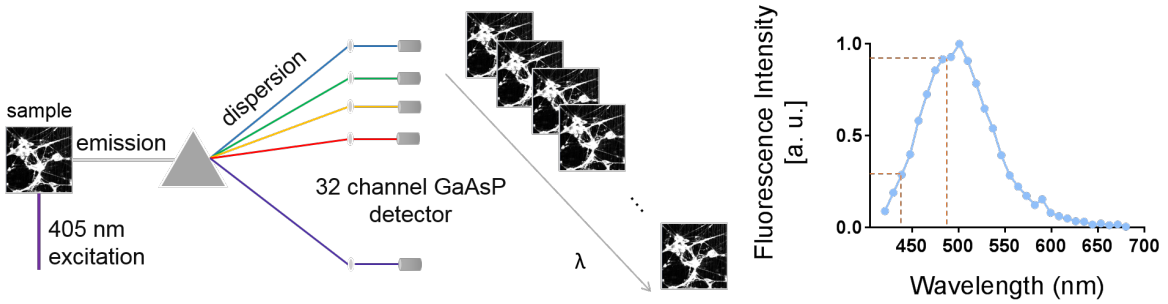


Figure 4.4: Spectral imaging acquisition for c-Laurdan imaging. The stained sample (left) was excited with 405 nm laser, and 32 split channel detector records within pre-set wavelength intervals (middle). Fluorescence intensity was plotted as a function of emission wavelength, and I_{440} and I_{490} are used to calculate generalised polarisation (GP).

excitation/emission) using the same acquisition settings for control and cholesterol-loaded cells, and average fluorescence intensity was measured in FIJI.

C-Laurdan Imaging

The lipid organisation of the cell membrane, commonly referred to as lipid packing, was calculated from the red- or blue-shift emission of a polarity-sensitive probe using c-Laurdan, a spectral imaging microscopy technique described previously [303, 304].

The neurons were labelled with c-Laurdan (SFC, Chunbuk, Republic of Korea), at a final concentration of 400 nM in fluorobrite-DMEM imaging media (FB-DMEM, ThermoFisher, UK), immediately prior to imaging. The cell sample was then excited with a 405 nm laser and imaged using a Zeiss 710 confocal microscope equipped with a 32-channel GaAsP detector array (figure 4.4). The intensity of the emission spectrum was detected and recorded in the 415-691 nm range.

The emission spectrum of c-Laurdan is related to the dipolar water relaxation in the proximity of the probe, indicating the degree of hydration within its surrounding micro-environment. This, in turn, is indicative of the lipid packing of the plasma membrane. Generalised polarisation (GP), a well-established parameter for quantification of membrane hydration, was used to quantify the relative degree of lipid packing on a scale of

-1 to 1, where -1 represents the most hydrated (least packed, most fluidised) and +1 represents the least hydrated (most packed, least fluidised) membrane state. GP was calculated by comparing the intensity of the emission at two specific wavelengths, 440 (I_{440}) and 490 nm (I_{490}) as GP = $\frac{I_{440}-I_{490}}{I_{440}+I_{490}}$. GP was calculated for cells before, during and after stretch, both with and without addition of soluble cholesterol. An automated MATLAB script was used to select image areas containing cells, segment cell profiles, isolate cell membranes, and calculate GP values [305].

Functional Calcium Imaging and Analysis

Imaging of intracellular free calcium was carried out using Oregon Green 488 BAPTA-1 (OGB1, Thermo Fisher, UK). A stock solution of the dye was made by dissolving OGB1 in DMSO containing 20% Pluronic F-127 (Sigma Aldrich, UK), used to avoid dye compartmentalisation within the cell [285]. The solution was first brought to a 1 mM concentration by addition of PBS and a then to 20 μm (stock solution), by further addition of PBS. Solution was sonicated for 5 minutes after each step. A 2 μM working solution was made by addition of FB-DMEM, a high-glucose medium formulated to reduce background fluorescence during imaging, with a free calcium content (1.8 mM) suitable for intracellular calcium recordings [306]. Cells were loaded with dye solution for 30 minutes at 37°C, washed in PBS, and incubated for a further 30 minutes in fresh FB-DMEM. Cells were then imaged using time-lapse microscopy, on a Nikon Ti-E microscope (10x lens), at 10 frames per second for four minutes for unstretched and stretched conditions (figure 4.2). Regions of interest were drawn around cell bodies, and fluorescent intensity plotted over time. A custom-written MATLAB code was used to filter and plot all traces, identify calcium spikes and measure spike magnitude, rise time, and fall time. Active cells were defined as those showing at least one rapid spike in fluorescence. Network activity

was measured as the percentage of active cells, and expressed normalised by the value for unstretched cells.

Statistical Analysis

Statistical analysis was carried out in PRISM v6 (Graphpad, USA). Data was tested for significance using paired or unpaired one-way ANOVA analysis with Tukey's multiple comparison (for any experiment involving comparisons between more than two conditions), or by paired student t-test (for any experiment involving two conditions). All data is reported as mean $\pm$ standard deviation.

4.2.3 Results

Strain in Neuron Membranes and Nuclei

To determine the localisation of applied deformation, strains were measured in individual cell membranes and nuclei. Human iPSC-derived neurons show a hierarchical strain partitioning, with average membrane deformation found to be significantly higher than nucleus deformation, for all magnitudes of applied strain (figure 4.5). Average strain in both nuclei and membranes increased with increasing substrate strain, confirming good adhesion between the deformable substrate and the cells. On average, 70% of the applied substrate strain is transferred to the membrane, and 25% to the nucleus, in line with previously reported strain transfer ratios in cells cultured on elastic substrates [307].

Effects of Strain and Cholesterol Addition on Membrane Lipid Packing

GP of neuron membranes was measured by imaging cells stained with c-Laurdan. GP decreased significantly with increasing applied strain (figure 4.6a), indicating a decrease in lipid packing at the cell membrane. To control for dye photobleaching, time-series imaging of c-Laurdan stained neurons was performed. Following an initial decrease due to stretch,

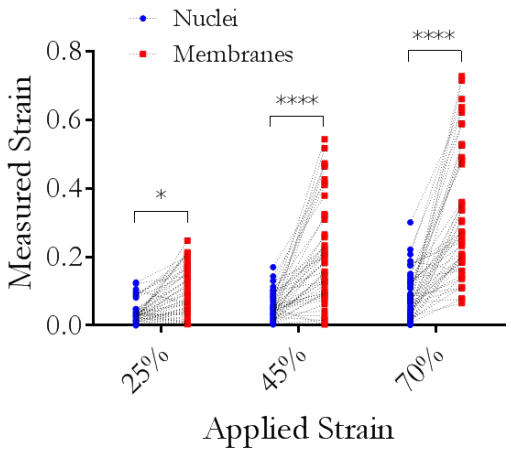


Figure 4.5: Strain in cell membranes and nuclei. For three applied substrate strains (25%, 45% and 70%), magnitude of deformation of individual cell membranes is higher than deformation of nuclei. n = 51 cells from three independent samples. Grey dotted lines show nucleus and membrane strain from the same cells. (**** p = < 0.0001, * p = 0.0169 by two-way ANOVA with Tukey's multiple comparison between each applied strain level, n = 49 cells).

GP remained constant for ten minutes, confirming no significant photobleaching effect (figure 4.6b).

Cholesterol content of iPS-derived neuron membranes was increased by incubation with cholesterol-loaded MβCD for 30 minutes, and confirmed by filipin staining (figure 4.6f). Addition of cholesterol increases baseline GP, indicating an increase in membrane lipid packing. In cholesterol-enriched cells the fluidisation effect of strain was less pronounced, compared to control cells (figure 4.6a). The effect of adding cholesterol was qualitatively visualised in lambda stack images, where an increase in red-shifted areas indicated higher lipid packing (figures 4.6c, 4.6d and 4.6e (i)). After substrate stretch release, axonal defects were observed with uneven lipid packing distribution (figure 4.6e, ii).

Effects of Strain and Cholesterol Addition on Electro-Mechanical Properties

Base activity, defined as percentage of active cells before stretching, remained unchanged following addition of cholesterol (figure 4.7f).

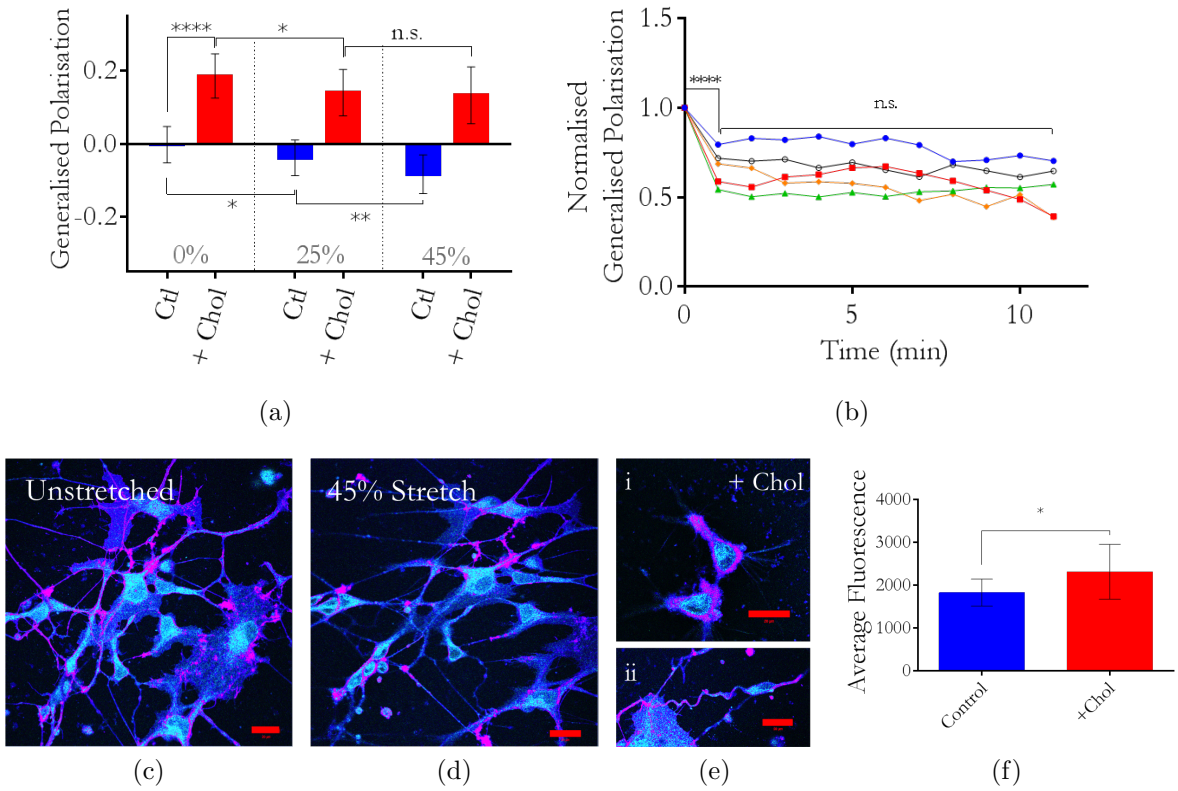


Figure 4.6: (a) GP of segmented membranes from multiple cells per image, subject to increasing strain (0%, 25% and 45%), in control cells ('Ctl') and with cholesterol addition ('+Chol'). Cholesterol increases GP in unstrained cells (**** p = $<$ 0.0001, n = 6 per group, unpaired *t*-test). Strain induces fluidisation in control cells (* p = 0.0103, ** p = 0.0018, n = 6 per group, paired one-way ANOVA with Tukey's multiple comparisons) and in cholesterol-enriched cells (* p = 0.0213, n.s. = not significant, n = 6 per group, paired one-way ANOVA with Tukey's multiple comparisons). Minimum 3 cells per n in each group. (b) Time-measurements of GP, with 45% strain applied after 1 minute. (**** p = $<$ 0.0001, n.s. p = $>$ 0.05 by paired t-test between timepoints for each sample. n $>$ 5 cells per sample). (c-d) C-Laurdan spectral imaging of unstretched and 45% strained human iPSC neurons (without cholesterol addition). (d) Cholesterol addition (i) and axonal damage (without cholesterol addition) following stretch (ii). Purple areas show regions with higher lipid packing. Scale bars = 20. (d) Quantification of average fluorescence intensity from filipin staining (c). Scale bars = 100 μm. * p = 0.0354 by unpaired t-test.

To measure the effect of mechanical deformation on spontaneous network activity, maturing human iPS-derived neuronal networks (N = 7, 83 cells average per N) were subject to increasing strains of up to 75% with calcium flux activity recorded at each strain level. Measurements immediately after strain release were used to assess immediate recovery. Cell calcium flux activity decreased significantly when strain was applied, proportionally to applied strain (figure 4.7a). After applying 25% strain, network activity decreased by

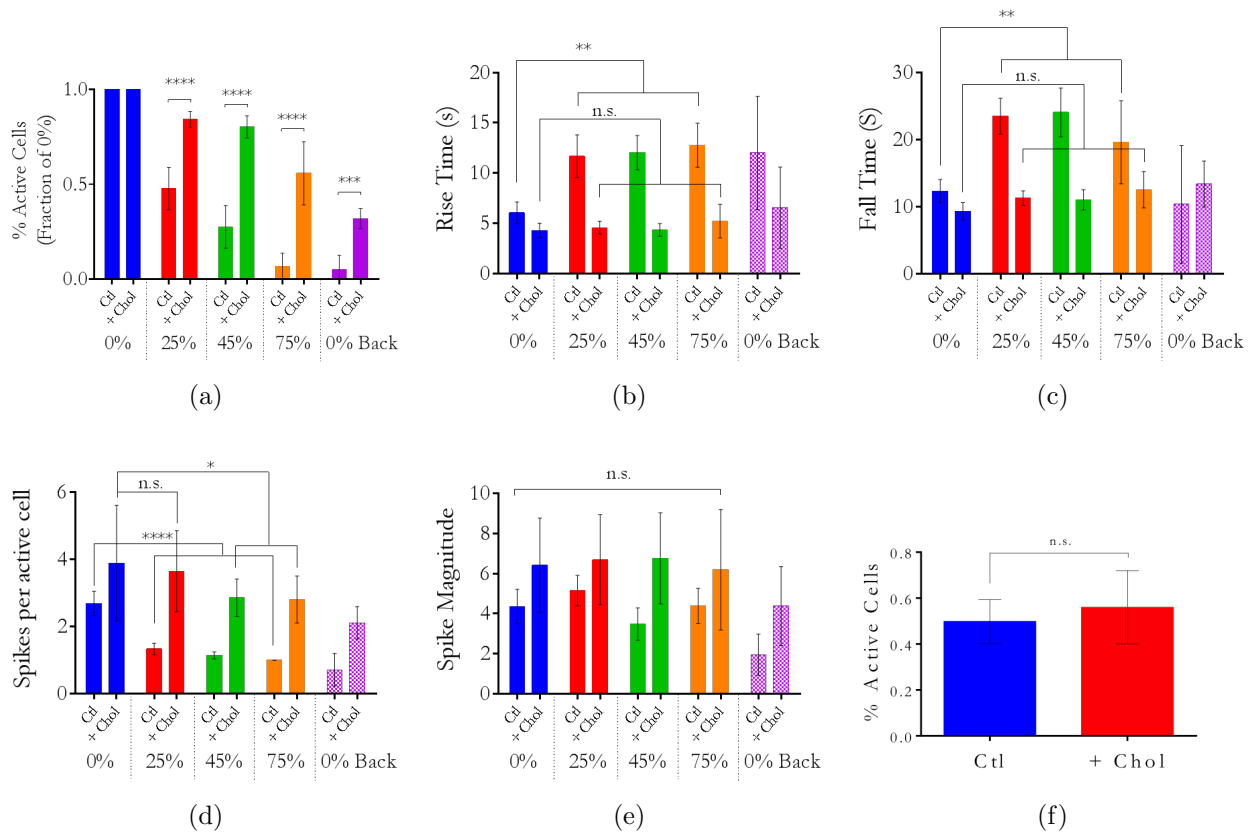


Figure 4.7: Changes in network electrophysiology with applied deformation for cholesterol-enriched and control cells. (a) Spontaneous activity (percentage active cells), normalised by the unstrained value for each condition (**** $p = < 0.0001$ by paired one-way ANOVA with Tukey's multiple comparisons between incremental strain conditions). (b) Spike rise time (** $p = 0.0046$, 0.0021, 0.0046 between unstrained and 25%, 45% and 70%). (c) Spike fall time (*** $p = 0.0003$, 0.0002, 0.0005 between unstrained and 25%, 45% and 70%) (d) Average number of spikes per active cell (**** $p < 0.0001$, n.s. $p = > 0.05$ between unstrained and 25%, * $p = 0.0450$, 0.0312 between unstrained and 45% and 70%.) (e) Average spike magnitude (n.s. $p > 0.05$) (f) Basal spontaneous activity is not significantly affected by addition of cholesterol (n.s. $= p > 0.05$ by unpaired t-test).

half. At 45% strain, the percentage of active cells decreased to 30%, further decreasing to 7% at 75% applied stretch. After release, no immediate recovery was found, instead a near-complete silencing of network spiking was observed. A significantly smaller reduction in number of active cells was observed in cholesterol-enriched cells for each level of applied strain (figure 4.7a), including after strain release.

Calcium spiking rise time (time from baseline to spike peak) and fall time (time from spike peak back to baseline) were both significantly increased by a factor of two at 25%

applied strain (figures 4.7b and 4.7c), and did not change with further strain. Rise and fall time of calcium spikes for cells with increased membrane cholesterol was not significantly altered by strain (figures 4.7b and 4.7c). Rise and fall time cells immediately after strain release were not included in analysis due to the low number of active cells.

The number of spikes per active cell, indicating spiking frequency, significantly decreased from 2.75 to 1.2 with increasing strain (figure 4.7d). The number of spikes per active cells decreased less in cholesterol-enriched cells compared to control cells, with a significant decrease only at 45% applied strain (figure 4.7d).

No significant change in spike magnitude was observed between control cells and cholesterol-loaded cells, for all strain conditions (figure 4.7e). In control cells, spike magnitude (percentage increase with respect to baseline) did not change between increasing strains, but decreased when strain was released (figure 4.7e).

4.2.4 Discussion

The aim of this work was to quantify the changes in spontaneous network activity of human iPSC-derived neurons subject to uniaxial strain, and to investigate the role of cell membrane mechanical properties in regulating the effects of stretch on neurons.

Cell Membrane Strain and Lipid Packing

The transfer of strain from the deformable substrate to the cell membrane and nucleus was measured in iPSCs subject to 25%, 45% and 70% substrate strain. Results showed that a larger percentage of substrate strain was transferred to the membrane compared to the nucleus. Previous studies hypothesised that this is due to higher nuclear stiffness, and to indirect or incomplete cytoskeletal mechanical linking to the nucleus [146]. Evidence of ion channel mechanosensitivity in cytoskeleton-depleted cells and in reconstructed artificial bilayers [271] points to the membrane regulating the mechanical

environment to which transmembrane proteins are exposed. The higher membrane strains measured suggest that the membrane mechanical environment is significantly altered during cell stretch, and that functional changes may therefore arise as a direct consequence of membrane deformation.

To quantify the effect of strain on the membrane, changes in lipid packing during cell straining were measured using c-Laurdan, a polarity-sensitive probe which produces a red or blue shifted signal depending on membrane hydration level [303, 304]. This technique has, to the best of our knowledge, never been applied to study structural changes neural membranes subject to deformation. Applying strain to human iPSC-derived neurons caused a decrease in generalised polarisation (GP), indicating a decrease in lipid packing and an increase in membrane fluidisation (figure 4.6, blue bars). Intuitively, stretch reduces the lateral packing density of membrane elements, increasing water permeability and shifting the membrane to a more hydrated state. In endothelial cells, GP has been shown to increase during stretch and decrease under fluid shear stress [308], a response thought to be due to cell specialisation in differentiating between mechanical stimuli [309]. In neurons, which are not required to differentiate between mechanical stimuli, the measured decrease in membrane lipid packing agrees with previously shown increase in membrane permeability with strain [207, 104], and shows that the membrane state is directly altered by strain. Increasing cholesterol content in iPSC-derived neurons increased the baseline membrane lipid packing, explained by an increase in molecular density in the membrane bilayer. Applying strain to cholesterol-loaded cells also caused a fluidisation effect, though smaller than that observed in control cells (figure 4.6). Cholesterol addition to lipid membranes has previously been shown to alter membrane mechanical properties, increasing storage and loss moduli [293] and stiffness [291], explaining the smaller decrease in lipid packing measured during stretch, showing how the addition of cholesterol modulates the mechanical properties of the cell membrane.

Lipid packing and membrane fluidity have been previously linked with neural activity. Anaesthetising agents such as ketamine [278] and alcohols [310] are known to alter synaptic and electrophysiological function of neurons by altering membrane lipid conformation and mechanical properties. C-Laurdan imaging results provide evidence that the cell membrane structural properties are being altered during stretch, and that cholesterol addition mitigates this effect by altering the membrane mechanical properties.

Alterations in Network Spontaneous Activity

Calcium flux imaging is a well-established technique used to indirectly record neural activity [199]. Fast spiking, caused by rapid calcium influx and efflux due to synaptic stimuli and AP propagation has been used to monitor network dynamics in cultured neurons [311]. Here, we used fast calcium spiking to assess the effect of changing membrane mechanical properties by cholesterol addition on network electrophysiology of human iPS-derived neurons during and after uniaxial strain.

Our results indicate that the onset of damage occurs immediately during stretch. The number of active cells decreased linearly with increasing applied strain and no immediate activity recovery was observed following release of strain (figure 4.7a). Spike analysis further revealed a significant increase in rise and fall time, indicative of impaired calcium dynamics [199]. This could be a result of a non-selective ion influx due to membrane mechanoporation, which has been shown to occur in rat cortical neurons both under shear flow [207] and equibiaxial strain [104] as well as *in vivo* [312, 62]. However, rapid re-sealing of membranes has been observed after injury [207], and would suggest a short-term recovery not seen here. Furthermore, our observations of reduced spiking per active cell and altered rise and fall time point to impaired mechanisms of ion influx and efflux, rather than a large immediate non-selective influx caused by membrane poration that would result in a long-term rise in intracellular calcium. This suggests that strain causes

damage in the ion channels and synapses at the cell membrane, altering their dynamic behaviour.

Previous work using calcium imaging has shown a decrease in spontaneous activity after stretch in rat cortical neurons, partly recovered after two days incubation [208]. Strain has also been shown to decrease AP firing frequency, and increase spike interval in neurons cultured on multi-electrode arrays [207]. In both cases, loss of spontaneous network activity was attributed to a combination of damaged synaptic connectivity and membrane structural damage. Post-synaptic currents have also been shown to decrease in rat cortical neurons following stretch, resulting in aberrant connectivity between neurons [208, 313]. Interestingly, developmental stretch (strain rates of 1 mm/day, approximately 0.5×10^{-5} s^{-1}), has been shown not to alter real-time calcium spiking and AP firing, suggesting an active growth process occurring faster than damage and that synaptic connections are maintained if neurons are stretched at low strain rates [45]. At very low strain rates, it is possible that the cell membrane undergoes an adaptive process, thereby limiting the changes in its mechanical state. Cell membrane resealing in electroporated cells has been shown to start minutes after damage, and complete re-sealing to occur after 20 minutes [314]. At higher strain rates such as those used here, the abrupt alteration in membrane mechanical state due to strain causes immediate changes in single cell activity and synaptic connectivity, reducing spontaneous network activity. Overall, the loss of network activity with applied strain is likely due to an interaction of multiple factors, including alterations of individual cell electrophysiology combined with aberrant synaptic communication. Our results show that the onset of connectivity dysfunction occurs immediately with strain application, and exacerbates with increasing strain magnitude. This short timeframe points to direct mechanical damage, rather than a secondary process, as being the cause of network dysfunction.

Cholesterol is a primary component of the cell membrane making up 50% of membrane molar fraction, and is crucial in membrane organisation and physiological function [315]. Altering the membrane mechanical properties by cholesterol addition to did not change the percentage of active cells within networks (figure 4.7f), however it increased the average number of spikes per cell and spike magnitude, indicating an increase in network excitability (figure 4.7d and 4.7e, blue bars). Increased cholesterol significantly reduced the severity of the decrease in spontaneous calcium spiking caused by strain (figure 4.7, 4.7d). Spike rise and fall times for cholesterol-enriched cells were not affected by strain, whilst in control cells strain increased average rise and fall time (figure 4.7b and 4.7c). Membrane stiffness has been shown to increase with cholesterol addition [291] and decrease with cholesterol depletion [316]. Gramicidin channels, widely used as molecular membrane force transducers, have also been used to show molecular stiffening in cholesterol-enriched membranes [287]. In neural membranes, depletion of cholesterol has been shown to increase lateral mobility of fluorescent lipid probe molecules [317], which suggests a decrease in molecular packing similar to what we observed by c-Laurdan imaging in strained neurons (figure 4.6). Neural activity and membrane cholesterol content have been directly linked by Guo et al., concluding that cholesterol levels can bi-directionally modify neural excitability by modulating ion currents [301]. Furthermore, depletion of cholesterol in presynaptic terminals has been shown to block evoked synaptic transmission [295, 296], similarly to how stretch decreases excitatory post-synaptic currents [208].

Our results show that cholesterol addition alters cell membrane mechanical properties, increasing lipid packing and limiting membrane fluidisation caused by strain. This results in a reduction of the effect of strain on spontaneous network activity, decreasing the loss of synaptic connectivity and alleviating the effect of stretch on mechanisms regulating ion influx and efflux. Membrane stiffening by increasing cholesterol content could act to protect the action potential (AP) firing mechanisms in neurons by reducing

the mechanical stress applied to ion channels during membrane stretch. Recently, Al-Rekabi and Contera have shown that increasing the cholesterol molar fraction of artificial lipid bilayers increases the storage and loss modulus, suggesting that cholesterol enrichment leads to increased energy dissipation properties in lipid membranes [293]. A greater energy dissipation would therefore lead to reduced mechanical stress on ion channel mechanisms and synapses, protecting neural functionality. These results indicate that altering membrane mechanical properties lessens the damaging effects of strain on spontaneous neural network activity, highlighting the crucial role of membrane mechanical properties on ion channel and synaptic function, supporting our hypothesis that acute stretch causes aberrant neural activity by altering the mechanical state of the membrane.

4.2.5 Conclusions and Limitations

The aim of this study was to investigate changes in network electrophysiological properties in human iPSC-derived neurons subject to mechanical stretch.

To the best of our knowledge, the experiments reported here are the first network and single-cell electrophysiological measurements of human iPSC-derived neurons *during* strain applied by substrate deformation. Compared to primary rodent cells, overwhelmingly used in *in vitro* studies of neural injury, the use of human iPSC-derived neurons provides a physiologically relevant model, increasing the translational significance of the results.

In summary, we have shown that spontaneous network activity of human iPSC-derived neurons decreases linearly with applied uniaxial stretch, indicating dysfunction of synaptic connections and of AP firing mechanisms. To understand the importance of cell membrane mechanical properties, c-Laurdan imaging was used to show that cell stretch decreases membrane lipid packing. Cholesterol addition to neural membranes reduces lipid packing decrease during strain, and reduced the loss in spontaneous network activity caused by

strain. Together these results indicate that the mechanism whereby cell injury causes impaired transmission of neural impulses is governed by the mechanical state of the cell membrane. This can help understand the onset of nerve conduction blocks, impacting preventive and treatment strategies for mechanical trauma.

Limitations of this Study

The mechanical parameters tested were not an extensive representation of injury, and the effect of different strain rates, as well as smaller strain increments, should be used to provide more information about injury mechanisms. Evaluating the recovery of activity after smaller strains could establish a threshold value after which the loss of network activity becomes irreversible.

Another limitation of this study is the focus on membrane processes, without investigating the role of cytoskeletal elements in the electrophysiological response to stretch. In future studies, pharmacological cytoskeletal manipulation will be investigated as a factor influencing electrophysiological response during stretch. At the membrane level, we do not directly measure the membrane properties during stretch and as a result of cholesterol addition, but instead rely on GP measurement. Direct elastic and visco-elastic mechanical characterisation of cholesterol-enriched neurons, for example by AFM, would provide stronger evidence of changes in membrane mechanical properties.

4.2.6 Acknowledgements:

Authors acknowledge China Regenerative Medicine Limited (CRMI) for funding and the EPSRC DTP (award number 1514540) for funding F.B. The authors declare no competing financial interests

4.3 Ion current and action potential alterations in peripheral neurons subject to uniaxial strain

Fabio Bianchi, Majid Malboubi, Julian H. George, Antoine Jerusalem, Mark S. Thompson and Hua Ye.

Under review, Journal of Neuroscience Research.

4.3.1 Introduction

Supraphysiological stretch of 5-20% in peripheral nerves, as a result of trauma, aberrant limb positioning, or surgery, is known to cause conduction blocks [25], however the mechanisms are not fully understood.

Although there is an extensive literature on *in vitro* neural mechanical damage, the focus has traditionally been on the central nervous system (CNS). Despite differences in tissue mechanical properties and structure between CNS and peripheral nervous system (PNS), these results can be used to help understand how mechanical strains affect neural functionality. Strain induces significant magnitude-dependent cell depolarisation [253], coupled with increased intracellular calcium [318, 319], which is thought to initiate mitochondrial failure [320] and protease activation [257, 312], leading to impaired cell functionality and death. Calcium influx following injury has also shown to be tetrodotoxin (TTX)-sensitive, indicating potential damage to sodium ion channels [258]. Additionally, even repeated mild trauma (strains $< 5\%$) has been shown to cause a TTX-sensitive increase in intracellular calcium levels [321], further indicating a direct effect of cell stretch on ion channel dynamics.

The forces regulating ion channel gating originate from the surrounding lipid membrane, suggesting a close relationship between membrane mechanics and ion channel function [287]. For example, membrane stiffening by stomatin-like protein-3 has been shown

to finely control mechanically gated ion channel activity in sensory neurons [288]. This is not limited to mechanosensitive channels, as voltage- and ligand-gated channels have also been shown to be variably mechanosensitive [267, 265].

Voltage-activated sodium channels have been shown to respond to localised deformation, with a left-shift in channel I-V relations, leading to reduced inactivation potential, sodium leakage, and a reduced rate of action potential (AP) firing [234]. Sodium channel-1.5 current activation has been observed to follow faster dynamics under pipette-suction deformation [322], and a left-shift in peak current and reversal potential have been shown [323]. Sodium channel activity, required for AP initiation, has been shown to depend on the mechanical state of the lipid bilayer, altered by amphiphilic treatment or cholesterol addition [290]. Voltage-gated potassium channels, required for repolarisation during AP firing, are also known to respond to mechanical stimuli, and their gating has been associated with the cell membrane's mechanical state [276, 324]. These results point to a close relationship between the mechanical environment of the cell membrane and ion channel function, suggesting that macroscopic membrane strains such as those occurring *in vivo* during supraphysiological nerve elongation can cause alterations in ion channel activity leading to impaired nerve electrophysiology. In the PNS, injury has been shown to alter surface distribution of axonal potassium and sodium channels, further pointing to a vulnerability of ion channel homeostasis to mechanical deformation [325, 102].

The effect of stretch on ion channel populations has been principally investigated using localised membrane suction [276, 234, 322, 323]. Although this allows simultaneous deformation and ion current recording, it does not closely replicate strains occurring in nerves *in vivo*.

The aim of this study was to investigate the effects of uniaxial strains on single cell electrophysiology in DRG-derived sensory neurons by whole-cell patch clamping, and to quantify changes in ion channel properties during straining. We achieved this by applying

strain macroscopically to the entire cell, and using whole-cell patch clamping on deformed cells to evaluate the immediate changes in ion channel and AP activity.

4.3.2 Materials and Methods

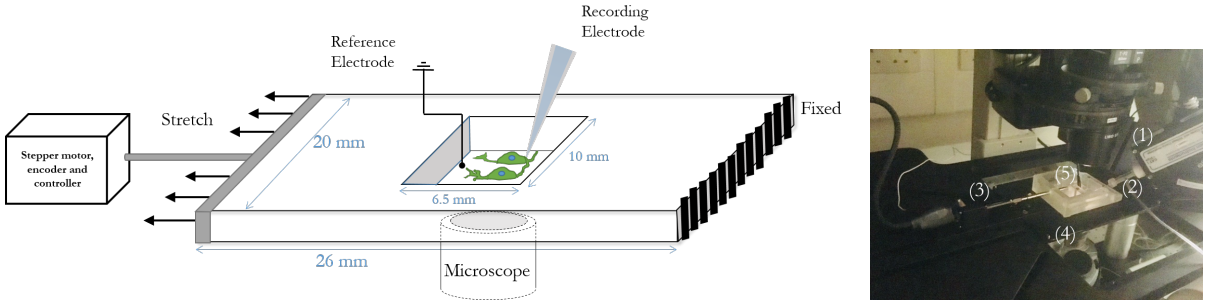
Cell Culture

F11 cells (ECACC, UK), a hybrid of rat neuroblastoma and primary DRG neurons commonly used as model peripheral sensory neurons [326], were chosen due to their well characterised AP firing and ease of culture [159, 248]. F11s were differentiated in high glucose dulbecco's modified eagle medium (ThermoFisher, UK), supplemented with 1% foetal bovine serum (ThermoFisher, UK), 1% penicillin/streptomycin , 0.5% insulin transferrin selenium (ThermoFisher, UK), 10 μM 3-isobutyl-1-methylxanthine (IBMX, Sigma-Aldrich, UK), 50 ng/ml nerve growth factor (Peprotech, UK), 2 μM retinoic acid (Sigma-Aldrich, UK) and 0.5 mM bromoadenosine 3,5-cyclic monophosphate. Cells were differentiated for 5 days prior to experiments.

Cell Stretching

Cells were deformed using a custom-built substrate stretching device (figure 4.2), delivering uniaxial strain to cells cultured on ultrathin (50-100 μm) polydimethylsiloxane (PDMS) substrates (Silex, UK), and allowing for simultaneous high-resolution microscopy and electrophysiological recording [Bianchi et al., 2018, under review]. F11 cells were seeded on deformable substrates at 5,000 cells/substrate to allow for cell proliferation during differentiation.

For patch clamping experiments, F11 cells were subjected to a 45% strain at 0.1 s^{-1} strain rate, and recordings were made either during strain, immediately after, or after 4 hours incubation at 37°C and 5% CO_2. Control recordings were taken from cells cultured on deformable membranes before strain to account for substrate material effects.



(a) (b)

Figure 4.8: Experimental setup for cell straining (a). Neurons cultured on deformable PDMS substrates as subjected to uniaxial strains, and single-cell activity is recorded simultaneously by whole-cell patch clamping, or network activity is measured by calcium imaging using an inverted fluorescence microscope. (b) Setup showing micromanipulator (1), micropipette (2), stepper motor and actuator rod (3), microscope stage and inverted objective (4) and deformable substrate and reference bath electrode (5).

Whole-Cell Patch Clamp Recording

The experimental setup for electrophysiological recording consisted of a digidata 1550A Digitizer and a MultiClamp 700B amplifier piloted through pCLAMP 10 Software (all from Molecular Devices, CA). Glass micropipettes were pulled from thin wall borosilicate capillary tubes (BF100-78-10, Sutter Instruments, CA), using a Flaming/Brown micropipette puller (Model P-1000, Sutter Instruments, CA), to a final resistance of 10 $\pm$ 1 MΩ. Pulling parameters were optimised according to previous work [250] in order to obtain the desired shape and surface properties of micropipettes. The intracellular solution contained: 140 mM KCl, 5 mM NaCl, 0.5 mM $CaCl_2$, 2 mM $MgCl_2$, 10 mM HEPES, 1 mM GTP, 2 mM ATP, with pH adjusted to 7.4 by addition of KOH and osmolarity adjusted to 300 $mOsml^{-1}$ by glucose addition. The bath solution contained: 130 mM NaCl, 5 mM KCl, 2 mM $CaCl_2$, 1 mM $MgCl_2$, 10 mM glucose, 10 mM HEPES, with pH adjusted to 7.4 by addition of NaOH and osmolarity adjusted to 300 $mOsml^{-1}$ by glucose addition.

Cells were chosen for patch clamping based on morphology, with selected cells displaying at least three processes and distinct pyramidal neuron-like somatas. Following establishment of whole-cell patches, only cells displaying both inwards and outwards cur-

rents were used for analysis. Cells were patched on unstretched deformable membranes (control), during an applied strain of 45%, immediately following stretch release, and after 4 hours recovery.

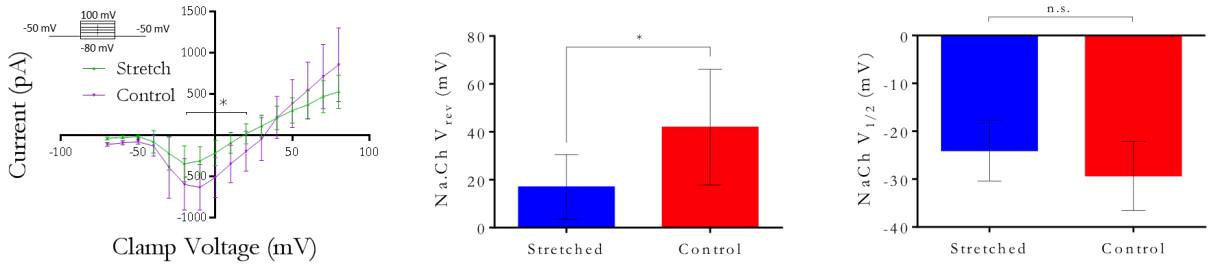
To evoke voltage dependent currents, cells were stimulated with a series of depolarizing pulses from -90 mV to +70 mV with a step size of 10 mV and currents were recorded in voltage clamp mode. APs were evoked in current clamp mode by a series of current pulses from -50 pA to +80 pA with a step size of 10 pA. Membrane resting potential (MRP) was measured upon breaking into whole cell mode with no current injection (I=0). Maximum channel conductance was measured as the slope of the linear section of the I-V curve, as measured from the reversal potential point V_r (V_r = V(I = 0)). Conductance (in nS) at each clamp voltage (V) was calculated as $G = (V - V_r)/I$, where I is the ion current (in pA) at each clamp voltage, and V_r the reversal potential (in mV). Conductance was plotted against clamp voltage, and fitted with a standard Boltzmann curve, from which half-maximal activation potential was calculated [283].

Statistical Analysis

Statistical analysis was carried out in PRISM v6 (Graphpad, USA). Data was tested for significance using paired or unpaired one-way ANOVA analysis with Tukey's multiple comparison, or by student t-test (paired statistics for data obtained from the same sample groups). All graphed data is reported as mean ± standard deviation, unless otherwise specified.

4.3.3 Results

To evaluate alterations in ion currents and AP firing, voltage and current clamp measurements were acquired from F11 cells subjected to 45% substrate strain. Peak inwards sodium currents and outwards rectifying potassium currents were plotted against clamp



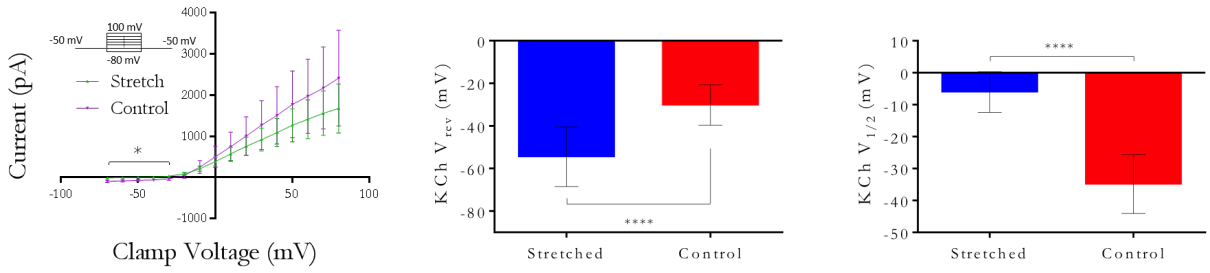
(a) (b) (c)

Figure 4.9: Whole-cell patch clamp of stretched and unstretched F11 neurons, showing sodium channel dynamics. (a) Inwards sodium peak I-V plots from voltage clamp recordings. * = $p < 0.05$ by unpaired t-test at each clamp voltage. (b) Reversal potential for stretched and unstretched cells. (c) Half-maximum activation potential for stretched and unstretched cells. n = 10 for stretched, n = 11 for control. n.s. = not significant. * = $p < 0.05$ by unpaired t-test.

voltage to produce peak I-V relations (figures 4.9a and 4.10a). A decrease in sodium current magnitude and a left-shift in reversal potential were found in stretched cells (figures 4.9a and 4.9b). Average maximum sodium channel conductance (slope of linear section of curves in figure 4.9a) was higher in control compared to stretched cells, and half maximum activation voltage was found not to be significantly changed (figure 4.9c). Potassium current magnitude was also decreased during stretch, with a left-shift in potassium reversal potential, and a lower maximum conductance compared to unstretched cells (figure 4.10a, 4.10b). Potassium channel half-maximum activation voltage was significantly right-shifted in stretched cells compared to control (figure 4.10c).

Membrane resting potentials (MRP), measured immediately after breaking into whole-cell configuration and in the absence of currents (I = 0), were not found to differ significantly between control and stretched cells, but were significantly depolarised four hours after stretch (figure 4.11c). Depolarisation was observed between cells cultured on deformable silicone membranes and on glass. Similar changes in MRP on different substrate stiffness have been reported [327].

Current clamp was used to induce AP firing in F11 neurons. Stretched and unstretched cells displaying both inwards and outwards currents were induced to fire APs by incre-



(a) (b) (c)

Figure 4.10: Whole-cell patch clamp of stretched and unstretched F11 neurons, showing potassium channel dynamics. (a) Inwards potassium peak I-V plots from voltage clamp recordings. * = $p < 0.05$ by unpaired t-test at each clamp voltage. (b) Reversal potential for stretched and unstretched cells. (c) Half-maximum activation potential for stretched and unstretched cells. n = 10 for stretched, n = 11 for control. **** = $p < 0.0001$ by unpaired t-test.

mentally increasing the clamp current magnitude (figure 4.11a). Average AP threshold current (the current clamp level needed to initiate AP firing) was significantly smaller in unstretched cells compared to stretched cells (figure 4.11b).

4.3.4 Discussion

The aim of this study was to investigate the effects of uniaxial strains on single cell electrophysiology in sensory neurons. Ion channels, which regulate inwards and outwards flux of ions in neurons are embedded in the cell membrane that is known to undergo high strains during cell deformation. Changes in the membrane mechanical environment may in turn alter the function of ion channels, leading to aberrant activity.

To evaluate changes in ion channel function during stretch, current and voltage responses of F11 DRG-like neurons were recorded in whole-cell patch clamp. To the best of our knowledge, the experiments reported here are the first patch clamping measurements of neurons *during* strain applied by substrate deformation. Previous work on the effect of mechanical deformation on ion channels used pipette suction to apply stretch to a membrane patch [276, 234, 322, 323]. This methods applies an uneven deformation, creating stress concentrations at the contact between pipette walls and cell, and providing impre-

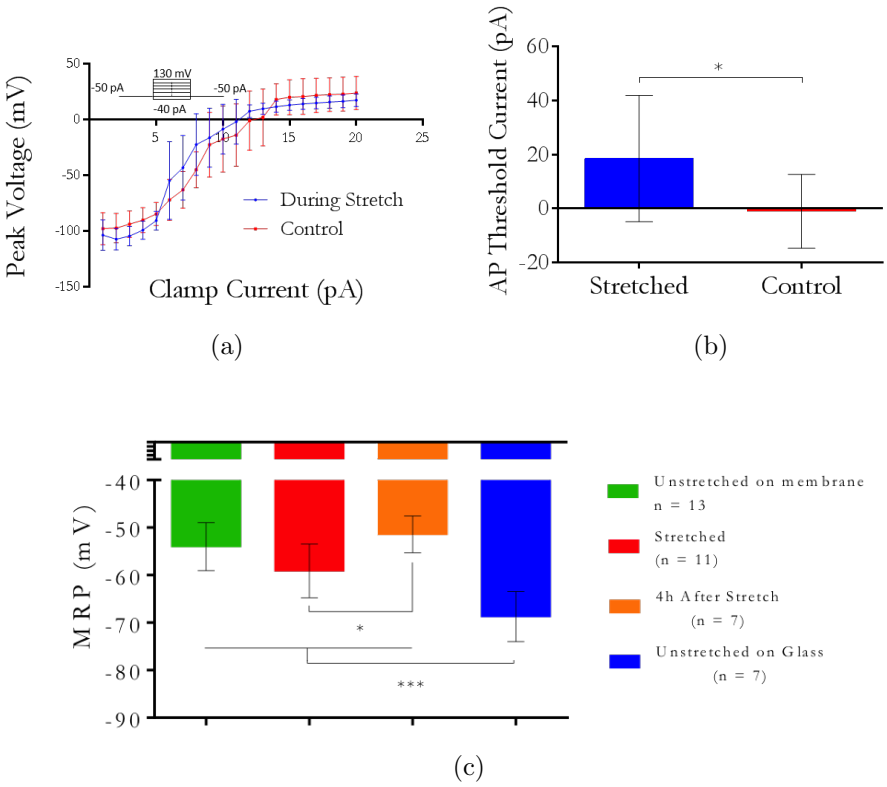


Figure 4.11: (a) Relation between peak membrane potential magnitude during AP firing and clamp current. (b) Comparison of threshold current for induced AP firing. n = 10 for stretch, n = 11 for control. * = $p < 0.05$ by unpaired t-test. (c) Membrane resting potentials (MRP) of cells subject to 45% substrate strain. MRPs were measured upon breaking into whole-cell clamp, for control (unstretched) conditions, for cells during deformation, and after 4 hours incubation following deformation. MRP of unstretched (control) cells on glass to show substrate material effect. *** = $p < 0.001$, * = $p < 0.05$ by unpaired t-test (b) and one-way unpaired ANOVA with Tukey's multiple comparisons (c).

cise control over stretch parameters. Furthermore, recent work (in preparation) indicates that the observed 'left-shift' in ion current dynamics is not related to ion channel damage [328]. By recording whole-cell patch clamping *during* whole-cell stretch we apply a repeatable, fully characterised strain field to a population of cells, which we believe is a closer representation of *in vivo* stretch conditions during traumatic injury or supraphysiological nerve extension.

MRP was not significantly different during stretch compared to unstretched controls, although a hyperpolarisation trend was observed (figure 4.11c). Four hours post-stretch, MRP was significantly depolarised compared to during stretch. Delayed depolarisation

has been shown to be a secondary effect of stretch [253], caused by calcium influx [329]. We show that *during* stretch, neurons are hyperpolarised, becoming depolarised only after stretch release and incubation. A similar transient hyperpolarisation followed by delayed calcium-mediated depolarisation has been reported in hypoxic neurons, where hyperpolarisation by opening of potassium channels is proposed to prevent excitotoxicity [330]. Stretch may therefore similarly cause alterations in ion channel activity causing immediate protective hyperpolarisation, further supported by the increased current threshold for AP initiation in strained cells (figure 4.11a).

Stretched cells retained the ability to fire induced APs under current clamp, indicating that damage due to acute stretch did not entirely impair AP firing. Although no differences were observed in AP peak magnitude, the current required to initialise firing was significantly larger in strained cells in comparison to control cells (figure 4.11a). This indicates neural hypoexcitability similar to that observed in anaesthetised nerves, where a decrease in postsynaptic excitability suppresses neural activity [331]. If stretch similarly subdues individual neuron excitability, this would in turn affect the activity of the underlying network as a whole, potentially leading to conduction blocks and impaired sensory function, explaining the decrease in compound action potential observed in strained nerves [25].

Inwards sodium and outwards potassium currents are both required for AP firing. We recorded ion currents from cells subject to 45% strain, and compared them with unstrained control cells. Peak magnitudes for both sodium and potassium currents were smaller in stretched cells, compared to control (figures 4.9a and 4.10a). Current reversal potentials, defined as the clamp voltage where ion current equals zero, were significantly hyperpolarised in stretched cells (figures 4.10b and 4.9b). Half-maximal activation potential ($V_{1/2}$) was less negative in both sodium and potassium channels (figure 4.10c and 4.9c). A depolarised $V_{1/2}$ value is consistent with the measured increase in AP initiation

threshold current, as a larger change in membrane potential would be needed in strained cells to achieve the same conductance (i.e. number of open channels) as in control cells.

Excessive strain may alter ion currents by damaging voltage-sensing mechanisms in ion channels, permanently or reversibly inhibiting the gating charge movement that regulates channel opening and closing. Strain may also alter the properties of the lipid membrane, in turn altering the function of ion channels. Treatment of membranes with nonionic surfactants Triton X-100 and *beta* octyl glucoside has been shown to inhibit current flow in sodium channels [287], bilayer fluidisation has been linked to altered voltage-gated ion channel function [332], and anaesthetics such as Ketamine have been shown to modulate ion channel activity by altering the lateral pressure profile of the lipid membrane [278]. From first principles, the Boltzmann equation relates channel conductance (and therefore channel 'open' configuration probability) to the energy required to move the gating charges of ion channels from the intracellular membrane side (closed configuration) to the extracellular membrane side (open configuration) [23]. The movement of gating charges has also been shown to induce a deformation in the surrounding bilayer, demonstrating the mechanical coupling between the two [333]. Therefore changes in conductance, half-maximum activation voltages and altered peak I-V relations can be explained if changes in membrane mechanical properties due to stretch make the transition between closed and open less energetically viable.

Overall, these results indicate an intimate relationship between ion channels and the mechanical state of the surrounding lipid membrane, suggesting that large mechanical strains cause direct, immediate damage to transmembrane proteins regulating ion flows and AP propagation, causing conduction blocks in peripheral nerves.

4.3.5 Conclusions and Limitations

The aim of this study was to investigate changes in electrophysiological properties at the single-cell scale in neurons subject to mechanical stretch.

Our results show that neurons undergo immediate hyperpolarisation during stretch and concurrent ion channel function impairment, resulting in lower peak ion currents and depolarised activation curves and leading to higher threshold current for AP initiation. These results can help understand the onset of conduction blocks, and can be used to inform computational models of the coupling between electrophysiological function and nerve deformation.

In summary, we have shown that ion currents and AP firing is altered in strained F11 cells. This can help understand the onset of nerve conduction blocks, impacting preventive and treatment strategies for mechanical trauma. Voltage-gated ion channels have been recently proposed as novel targets for neuropathic pain therapy [279], and a better understanding of their association with the neural membrane mechanics can aid the development of therapies.

Limitations of this Study

The mechanical parameters tested were not an extensive representation of injury. Evaluating the effect of different strain rates, as well as smaller strain increments, would provide more information about injury mechanisms.

A challenge of working with sensory neurons, rather than with modified cells expressing single ion channel populations, was that the response of individual types of ion channels cannot be isolated. In our experiments, we did not therefore differentiate ion channel sub-classes, but instead analysed the average behaviour of inwards and outwards voltage-

gated ion currents from neural membranes, capturing the whole-cell electrophysiological behaviour and more closely resembling *in vivo* conditions of nerve stretch.

4.3.6 Acknowledgements

Authors acknowledge China Regenerative Medicine Limited (CRMI) for funding and the EPSRC DTP award number 1514540 for F.B. funding. M.B. and A.J. acknowledge funding from the European Union's Seventh Framework Programme (FP7 20072013) ERC Grant Agreement No. 306587.

4.4 Chapter Summary

The work presented in this chapter aimed at linking the deformation of cultured neurons with changes in cell function, investigating the changes in network and single-cell electrophysiology during strain using the uniaxial strain device presented in chapter three.

Compared to previously published work, the results presented here show electrophysiological measurements of neurons *during* strain application, a more representative method to investigate neural traumatic injury compared to localised membrane stretch by pipette suction. These results can help understand the immediate effects of traumatic conduction blocks, impacting preventive and treatment strategies for mechanical neural trauma. Furthermore, understanding the link between mechanical input and electrical output in neurons can help inform computational models of peripheral nerve injury that can be applied to investigate further loading conditions and to optimise the design of tissue engineered nerve replacements.

Statement of Authorship for joint/multi-authored papers for PGR thesis

To appear at the end of each thesis chapter submitted as an article/paper

The statement shall describe the candidate's and co-authors' independent research contributions in the thesis publications. For each publication there should exist a complete statement that is to be filled out and signed by the candidate and supervisor

Title of Paper	Membrane mechanical properties regulate the effect of strain on network electrophysiology in iPSC-derived neurons
Publication Status	☐ Published ☐ Accepted for Publication ☑ Submitted for Publication ☐ Unpublished and unsubmitted work written in a manuscript style
Publication Details	Submitted to Journal of Neuroscience, August 2018.

Main Author

Name of Principal Author (Candidate)	Fabio Bianchi		
Contribution to the Paper	Planned and designed experiments, carried out experiments, carried out analysis (unless specified), wrote manuscript		
Signature		Date	06/08/2018

Co-Author Contributions

Name of Co-Author	Dr. Julian H. George
Contribution to the Paper	Reviewed manuscript

Name of Co-Author	Valerio Pereno
Contribution to the Paper	Helped carry out c-Laurdan imaging experiments, reviewed manuscript

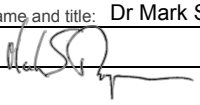
Name of Co-Author	Dr. Mark S. Thompson / Dr. Hua (Cathy) Ye
Contribution to the Paper	Supervised work, reviewed manuscript

Name of Co-Author	
Contribution to the Paper	

Please cut and paste additional co-author panels here as required.

Supervisor Confirmation

By signing the Statement of Authorship, you are certifying that the candidate made a substantial contribution to the publication, and that the description described above is accurate.

Supervisor name and title:	Dr Mark S Thompson		
Signature		Date	09/08/18

This completed form should be included in the thesis, at the end of the relevant chapter.

Statement of Authorship for joint/multi-authored papers for PGR thesis

To appear at the end of each thesis chapter submitted as an article/paper

The statement shall describe the candidate's and co-authors' independent research contributions in the thesis publications. For each publication there should exist a complete statement that is to be filled out and signed by the candidate and supervisor

Title of Paper	Ionic current and Action Potential alterations in peripheral neurons subject to uniaxial strain
Publication Status	☐ Published ☐ Accepted for Publication ☑ Submitted for Publication ☐ Unpublished and unsubmitted work written in a manuscript style
Publication Details	Submitted to Neuroscience Letters, August 2018.

Main Author

Name of Principal Author (Candidate)	Fabio Bianchi		
Contribution to the Paper	Planned and designed experiments, carried out experiments, carried out analysis (unless specified), wrote manuscript		
Signature		Date	06/08/2018

Co-Author Contributions

Name of Co-Author	Dr. Majid Malboubi
Contribution to the Paper	Helped with patch-clamping experiments, reviewed manuscript

Name of Co-Author	Dr. Julian H. George
Contribution to the Paper	Reviewed manuscript

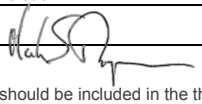
Name of Co-Author	Dr. Antoine Jerusalem
Contribution to the Paper	Reviewed manuscript

Name of Co-Author	Dr. Mark S. Thompson / Dr. Hua (Cathy) Ye
Contribution to the Paper	Supervised work, reviewed manuscript

Please cut and paste additional co-author panels here as required.

Supervisor Confirmation

By signing the Statement of Authorship, you are certifying that the candidate made a substantial contribution to the publication, and that the description described above is accurate.

Supervisor name and title:	Dr Mark S Thompson		
Signature		Date	09/08/2018

This completed form should be included in the thesis, at the end of the relevant chapter.

CHAPTER 5

Future Work: Towards A Full *In Vitro* PNS Stretch Model

Building upon the results shown in chapters three and four, this chapter explores the use of SC-like cells differentiated from mesenchymal stem cells to model the peripheral nerve environment, integrated with the *in vitro* uniaxial strain device with the aim of providing a physiological model of stretch deformation in myelinated co-cultures.

5.1 Introduction

In order to extend the results presented in this thesis with the aim of creating a platform for the experimental study of mechanical effects on peripheral nerve, and to provide comprehensive data to inform a computational model of peripheral nerve stretch, the current model needs to be extended.

A full PNS model should include three elements: neural cells, myelinating Schwann cells (SCs), and an underlying structure inducing cell alignment and providing physical support. The simplest existing models use explanted embryonic dorsal root ganglions (DRGs) from rat or mouse, which contain sensory neurons and meylinating SCs and extend neurites rapidly. However, explanted DRGs do not allow control over the number of cells, the mechanical environment, and do not allow direct access to individual cells for electrophysiology. Co-cultures of primary neurons and SCs on aligned fibres [66] or in 3D collagen gels [67] provide oriented, myelinated systems that impressively replicate PNS structure, but are difficult to implement in mechanical deformation experiments. 'Nerve on a chip' devices have recently been developed, providing small scale organotypic models of peripheral nerve with the aim of replacing animal models in drug testing and nerve regeneration studies, but cannot be applied to studies of mechanical damage due to their enclosed nature [334, 335].

The model presented in chapter three of this thesis provides a flexible platform to study the effect of variable mechanical loading on cultured peripheral neurons. Increasing the complexity of the culture model by introducing myelinating cells would provide further information about the effects of stretch on peripheral nerves, including direct effects on the myelin sheath and on Schwann cells, as well as a differentiation between myelinated and unmyelinated nerve fibres. The aim of this chapter is to introduce preliminary work aimed at developing a myelinating co-culture model based on human induced pluripotent stem cell-derived neurons and primary or mesenchymal stem cell-derived Schwann cells grown on deformable substrates with aligned microgrooves, for the study of mechanical disruption and subsequent regeneration of peripheral nerve.

5.2 *In Vitro* Myelination

The myelin sheath is the most important non-neural cellular component in the peripheral nerve. It allows high-speed saltatory conduction, establishes cues for re-growth during regeneration, and provides physical support to axons. Bands of Büngner, formed by aligned SCs after neural damage, provide topographical guidance for neurons to extend growth cones. In PNS models, microfibres, neurotrophic factor gradients, and aligned collagen gels have previously been used to replicate structures resembling bands of Büngner, with the aim of producing regenerative materials [336, 67], but do not integrate with existing models of stretch.

In vitro dissociated cell myelination models rely on co-cultures of neurons and SCs, most commonly isolated from rat or mouse peripheral nerve biopsies. When co-cultured with primary neurons, SCs will only associate with axons when growth medium is supplemented with ascorbic acid, which promotes basal lamina formation and myelin production [337]. The use of autologous SCs for nerve regeneration and PNS modelling is however impractical, as they require lengthy protocols for isolation and purification, and entail high donor site morbidity.

A growing interest exists towards using mesenchymal stem cell-derived 'Schwann-like cells' (SlCs) to myelinate axons and promote neural regeneration [338]. Xenoculture studies have show that human iPSC-derived neurons can be myelinated by rat SCs, and that rat primary neurons can be myelinated by human MSC- and iPSC-derived SCs, suggesting that myelination mechanisms are conserved between species [209, 339]. However, co-cultures of stem cell derived neurons and stem cell derived Schwann cells have only been achieved in rat models, never in humans [340].

Pluripotent stem cells can be differentiated to SlCs by treatment with transforming growth factor-β (TGF-β) and GSK-3 inhibitors to induce neural crest stem cells (NCSC),

followed by neregulin-1 treatment resulting in SlCs capable of producing neurotrophic factors (BDNF, NGF, NT-3, and GDNF) and of myelinating axons when co-cultured with neurons [339]. Human and rodent adipose [341], bone marrow [342], and dental pulp [343] mesenchymal stem cells have all been differentiated to SlCs using both adherent and neurosphere culture protocols [344]. Adipose tissue, with higher stem-cell fraction and lowest associated donor site morbidity, represent the most promising clinical source of cells for SlC differentiation [345]. Despite this, *in vitro* de-differentiation is observed rapidly after withdrawal of key growth factors, suggesting that MSC myelination models may be unsuitable for long-term co-cultures, and better suited for short-term applications such as modelling of mechanical trauma [346].

Here, human and rat MSCs were differentiated to SlCs using two methods; an adherent and a neurosphere protocol. MSCs were characterised by FACS surface marker expression. Differentiated SlCs were characterised by immunocytotochemistry, and co-cultured with primary and iPSC-derived neurons. These results are the starting point towards integrating a neuron-SC co-culture system with the stretching device and experimental protocols presented in chapters three and four.

5.2.1 Materials, Methods and Preliminary Results

Isolation of Primary Schwann Cells and Neurons

Primary Schwann cells were isolated from the sciatic nerves of 300-350 g (10-12 week old) male Sprague-Dawley rats sacrificed for an unrelated study. Nerves were stripped of the epineurium, cut into 2 mm-long sections, and enzymatically digested in 0.05% (w/v) collagenase (Sigma Aldrich) for 30 minutes at 37°C, followed by two rinses in phosphate buffered saline (PBS, ThermoFisher) and 10 minutes digestion in Trypsin/EDTA (Sigma-Aldrich) at 37°C. Following centrifugation, the supernatant was discarded, and the remaining cell pellet re-suspended in warm dulbecco's modified eagle medium (DMEM,

Sigma-Aldrich) supplemented with 10% foetal bovine serum (FBS, ThermoFisher) and 1% penicillin/streptomycin (P/S, ThermoFisher), and plated on poly-L-ornithine (PLO, Sigma-Aldrich) coated tissue culture plates and/or flasks. Purification was carried out by a 2-day cycle of cytosine arabinoside (ARA-C, Sigma Aldrich) at 1μM concentration in culture medium.

Primary neurons were isolated from embryonic mouse spinal cords. 14.5 day pregnant mice were sacrificed by cervical dislocation and the embryos removed through an abdominal incision. All animals were euthanised by a Schedule 1 method (cervical dislocation for adults, decapitation for embryos) as described under ASPA. The person performing Schedule 1 was certified as competent by the Named Animal Care and Welfare Officer (NACWO), Department of Biomedical Sciences, University of Oxford.

Embryos were decapitated under a dissection microscope on ice, the caudal end of the embryo cleaned of connective tissues and red organs, and the spinal cord exposed. Spinal cord matter and dorsal root ganglia were collected in ice-cold leibovitz-15 medium (Sigma Aldrich). Cells were then isolated by Trypsin/EDTA incubation of tissues at 37°C for 25 minutes with gentle agitation every 5 minutes. The resulting suspension was centrifuged for 5 minutes at 500 $\times$ g, after which the supernatant was discarded and the resulting pellet re-suspended and plated on PLO and laminin or matrigel coated plates. Cells were cultured in neural maintenance medium, consisting of a 50% DMEM:F12 medium (ThermoFisher) and 50% neural basal medium (NBM, ThermoFisher) supplemented with 1% P/S, 0.5 % N2 neural supplement (ThermoFisher), 1% B27 serum-free neural supplement (ThermoFisher), 50 ng/ml brain derived neurotrophic factor (BDNF, Peprotech) and 10 ng/ml neural growth factor-β (NGF-β, Peprotech).

Immunocytochemical staining was performed to evaluate phenotype of isolated primary cells. Monolayers were fixed in 4% paraformaldehyde (PFA, Sigma-Aldrich) for 20 minutes at 4°C, followed by blocking and permeabilisation for 30 minutes at 37°C

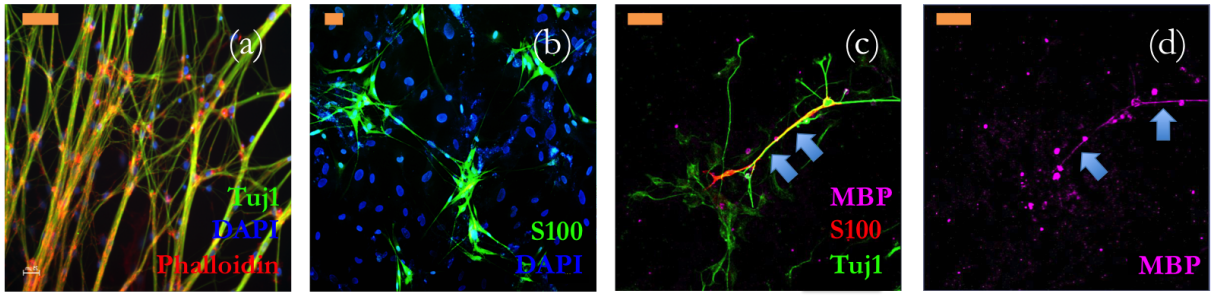


Figure 5.1: Characterisation of primary cells for myelination assays. (a) Primary embryonic mouse neurons, (b) Primary adult rat Schwann cells, (c) Myelinated co-culture of primary neurons and Schwann cells. Arrows show co-localisation of neurons and Schwann Cells (d) Myelin base protein stain only, arrows showing myelin co-localised with neural extensions. Scale bars = 50 μm

in 0.1% tritonX-100, 0.1% tween-20 and 0.5% bovine serum albumen (all from Sigma-Aldrich) in PBS. Cells were then washed thoroughly in PBS, and incubated overnight in primary antibody solution, followed by three PBS washes, and a further four hour incubation in secondary antibody solution. For SC characterisation, S100 and P75-low affinity nerve growth factor receptor (P75-LANGFR) were used (both from AbCam, used at 1:500 concentration), and for neuron characterisation, Tuj1 (β-III tubulin, AbCam, at 1:500 concentration) was used. In myelinating co-cultures, S100 and Tuj1 stains were combined with myelin basic protein, a protein making up 5-18% of PNS myelin contents (MBP, AbCam, used at 1:250 concentration). In all cases, cultures were counter-stained with nucblue (2 drops/ml) or DAPI (10 μg/ml) for nuclei.

Primary Cell Myelination Assay

Primary neurons and SCs were co-cultured in neural maintenance medium, at a ratio of 1:1. Initially, cells attach and grow separately, with little interaction. Addition of 50 ng/ml L-ascorbic acid (L-AA, Sigma-Aldrich) at day five in culture initiated elongation of SCs along neural axons and myelination. After 14 days (9 after start of L-AA addition), co-cultures showed co-localisation of SCs and neurons and positive myelin base protein expression, indicating successful myelination (figure 5.1, (C) and (D)).

Isolation and Characterisation of Adipose-Derived Stem Cells (ADSCs)

Adipose inguinal pads were dissected from 300-350 g (10-12 week old) male Sprague-Dawley rats sacrificed for an unrelated study, within four hours of euthanisation. Adipose tissues were finely minced using sterile scalpels, washed in PBS, and digested for 75 minutes 37°C in 0.15% collagenase solution in PBS with mechanical agitation. The resulting liquid was filtered through a 70 μm mesh, and centrifuged at 800 $\times$ g resulting in a hematopeic cell fraction distinctly layered above a cell pellet. The hematopeic layer was discarded, and the pellet washed for 5 minutes in 160 mM ammonium chloride to lyse remaining erythrocytes. Following further 5 minute centrifugation the cell pellet was re-suspended in DMEM supplemented with 10% FBS and 1% P/S, and plated on tissue culture treated plastic plates. ADSCs were differentiated within 8 passages post isolation, or cryopreserved in expansion medium supplemented with 10% dimethylsulfoxide (DMSO, Simga-Aldrich).

ADSC multi-potency was evaluated by fluorescence-activated cell sorting (FACS), using stained cell suspensions passing through multi-wavelength lasers for high-throughput phenotyping. Cell suspension was prepared by monolayer trypsinisation and adjusted to 100'000 cells/ml in PBS supplemented with 0.2% BSA. Cells were then fixed in 2% PFA for 5 minutes at 4°C and incubated for 10 minutes at 4°C in a 1:10 dilution of fluorophore-conjugated antibodies in PBS-BSA. A total of six antibodies were tested, three positive and three negative (all from Miltenyi biotech). Positive antibodies included CD29-FITC, CD44-PE and CD90-APC, and negative antibodies included CD45-FITC, CD106-PE and CD31-APC, as previously characterised in literature [344].

FACS was performed on a BD LSR II flow cytometer, configured with three laser lines (FITC, PE, APC) on both freshly isolated and freeze-thawed cells to evaluate stem cell quality before and after cryopreservation. Results showed strong positive marker expression and negligible negative marker expression, confirming multipotent phenotype

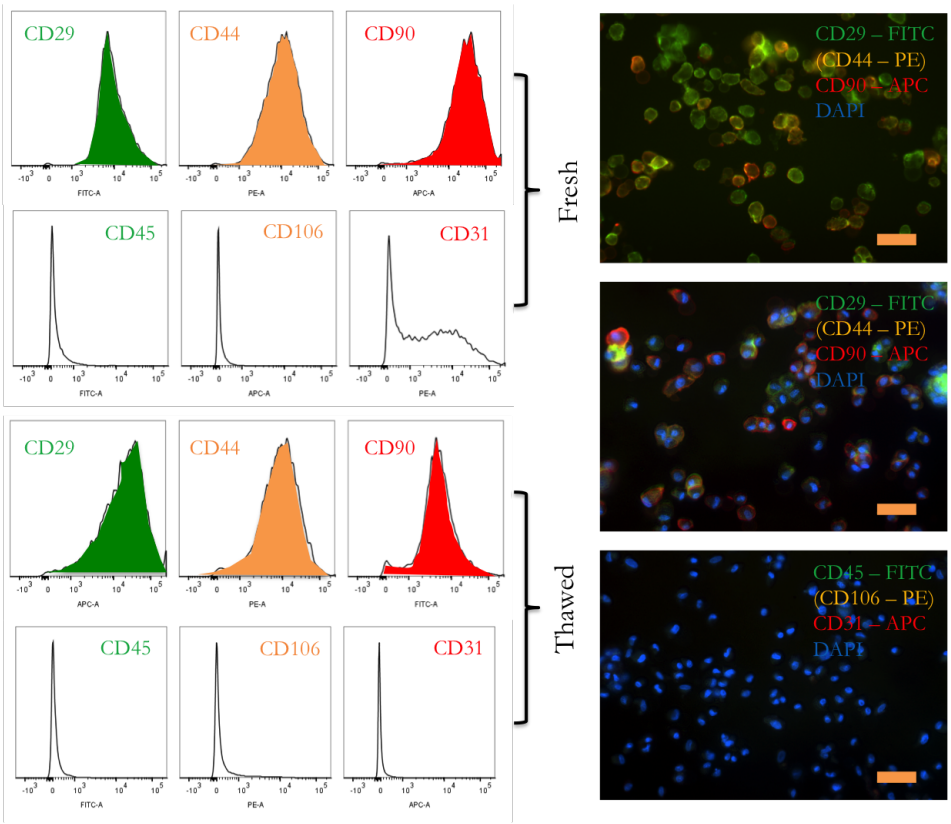


Figure 5.2: Flow cytometry characterisation of ADSC multipotency markers, for freshly isolated cells and frozen/thawed cells. Y-axis represents number of events (cell count), and x-axis represents fluorescence. Colours (manually added) represent different laser lines. Micrographs show visual confirmation of positive and negative staining. Scale bar = 50 μm

and purity for both fresh and cryopreserved cells (figure 5.2). Positive assay showed peaks at high fluorescence representing large populations expressing the required surface marker. Negative assay showed peak at low fluorescence indicating unlabelled cells. Results were visually confirmed by fluorescence microscopy, showing positive expression in DAPI-counterstained samples and no fluorescence signal in negative samples (figure 5.2 micrographs).

Schwann-Like Cell Differentiation of Mesenchymal Stem Cells

Two kinds of stem cells were used for differentiation: primary rat adipose-derived stem cells and human GFP-expressing, HTERT-immortalised mesenchymal stem cell (kindly

donated by Dr. James Li, Hong Kong University). MSCs were differentiated to Schwann-like cells (SlCs) using two methods: adherent monolayer culture or neurosphere differentiation.

In adherent cultures, cells were differentiated at 60% confluency. Firstly, 1 mM β-mercaptethanol (Sigma-Aldrich) was added in culture medium for 24 hours pre-differentiation to reduce the risk of cell death from oxidative stress. MSCs were then differentiated by addition of 350 ng/ml retinoic acid (RA, Sigma Aldrich) for 72 hours, with daily medium changes. Subsequently, cells were washed in PBS, and cultured in SC-differentiation medium, consisting of DMEM supplemented with 1% P/S, 10% FBS, 14 uM forskolin (Sigma Aldrich), 5 ng/ml platelet derived growth factor (PDGF, Peprotech), 10 ng/ml fibroblast growth factor-β (bFGF, Peprotech) and 200 ng/ml heregulin β-1 (HRGβ-1, Peprotech) with complete medium changes every 48 hours for 8 days.

For neurosphere cultures, cells were dissociated and resuspended in NBM supplemented with 2% B27, 1% N2, 10 ng/ml bFGF, 10 ng/ml epidermal growth factor (EGF, Peprotech), 14 uM forskolin and 200 ng/ml HRG-β1, and seeded at high density on non-treated suspension culture well plates. Neurospheres were kept in culture for 8 days with medium replaced every 48 hours. After differentiation, neurospheres were dissociated by addition of accutase (StemCell Technologies) for 10 minutes at room temperature, and re-plated on PLO-coated tissue culture plastic in SC-differentiation medium.

Schwann-like cells were characterised by expression of S100, P75-LANGFR and nestin, three commonly used markers for Schwann cell detection [344, 347]. Neurospheres were stained both pre- and post-dissociation, and were immunopositive to S100 and nestin in both cases, with high differentiation efficiency.

Adherent MSCs from both rat and human were stained for S100 and P75-LANGFR. A higher differentiation efficiency was observed in human MSCs, compared with primary rat ADSCs (figure 5.3, (D) to (I)), although in both cases the number of cells expressing

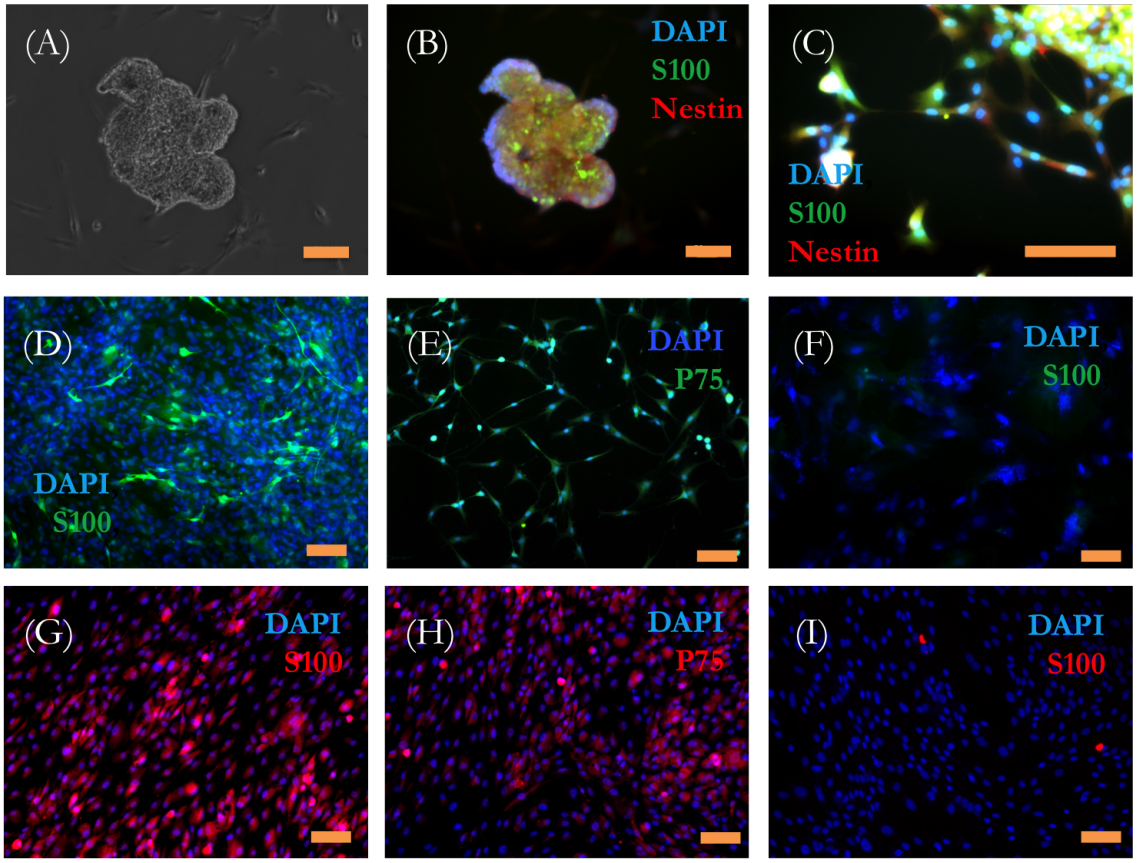


Figure 5.3: Differentiation of rat ADSC (A-F) and human MSC (G-I) to Schwann-like cells, following neurosphere (A-C) and adherent (D-I) differentiation protocols. (A) Phase contrast imaging of neurosphere before dissociation. (B) Staining of neurosphere after 8 days differentiation, before dissociation, showing expression of S100 and nestin. (C) Dissociated neurosphere cells, expressing S100 and nestin. (D) Differentiated SlCs, showing partial expression of S100 and (E) P75-LANGFR. (F) Control, undifferentiated ADSCs, showing no expression of S100. (G) SlCs expressing S100 and (H) P75-LANGFR. (I) Control, undifferentiated MSCs, showing no S100 expression. Scale bars = 100 μm

S100 was qualitatively comparable to primary Schwann cell cultures established from rat sciatic nerve (figure 5.1 b).

5.2.2 ADSC-SC Co-Culture with Primary Neurons

SC-differentiated ADSCs were co-cultured with primary neurons in neural maintenance medium to evaluate the effect on neurite extension. Neurite outgrowth quantification was performed using HCA-Vision, and includes all visible neurites. Average neurite out-

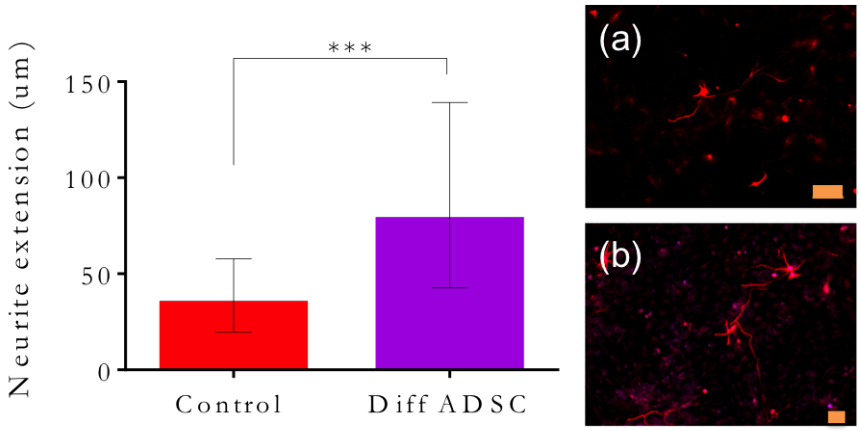


Figure 5.4: Neurite extension for primary neurons co-cultured with undifferentiated (A) and differentiated (B) ADSCs. N = 6, > 20 cells/N, for each condition. *** = P < 0.01 by unpaired t-test. Bars show median, error bars show IQ range. Scale bars = 100 μm

growth was significantly higher for neurons co-cultured with differentiated cells compared to undifferentiated (figure 5.4).

Significantly longer neurites suggest that differentiated ADSCs support and stimulate neurons to extend further, as previously reported in literature [348]. Increased neurite extension could be due to secretion of neurotrophic factors BDNF, NGF and GDNF by differentiated MSCs [341], or to topographical guidance alone, which has been shown to play a key role in neurite alignment and extension [349].

5.2.3 SlC Culture on Aligned Grooves

In order to test the feasibility of PNS modelling with MSC-derived SlCs, cells were cultured on aligned microgrooved surfaces, prepared as previously described in section 3.5.2. GFP-expressing cells localise in grooves, and align with the direction of the grooves, forming bands of higher cell concentration in the same direction as the underlying patterned surface (figure 5.5). Topographically, the aim was to replicate an environment akin to that of Bands on Büngner, in order to promote aligned neurite extension.

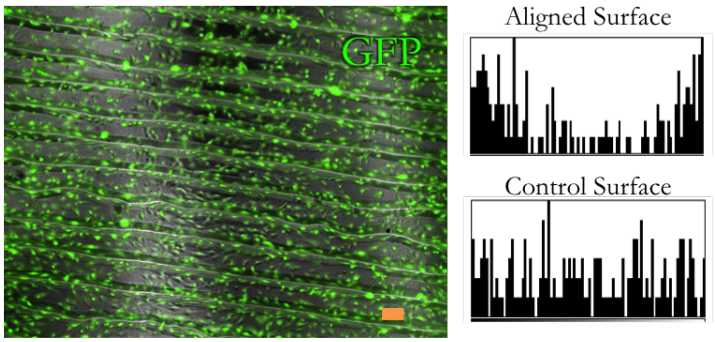


Figure 5.5: GFP-expressing MSCs respond to microgrooved surfaces, forming aligned bands. Histograms show distribution of cell angles with respect to the horizontal, for aligned and non-aligned surfaces. Scale Bars = 200 μm

5.3 Chapter Summary and Future Work

A fully characterised *in vitro* PNS surrogate must show propagation of action potentials from neurons, correct expression of myelin proteins from SCs, and take into account the mechanical properties of the PNS tissue it aims to replicate. As discussed in chapter two of this thesis, the mechanical environment of peripheral nerve is fundamental to determine the functionality of cells within, and needs to be considered and reproduced in *in vitro* designs. Current development of peripheral nerve models for the *in vitro* study of mechanically-induced alterations is lacking. 3D tissue models in collagen gel materials providing aligned, growth-permissive environments for both Schwann cells and neurons to extend in parallel [67, 336] have achieved remarkable structural similarities to native tissue. These models have been tested with adipose and neural pulp stem-cell derived SCs [350, 343], but having originally been designed as materials for nerve conduits [67] and later become engineered neural tissue [350], integrating these tissue constructs with a model of mechanical deformation would be challenging. The proposed model of 2-D monolayer co-culture on aligned microgrooves directly patterned onto a deformable substrate would allow the model tissue to be grown directly onto a model of mechanical deformation.

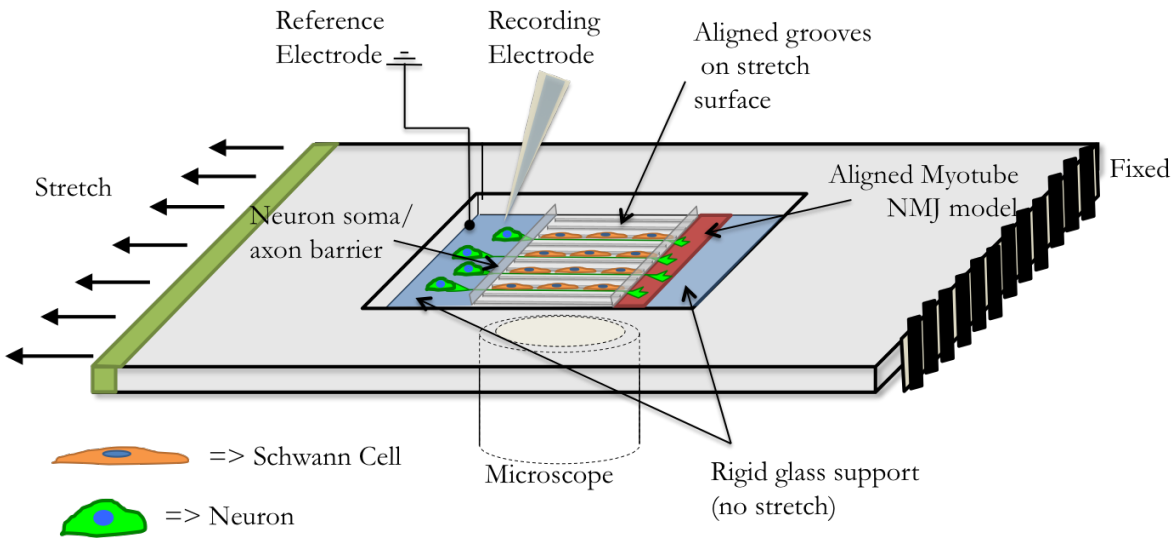


Figure 5.6: Towards a full PNS model of mechanical damage. Integrating the previously developed NMJ model [351] with the stretching device and microgrooved surfaces shown in chapter 3, and using cells described in chapters 3 and 5 would result in a myelinated, aligned PNS model to study the effcts of mechanical stretch on peripheral nerve function.

In future work, the aligned microgroove stretch model presented in chapter three will be combined with the stem-cell co-cultures presented in this chapter, with the aim of producing a myelinated and aligned tissue model allowing experimental investigation of neuronal and Schwann cell behaviour during uniaxial tensile deformation. Full characterisation of the model should include proof of myelin sheath formation, by immunocytochemical staining as well as transmitted electron microscopy (TEM) of osmium tetroxide-stained sections [352]. Neural activity within the tissue model should also be shown, thus requiring the use of electrophysiologically active neural cells. Using iPSCs as the base for neural differentiation allows for multiple neural phenotypes to be combined within the modes, to further replicate the combination of motor and sensory fibres found in human PNS tissues. For both neurons ad SCs, differentiated stem cells populations can be purified by flow sorting, immunopanning or magnetic sorting, in order to finely control the proportion of cell types included in the co-culture,

Separation between neural cell bodies and axons could also be included, to allow cell bodies and axons to be subjected to different strains. This can be achieved using compartmentalised culture models, such as those used in nerve-on-chip devices [335], combined with substrates of different stiffnesses. A further extension would be the integration with a model of the neuromuscular junction (NMJ) to model the effects of stretch on the neuron-muscle association. A previously developed method for *in vitro* NMJ production [351], using engineered sheets of muscle tissue, could be integrated with the stretch model downstream of the axon compartment. The ultimate design for a future *in vitro* model of peripheral nerve stretch is shown diagrammatically in figure 5.6.

CHAPTER 6

Conclusions

6.1 Overview

Although reports of nerve damage span thousands of years, contemporary clinical data highlights how traumatic neuropathy is a common problem that imposes a burden on health services and dramatically affects patients' quality of life.

Current approaches to prevention, treatment, and repair of nerve damage would benefit from a better understanding of the multi-scale processes involved, from the macroscopic tissue level to the microscopic cellular level. The results presented in this thesis can contribute to this in two ways. Taken together, these results can provide the experimental data to construct a biomechanical-functional model of peripheral nerve stretch, similar to computational end-to-end models developed for brain injury [61]. Experimental results offer information about the effect of stretch at different length scales within peripheral nerves, providing experimental validation and calibration. A computation model can then

be used to model further loading regimes, and to aid the design of novel tissue engineering designs for nerve repair. Computational modelling has been previously been proposed as a method to streamline and facilitate the design of tissue engineered nerve replacement materials [353], and this notion can be extended to include the biomechanical properties of peripheral nerves based on experimental data. Individually, the results presented in each chapter can also be applied to more specific sub-sets of multi-scale peripheral nerve modelling.

Chapter two reported work using crystallography techniques and multi-photon imaging to probe the microscopic deformations within whole nerve tissues, to establish the mechanical relationship between nerve macro- and micro-mechanics. This work can help improve the design on novel biomaterials and tissue engineered solutions for nerve repair by providing novel information about the mechanical properties of nerve and connective tissues, which affect the regeneration capabilities of replacement materials.

Chapter three presented the development and characterisation of a human induced pluripotent stem cell derived motor neuron model of neural damage, and of a custom-built uniaxial strain experimental setup allowing electrophysiological and microscopy measurements of cells undergoing stretch. *In vitro* models represent a sustainable alternative to human tissue and animal models for experimentation, but require extensive characterisation and verification. Currently, no *in vitro* models aim to reproduce the conditions which *in vivo* neurons are subjected to during nerve deformation. Furthermore, the vast majority of studies on mechanical damage to neural function are centred on primary animal cells or immortalised cell lines, significantly diminishing their translational value. With the current development of stem cell technologies, as well as advances in rapid fabrication, the cost and complexity of making *in vitro* surrogates is set to decrease significantly. The results presented in chapter three aimed at encouraging the use of human stem cells in

neural injury modelling, as well as the design and production of cell-stretching devices that allow flexible experimental conditions and multi-physics measurements.

In chapter four, the effect of strain and cell membrane mechanical properties on neural function was investigated by measuring spontaneous network activity and individual cell electrophysiology from cells subject to uniaxial strain. Strain partitioning between macroscopic and microscopic length scales translates to injury forces to the micro- and nanoscopic domain. Elements of individual cells are in turn loaded by cellular deformation, altering network and singe-cell functionality. Membrane lipid packing changes with applied strain, indicative of the mechanical state of the neural membrane, were probed using c-Laurdan imaging. Ion channels, transmembrane pore-forming proteins that fundamentally regulate the excitability of the cell and their function, are intrinsically linked with the mechanical state of the cell membrane, and their function can be damaged by nerve stretch. Synaptic connections between neurons forming spontaneously active networks are also vulnerable to mechanical trauma. These results provide novel insight into the underlying mechanisms of functional alterations in stretched neurons, and can be useful in developing novel prevention or treatment strategies for neuropathies caused by supraphysiological straining of peripheral nerves aimed at reversing or preventing the effect of stretch on electrophysiological properties of nerve fibres.

The future of this project, involving further development of the *in vitro* model aimed towards a more representative reproduction of peripheral nerve structure with the introduction of multiple cell types in co-culture, could provide a flexible platform of high translational value for the study of peripheral nerve injury and repair. Experimental investigation of the effects of stretch on myelination, and on the electrophysiological properties of both myelinated and unmyelinated axons would allow further development of a comprehensive computational model validated by experimental results.

6.2 Ethical Considerations

Throughout this project, the breadth of experimental techniques used unavoidably resulted in close encounters with topics that entail ethical debate. It is important to evaluate the experimental methods used, and the results presented here, in light of the growing efforts to reduce animal experiments and within the increasingly complex debate over the ethics of stem cell and *in vitro* human neural cultures.

The advent of tissue engineering has enabled researchers to carry out testing on *in vitro* tissue surrogates, and has fuelled the debate around the use of animals in biomedical research. Aside from well-documented concerns about the predictive power of animal models in biomedical research [354], the increased availability of tissue engineered alternatives has strengthened arguments for the reduction of animal research, with funding bodies such as the national centre for replacement, refinement and reduction of animals in research (NC3Rs) supporting work aimed at developing alternatives to animal models.

The response of animal tissues to drugs, disease models, and external stimuli has been repeatedly shown to be an unreliable predictor of human behaviour [355]. Therefore, the use of animals as models to predict the response of human tissues and cells needs to be questioned, and the immediate translational value of results obtained in animal models should not be taken for granted [354].

Rat models remain the gold standard for peripheral nerve research, both as a source of tissues and as a model to test nerve replacement designs [58]. To some, this has skewed research into peripheral nerve damage and regeneration towards technologies aimed at passing validation in rat models, which are then ineffectively translated into the clinic due to size limitations and species-specific nerve regeneration mechanism found in rats [57].

In this thesis, rat sciatic nerves were used as model tissues in chapter two, to investigate the partitioning of strain within peripheral nerve structures. Rat and human peripheral nerves share structural similarities, and differ primarily in scale [356]. Due to this similarity and because of the complexity associated with obtaining human tissue samples, the use of rat sciatic nerves for these experiments aimed at understanding the tissue-specific mechanical properties can be justified.

Chapter three of this thesis describes the validation of a protocol for the differentiation of functional human motor neurons from induced pluripotent stem cells (iPSCs), and the development of a novel *in vitro* cell-stretching device. Both require separate ethical considerations.

From their isolation in 1981, stem cells have been one of the great biomedical advances of the late 20th century. Initial ethical concerns about the use of human embryonic tissue were surpassed when, in 2006, Takahashi and Yamanaka successfully reprogrammed adult mouse cells to an embryonic-like state, introducing induced pluripotent stem cells [163]. A year later, this was repeated in human cells [164]. The high cost associated with using iPSCs for *in vitro* testing still significantly hinders their use in research. In chapter three of this thesis, it was argued that the superior translational value of human neurons compared to animal primary neurons for studies of PNI outweighs the increased cost and experimental complexity. With future development and refinement of iPSC production and differentiation protocols, the cost of research is bound to further decrease, to the point where using dissociated animal primary neurons will no longer be justifiable.

Using human neurons generated from iPSCs introduces two further ethical hurdles: informed patient consent and duty of care. Although the production of iPSCs from adult tissues does not raise ethical concerns in itself, the subsequent handling, distribution and use of the iPSC lines is a more complex issue. The case of Henrietta Lacks, from whom HeLa cells were isolated in 1951, lead to decades of legal and personal distress

for the family involved, and intimates caution [357]. Should donors be allowed to claim a share of profits from commercialisation of cells induced from their tissues, or should all donated tissue be de-identified to the extent where it is impossible to retrace their origin? Furthermore, should donors have the right to oppose specific uses of iPSCs derived from their tissues? With the development and refinement of protocols for differentiation of iPSCs into an increasing number of cell phenotypes, careful consideration of these questions will be necessary.

The second issue arising with human iPSC-derived neuron cultures is to do with the treatment of the cultures themselves. The production of cerebral organoids from human iPSCs has sparked debate around whether, with increasing complexity and size, these artificial tissues will exhibit characteristics akin to consciousness, and whether this introduces far more complex requirements for handling and experimentation [358, 359]. Even monolayer cultures of iPSC-derived neurons form functional connections, and display spontaneous electrophysiological activity, and although this is far from a manifestation of consciousness, a future where surrogate tissues increase in complexity is not far. In chapter four of this thesis, spontaneously active iPSC-derived neurons were subject to strain, to monitor the effect of a mechanical input on network activity. The abstraction of this being a form of conscious response to input, rather than simply a direct mechanical effect, could provide a basis for an argument against this type of research in larger, more morphologically complex nervous system surrogates.

Overall, the ethical concerns raised by the research presented in this thesis are relatively minor, but should not be disregarded. Such considerations are of fundamental importance for a healthy progress of scientific research, and should be an integral part of any researcher's work, regardless of how distant from practical application they may be. Biomedical research should be gently steered away from animal models and towards surrogate tissues produced from human stem cell technology, but this should be carried out

with conscious consideration of cell donor consent, of the commercial implications of cell line production, and of the extent of protection researchers should give to the surrogates they produce.

6.3 Unanswered Research Questions

Aside from the future direction of this project (presented in chapter five), and from the limitations presented in each paper contained in this thesis, the following section details some shortcomings of the work presented here, as well as possible extension of the experimental results presented.

6.3.1 Macroscopic Nerve Mechanics

Questions remain unanswered in the study of the biomechanical properties of peripheral nerves. It is still unclear how the various components of nerves work in synergy to provide mechanical properties, and despite different theories and experimental campaigns, the load-bearing mechanisms in nerve are still not entirely clear. Only an understanding of nerve mechanics at all length scales can lead to the establishment of a unified model of peripheral nerve biomechanics, which can be used to understand the onset of mechanical damage.

The techniques presented in chapter two could further be applied to study the multi-scale mechanics of peripheral nerve in models of disease and damage. Wallarian degeneration can be induced by keeping severed nerves in culture medium, and demyelinating diseases such as amyotrophic lateral sclerosis (ALS) can be modelled pharmacologically [360]. Demyelination could be coupled with mechanical damage, by plastically deforming degenerated or demyelinated nerves and comparing the mechanical behaviour of axons, myelin, and collagen. This would result in a complete representation of the mechanical properties of the microstructure of peripheral nerve, both by X-ray diffraction and

multi-photon microscopy, including the way in which disease and degeneration alter strain partitioning between length scales. This would help understand whether debilitating conditions are associated with an alteration of the mechanical properties of nerve, suggesting possible treatment strategies.

6.3.2 Microscopic Neuron Mechanics

The biophysical mechanisms that causes electrophysiological disruptions during stretch remains unclear although evidence points towards a direct effect of mechanical force on ion channels, synapses, and other transmembrane domains involved in action potential generation and propagation.

The results presented here were collected from two cell sources: human iPSC-derived motor neurons (used for network experiments) and rodent F11 DRG-derived sensory neuron cells (for single-cell experiments). The difference in response to strain of these two cell kinds in unknown, and therefore the two results cannot be robustly used in the same discussion. Further extension of the work presented should homogenise the cell sources, and aim at comparing the response of different neural phenotypes, which are known to respond differently to stretch [275], as well as refining the understanding of ion channel response by selectively blocking families of channels before cell stretching. By using the same iPSC source to differentiate multiple neural phenotypes, any sources of inter-species or inter-subject variability would be eliminated.

The investigation of the effects of strain on network and single-cell activity should be extended to include multiple strain rates. This would help model different modes of injury, such as blast trauma, which occur at very high strain rates. Furthermore, a full study of recovery after strain release should include data from cells subjected to low strain magnitudes to attempt to determine the threshold where irrecoverable damage occurs.

In this thesis, strain partitioning within cells was evaluated only between nucleus and membrane, treating the cytoskeleton as a passive mechanical linker between the two. However, the cytoskeleton is known to play an active role in mechanosensation [267]. Furthermore, ion channels and lipid rafts have been shown to associate with cytoskeletal elements [361], although mechanosensitivity has been shown to be independent of the cytoskeleton [271, 269]. An experimental investigation of the combined effect of stretch and pharmacological cytoskeletal depolymerisation could isolate the role of the cytoskeleton in altered neural functionality due to mechanical damage. At the membrane level, further manipulation of membrane mechanics by reduction of cholesterol or amphiphilic treatment could confirm the importance of membrane mechanical properties in protecting ion channel function from injury.

6.4 Summary of Findings and Conclusions

The aim of the work presented in this thesis was to investigate the multi-scale effects that mechanical tension produces in peripheral nerves. Starting from the macroscopic tissue scale, the effect of stretch on peripheral nerve structure was investigated experimentally, and the transfer of strain to the microscopic scale was determined, where the effect of strain on cellular function was investigated.

In chapter two of this thesis, X-ray diffraction and multi-photon microscopy were used to probe the effect of tensile loading on peripheral nerves. It was shown that axially aligned collagen present in the outer sheath layer of peripheral nerve exhibits characteristics similar to those of load-bearing collagenous tissues such as tendons, suggesting a significant contribution to axial nerve stiffness. By examining changes in collagen structure and mechanical properties at the molecular level, it was shown that plastic damage appears to be localised *between* molecules, rather than within the collagen molecule itself, indicating damage to the intra-molecular cross linking. Tensile strain applied at the tissue

scale was further shown to induce axial strain at the axon level by multi-photon imaging of Nodes of Ranvier during stretch, a fundamental step in establishing a relation between tissue stretch and altered cell functionality.

Axial tensile loading was shown to induce a radial compression in the nerves. This compression is non-linear, suggesting a two-phase process. At first, structures within the nerve core rearrange, without bearing much load. After a threshold, the nerve core opposes compression and bears load. X-ray diffraction shows that the myelin sheath is compressed during axial elongation, though it only takes up a very small fraction of the whole nerve trunk compression. This suggests high myelin compressive stiffness and a role in protecting axons from compressive trauma. These results have implications in tissue engineering, where the understanding of material mechanics is key to developing artificial substitutes, but also help explain the mechanisms underlying the onset of conduction blocks and functionality impairment in stretched and diseased nerves. Furthermore, these results can be used to calibrate a computational model aimed of nerve stretch, which can be used to evaluate the performance of artificial nerve conduits and other tissue engineering technologies.

In order to study the effect of mechanical loading on individual neurons, *in vitro* models were developed. In chapter three of this thesis, a protocol for the differentiation of human motor neurons from induced pluripotent stem cells was presented. Within five weeks of iPSC thawing, cells were shown to successfully differentiate to neurons forming functional active *in vitro* networks and responding to stretch injury by decreasing spontaneous activity. The protocol was validated in two independent iPSC lines, and is presented as a valid alternative to primary cells and immortalised cell lines for neural injury studies providing a higher translational value. The development of a novel device to apply uniaxial strain to populations of cultured neurons was also presented in chapter three. The device allows both direct and indirect electrophysiological measurements from

cells subject to strain, and was characterised experimentally and by finite element method simulations. Combining the iPSC differential protocol with the stretching device produces an *in vitro* platform for the study of the effect of strain on neural functionality, where the response of neurons can be studied in isolation, providing further experimental information to build a complete model of the effect of strain on peripheral nerves.

Chapter four of this thesis was focussed on using the models developed in chapter three to investigate the effect of stretch at the single-cell level. It was shown that network activity is modulated by stretch, with a linear decrease in the number of active cells with applied deformation. Furthermore, it was shown that fast calcium spiking rise and fall time, indirectly representative of action potential firing within the network, were slowed during stretch. This indicates immediate strain-induced damage to ion channels and synaptic connectivity. Due to the intimate mechanical link between the cell membrane and neural electrophysiological activity, the effect of stretch on the membrane state was probed. By imaging lipid packing in iPSC-derived neurons subject to strain, it was shown that the cell membrane lipid bilayer fluidises as the cell is stretched, indicating an alteration in the membrane mechanical state. Subsequently, it was shown that stiffening the membrane by increasing the molar fraction of cholesterol causes a shift in baseline lipid packing, as well as a decrease in the rate at which the membrane fluidises during straining. This suggests that cholesterol addition modulates the mechanical state of the membrane. When cholesterol-enriched neurons were subject to strain, the loss of network spontaneous activity was significantly reduced compared to untreated cells, indicating that reducing the fluidisation of the lipid membrane during strain mitigates the loss of spontaneous electrophysiological activity. Whole-cell patch clamping of stretched sensory neurons was used to show a decrease in ion current magnitudes, steady-state ion channel conductances, and larger thresholds for action potential firing, further indicating damage at the ion channel level. Overall results indicate that strain has an immediate effect on neural

function, decreasing spontaneous activity and causing changes in ion channel dynamics, and that the mechanical state of the cell membrane has a significant effect in regulating the consequences of strain on neural activity. These results provide further information about the effect of strain on peripheral nerves, showing how strain transferred from the macroscopic scale alters functionality by affecting cell membranes and ion channels at the micro- and nano-scale.

The final chapter of this thesis presented partial work towards the establishment of a platform for the study of the effect of stretch on a physiologically representative model of the peripheral nerve. Using the same stretching device presented in chapter three, combined with a co-culture of stem-cell derived neurons and Schwann cells, a myelinated model of the peripheral nerve can be studied during axial stretch. It was shown that Schwann-like cells can be differentiated from human and rat mesenchymal stem cells, and that these promote neurite extension in co-culture with neurons. The establishment of an *in vitro* model of the effect of strain on a representative surrogate of peripheral nerve would provide a platform to help the development of treatment strategies for conduction blocks, investigate mechanical stimulus as a regenerative cue, and use pharmacological and genetic models of peripheral nerve diseases to study the changes in response to strain in diseased nerves. Furthermore, results combining the effect of strain on nerve structure, on neuronal function, on muscle innervation, and on myelination, can be combined to experimentally inform an end-to-end multi-scale biomechanical-functional model of peripheral nerve injury.

6.5 Concluding Remarks

Peripheral nerve response to mechanical stress and injury affects interdependent components at all length scales. Intervention at the macroscopic scale without knowledge of how it affects cells at the microscopic scale, and intervention at the single-cell level without un-

derstanding the macroscopic mechanical environment are both limited in effectiveness. An understanding of multi-scale mechanics is paramount to further the knowledge of damage mechanisms leading to pain and impaired function, and to refine and develop techniques for nerve repair. In line with growing ethical concerns around the use of animal models, developing and refining *in vitro* models both for independent experimental study and to validate computational models represents the future of nerve damage studies.

Bibliography

[1] J. H. Wang and B. P. Thampatty, "An introductory review of cell mechanobiology," *Biomech. Model. Mechanobiol.*, vol. 5, pp. 1–16, 2006.

[2] L. J. Hoenig, "Jacob's limp," *Semin. Arthritis Rheum.*, vol. 26, pp. 684–688, Feb. 1997.

[3] D. Grinsell and C. P. Keating, "Peripheral nerve reconstruction after injury: a review of clinical and experimental therapies," *Biomed Res. Int.*, vol. 2014, p. 698256, 2014.

[4] S. Ichihara, Y. Inada, and T. Nakamura, "Artificial nerve tubes and their application for repair of peripheral nerve injury: an update of current concepts," *Injury*, vol. 39 Suppl 4, pp. 29–39, Oct. 2008.

[5] L. R. Robinson, "Traumatic injury to peripheral nerves," *Muscle Nerve*, vol. 23, pp. 863–873, June 2000.

[6] R. Cornwall and T. E. Radomisli, "Nerve injury in traumatic dislocation of the hip," *Clin. Orthop. Relat. Res.*, pp. 84–91, Aug. 2000.

[7] W. M. Gilbert, T. S. Nesbitt, and B. Danielsen, "Associated factors in 1611 cases of brachial plexus injury," *Obstet. Gynecol.*, vol. 93, pp. 536–540, Apr. 1999.

[8] S. Aroori and R. A. J. Spence, "Carpal tunnel syndrome," *Ulster Med. J.*, vol. 77, pp. 6–17, Jan. 2008.

[9] F. D. Burke, "Carpal tunnel syndrome: Reconciling "demand management" with clinical need," *J. Hand Surg. Am.*, vol. 25, pp. 121–127, Apr. 2000.

[10] A. G. Lalkhen and K. Bhatia, "Perioperative peripheral nerve injuries," *Contin Educ Anaesth Crit Care Pain*, vol. 12, pp. 38–42, Feb. 2012.

[11] C. E. Schmidt and J. B. Leach, "Neural tissue engineering: strategies for repair and regeneration," *Annu. Rev. Biomed. Eng.*, vol. 5, pp. 293–347, 2003.

[12] F. R. Bueno and S. B. Shah, "Implications of tensile loading for the tissue engineering of nerves," *Tissue Eng. Part B Rev.*, vol. 14, pp. 219–233, Sept. 2008.

[13] X. Gu, F. Ding, Y. Yang, and J. Liu, "Construction of tissue engineered nerve grafts and their application in peripheral nerve regeneration," *Prog. Neurobiol.*, vol. 93, pp. 204–230, Feb. 2011.

[14] X. F. Zhang, H. O'Shea, S. Kehoe, and D. Boyd, "Time-dependent evaluation of mechanical properties and in vitro cytocompatibility of experimental composite-based nerve guidance conduits," *J. Mech. Behav. Biomed. Mater.*, vol. 4, pp. 1266–1274, Oct. 2011.

[15] S. Mobini, B. S. Spearman, C. S. Lacko, and C. E. Schmidt, "Recent advances in strategies for peripheral nerve tissue engineering," *Current Opinion in Biomedical Engineering*, vol. 4, pp. 134–142, Dec. 2017.

[16] J. D. Fix, *Neuroanatomy*. Philadelphia, Pa. ; London: Lippincott Williams and Wilkins, 4th ed. ed., 2008.

[17] T. Ushiki and C. Ide, "Three-dimensional organization of the collagen fibrils in the rat sciatic nerve as revealed by transmission- and scanning electron microscopy," *Cell Tissue Res.*, vol. 260, pp. 175–184, Apr. 1990.

[18] S. Mason and J. B. Phillips, "An ultrastructural and biochemical analysis of collagen in rat peripheral nerves: the relationship between fibril diameter and mechanical properties," *J. Peripher. Nerv. Syst.*, vol. 16, pp. 261–269, Sept. 2011.

[19] E. T. Walbeehm, A. Afoke, T. de Wit, F. Holman, S. E. R. Hovius, and R. A. Brown, "Mechanical functioning of peripheral nerves: linkage with the "mushrooming" effect," *Cell Tissue Res.*, vol. 316, pp. 115–121, Apr. 2004.

[20] K. S. Topp and B. S. Boyd, "Structure and biomechanics of peripheral nerves: nerve responses to physical stresses and implications for physical therapist practice," *Phys. Ther.*, vol. 86, pp. 92–109, Jan. 2006.

[21] A. L. Hodgkin and A. F. Huxley, "A quantitative description of membrane current and its application to conduction and excitation in nerve," *J. Physiol.*, vol. 117, pp. 500–544, Aug. 1952.

[22] B. Hille and Others, *Ion channels of excitable membranes*, vol. 507. Sinauer Sunderland, MA, 2001.

[23] F. J. Sigworth, "Voltage gating of ion channels," *Q. Rev. Biophys.*, vol. 27, pp. 1–40, Feb. 1994.

[24] A. Neishabouri and A. A. Faisal, "Saltatory conduction in unmyelinated axons: clustering of na(+) channels on lipid rafts enables micro-saltatory conduction in c-fibers," *Front. Neuroanat.*, vol. 8, p. 109, Oct. 2014.

[25] T. Rickett, S. Connell, J. Bastijanic, S. Hegde, and R. Shi, "Functional and mechanical evaluation of nerve stretch injury," *J. Med. Syst.*, vol. 35, pp. 787–793, Oct. 2011.

[26] J. Li and R. Shi, "Stretch-induced nerve conduction deficits in guinea pig ex vivo nerve," *J. Biomech.*, vol. 40, no. 3, pp. 569–578, 2007.

[27] S. Sunderland, "A classification of peripheral nerve injuries producing loss of function," *Brain*, vol. 74, pp. 491–516, 1951.

[28] I. Allodi, E. Udina, and X. Navarro, "Specificity of peripheral nerve regeneration: interactions at the axon level," *Prog. Neurobiol.*, vol. 98, pp. 16–37, 2012.

[29] A. Faroni, S. A. Mobasseri, P. J. Kingham, and A. J. Reid, "Peripheral nerve regeneration: experimental strategies and future perspectives," *Adv. Drug Deliv. Rev.*, vol. 82-83, pp. 160–167, 2015.

[30] S. Sunderland, "The anatomy and physiology of nerve injury," *Muscle Nerve*, vol. 13, pp. 771–784, 1990.

[31] R. M. G. Menorca, T. S. Fussell, and J. C. Elfar, "Nerve physiology: mechanisms of injury and recovery," *Hand Clin.*, vol. 29, pp. 317–330, Aug. 2013.

[32] J. T. Wang, Z. A. Medress, and B. A. Barres, "Axon degeneration: molecular mechanisms of a self-destruction pathway," *J. Cell Biol.*, vol. 196, pp. 7–18, Jan. 2012.

[33] M. Bendszus, C. Wessig, L. Solymosi, K. Reiners, and M. Koltzenburg, "MRI of peripheral nerve degeneration and regeneration: correlation with electrophysiology and histology," *Exp. Neurol.*, vol. 188, pp. 171–177, July 2004.

[34] S. Takai, H. Dohno, Y. Watanabe, N. Yoshino, T. Ogura, and Y. Hirasawa, "In situ strain and stress of nerve conduction blocking in the brachial plexus," *J. Orthop. Res.*, vol. 20, pp. 1311–1314, Nov. 2002.

[35] B. J. Pfister, T. Gordon, J. R. Loverde, A. S. Kochar, S. E. Mackinnon, and D. K. Cullen, "Biomedical engineering strategies for peripheral nerve repair: surgical applications, state of the art, and future challenges," *Crit. Rev. Biomed. Eng.*, vol. 39, no. 2, pp. 81–124, 2011.

[36] B. J. Pfister, A. Iwata, D. F. Meaney, and D. H. Smith, "Extreme stretch growth of integrated axons," *J. Neurosci.*, vol. 24, pp. 7978–7983, Sept. 2004.

[37] T.-H. Chuang, R. E. Wilson, J. M. Love, J. P. Fisher, and S. B. Shah, "A novel internal fixator device for peripheral nerve regeneration," *Tissue Eng. Part C Methods*, vol. 19, pp. 427–437, June 2013.

[38] K. M. Vaz, J. M. Brown, and S. B. Shah, "Peripheral nerve lengthening as a regenerative strategy," *Neural Regeneration Res.*, vol. 9, pp. 1498–1501, Aug. 2014.

[39] A. Iwata, K. D. Browne, B. J. Pfister, J. A. Gruner, and D. H. Smith, "Long-term survival and outgrowth of mechanically engineered nervous tissue constructs implanted into spinal cord lesions," *Tissue Eng.*, vol. 12, pp. 101–110, 2006.

[40] K. Franze, P. A. Janmey, and J. Guck, "Mechanics in neuronal development and repair," *Annu. Rev. Biomed. Eng.*, vol. 15, pp. 227–251, 2013.

[41] D. M. Suter and K. E. Miller, "The emerging role of forces in axonal elongation," *Prog. Neurobiol.*, vol. 94, pp. 91–101, July 2011.

[42] D. Bray, "Axonal growth in response to experimentally applied mechanical tension," *Dev. Biol.*, vol. 102, pp. 379–389, 1984.

[43] J. Zheng, P. Lamoureux, V. Santiago, T. Dennerll, R. E. Buxbaum, and S. R. Heidemann, "Tensile regulation of axonal elongation and initiation," *J. Neurosci.*, vol. 11, pp. 1117–1125, Apr. 1991.

[44] B. J. Pfister, D. P. Bonislawski, D. H. Smith, and A. S. Cohen, "Stretch-grown axons retain the ability to transmit active electrical signals," *FEBS Lett.*, vol. 580, pp. 3525–3531, 2006.

[45] J. R. Loverde and B. J. Pfister, "Developmental axon stretch stimulates neuron growth while maintaining normal electrical activity, intracellular calcium flux, and somatic morphology," *Front. Cell. Neurosci.*, vol. 9, p. 308, Aug. 2015.

[46] I. Abe, N. Ochiai, H. Ichimura, A. Tsujino, J. Sun, and Y. Hara, "Internodes can nearly double in length with gradual elongation of the adult rat sciatic nerve," *J. Orthop. Res.*, vol. 22, pp. 571–577, May 2004.

[47] K. H. Pfenninger, "Plasma membrane expansion: a neuron's herculean task," *Nat. Rev. Neurosci.*, vol. 10, pp. 251–261, 2009.

[48] S. A. Smith, J. B. Massie, R. Chesnut, and S. R. Garfin, "Straight leg raising. anatomical effects on the spinal nerve root without and with fusion," *Spine*, vol. 18, pp. 992–999, June 1993.

[49] M. W. Coppieters, A. M. Alshami, A. S. Babri, T. Souvlis, V. Kippers, and P. W. Hodges, "Strain and excursion of the sciatic, tibial, and plantar nerves during a modified straight leg raising test," *J. Orthop. Res.*, vol. 24, pp. 1883–1889, Sept. 2006.

[50] J. B. Phillips, X. Smit, N. De Zoysa, A. Afoke, and R. A. Brown, "Peripheral nerves in the rat exhibit localized heterogeneity of tensile properties during limb movement," *J. Physiol.*, vol. 557, pp. 879–887, June 2004.

[51] H. Millesi, G. Zöch, and T. Rath, "The gliding apparatus of peripheral nerve and its clinical significance," *Ann. Chir. Main Memb. Super.*, vol. 9, no. 2, pp. 87–97, 1990.

[52] R. L. Tillett, A. Afoke, S. M. Hall, R. A. Brown, and J. B. Phillips, "Investigating mechanical behaviour at a core-sheath interface in peripheral nerve," *J. Peripher. Nerv. Syst.*, vol. 9, pp. 255–262, Dec. 2004.

[53] J. M. Love, T.-H. Chuang, R. L. Lieber, and S. B. Shah, "Nerve strain correlates with structural changes quantified by fourier analysis," *Muscle Nerve*, vol. 48, pp. 433–435, Sept. 2013.

[54] E. B. Sinclair, N. Andarawis-Puri, S. J. Ros, D. M. Laudier, K. J. Jepsen, and M. R. Hausman, "Relating applied strain to the type and severity of structural damage in the rat median nerve using second harmonic generation microscopy," *Muscle Nerve*, vol. 46, pp. 899–907, Dec. 2012.

[55] M. A. Lillie, A. W. Vogl, K. N. Gil, J. M. Gosline, and R. E. Shadwick, "Two levels of waviness are necessary to package the highly extensible nerves in rorqual whales," *Curr. Biol.*, vol. 27, pp. 673–679, Mar. 2017.

[56] S. Geuna, S. Raimondo, F. Fregnan, K. Haastert-Talini, and C. Grothe, "In vitro models for peripheral nerve regeneration," *Eur. J. Neurosci.*, vol. 43, pp. 287–296, Feb. 2016.

[57] H. M. Kaplan, P. Mishra, and J. Kohn, "The overwhelming use of rat models in nerve regeneration research may compromise designs of nerve guidance conduits for humans," *J. Mater. Sci. Mater. Med.*, vol. 26, p. 226, Aug. 2015.

[58] S. Geuna, "The sciatic nerve injury model in pre-clinical research," *J. Neurosci. Methods*, vol. 243, pp. 39–46, Mar. 2015.

[59] E. Giannessi, M. R. Stornelli, and P. N. Sergi, "A unified approach to model peripheral nerves across different animal species," *PeerJ*, vol. 5, p. e4005, Nov. 2017.

[60] A. Jerusalem, J. A. Garcia-Grajales, A. Merchan-Perez, and J. M. Pena, "A computational model coupling mechanics and electrophysiology in spinal cord injury," *Biomech. Model. Mechanobiol.*, vol. 13, pp. 883–896, 2014.

[61] L. J. Ng, V. Volman, M. M. Gibbons, P. Phohomsiri, J. Cui, D. J. Swenson, and J. H. Stuhmiller, "A mechanistic End-to-End concussion model that translates head kinematics to neurologic injury," *Front. Neurol.*, vol. 8, 2017.

[62] M. C. LaPlaca, M. C. Lessing, G. R. Prado, R. Zhou, C. C. Tate, D. Geddes-Klein, D. F. Meaney, and L. Zhang, "Mechanoporation is a potential indicator of tissue strain and subsequent degeneration following experimental traumatic brain injury," *Clin. Biomech.*, June 2018.

[63] A. C. Bain and D. F. Meaney, "Tissue-level thresholds for axonal damage in an experimental model of central nervous system white matter injury," *J. Biomech. Eng.*, vol. 122, pp. 615–622, Dec. 2000.

[64] M. Gingras, J. Bergeron, J. Déry, H. D. Durham, and F. Berthod, "In vitro development of a tissue-engineered model of peripheral nerve regeneration to study neurite growth," *FASEB J.*, vol. 17, pp. 2124–2126, Nov. 2003.

[65] A. C. de Luca, A. Faroni, and A. J. Reid, "Dorsal root ganglia neurons and differentiated adipose-derived stem cells: an in vitro co-culture model to study peripheral nerve regeneration," *J. Vis. Exp.*, 2015.

[66] M. F. B. Daud, K. C. Pawar, F. Claeyssens, A. J. Ryan, and J. W. Haycock, "An aligned 3D neuronal-glial co-culture model for peripheral nerve studies," *Biomaterials*, vol. 33, pp. 5901–5913, Sept. 2012.

[67] M. Georgiou, S. C. J. Bunting, H. A. Davies, A. J. Loughlin, J. P. Golding, and J. B. Phillips, "Engineered neural tissue for peripheral nerve repair," *Biomaterials*, vol. 34, pp. 7335–7343, Oct. 2013.

[68] J. Brandt, L. B. Dahlin, and G. Lundborg, "Autologous tendons used as grafts for bridging peripheral nerve defects," *J. Hand Surg. Br.*, vol. 24, pp. 284–290, June 1999.

[69] E. J. Wall, J. B. Massie, M. K. Kwan, B. L. Rydevik, R. R. Myers, and S. R. Garfin, "Experimental stretch neuropathy. changes in nerve conduction under tension," *J. Bone Joint Surg. Br.*, vol. 74, pp. 126–129, Jan. 1992.

[70] B. L. Rydevik, M. K. Kwan, R. R. Myers, R. A. Brown, K. J. Triggs, S. L. Woo, and S. R. Garfin, "An in vitro mechanical and histological study of acute stretching on rabbit tibial nerve," *J. Orthop. Res.*, vol. 8, pp. 694–701, Sept. 1990.

[71] K. Ikeda, K. Tomita, and S. Tanaka, "Experimental study of peripheral nerve injury during gradual limb elongation," *Hand Surg.*, vol. 5, pp. 41–47, July 2000.

[72] H. Millesi, G. Zöch, and R. Reihsner, "Mechanical properties of peripheral nerves," *Clin. Orthop. Relat. Res.*, pp. 76–83, May 1995.

[73] J. Haftek, "Stretch injury of peripheral nerve. acute effects of stretching on rabbit nerve," *J. Bone Joint Surg. Br.*, vol. 52, pp. 354–365, May 1970.

[74] S. Sunderland and K. C. Bradley, "Stress-strain phenomena in human peripheral nerve trunks," *Brain*, vol. 84, no. 1, pp. 102–119, 1961.

[75] G. A. Georgeu, E. T. Walbeehm, R. Tillett, A. Afoke, R. A. Brown, and J. B. Phillips, "Investigating the mechanical shear-plane between core and sheath elements of peripheral nerves," *Cell Tissue Res.*, vol. 320, pp. 229–234, May 2005.

[76] N. C. Voermans, G. Drost, A. van Kampen, A. A. Gabreëls-Festen, M. Lammens, B. C. Hamel, J. Schalkwijk, and B. G. van Engelen, "Recurrent neuropathy associated with Ehlers–Danlos syndrome," *J. Neurol.*, vol. 253, pp. 670–671, May 2006.

[77] G. H. Borschel, K. F. Kia, W. M. Kuzon, Jr, and R. G. Dennis, "Mechanical properties of acellular peripheral nerve," *J. Surg. Res.*, vol. 114, pp. 133–139, Oct. 2003.

[78] D. I. Shreiber, H. Hao, and R. A. I. Elias, "Probing the influence of myelin and glia on the tensile properties of the spinal cord," *Biomech. Model. Mechanobiol.*, vol. 8, pp. 311–321, Aug. 2009.

[79] G. Rosso, I. Liashkovich, B. Gess, P. Young, A. Kun, and V. Shahin, "Unravelling crucial biomechanical resilience of myelinated peripheral nerve fibres provided by the schwann cell basal lamina and PMP22," *Sci. Rep.*, vol. 4, p. 7286, Dec. 2014.

[80] A. Heredia, C. C. Bui, U. Suter, P. Young, and T. E. Schäffer, "AFM combines functional and morphological analysis of peripheral myelinated and demyelinated nerve fibers," *Neuroimage*, vol. 37, pp. 1218–1226, Oct. 2007.

[81] G. Koopmans, B. Hasse, and N. Sinis, "Chapter 19: The role of collagen in peripheral nerve repair," *Int. Rev. Neurobiol.*, vol. 87, pp. 363–379, 2009.

[82] M. E. Nimni, "Collagen: structure, function, and metabolism in normal and fibrotic tissues," *Semin. Arthritis Rheum.*, vol. 13, pp. 1–86, 1983.

[83] G. N. Ramachandran and A. H. Reddi, *Biochemistry of Collagen*. New York ; London: Basic Books, Jan. 1976.

[84] J. A. Petruska and A. J. Hodge, "A subunit model for the tropocollagen macromolecule," *Proc. Natl. Acad. Sci. U. S. A.*, vol. 51, pp. 871–876, May 1964.

[85] B. E. Warren, *X-ray Diffraction*. Courier Corporation, 1969.

[86] N. Sasaki and S. Odajima, "Stress-strain curve and young's modulus of a collagen molecule as determined by the x-ray diffraction technique," *J. Biomech.*, vol. 29, pp. 655–658, 1996.

[87] C. A. Maxwell, T. J. Wess, and C. J. Kennedy, "X-ray diffraction study into the effects of liming on the structure of collagen," *Biomacromolecules*, vol. 7, pp. 2321–2326, Aug. 2006.

[88] J. B. Finean, "Electron microscope and x-ray diffraction studies of the effects of dehydrations on the structure of nerve myelin. i. peripheral nerve," *J. Biophys. Biochem. Cytol.*, vol. 8, pp. 13–29, Sept. 1960.

[89] H. Inouye, J. Liu, L. Makowski, M. Palmisano, M. Burghammer, C. Riekel, and D. A. Kirschner, "Myelin organization in the nodal, paranodal, and juxtaparanodal regions revealed by scanning x-ray microdiffraction," *PLoS One*, vol. 9, p. e100592, July 2014.

[90] T. Kurg, R. H. Stinson, and B. M. Millman, "X-ray diffraction from striated muscles and nerves in normal and dystrophic mice," *Muscle Nerve*, vol. 5, pp. 238–246, Mar. 1982.

[91] G. Fessel, Y. Li, V. Diederich, M. Guizar-Sicairos, P. Schneider, D. R. Sell, V. M. Monnier, and J. G. Snedeker, "Advanced glycation end-products reduce collagen molecular sliding to affect collagen fibril damage mechanisms but not stiffness," *PLoS One*, vol. 9, p. e110948, Nov. 2014.

[92] S. Rigozzi, A. Stemmer, R. Muller, and J. G. Snedeker, "Mechanical response of individual collagen fibrils in loaded tendon as measured by atomic force microscopy," *J. Struct. Biol.*, vol. 176, pp. 9–15, 2011.

[93] N. Sasaki, N. Shukunami, N. Matsushima, and Y. Izumi, "Time-resolved x-ray diffraction from tendon collagen during creep using synchrotron radiation," *J. Biomech.*, vol. 32, pp. 285–292, Mar. 1999.

[94] E. Mosler, W. Folkhard, E. Knorzer, H. Nemetschek-Gansler, T. Nemetschek, and M. H. Koch, "Stress-induced molecular rearrangement in tendon collagen," *J. Mol. Biol.*, vol. 182, pp. 589–596, 1985.

[95] P. Fratzl, K. Misof, I. Zizak, G. Rapp, H. Amenitsch, and S. Bernstorff, "Fibrillar structure and mechanical properties of collagen," *J. Struct. Biol.*, vol. 122, no. 1-2, pp. 119–122, 1998.

[96] N. Sasaki and S. Odajima, "Elongation mechanism of collagen fibrils and force-strain relations of tendon at each level of structural hierarchy," *J. Biomech.*, vol. 29, pp. 1131–1136, Sept. 1996.

[97] F. Bianchi, F. Hofmann, A. J. Smith, H. Ye, and M. S. Thompson, "Probing multi-scale mechanics of peripheral nerve collagen and myelin by x-ray diffraction," *J. Mech. Behav. Biomed. Mater.*, July 2018.

[98] Saijilafu, Y. Nishiura, Y. Hara, Y. Yoshii, and N. Ochiai, "Simultaneous gradual lengthening of both proximal and distal nerve stumps for repair of peripheral nerve defect in rats," *Muscle Nerve*, vol. 38, pp. 1474–1480, Nov. 2008.

[99] K. Ogata and M. Naito, "Blood flow of peripheral nerve effects of dissection, stretching and compression," *J. Hand Surg. Br.*, vol. 11, pp. 10–14, Feb. 1986.

[100] S. Aomura, H. Nakadate, Y. Kaneko, A. Nishimura, and R. Willinger, "Stretch-induced functional disorder of axonal transport in the cultured rat cortex neuron," *Integr Mol Med*, vol. 3, no. 3, pp. 654–660, 2016.

[101] M. H. Magdesian, F. S. Sanchez, M. Lopez, P. Thostrup, N. Durisic, W. Belkaid, D. Liazoghli, P. Grütter, and D. R. Colman, "Atomic force microscopy reveals important differences in axonal resistance to injury," *Biophys. J.*, vol. 103, pp. 405–414, Aug. 2012.

[102] H. Ichimura, T. Shiga, I. Abe, Y. Hara, N. Terui, A. Tsujino, and N. Ochiai, "Distribution of sodium channels during nerve elongation in rat peripheral nerve," *J. Orthop. Sci.*, vol. 10, no. 2, pp. 214–220, 2005.

[103] Y. C. Yap, A. E. King, R. M. Guijt, T. Jiang, C. A. Blizzard, M. C. Breadmore, and T. C. Dickson, "Mild and repetitive very mild axonal stretch injury triggers cystoskeletal mislocalization and growth cone collapse," *PLoS One*, vol. 12, p. e0176997, May 2017.

[104] D. M. Geddes, R. S. Cargill, 2nd, and M. C. LaPlaca, "Mechanical stretch to neurons results in a strain rate and magnitude-dependent increase in plasma membrane permeability," *J. Neurotrauma*, vol. 20, pp. 1039–1049, Oct. 2003.

[105] D. Kilinc, G. Gallo, and K. A. Barbee, "Mechanically-induced membrane poration causes axonal beading and localized cytoskeletal damage," *Exp. Neurol.*, vol. 212, pp. 422–430, Aug. 2008.

[106] H. Inouye and C. R. Worthington, "X-ray observations on a collagen fibril lattice structure in peripheral nerve," *Int. J. Biol. Macromol.*, vol. 5, pp. 199–203, Aug. 1983.

[107] A. Bruneau, N. Champagne, P. Cousineau-Pelletier, G. Parent, and E. Langelier, "Preparation of rat tail tendons for biomechanical and mechanobiological studies," *J. Vis. Exp.*, July 2010.

[108] T. Sea, M. L. Ballinger, and G. D. Bittner, "Cooling of peripheral myelinated axons retards wallerian degeneration," *Exp. Neurol.*, vol. 133, pp. 85–95, May 1995.

[109] F. Bianchi, F. Hofmann, A. J. Smith, and M. S. Thompson, "Probing multi-scale mechanical damage in connective tissues using x-ray diffraction," *Acta Biomater.*, vol. 45, pp. 321–327, Nov. 2016.

[110] A. J. Flores, C. J. Lavernia, and P. W. Owens, "Anatomy and physiology of peripheral nerve injury and repair," *Am. J. Orthop.*, vol. 29, pp. 167–173, Mar. 2000.

[111] B. S. Oxlund, G. Ørtoft, A. Brüel, C. C. Danielsen, P. Bor, H. Oxlund, and N. Uldbjerg, "Collagen concentration and biomechanical properties of samples from the lower uterine cervix in relation to age and parity in non-pregnant women," *Reprod. Biol. Endocrinol.*, vol. 8, p. 82, July 2010.

[112] M. S. Islam, M. C. Oliveira, Y. Wang, F. P. Henry, M. A. Randolph, B. H. Park, and J. F. de Boer, "Extracting structural features of rat sciatic nerve using polarization-sensitive spectral domain optical coherence tomography," *J. Biomed. Opt.*, vol. 17, p. 056012, May 2012.

[113] W. L. Maxwell, "Histopathological changes at central nodes of ranvier after stretch-injury," *Microsc. Res. Tech.*, vol. 34, pp. 522–535, Aug. 1996.

[114] A. Yokota, M. Doi, H. Ohtsuka, and M. Abe, "Nerve conduction and microanatomy in the rabbit sciatic nerve after gradual limb lengthening-distraction neurogenesis," *J. Orthop. Res.*, vol. 21, pp. 36–43, Jan. 2003.

[115] J. Kerns, T. Urabe, T. Bleasdale, Q. Zhao, G. Lundborg, and N. Danielsen, "Effects of gradual bone lengthening on the rabbit tibial nerve," *Scand. J. Plast. Reconstr. Surg. Hand Surg.*, vol. 35, pp. 361–368, Dec. 2001.

[116] M. S. Thompson, "Tendon mechanobiology: experimental models require mathematical underpinning," *Bull. Math. Biol.*, vol. 75, pp. 1238–1254, Aug. 2013.

[117] A. S. LaCroix, S. E. Duenwald-Kuehl, R. S. Lakes, and R. Vanderby, Jr, "Relationship between tendon stiffness and failure: a metaanalysis," *J. Appl. Physiol.*, vol. 115, pp. 43–51, July 2013.

[118] S. Singh, A. A. Pelegri, and D. I. Shreiber, "Estimating axonal strain and failure following white matter stretch using contactin-associated protein as a fiduciary marker," *J. Biomech.*, vol. 51, pp. 32–41, Jan. 2017.

[119] A. Neviaser, N. Andarawis-Puri, and E. Flatow, "Basic mechanisms of tendon fatigue damage," *J. Shoulder Elbow Surg.*, vol. 21, pp. 158–163, Feb. 2012.

[120] P. Sharma and N. Maffulli, "Tendon injury and tendinopathy: healing and repair," *J. Bone Joint Surg. Am.*, vol. 87, pp. 187–202, Jan. 2005.

[121] T. J. Wess, A. P. Hammersley, L. Wess, and A. Miller, "Molecular packing of type I collagen in tendon," *J. Mol. Biol.*, vol. 275, pp. 255–267, 16 Jan. 1998.

[122] J. P. Orgel, T. J. Wess, and A. Miller, "The in situ conformation and axial location of the intermolecular cross-linked non-helical telopeptides of type I collagen," *Structure*, vol. 8, pp. 137–142, 15 Feb. 2000.

[123] T. J. Wess and D. E. Cairns, "Nanoarchitectures of the animal extracellular matrix: opportunities for synchrotron radiation studies on collagen and fibrillin," *J. Synchrotron Radiat.*, vol. 12, pp. 751–757, Nov. 2005.

[124] P. M. Cowan, A. North, and J. T. Randall, "X-ray diffraction studies of collagen fibres," in *Symposia of the Society for Experimental Biology*, vol. 9, pp. 115–126, bcin.ca, 1955.

[125] F. Berenguer, R. J. Bean, L. Bozec, J. Vila-Comamala, F. Zhang, C. M. Kewish, O. Bunk, J. M. Rodenburg, and I. K. Robinson, "Coherent x-ray imaging of collagen fibril distributions within intact tendons," *Biophys. J.*, vol. 106, pp. 459–466, 21 Jan. 2014.

[126] T. J. Wess and J. P. Orgel, "Changes in collagen structure: drying, dehydrothermal treatment and relation to long term deterioration," *Thermochim. Acta*, vol. 365, pp. 119–128, 29 Dec. 2000.

[127] D. T. Fung, V. M. Wang, N. Andarawis-Puri, J. Basta-Pljakic, Y. Li, D. M. Laudier, H. B. Sun, K. J. Jepsen, M. B. Schaffler, and E. L. Flatow, "Early response to tendon fatigue damage accumulation in a novel in vivo model," *J. Biomech.*, vol. 43, pp. 274–279, 19 Jan. 2010.

[128] R. I. Price, S. Lees, and D. A. Kirschner, "X-ray diffraction analysis of tendon collagen at ambient and cryogenic temperatures: role of hydration," *Int. J. Biol. Macromol.*, vol. 20, pp. 23–33, 1997.

[129] R. Puxkandl, I. Zizak, O. Paris, J. Keckes, W. Tesch, S. Bernstorff, P. Purslow, and P. Fratzl, "Viscoelastic properties of collagen: synchrotron radiation investigations and structural model," *Philos. Trans. R. Soc. Lond. B Biol. Sci.*, vol. 357, pp. 191–197, 28 Feb. 2002.

[130] S. P. Veres, J. M. Harrison, and J. M. Lee, "Mechanically overloading collagen fibrils uncoils collagen molecules, placing them in a stable, denatured state," *Matrix Biol.*, vol. 33, pp. 54–59, Jan. 2014.

[131] S. P. Veres and J. M. Lee, "Designed to fail: a novel mode of collagen fibril disruption and its relevance to tissue toughness," *Biophys. J.*, vol. 102, pp. 2876–2884, 20 June 2012.

[132] A. Bigi, A. M. Fichera, N. Roveri, and M. H. J. Koch, "Structural modifications of Air-Dried tendon collagen on heating," *Int. J. Biol. Macromol.*, vol. 9, pp. 176–180, 1987.

[133] R. D. Fraser, T. P. MacRae, A. Miller, and E. Suzuki, "Molecular conformation and packing in collagen fibrils," *J. Mol. Biol.*, vol. 167, pp. 497–521, 25 June 1983.

[134] A. Masic, L. Bertinetti, R. Schuetz, S.-W. Chang, T. H. Metzger, M. J. Buehler, and P. Fratzl, "Osmotic pressure induced tensile forces in tendon collagen," *Nat. Commun.*, vol. 6, p. 5942, 22 Jan. 2015.

[135] H. D. Barth, E. A. Zimmermann, E. Schaible, S. Y. Tang, T. Alliston, and R. O. Ritchie, "Characterization of the effects of x-ray irradiation on the hierarchical structure and mechanical properties of human cortical bone," *Biomaterials*, vol. 32, pp. 8892–8904, Dec. 2011.

[136] I. Gusachenko, V. Tran, Y. Goulam Houssen, J. M. Allain, and M. C. Schanne-Klein, "Polarization-resolved second-harmonic generation in tendon upon mechanical stretching," *Biophys. J.*, vol. 102, pp. 2220–2229, 2012.

[137] F. Bianchi, R. Sedgwick, H. Ye, and M. S. Thompson, "Strain partitioning between nerves and axons: estimating axonal strain using sodium channel staining in intact peripheral nerves," *J. Neurosci. Methods*, Aug. 2018.

[138] C. A. Taylor, D. Braza, J. B. Rice, and T. Dillingham, "The incidence of peripheral nerve injury in extremity trauma," *Am. J. Phys. Med. Rehabil.*, vol. 87, p. 381, May 2008.

[139] A. B. Schmid, J. D. P. Bland, M. A. Bhat, and D. L. H. Bennett, "The relationship of nerve fibre pathology to sensory function in entrapment neuropathy," *Brain*, vol. 137, pp. 3186–3199, Dec. 2014.

[140] W. M. Han, S.-J. Heo, T. P. Driscoll, L. J. Smith, R. L. Mauck, and D. M. Elliott, "Macro- to microscale strain transfer in fibrous tissues is heterogeneous and tissue-specific," *Biophys. J.*, vol. 105, pp. 807–817, Aug. 2013.

[141] K. Ueno, J. W. Melvin, L. Li, and J. W. Lighthall, "Development of tissue level brain injury criteria by finite element analysis," *J. Neurotrauma*, vol. 12, pp. 695–706, Aug. 1995.

[142] S.-O. Kim, J. Kim, T. Okajima, and N.-J. Cho, "Mechanical properties of paraformaldehyde-treated individual cells investigated by atomic force microscopy and scanning ion conductance microscopy," *Nano Converg*, vol. 4, p. 5, Mar. 2017.

[143] J. S. Cartmell and M. G. Dunn, "Effect of chemical treatments on tendon cellularity and mechanical properties," *J. Biomed. Mater. Res.*, vol. 49, pp. 134–140, Jan. 2000.

[144] S. Namadurai, N. R. Yereddi, F. S. Cusdin, C. L. H. Huang, D. Y. Chirgadze, and A. P. Jackson, "A new look at sodium channel β subunits," *Open Biol.*, vol. 5, p. 140192, Jan. 2015.

[145] M. L. Upton, C. L. Gilchrist, F. Guilak, and L. A. Setton, "Transfer of macroscale tissue strain to microscale cell regions in the deformed meniscus," *Biophys. J.*, vol. 95, pp. 2116–2124, Aug. 2008.

[146] C. L. Gilchrist, S. W. Witvoet-Braam, F. Guilak, and L. A. Setton, "Measurement of intracellular strain on deformable substrates with texture correlation," *J. Biomech.*, vol. 40, no. 4, pp. 786–794, 2007.

[147] Z. Ma, S. Hu, J. S. Tan, C. Myer, N. M. Njus, and Z. Xia, "In vitro and in vivo mechanical properties of human ulnar and median nerves," *J. Biomed. Mater. Res. A*, vol. 101, pp. 2718–2725, Sept. 2013.

[148] G. Fessel, K. Frey, A. Schweizer, M. Calcagni, O. Ullrich, and J. G. Snedeker, "Suitability of thiel embalmed tendons for biomechanical investigation," *Ann. Anat.*, vol. 193, pp. 237–241, May 2011.

[149] J. Hornsby, D. M. Daly, D. Grundy, F. Cheng, A. M. Robertson, P. N. Watton, and M. S. Thompson, "Quantitative multiphoton microscopy of murine urinary bladder morphology during in situ uniaxial loading," *Acta Biomater.*, vol. 64, pp. 59–66, Dec. 2017.

[150] C. Stolinski, "Structure and composition of the outer connective tissue sheaths of peripheral nerve," *J. Anat.*, vol. 186 (Pt 1), pp. 123–130, Feb. 1995.

[151] K. K. Gilbert, J.-M. Brismée, D. L. Collins, C. R. James, R. V. Shah, S. F. Sawyer, and P. S. Sizer, Jr, "2006 young investigator award winner: lumbosacral nerve root displacement and strain: part 1. a novel measurement technique during straight leg raise in unembalmed cadavers," *Spine*, vol. 32, pp. 1513–1520, June 2007.

[152] M. Wadman, "The truth about fetal tissue research," *Nature*, vol. 528, pp. 178–181, Dec. 2015.

[153] J. A. Galbraith, L. E. Thibault, and D. R. Matteson, "Mechanical and electrical responses of the squid giant axon to simple elongation," *J. Biomech. Eng.*, vol. 115, pp. 13–22, Feb. 1993.

[154] Y. Xiong, A. Mahmood, and M. Chopp, "Animal models of traumatic brain injury," *Nat. Rev. Neurosci.*, vol. 14, pp. 128–142, Feb. 2013.

[155] S. Higgins, J. S. Lee, L. Ha, and J. Y. Lim, "Inducing neurite outgrowth by mechanical cell stretch," *Biores. Open Access*, vol. 2, pp. 212–216, 2013.

[156] H. Nakadate, H. Umahashi, A. Kakuta, and S. Aomura, "Progression to cell death correlates with neurite swelling induced by stretch injury," *Journal of Biomechanical Science and Engineering*, vol. 7, no. 4, pp. 406–415, 2012.

[157] D. M. Geddes and R. S. Cargill, 2nd, "An in vitro model of neural trauma: device characterization and calcium response to mechanical stretch," *J. Biomech. Eng.*, vol. 123, pp. 247–255, June 2001.

[158] M. C. LaPlaca and L. E. Thibault, "Anin vitro traumatic injury model to examine the response of neurons to a hydrodynamically-induced deformation," *Ann. Biomed. Eng.*, vol. 25, pp. 665–677, July 1997.

[159] S. F. Fan, K. F. Shen, M. A. Scheideler d, and S. M. Crain a, "Fll neuroblastoma × DRG neuron hybrid cells express inhibitory/.l- and 6-opioid receptors which increase voltage-dependent K + currents upon activation," *Brain Res.*, vol. 590, pp. 329–333, 1992.

[160] J. Gordon, S. Amini, and M. K. White, "General overview of neuronal cell culture," *Methods Mol. Biol.*, vol. 1078, pp. 1–8, 2013.

[161] X.-J. Li, Z.-W. Du, E. D. Zarnowska, M. Pankratz, L. O. Hansen, R. A. Pearce, and S.-C. Zhang, "Specification of motoneurons from human embryonic stem cells," *Nat. Biotechnol.*, vol. 23, pp. 215–221, Feb. 2005.

[162] J. Poulos, "The limited application of stem cells in medicine: a review," *Stem Cell Res. Ther.*, vol. 9, p. 1, Jan. 2018.

[163] K. Takahashi and S. Yamanaka, "Induction of pluripotent stem cells from mouse embryonic and adult fibroblast cultures by defined factors," *Cell*, vol. 126, pp. 663–676, Aug. 2006.

[164] K. Takahashi, K. Tanabe, M. Ohnuki, M. Narita, T. Ichisaka, K. Tomoda, and S. Yamanaka, "Induction of pluripotent stem cells from adult human fibroblasts by defined factors," *Cell*, vol. 131, pp. 861–872, Nov. 2007.

[165] J.-H. Chuang, L.-C. Tung, and Y. Lin, "Neural differentiation from embryonic stem cells in vitro: An overview of the signaling pathways," *World J. Stem Cells*, vol. 7, pp. 437–447, Mar. 2015.

[166] R. G. Miller, "AAEE minimonograph #28: injury to peripheral motor nerves," *Muscle Nerve*, vol. 10, pp. 698–710, Oct. 1987.

[167] A. Abid, "Brachial plexus birth palsy: Management during the first year of life," *Orthop. Traumatol. Surg. Res.*, vol. 102, pp. S125–32, Feb. 2016.

[168] W. Sun, Y. Fu, Y. Shi, J.-X. Cheng, P. Cao, and R. Shi, "Paranodal myelin damage after acute stretch in guinea pig spinal cord," *J. Neurotrauma*, vol. 29, pp. 611–619, Feb. 2012.

[169] E. Bar-Kochba, M. T. Scimone, J. B. Estrada, and C. Franck, "Strain and rate-dependent neuronal injury in a 3D in vitro compression model of traumatic brain injury," *Sci. Rep.*, vol. 6, p. 30550, Aug. 2016.

[170] W. H. Kang, W. Cao, O. Graudejus, T. P. Patel, S. Wagner, D. F. Meaney, and B. Morrison, 3rd, "Alterations in hippocampal network activity after in vitro traumatic brain injury," *J. Neurotrauma*, vol. 32, pp. 1011–1019, July 2015.

[171] E. Kurtoglu, H. Nakadate, K. Kikuta, S. Aomura, and A. Kakuta, "Uniaxial stretch-induced axonal injury thresholds for axonal dysfunction and disruption and strain rate effects on thresholds for mouse neuronal stem cells," *Journal of Biomechanical Science and Engineering*, vol. 12, no. 1, pp. 16–00598–16–00598, 2017.

[172] M. Skotak, F. Wang, and N. Chandra, "An in vitro injury model for SH-SY5Y neuroblastoma cells: effect of strain and strain rate," *J. Neurosci. Methods*, vol. 205, pp. 159–168, Mar. 2012.

[173] N. Marklund, A. Bakshi, D. J. Castelbuono, V. Conte, and T. K. McIntosh, "Evaluation of pharmacological treatment strategies in traumatic brain injury," *Curr. Pharm. Des.*, vol. 12, no. 13, pp. 1645–1680, 2006.

[174] S. Kobold, A. Guhr, A. Kurtz, and P. Löser, "Human embryonic and induced pluripotent stem cell research trends: complementation and diversification of the field," *Stem Cell Reports*, vol. 4, pp. 914–925, May 2015.

[175] D.-S. Kim, P. J. Ross, K. Zaslavsky, and J. Ellis, "Optimizing neuronal differentiation from induced pluripotent stem cells to model ASD," *Front. Cell. Neurosci.*, vol. 8, p. 109, Apr. 2014.

[176] P. Zhang, N. Xia, and R. A. Reijo Pera, "Directed dopaminergic neuron differentiation from human pluripotent stem cells," *J. Vis. Exp.*, p. 51737, Sept. 2014.

[177] A. X. Sun, Q. Yuan, S. Tan, Y. Xiao, D. Wang, A. T. T. Khoo, L. Sani, H.-D. Tran, P. Kim, Y. S. Chiew, K. J. Lee, Y.-C. Yen, H. H. Ng, B. Lim, and H. S. Je, "Direct induction and functional maturation of forebrain GABAergic neurons from human pluripotent stem cells," *Cell Rep.*, vol. 16, pp. 1942–1953, Aug. 2016.

[178] I. Faravelli, M. Bucchia, P. Rinchetti, M. Nizzardo, C. Simone, E. Frattini, and S. Corti, "Motor neuron derivation from human embryonic and induced pluripotent stem cells: experimental approaches and clinical perspectives," *Stem Cell Res. Ther.*, vol. 5, p. 87, July 2014.

[179] Y. Tao and S.-C. Zhang, "Neural subtype specification from human pluripotent stem cells," *Cell Stem Cell*, vol. 19, pp. 573–586, Nov. 2016.

[180] S. Sances, L. I. Bruijn, S. Chandran, K. Eggan, R. Ho, J. R. Klim, M. R. Livesey, E. Lowry, J. D. Macklis, D. Rushton, C. Sadegh, D. Sareen, H. Wichterle, S.-C. Zhang, and C. N. Svendsen, "Modeling ALS with motor neurons derived from human induced pluripotent stem cells," *Nat. Neurosci.*, vol. 19, pp. 542–553, Apr. 2016.

[181] S. A. Sherman, J. K. Phillips, J. T. Costa, F. S. Cho, S. R. Oungoulian, and J. D. Finan, "Stretch injury of human induced pluripotent stem cell derived neurons in a 96 well format," *Sci. Rep.*, vol. 6, p. 34097, Sept. 2016.

[182] J. T. Dimos, K. T. Rodolfa, K. K. Niakan, L. M. Weisenthal, H. Mitsumoto, W. Chung, G. F. Croft, G. Saphier, R. Leibel, R. Goland, H. Wichterle, C. E. Henderson, and K. Eggan, "Induced pluripotent stem cells generated from patients with ALS can be differentiated into motor neurons," *Science*, vol. 321, pp. 1218–1221, Aug. 2008.

[183] D. Shimojo, K. Onodera, Y. Doi-Torii, Y. Ishihara, C. Hattori, Y. Miwa, S. Tanaka, R. Okada, M. Ohyama, M. Shoji, A. Nakanishi, M. Doyu, H. Okano, and Y. Okada, "Rapid, efficient, and simple motor neuron differentiation from human pluripotent stem cells," *Mol. Brain*, vol. 8, p. 79, Dec. 2015.

[184] Y. Maury, J. Côme, R. A. Piskorowski, N. Salah-Mohellibi, V. Chevaleyre, M. Peschanski, C. Martinat, and S. Nedelec, "Combinatorial analysis of developmental cues efficiently converts human pluripotent stem cells into multiple neuronal subtypes," *Nat. Biotechnol.*, vol. 33, pp. 89–96, Jan. 2015.

[185] A. Salimi, S. Nadri, M. Ghollasi, K. Khajeh, and M. Soleimani, "Comparison of different protocols for neural differentiation of human induced pluripotent stem cells," *Mol. Biol. Rep.*, vol. 41, pp. 1713–1721, Mar. 2014.

[186] M. W. Amoroso, G. F. Croft, D. J. Williams, S. O'Keeffe, M. A. Carrasco, A. R. Davis, L. Roybon, D. H. Oakley, T. Maniatis, C. E. Henderson, and H. Wichterle, "Accelerated high-yield generation of limb-innervating motor neurons from human stem cells," *J. Neurosci.*, vol. 33, pp. 574–586, Jan. 2013.

[187] S. M. Chambers, C. A. Fasano, E. P. Papapetrou, M. Tomishima, M. Sadelain, and L. Studer, "Highly efficient neural conversion of human ES and iPS cells by dual inhibition of SMAD signaling," *Nat. Biotechnol.*, vol. 27, pp. 275–280, Mar. 2009.

[188] B. Surmacz, H. Fox, A. Gutteridge, P. Fish, S. Lubitz, and P. Whiting, "Directing differentiation of human embryonic stem cells toward anterior neural ectoderm using small molecules," *Stem Cells*, vol. 30, pp. 1875–1884, Sept. 2012.

[189] W. Li, W. Sun, Y. Zhang, W. Wei, R. Ambasudhan, P. Xia, M. Talantova, T. Lin, J. Kim, X. Wang, W. R. Kim, S. A. Lipton, K. Zhang, and S. Ding, "Rapid induction and long-term self-renewal of primitive neural precursors from human embryonic stem cells by small molecule inhibitors," *Proc. Natl. Acad. Sci. U. S. A.*, vol. 108, pp. 8299–8304, May 2011.

[190] M. D. Neely, M. J. Litt, A. M. Tidball, G. G. Li, A. A. Aboud, C. R. Hopkins, R. Chamberlin, C. C. Hong, K. C. Ess, and A. B. Bowman, "DMH1, a highly selective small molecule BMP inhibitor promotes neurogenesis of hiPSCs: comparison of PAX6 and SOX1 expression during neural induction," *ACS Chem. Neurosci.*, vol. 3, pp. 482–491, June 2012.

[191] J. Zhou, P. Su, D. Li, S. Tsang, E. Duan, and F. Wang, "High-efficiency induction of neural conversion in human ESCs and human induced pluripotent stem cells with a single chemical inhibitor of transforming growth factor beta superfamily receptors," *Stem Cells*, vol. 28, pp. 1741–1750, Oct. 2010.

[192] G. J. Inman, F. J. Nicolás, J. F. Callahan, J. D. Harling, L. M. Gaster, A. D. Reith, N. J. Laping, and C. S. Hill, "SB-431542 is a potent and specific inhibitor of transforming growth factor-beta superfamily type I activin receptor-like kinase (ALK) receptors ALK4, ALK5, and ALK7," *Mol. Pharmacol.*, vol. 62, pp. 65–74, July 2002.

[193] Z.-W. Du, H. Chen, H. Liu, J. Lu, K. Qian, C.-L. Huang, X. Zhong, F. Fan, and S.-C. Zhang, "Generation and expansion of highly pure motor neuron progenitors from human pluripotent stem cells," *Nat. Commun.*, vol. 6, p. 6626, Mar. 2015.

[194] J. Muhr, E. Graziano, S. Wilson, T. M. Jessell, and T. Edlund, "Convergent inductive signals specify midbrain, hindbrain, and spinal cord identity in gastrula stage chick embryos," *Neuron*, vol. 23, pp. 689–702, Aug. 1999.

[195] F. Ulloa and E. Martí, "Wnt won the war: antagonistic role of wnt over shh controls dorso-ventral patterning of the vertebrate neural tube," *Dev. Dyn.*, vol. 239, pp. 69–76, Jan. 2010.

[196] H. Zeng, M. Guo, K. Martins-Taylor, X. Wang, Z. Zhang, J. W. Park, S. Zhan, M. S. Kronenberg, A. Lichtler, H.-X. Liu, F.-P. Chen, L. Yue, X.-J. Li, and R.-H. Xu, "Specification of region-specific neurons including forebrain glutamatergic neurons from human induced pluripotent stem cells," *PLoS One*, vol. 5, p. e11853, July 2010.

[197] R. Patani, A. J. Hollins, T. M. Wishart, C. A. Puddifoot, S. Alvarez, A. R. de Lera, D. J. A. Wyllie, D. A. S. Compston, R. A. Pedersen, T. H. Gillingwater, G. E. Hardingham, N. D. Allen, and S. Chandran, "Retinoid-independent motor neurogenesis from human embryonic stem cells reveals a medial columnar ground state," *Nat. Commun.*, vol. 2, p. 214, 2011.

[198] B.-Y. Hu, J. P. Weick, J. Yu, L.-X. Ma, X.-Q. Zhang, J. A. Thomson, and S.-C. Zhang, "Neural differentiation of human induced pluripotent stem cells follows developmental principles but with variable potency," *Proc. Natl. Acad. Sci. U. S. A.*, vol. 107, pp. 4335–4340, Mar. 2010.

[199] C. Grienberger and A. Konnerth, "Imaging calcium in neurons," *Neuron*, vol. 73, pp. 862–885, Mar. 2012.

[200] G. C. Magou, B. J. Pfister, and J. R. Berlin, "Effect of acute stretch injury on action potential and network activity of rat neocortical neurons in culture," *Brain Res.*, vol. 1624, pp. 525–535, Oct. 2015.

[201] B. J. Pfister, T. P. Weihs, M. Betenbaugh, and G. Bao, "An in vitro uniaxial stretch model for axonal injury," *Ann. Biomed. Eng.*, vol. 31, pp. 589–598, May 2003.

[202] X. Wang and E. I. Gruenstein, "Mechanism of synchronized ca2+ oscillations in cortical neurons," *Brain Res.*, vol. 767, pp. 239–249, Sept. 1997.

[203] K. Mann, C. L. Gallen, and T. R. Clandinin, "Whole-Brain calcium imaging reveals an intrinsic functional network in drosophila," *Curr. Biol.*, vol. 27, pp. 2389–2396.e4, Aug. 2017.

[204] B.-Y. Hu and S.-C. Zhang, "Directed differentiation of neural-stem cells and subtype-specific neurons from hESCs," *Methods Mol. Biol.*, vol. 636, pp. 123–137, 2010.

[205] S. Karumbayaram, B. G. Novitch, M. Patterson, J. A. Umbach, L. Richter, A. Lindgren, A. E. Conway, A. T. Clark, S. A. Goldman, K. Plath, M. Wiedau-Pazos, H. I. Kornblum, and W. E. Lowry, "Directed differentiation of human-induced pluripotent stem cells generates active motor neurons," *Stem Cells*, vol. 27, pp. 806–811, Apr. 2009.

[206] E. Biffi, G. Regalia, A. Menegon, G. Ferrigno, and A. Pedrocchi, "The influence of neuronal density and maturation on network activity of hippocampal cell cultures: a methodological study," *PLoS One*, vol. 8, p. e83899, Dec. 2013.

[207] G. R. Prado, J. D. Ross, S. P. DeWeerth, and M. C. LaPlaca, "Mechanical trauma induces immediate changes in neuronal network activity," *J. Neural Eng.*, vol. 2, pp. 148–158, Dec. 2005.

[208] P. B. Goforth, J. Ren, B. S. Schwartz, and L. S. Satin, "Excitatory synaptic transmission and network activity are depressed following mechanical injury in cortical neurons," *J. Neurophysiol.*, vol. 105, pp. 2350–2363, May 2011.

[209] A. J. Clark, M. S. Kaller, J. Galino, H. J. Willison, S. Rinaldi, and D. L. H. Bennett, "Co-cultures with stem cell-derived human sensory neurons reveal regulators of peripheral myelination," *Brain*, vol. 140, pp. 898–913, Apr. 2017.

[210] P. G. Mazzara, L. Massimino, M. Pellegatta, G. Ronchi, A. Ricca, A. Iannielli, S. G. Giannelli, M. Cursi, C. Cancellieri, A. Sessa, U. Del Carro, A. Quattrini, S. Geuna, A. Gritti, C. Taveggia, and V. Broccoli, "Two factor-based reprogramming of rodent and human fibroblasts into schwann cells," *Nat. Commun.*, vol. 8, p. 14088, Feb. 2017.

[211] C. Rostock, K. Schrenk-Siemens, J. Pohle, and J. Siemens, "Human vs. mouse nociceptors - similarities and differences," *Neuroscience*, Dec. 2017.

[212] J. T. Povlishock, R. L. Hayes, M. E. Michel, and T. K. McINTOSH, "Workshop on animal models of traumatic brain injury," *J. Neurotrauma*, vol. 11, pp. 723–732, Dec. 1994.

[213] D. A. Claassen, M. M. Desler, and A. Rizzino, "ROCK inhibition enhances the recovery and growth of cryopreserved human embryonic stem cells and human induced pluripotent stem cells," *Mol. Reprod. Dev.*, vol. 76, pp. 722–732, Aug. 2009.

[214] U. Singh, R. H. Quintanilla, S. Grecian, K. R. Gee, M. S. Rao, and U. Lakshmipathy, "Novel live alkaline phosphatase substrate for identification of pluripotent stem cells," *Stem Cell Rev.*, vol. 8, pp. 1021–1029, Sept. 2012.

[215] H. Kamble, M. J. Barton, M. Jun, S. Park, and N.-T. Nguyen, "Cell stretching devices as research tools: engineering and biological considerations," *Lab Chip*, vol. 16, pp. 3193–3203, Aug. 2016.

[216] B. Morrison, 3rd, B. S. Elkin, J.-P. Dollé, and M. L. Yarmush, "In vitro models of traumatic brain injury," *Annu. Rev. Biomed. Eng.*, vol. 13, pp. 91–126, Aug. 2011.

[217] A. Kumaria and C. M. Tolias, "In vitro models of neurotrauma," *Br. J. Neurosurg.*, vol. 22, pp. 200–206, Apr. 2008.

[218] R. F. Regan and D. W. Choi, "The effect of NMDA, AMPA/kainate, and calcium channel antagonists on traumatic cortical neuronal injury in culture," *Brain Res.*, vol. 633, pp. 236–242, Jan. 1994.

[219] A. G. Mukhin, S. A. Ivanova, J. W. Allen, and A. I. Faden, "Mechanical injury to neuronal/glial cultures in microplates: role of NMDA receptors and ph in secondary neuronal cell death," *J. Neurosci. Res.*, vol. 51, pp. 748–758, Mar. 1998.

[220] A. G. Mukhin, S. A. Ivanova, S. M. Knoblach, and A. I. Faden, "New in vitro model of traumatic neuronal injury: evaluation of secondary injury and glutamate receptor-mediated neurotoxicity," *J. Neurotrauma*, vol. 14, pp. 651–663, Sept. 1997.

[221] J. B. Kirkpatrick, M. L. Higgins, J. H. Lucas, and G. W. Gross, "In vitro simulation of neural trauma by laser," *J. Neuropathol. Exp. Neurol.*, vol. 44, pp. 268–284, May 1985.

[222] F. Sieg, P. Wahle, and H. C. Pape, "Cellular reactivity to mechanical axonal injury in an organotypic in vitro model of neurotrauma," *J. Neurotrauma*, vol. 16, pp. 1197–1213, Dec. 1999.

[223] M. D. Tang-Schomer, J. D. White, L. W. Tien, L. I. Schmitt, T. M. Valentin, D. J. Graziano, A. M. Hopkins, F. G. Omenetto, P. G. Haydon, and D. L. Kaplan, "Bioengineered functional brain-like cortical tissue," *Proc. Natl. Acad. Sci. U. S. A.*, vol. 111, pp. 13811–13816, 2014.

[224] L. J. Drew and J. N. Wood, "FM1-43 is a permeant blocker of mechanosensitive ion channels in sensory neurons and inhibits behavioural responses to mechanical stimuli," *Mol. Pain*, vol. 3, p. 1, Jan. 2007.

[225] J. H. Lucas and A. Wolf, "In vitro studies of multiple impact injury to mammalian CNS neurons: prevention of perikaryal damage and death by ketamine," *Brain Res.*, vol. 543, pp. 181–193, Mar. 1991.

[226] M. C. LaPlaca, D. K. Cullen, J. J. McLoughlin, and R. S. Cargill, 2nd, "High rate shear strain of three-dimensional neural cell cultures: a new in vitro traumatic brain injury model," *J. Biomech.*, vol. 38, pp. 1093–1105, 2005.

[227] R. S. Chung, J. A. Staal, G. H. McCormack, T. C. Dickson, M. A. Cozens, J. A. Chuckowree, M. C. Quilty, and J. C. Vickers, "Mild axonal stretch injury in vitro induces a progressive series of neurofilament alterations ultimately leading to delayed axotomy," *J. Neurotrauma*, vol. 22, pp. 1081–1091, Oct. 2005.

[228] B.-N. B. Nguyen, J. Chetta, and S. B. Shah, "A novel technology for simultaneous tensile loading and High-Resolution imaging of cells," *Cell. Mol. Bioeng.*, vol. 5, pp. 504–513, Dec. 2012.

[229] E. F. Ellis, J. S. McKinney, K. A. Willoughby, S. Liang, and J. T. Povlishock, "A new model for rapid stretch-induced injury of cells in culture: characterization of the model using astrocytes," *J. Neurotrauma*, vol. 12, pp. 325–339, June 1995.

[230] D. H. Smith, J. A. Wolf, T. A. Lusardi, V. M. Lee, and D. F. Meaney, "High tolerance and delayed elastic response of cultured axons to dynamic stretch injury," *J. Neurosci.*, vol. 19, pp. 4263–4269, June 1999.

[231] B. Morrison, 3rd, D. F. Meaney, and T. K. McIntosh, "Mechanical characterization of an in vitro device designed to quantitatively injure living brain tissue," *Ann. Biomed. Eng.*, vol. 26, pp. 381–390, May 1998.

[232] C.-M. Cheng, Y.-W. Lin, R. M. Bellin, R. L. Steward, Jr, Y.-R. Cheng, P. R. LeDuc, and C.-C. Chen, "Probing localized neural mechanotransduction through surface-modified elastomeric matrices and electrophysiology," *Nat. Protoc.*, vol. 5, pp. 714–724, Apr. 2010.

[233] S. Kobayashi, N. Shizu, Y. Suzuki, T. Asai, and H. Yoshizawa, "Changes in nerve root motion and intraradicular blood flow during an intraoperative straight-leg-raising test," *Spine*, vol. 28, pp. 1427–1434, July 2003.

[234] J. A. Wang, W. Lin, T. Morris, U. Banderali, P. F. Juranka, and C. E. Morris, "Membrane trauma and na+ leak from nav1.6 channels," *Am. J. Physiol. Cell Physiol.*, vol. 297, pp. C823–34, Oct. 2009.

[235] H. Nakadate, Y. Fukumura, Y. Kaneko, A. Kakuta, H. Furukawa, and S. Aomura, "In vitro uniaxial stretch model for evaluating the effect of strain along axon on damage to neurons," *Journal of Biomechanical Science and Engineering*, vol. 9, no. 3, pp. 14–00136, 2014.

[236] Y. Kamotani, T. Bersano-Begey, N. Kato, Y.-C. Tung, D. Huh, J. W. Song, and S. Takayama, "Individually programmable cell stretching microwell arrays actuated by a braille display," *Biomaterials*, vol. 29, pp. 2646–2655, June 2008.

[237] Y. Iwadate and S. Yumura, "Cyclic stretch of the substratum using a shape-memory alloy induces directional migration in dictyostelium cells," *Biotechniques*, vol. 47, pp. 757–767, Sept. 2009.

[238] S. P. Lacour, S. Benmerah, E. Tarte, J. FitzGerald, J. Serra, S. McMahon, J. Fawcett, O. Graudejus, Z. Yu, and B. Morrison, 3rd, "Flexible and stretchable micro-electrodes for in vitro and in vivo neural interfaces," *Med. Biol. Eng. Comput.*, vol. 48, pp. 945–954, Oct. 2010.

[239] M. R. C. Bhattacharya, D. M. Bautista, K. Wu, H. Haeberle, E. A. Lumpkin, and D. Julius, "Radial stretch reveals distinct populations of mechanosensitive mammalian somatosensory neurons," *Proc. Natl. Acad. Sci. U. S. A.*, vol. 105, pp. 20015–20020, Dec. 2008.

[240] K. Shibasaki, N. Murayama, K. Ono, Y. Ishizaki, and M. Tominaga, "TRPV2 enhances axon outgrowth through its activation by membrane stretch in developing sensory and motor neurons," *Journal of Neuroscience*, vol. 30, no. 13, pp. 4601–4612, 2010.

[241] P. Weiss, "Experiments on cell and axon orientation in vitro; the role of colloidal exudates in tissue organization," *J. Exp. Zool.*, vol. 100, pp. 353–386, Dec. 1945.

[242] M. D. Tang-Schomer, A. R. Patel, P. W. Baas, and D. H. Smith, "Mechanical breaking of microtubules in axons during dynamic stretch injury underlies delayed elasticity, microtubule disassembly, and axon degeneration," *FASEB J.*, vol. 24, pp. 1401–1410, May 2010.

[243] Y. C. Yap, T. C. Dickson, A. E. King, M. C. Breadmore, and R. M. Guijt, "Microfluidic culture platform for studying neuronal response to mild to very mild axonal stretch injury," *Biomicrofluidics*, vol. 8, p. 044110, July 2014.

[244] T. K. Kim, J. K. Kim, and O. C. Jeong, "Measurement of nonlinear mechanical properties of PDMS elastomer," *Microelectron. Eng.*, vol. 88, no. 8, pp. 1982–1985, 2011.

[245] I. D. Johnston, D. K. McCluskey, C. Tan, and others, "Mechanical characterization of bulk sylgard 184 for microfluidics and microengineering," *Journal of*, 2014.

[246] F. H. Bieler, C. E. Ott, M. S. Thompson, R. Seidel, S. Ahrens, D. R. Epari, U. Wilkening, K. D. Schaser, S. Mundlos, and G. N. Duda, "Biaxial cell stimulation: A mechanical validation," *J. Biomech.*, vol. 42, pp. 1692–1696, Aug. 2009.

[247] F. Bianchi, M. Malboubi, Y. Li, J. H. George, A. Jerusalem, F. Szele, M. S. Thompson, and H. Ye, "Rapid and efficient differentiation of functional motor neurons from human iPSC for neural injury modelling," *Stem Cell Res.*, vol. 32, pp. 126–134, Oct. 2018.

[248] K. Kusano and H. Gainer, "Modulation of voltage-activated ca currents by pain-inducing agents in a dorsal root ganglion neuronal line, F-11," *J. Neurosci. Res.*, vol. 34, pp. 158–169, Feb. 1993.

[249] P. Thévenaz, R. Delgado-Gonzalo, and M. Unser, "The ovuscule," *IEEE Trans. Pattern Anal. Mach. Intell.*, vol. 33, pp. 382–393, Feb. 2011.

[250] M. Malboubi, Y. Gu, and K. Jiang, "Characterization of surface properties of glass micropipettes using SEM stereoscopic technique," *Microelectron. Eng.*, vol. 88, pp. 2666–2670, Aug. 2011.

[251] J. Brandrup, E. H. Immergut, E. A. Grulke, A. Abe, and D. R. Bloch, *Polymer handbook*, vol. 7. Wiley New York etc, 1989.

[252] D. Tremblay, L. Andrzejewski, A. Leclerc, and A. E. Pelling, "Actin and microtubules play distinct roles in governing the anisotropic deformation of cell nuclei in response to substrate strain," *Cytoskeleton*, vol. 70, pp. 837–848, Dec. 2013.

[253] S. J. Tavalin, E. F. Ellis, and L. S. Satin, "Mechanical perturbation of cultured cortical neurons reveals a stretch-induced delayed depolarization," *J. Neurophysiol.*, vol. 74, pp. 2767–2773, Dec. 1995.

[254] G. C. McCarter, D. B. Reichling, and J. D. Levine, "Mechanical transduction by rat dorsal root ganglion neurons in vitro," *Neurosci. Lett.*, vol. 273, pp. 179–182, Oct. 1999.

[255] S. B. Khatau, C. M. Hale, P. J. Stewart-Hutchinson, M. S. Patel, C. L. Stewart, P. C. Searson, D. Hodzic, and D. Wirtz, "A perinuclear actin cap regulates nuclear shape," *Proc. Natl. Acad. Sci. U. S. A.*, vol. 106, pp. 19017–19022, Nov. 2009.

[256] K. Haase, J. K. L. Macadangdang, C. H. Edrington, C. M. Cuerrier, S. Hadjiantoniou, J. L. Harden, I. S. Skerjanc, and A. E. Pelling, "Extracellular forces cause the nucleus to deform in a highly controlled anisotropic manner," *Sci. Rep.*, vol. 6, p. 21300, Feb. 2016.

[257] A. Iwata, P. K. Stys, J. A. Wolf, X.-H. Chen, A. G. Taylor, D. F. Meaney, and D. H. Smith, "Traumatic axonal injury induces proteolytic cleavage of the voltage-gated sodium channels modulated by tetrodotoxin and protease inhibitors," *J. Neurosci.*, vol. 24, pp. 4605–4613, May 2004.

[258] J. A. Wolf, P. K. Stys, T. Lusardi, D. Meaney, and D. H. Smith, "Traumatic axonal injury induces calcium influx modulated by tetrodotoxin-sensitive sodium channels," *Journal of Neuroscience*, vol. 21, no. 6, pp. 1923–1930, 2001.

[259] M. D. Tang-Schomer, V. E. Johnson, P. W. Baas, W. Stewart, and D. H. Smith, "Partial interruption of axonal transport due to microtubule breakage accounts for the formation of periodic varicosities after traumatic axonal injury," *Exp. Neurol.*, vol. 233, pp. 364–372, Jan. 2012.

[260] S. P. Lacour, C. Tsay, S. Wagner, Z. Yu, and B. Morrison, "Stretchable micro-electrode arrays for dynamic neuronal recording of in vitro mechanically injured brain," in *IEEE Sensors, 2005.*, pp. 4 pp.–, Oct. 2005.

[261] A. J. Maniotis, C. S. Chen, and D. E. Ingber, "Demonstration of mechanical connections between integrins, cytoskeletal filaments, and nucleoplasm that stabilize nuclear structure," *Proc. Natl. Acad. Sci. U. S. A.*, vol. 94, pp. 849–854, Feb. 1997.

[262] S. P. H. Alexander, J. Striessnig, E. Kelly, N. V. Marrion, J. A. Peters, E. Faccenda, S. D. Harding, A. J. Pawson, J. L. Sharman, C. Southan, and Others, "The concise guide to pharmacology 2017/18: Voltage-gated ion channels," *Br. J. Pharmacol.*, vol. 174, no. S1, 2017.

[263] J.-M. Dubois, G. Ouanounou, and B. Rouzaire-Dubois, "The boltzmann equation in molecular biology," *Prog. Biophys. Mol. Biol.*, vol. 99, pp. 87–93, Feb. 2009.

[264] L. P. Endresen, K. Hall, J. S. Høye, and J. Myrheim, "A theory for the membrane potential of living cells," *Eur. Biophys. J.*, vol. 29, no. 2, pp. 90–103, 2000.

[265] R. Phillips, T. Ursell, P. Wiggins, and P. Sens, "Emerging roles for lipids in shaping membrane-protein function," *Nature*, vol. 459, pp. 379–385, May 2009.

[266] A. Longstaff, *Neuroscience (Instant notes)*. Springer, 2000.

[267] W. J. Tyler, "The mechanobiology of brain function," *Nat. Rev. Neurosci.*, vol. 13, pp. 867–878, Dec. 2012.

[268] H. Y. Kueh and T. J. Mitchison, "Structural plasticity in actin and tubulin polymer dynamics," *Science*, vol. 325, pp. 960–963, Aug. 2009.

[269] S. I. Sukharev, P. Blount, B. Martinac, and C. Kung, "Mechanosensitive channels of escherichia coli: the MscL gene, protein, and activities," *Annu. Rev. Physiol.*, vol. 59, pp. 633–657, 1997.

[270] J. Teng, S. Loukin, A. Anishkin, and C. Kung, "The force-from-lipid (FFL) principle of mechanosensitivity, at large and in elements," *Pflugers Arch.*, vol. 467, pp. 27–37, Jan. 2015.

[271] S. G. Brohawn, Z. Su, and R. MacKinnon, "Mechanosensitivity is mediated directly by the lipid membrane in TRAAK and TREK1 k+ channels," *Proc. Natl. Acad. Sci. U. S. A.*, vol. 111, pp. 3614–3619, Mar. 2014.

[272] I. Tasaki, K. Kusano, and P. M. Byrne, "Rapid mechanical and thermal changes in the garfish olfactory nerve associated with a propagated impulse," *Biophys. J.*, vol. 55, pp. 1033–1040, June 1989.

[273] L. A. MacQueen, M. D. Buschmann, and M. R. Wertheimer, "Mechanical properties of mammalian cells in suspension measured by electro-deformation," *J. Micromech. Microeng.*, vol. 20, p. 065007, May 2010.

[274] G. H. Kim, P. Kosterin, A. L. Obaid, and B. M. Salzberg, "A mechanical spike accompanies the action potential in mammalian nerve terminals," *Biophys. J.*, vol. 92, pp. 3122–3129, May 2007.

[275] V. Viatchenko-Karpinski and J. G. Gu, "Mechanical sensitivity and electrophysiological properties of acutely dissociated dorsal root ganglion neurons of rats," *Neurosci. Lett.*, vol. 634, pp. 70–75, Nov. 2016.

[276] C. E. Morris, E. A. Prikryl, and B. Joós, "Mechanosensitive gating of kv channels," *PLoS One*, vol. 10, p. e0118335, Feb. 2015.

[277] C. E. Morris, "Voltage-gated channel mechanosensitivity: fact or friction?," *Front. Physiol.*, vol. 2, p. 25, May 2011.

[278] H. Jerabek, G. Pabst, M. Rappolt, and T. Stockner, "Membrane-mediated effect on ion channels induced by the anesthetic drug ketamine," *J. Am. Chem. Soc.*, vol. 132, pp. 7990–7997, June 2010.

[279] G. R. Tibbs, D. J. Posson, and P. A. Goldstein, "Voltage-Gated ion channels in the PNS: Novel therapies for neuropathic pain?," *Trends Pharmacol. Sci.*, vol. 37, pp. 522–542, July 2016.

[280] A. Verkhratsky, O. A. Krishtal, and O. H. Petersen, "From galvani to patch clamp: the development of electrophysiology," *Pflugers Arch.*, vol. 453, pp. 233–247, Dec. 2006.

[281] E. Neher and B. Sakmann, "Single-channel currents recorded from membrane of denervated frog muscle fibres," *Nature*, vol. 260, pp. 799–802, 1976.

[282] O. P. Hamill, A. Marty, E. Neher, B. Sakmann, and F. J. Sigworth, "Improved patch-clamp techniques for high-resolution current recording from cells and cell-free membrane patches," *Pflugers Arch.*, vol. 391, pp. 85–100, 1981.

[283] H. Sontheimer and M. L. Olsen, "Whole-Cell Patch-Clamp recordings," in *Patch-Clamp Analysis*, Neuromethods, pp. 35–68, Humana Press, 2007.

[284] Y. Zhao, S. Inayat, D. A. Dikin, J. H. Singer, R. S. Ruoff, and J. B. Troy, "Patch clamp technique: Review of the current state of the art and potential contributions from nanoengineering," *Proceedings of the Institution of Mechanical Engineers, Part N: Journal of Nanoengineering and Nanosystems*, vol. 222, pp. 1–11, Mar. 2008.

[285] D. Smetters, A. Majewska, and R. Yuste, "Detecting action potentials in neuronal populations with calcium imaging," *Methods*, vol. 18, pp. 215–221, June 1999.

[286] D. J. Sharp, G. Scott, and R. Leech, "Network dysfunction after traumatic brain injury," *Nat. Rev. Neurol.*, vol. 10, pp. 156–166, Mar. 2014.

[287] J. A. Lundbæk, P. Birn, J. Girshman, A. J. Hansen, and O. S. Andersen, "Membrane stiffness and channel function," *Biochemistry*, vol. 35, no. 12, pp. 3825–3830, 1996.

[288] Y. Qi, L. Andolfi, F. Frattini, F. Mayer, M. Lazzarino, and J. Hu, "Membrane stiffening by STOML3 facilitates mechanosensation in sensory neurons," *Nat. Commun.*, vol. 6, p. 8512, Oct. 2015.

[289] U. Laitko, P. F. Juranka, and C. E. Morris, "Membrane stretch slows the concerted step prior to opening in a kv channel," *J. Gen. Physiol.*, vol. 127, pp. 687–701, June 2006.

[290] J. A. Lundbaek, P. Birn, A. J. Hansen, R. Søgaard, C. Nielsen, J. Girshman, M. J. Bruno, S. E. Tape, J. Egebjerg, D. V. Greathouse, G. L. Mattice, R. E. Koeppe, 2nd, and O. S. Andersen, "Regulation of sodium channel function by bilayer elasticity: the importance of hydrophobic coupling. effects of micelle-forming amphiphiles and cholesterol," *J. Gen. Physiol.*, vol. 123, pp. 599–621, May 2004.

[291] D. Needham and R. S. Nunn, "Elastic deformation and failure of lipid bilayer membranes containing cholesterol," *Biophys. J.*, vol. 58, pp. 997–1009, Oct. 1990.

[292] A. E. Christian, M. P. Haynes, M. C. Phillips, and G. H. Rothblat, "Use of cyclodextrins for manipulating cellular cholesterol content," *J. Lipid Res.*, vol. 38, pp. 2264–2272, Nov. 1997.

[293] Z. Al-Rekabi and S. Contera, "Multifrequency AFM reveals lipid membrane mechanical properties and the effect of cholesterol in modulating viscoelasticity," *Proc. Natl. Acad. Sci. U. S. A.*, vol. 115, pp. 2658–2663, Mar. 2018.

[294] Y.-T. Yang, J.-D. Liao, C.-C. K. Lin, C.-T. Chang, S.-H. Wang, and M.-S. Ju, "Characterization of cholesterol-depleted or -restored cell membranes by depth-sensing nano-indentation," *Soft Matter*, vol. 8, pp. 682–687, Dec. 2011.

[295] O. Zamir and M. P. Charlton, "Cholesterol and synaptic transmitter release at crayfish neuromuscular junctions," *J. Physiol.*, vol. 571, pp. 83–99, Feb. 2006.

[296] A. R. Koudinov and N. V. Koudinova, "Essential role for cholesterol in synaptic plasticity and neuronal degeneration," *FASEB J.*, vol. 15, pp. 1858–1860, Aug. 2001.

[297] F. J. Barrantes, "Structural basis for lipid modulation of nicotinic acetylcholine receptor function," *Brain Res. Rev.*, vol. 47, pp. 71–95, Dec. 2004.

[298] I. Levitan, Y. Fang, A. Rosenhouse-Dantsker, and V. Romanenko, "Cholesterol and ion channels," in *Cholesterol Binding and Cholesterol Transport Proteins:*, vol. 51 of *Subcellular Biochemistry*, pp. 509–549, Springer, Dordrecht, 2010.

[299] T. S. Tillman and M. Cascio, "Effects of membrane lipids on ion channel structure and function," *Cell Biochem. Biophys.*, vol. 38, no. 2, pp. 161–190, 2003.

[300] A. A. Spector and M. A. Yorek, "Membrane lipid composition and cellular function," *J. Lipid Res.*, vol. 26, pp. 1015–1035, Sept. 1985.

[301] J. Guo, S. Chi, H. Xu, G. Jin, and Z. Qi, "Effects of cholesterol levels on the excitability of rat hippocampal neurons," *Mol. Membr. Biol.*, vol. 25, pp. 216–223, Apr. 2008.

[302] R. Zidovetzki and I. Levitan, "Use of cyclodextrins to manipulate plasma membrane cholesterol content: evidence, misconceptions and control strategies," *Biochim. Biophys. Acta*, vol. 1768, pp. 1311–1324, June 2007.

[303] E. Sezgin, T. Sadowski, and K. Simons, "Measuring lipid packing of model and cellular membranes with environment sensitive probes," *Langmuir*, vol. 30, pp. 8160–8166, July 2014.

[304] V. Pereno, D. Carugo, L. Bau, E. Sezgin, J. Bernardino de la Serna, C. Eggeling, and E. Stride, "Electroformation of giant unilamellar vesicles on stainless steel electrodes," *ACS Omega*, vol. 2, pp. 994–1002, Mar. 2017.

[305] M. Aron, R. Browning, D. Carugo, E. Sezgin, J. Bernardino de la Serna, C. Eggeling, and E. Stride, "Spectral imaging toolbox: segmentation, hyperstack reconstruction, and batch processing of spectral images for the determination of cell and model membrane lipid order," *BMC Bioinformatics*, vol. 18, p. 254, May 2017.

[306] T. J. B. Simons, "Calcium and neuronal function," *Neurosurg. Rev.*, vol. 11, pp. 119–129, June 1988.

[307] M. E. Wall, P. S. Weinhold, T. Siu, T. D. Brown, and A. J. Banes, "Comparison of cellular strain with applied substrate strain in vitro," *J. Biomech.*, vol. 40, no. 1, pp. 173–181, 2007.

[308] K. Yamamoto and J. Ando, "Endothelial cell and model membranes respond to shear stress by rapidly decreasing the order of their lipid phases," *J. Cell Sci.*, vol. 126, pp. 1227–1234, Mar. 2013.

[309] K. Yamamoto and J. Ando, "Vascular endothelial cell membranes differentiate between stretch and shear stress through transitions in their lipid phases," *Am. J. Physiol. Heart Circ. Physiol.*, vol. 309, pp. H1178–85, Oct. 2015.

[310] G. Y. Sun and A. Y. Sun, "Ethanol and membrane lipids," *Alcohol. Clin. Exp. Res.*, vol. 9, pp. 164–180, Mar. 1985.

[311] Y. Jimbo, H. P. Robinson, and A. Kawana, "Simultaneous measurement of intracellular calcium and electrical activity from patterned neural networks in culture," *IEEE Trans. Biomed. Eng.*, vol. 40, pp. 804–810, Aug. 1993.

[312] E. H. Pettus, C. W. Christman, M. L. Giebel, and J. T. Povlishock, "Traumatically induced altered membrane permeability: its relationship to traumatically induced reactive axonal change," *J. Neurotrauma*, vol. 11, pp. 507–522, Oct. 1994.

[313] B. M. Witgen, J. Lifshitz, M. L. Smith, E. Schwarzbach, S.-L. Liang, M. S. Grady, and A. S. Cohen, "Regional hippocampal alteration associated with cognitive deficit following experimental brain injury: A systems, network and cellular evaluation," *Neuroscience*, vol. 133, pp. 1–15, Jan. 2005.

[314] G. Saulis, M. S. Venslauskas, and J. Naktinis, "Kinetics of pore resealing in cell membranes after electroporation," *J. Electroanal. Chem. Interfacial Electrochem.*, vol. 321, pp. 1–13, Aug. 1991.

[315] F. Schroeder, J. K. Woodford, J. Kavecansky, W. G. Wood, and C. Joiner, "Cholesterol domains in biological membranes," *Mol. Membr. Biol.*, vol. 12, pp. 113–119, Jan. 1995.

[316] N. E. Vlahakis, M. A. Schroeder, R. E. Pagano, and R. D. Hubmayr, "Role of deformation-induced lipid trafficking in the prevention of plasma membrane stress failure," *Am. J. Respir. Crit. Care Med.*, vol. 166, pp. 1282–1289, Nov. 2002.

[317] T. J. Pucadyil and A. Chattopadhyay, "Effect of cholesterol on lateral diffusion of fluorescent lipid probes in native hippocampal membranes," *Chem. Phys. Lipids*, vol. 143, pp. 11–21, Sept. 2006.

[318] J. T. Weber, B. A. Rzigalinski, K. A. Willoughby, S. F. Moore, and E. F. Ellis, "Alterations in calcium-mediated signal transduction after traumatic injury of cortical neurons," *Cell Calcium*, vol. 26, pp. 289–299, Dec. 1999.

[319] G. G. Gurkoff, K. Shahlaie, and B. G. Lyeth, "In vitro mechanical strain trauma alters neuronal calcium responses: Implications for posttraumatic epilepsy," *Epilepsia*, vol. 53 Suppl 1, pp. 53–60, June 2012.

[320] S. M. Ahmed, B. A. Rzigalinski, K. A. Willoughby, H. A. Sitterding, and E. F. Ellis, "Stretch-induced injury alters mitochondrial membrane potential and cellular ATP in cultured astrocytes and neurons," *J. Neurochem.*, vol. 74, pp. 1951–1960, May 2000.

[321] T. J. Yuen, K. D. Browne, A. Iwata, and D. H. Smith, "Sodium channelopathy induced by mild axonal trauma worsens outcome after a repeat injury," *J. Neurosci. Res.*, vol. 87, pp. 3620–3625, Dec. 2009.

[322] C. E. Morris and P. F. Juranka, "Nav channel mechanosensitivity: activation and inactivation accelerate reversibly with stretch," *Biophys. J.*, vol. 93, pp. 822–833, Aug. 2007.

[323] A. Beyder, J. L. Rae, C. Bernard, P. R. Strege, F. Sachs, and G. Farrugia, "Mechanosensitivity of nav1. 5, a voltage-sensitive sodium channel," *J. Physiol.*, vol. 588, no. 24, pp. 4969–4985, 2010.

[324] D. Schmidt and R. MacKinnon, "Voltage-dependent k+ channel gating and voltage sensor toxin sensitivity depend on the mechanical state of the lipid membrane," *Proc. Natl. Acad. Sci. U. S. A.*, vol. 105, pp. 19276–19281, Dec. 2008.

[325] S. H. Romer, K. M. Dominguez, M. W. Gelpi, A. S. Deardorff, R. C. Tracy, and R. E. W. Fyffe, "Redistribution of kv2.1 ion channels on spinal motoneurons following peripheral nerve injury," *Brain Res.*, vol. 1547, pp. 1–15, Feb. 2014.

[326] J. Prucha, J. Krusek, I. Dittert, V. Sinica, A. Kadkova, and V. Vlachova, "Acute exposure to high-induction electromagnetic field affects activity of model peripheral sensory neurons," *J. Cell. Mol. Med.*, vol. 22, no. 2, pp. 1355–1362, 2018.

[327] Q. Y. Zhang, Y. Y. Zhang, J. Xie, C. X. Li, W. Y. Chen, and others, "Stiff substrates enhance cultured neuronal network activity," *Scientific Reports*, 2014.

[328] M. Kwong and A. Jrusalem, "Localised membrane geometrical deformation by bleb-inducing aspiration causes patch-clamp 'left-shift'," *In prepartion*, 2018.

[329] D. M. Geddes-Klein, K. B. Schiffman, and D. F. Meaney, "Mechanisms and consequences of neuronal stretch injury in vitro differ with the model of trauma," *J. Neurotrauma*, vol. 23, pp. 193–204, Feb. 2006.

[330] L. Huang, W. Li, B. Li, and F. Zou, "Activation of ATP-sensitive K channels protects hippocampal CA1 neurons from hypoxia by suppressing p53 expression," *Neurosci. Lett.*, vol. 398, pp. 34–38, May 2006.

[331] M. Tabatabai and A. M. Booth, "Effects of lidocaine on the excitability and membrane properties of the nerve cell soma," *Clin. Physiol. Biochem.*, vol. 8, no. 6, pp. 289–296, 1990.

[332] C. E. Morris, P. F. Juranka, and B. Joós, "Perturbed voltage-gated channel activity in perturbed bilayers: implications for ectopic arrhythmias arising from damaged membrane," *Prog. Biophys. Mol. Biol.*, vol. 110, pp. 245–256, Oct. 2012.

[333] D. Krepkiy, M. Mihailescu, J. A. Freites, E. V. Schow, D. L. Worcester, K. Gawrisch, D. J. Tobias, S. H. White, and K. J. Swartz, "Structure and hydration of membranes embedded with voltage-sensing domains," *Nature*, vol. 462, pp. 473–479, Nov. 2009.

[334] B. N. Johnson, K. Z. Lancaster, I. B. Hogue, F. Meng, Y. L. Kong, L. W. Enquist, and M. C. McAlpine, "3D printed nervous system on a chip," *Lab Chip*, vol. 16, pp. 1393–1400, Apr. 2016.

[335] R. M. Huval, O. H. Miller, J. L. Curley, Y. Fan, B. J. Hall, and M. J. Moore, "Microengineered peripheral nerve-on-a-chip for preclinical physiological testing," *Lab Chip*, vol. 15, pp. 2221–2232, May 2015.

[336] V. T. Ribeiro-Resende, B. Koenig, S. Nichterwitz, S. Oberhoffner, and B. Schlosshauer, "Strategies for inducing the formation of bands of büngner in peripheral nerve regeneration," *Biomaterials*, vol. 30, pp. 5251–5259, Oct. 2009.

[337] N. Callizot, M. Combes, R. Steinschneider, and P. Poindron, "A new long term in vitro model of myelination," *Exp. Cell Res.*, vol. 317, pp. 2374–2383, 2011.

[338] S. D. Zack-Williams, P. E. Butler, and D. M. Kalaskar, "Current progress in use of adipose derived stem cells in peripheral nerve regeneration," *World J. Stem Cells*, vol. 7, pp. 51–64, Jan. 2015.

[339] H.-S. Kim, J. Lee, D. Y. Lee, Y.-D. Kim, J. Y. Kim, H. J. Lim, S. Lim, and Y. S. Cho, "Schwann cell precursors from human pluripotent stem cells as a potential therapeutic target for myelin repair," *Stem Cell Reports*, vol. 8, pp. 1714–1726, June 2017.

[340] B. E. Kerman, H. J. Kim, K. Padmanabhan, A. Mei, S. Georges, M. S. Joens, J. A. J. Fitzpatrick, R. Jappelli, K. J. Chandross, P. August, and F. H. Gage, "In vitro myelin formation using embryonic stem cells," *Development*, vol. 142, pp. 2213–2225, June 2015.

[341] S. Xie, F. Lu, J. Han, K. Tao, H. Wang, A. Simental, D. Hu, and H. Yang, "Efficient generation of functional schwann cells from adipose-derived stem cells in defined conditions," *Cell Cycle*, vol. 16, pp. 841–851, May 2017.

[342] S. Cai, Y.-P. Tsui, K.-W. Tam, G. K.-H. Shea, R. S.-K. Chang, Q. Ao, D. K.-Y. Shum, and Y.-S. Chan, "Directed differentiation of human bone marrow stromal cells to Fate-Committed schwann cells," *Stem Cell Reports*, vol. 9, pp. 1097–1108, Oct. 2017.

[343] K. Sanen, W. Martens, M. Georgiou, M. Ameloot, I. Lambrichts, and J. Phillips, "Engineered neural tissue with schwann cell differentiated human dental pulp stem cells: potential for peripheral nerve repair?," *J. Tissue Eng. Regen. Med.*, vol. 11, pp. 3362–3372, Dec. 2017.

[344] Y. Xu, Z. Liu, L. Liu, C. Zhao, F. Xiong, C. Zhou, Y. Li, Y. Shan, F. Peng, and C. Zhang, "Neurospheres from rat adipose-derived stem cells could be induced into functional schwann cell-like cells in vitro," *BMC Neurosci.*, vol. 9, p. 21, Feb. 2008.

[345] N. G. Fairbairn, A. M. Meppelink, J. Ng-Glazier, M. A. Randolph, and J. M. Winograd, "Augmenting peripheral nerve regeneration using stem cells: A review of current opinion," *World J. Stem Cells*, vol. 7, pp. 11–26, Jan. 2015.

[346] A. Faroni, R. J. P. Smith, L. Lu, and A. J. Reid, "Human schwann-like cells derived from adipose-derived mesenchymal stem cells rapidly de-differentiate in the absence of stimulating medium," *Eur. J. Neurosci.*, Aug. 2015.

[347] D. Widera, P. Heimann, C. Zander, Y. Imielski, M. Heidbreder, M. Heilemann, C. Kaltschmidt, and B. Kaltschmidt, "Schwann cells can be reprogrammed to multipotency by culture," *Stem Cells Dev.*, vol. 20, pp. 2053–2064, Dec. 2011.

[348] M. Brohlin, D. Mahay, L. N. Novikov, G. Terenghi, M. Wiberg, S. G. Shawcross, and L. N. Novikova, "Characterisation of human mesenchymal stem cells following differentiation into schwann cell-like cells," *Neurosci. Res.*, vol. 64, pp. 41–49, May 2009.

[349] J. A. Richardson, C. W. Rementer, J. M. Bruder, and D. Hoffman-Kim, "Guidance of dorsal root ganglion neurites and schwann cells by isolated schwann cell topography on poly(dimethyl siloxane) conduits and films," *J. Neural Eng.*, vol. 8, p. 046015, 2011.

[350] M. Georgiou, J. P. Golding, A. J. Loughlin, P. J. Kingham, and J. B. Phillips, "Engineered neural tissue with aligned, differentiated adipose-derived stem cells promotes peripheral nerve regeneration across a critical sized defect in rat sciatic nerve," *Biomaterials*, vol. 37, pp. 242–251, 2015.

[351] E. Soliman, F. Bianchi, J. N. Sleigh, J. H. George, M. Z. Cader, Z. Cui, and H. Ye, "Engineered method for directional growth of muscle sheets on electrospun fibers," *J. Biomed. Mater. Res. A*, Dec. 2017.

[352] M. Stettner, K. Wolffram, A. K. Mausberg, C. Wolf, S. Heikaus, A. Derksen, T. Dehmel, and B. C. Kieseier, "A reliable in vitro model for studying peripheral nerve myelination in mouse," *J. Neurosci. Methods*, vol. 214, pp. 69–79, Mar. 2013.

[353] R. H. Coy, O. R. Evans, J. B. Phillips, and R. J. Shipley, "An integrated theoretical-experimental approach to accelerate translational tissue engineering," *J. Tissue Eng. Regen. Med.*, vol. 12, no. 1, pp. e53–e59, 2018.

[354] N. Shanks, R. Greek, and J. Greek, "Are animal models predictive for humans?," *Philos. Ethics Humanit. Med.*, vol. 4, p. 2, Jan. 2009.

[355] R. Heywood, "Clinical Toxicity–Could it have been predicted? post-marketing experience," *Animal Toxicity Studies: Their Relevance for Man*, pp. 57–67, 1990.

[356] B. E. Layton and A. M. Sastry, "A mechanical model for collagen fibril load sharing in peripheral nerve of diabetic and nondiabetic rats," *J. Biomech. Eng.*, vol. 126, pp. 803–814, Dec. 2004.

[357] R. Skloot, *The immortal life of Henrietta Lacks*. Crown Publishers, New York, 2010.

[358] A. Lavazza and M. Massimini, "Cerebral organoids: ethical issues and consciousness assessment," *J. Med. Ethics*, Feb. 2018.

[359] N. A. Farahany, H. T. Greely, S. Hyman, C. Koch, C. Grady, S. P. Paca, N. Sestan, P. Arlotta, J. L. Bernat, J. Ting, J. E. Lunshof, E. P. R. Iyer, I. Hyun, B. H. Capestany, G. M. Church, H. Huang, and H. Song, "The ethics of experimenting with human brain tissue," *Nature*, vol. 556, pp. 429–432, Apr. 2018.

[360] G. Stoll I, Y. L. C., B. D. Trapp, and J. W. Griffin, "Expression of NGF-receptors during immune-mediated and lysolecithin-induced demyelination of the peripheral nervous system," *J. Neurocytol.*, vol. 22, pp. 1022–1029, 1993.

[361] D. M. Geddes-Klein, G. Serbest, M. N. Mesfin, A. S. Cohen, and D. F. Meaney, "Pharmacologically induced calcium oscillations protect neurons from increases in cytosolic calcium after trauma," *J. Neurochem.*, vol. 97, pp. 462–474, Apr. 2006.